FORMATION AND GROWTH MECHANISMS OF SINGLE-WALLED METAL OXIDE NANOTUBES

A Dissertation
Presented to
The Academic Faculty

by

Gulfem Ipek Yucelen

In Partial Fulfillment
of the Requirements for the Degree
Doctor of Philosophy in the
School of Materials Science and Engineering

Georgia Institute of Technology
August 2012

FORMATION AND GROWTH MECHANISMS OF SINGLE-WALLED METAL OXIDE NANOTUBES

Approved by:

Dr. Haskell W. Beckham, Advisor
School of Materials Science and Engineering
Georgia Institute of Technology

Dr. Elizabeth R. Wright
School of Medicine and Children's Healthcare of Atlanta
Emory University

Dr. Sankar Nair, Advisor
School of Chemical and Biomolecular Engineering
Georgia Institute of Technology

Dr. Facundo M. Fernandez
School of Chemistry and Biochemistry
Georgia Institute of Technology

Dr. Christopher W. Jones
School of Chemical and Biomolecular Engineering
Georgia Institute of Technology

Dr. Gleb Yushin
School of Materials Science and Engineering
Georgia Institute of Technology

Date Approved: May 30th, 2012

This dissertation is dedicated to the memory of my grandmother

ACKNOWLEDGEMENTS

I would like to thank my advisors Prof. Sankar Nair and Prof. Haskell W. Beckham for their continuous support, advice, and guidance at all times during my PhD research. Without their persistent help this dissertation would not have been possible. My special thanks go also to the members of my advisory committee, Prof. Christopher W. Jones, Prof. Elizabeth R. Wright, Prof. Facundo M. Fernandez, and Prof. Gleb Yushin for their insightful comments and valuable suggestions.

I wish to express my warm and sincere thanks to Prof. Elizabeth R. Wright and Dr. Ricardo C. Guerrero-Ferreira for their help and support during cyro-EM experiments. I also warmly thank Prof. Facundo M. Fernandez for giving me the opportunity to use his Q-TOF mass spectrometer; and his student Christina Jones for her friendly help in data collection. I am deeply grateful to Prof. Ingeborg Schmidt-Krey for giving me the opportunity to use JEOL JEM-1400 microscope as an independent user and for her kind assistance while working on the microscope.

I owe my sincere gratitude to Dr. Johannes Leisen who helped me for solid-state NMR measurements. His kind support and guidance have been of great value in this study.

I also wish to thank my colleagues Dr. Ryan Kincer and Dr. Dun-Yen Kang for their continuous help with my experiments.

Finally, I would like to express my deepest gratitude to my family for their never-ending love and support.

TABLE OF CONTENTS

LIST OF TABLES

Page

LIST OF FIGURES

Page

SUMMARY

Single-walled metal oxide nanotubes have emerged as an important class of 'building block' materials for molecular recognition-based applications in catalysis, separations, sensing, and molecular encapsulation due to their vast range of potentially accessible compositions and structures, and their unique properties such as well-defined wall structure and porosity, tunable dimensions, and chemically modifiable interior and exterior surfaces. However, their widespread application will depend on the development of synthesis processes that can yield structurally and compositionally well-controlled nanotubes. Moreover, such processes should be amenable to scale-up and preferably operate via benign chemistries under mild conditions. There is currently very little knowledge on the molecular-level 'design rules' underlying the engineering of such materials.

The capability to engineer single-walled tubular materials would lead to a range of structures, with novel properties relevant to diverse applications. In this thesis, main objectives are to discover the first molecular-level mechanistic framework governing the formation and growth of single-walled metal-oxide nanotubes, apply this framework to demonstrate the engineering of nanotubular materials of controlled dimensions, and to progress towards a quantitative multiscale understanding of nanotube formation. The class of aluminosilicate (AlSiOH)/germanate (AlGeOH) nanotubes are of particular interest to us, and serve as the exemplar materials for single-walled metal oxide nanotubes. They can be synthesized in pure form from inexpensive and easily accessible

reactants at low temperatures (95 ˚C) from aqueous solutions. The synthesis of nanotubes occurs on a time-scale of hours to days, making them an ideal model system to study the nanotube formation mechanism.

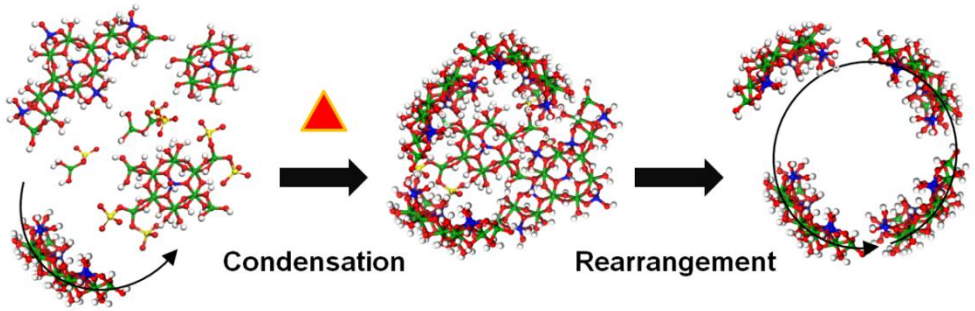

Chapter 2 – Experimental and computational investigations are combined to construct the first molecular-level mechanism of the formation of single-walled aluminosilicate nanotube objects. It is shown that specific "proto-nanotube-like" intermediates with inherent curvature form in aqueous synthesis solutions immediately after initial hydrolysis of reactants. Upon heating, they condense and rearrange to form ordered single-walled aluminosilicate nanotubes. The presented study clearly indicates a path towards engineering new classes of nanoscale materials in the liquid phase *via* identification and control of the molecular precursor species present in synthesis solutions [1].

In Chapter 2, the identification and elucidation of the mechanistic role of molecular precursors and nanoscale (1−3 nm) intermediates with intrinsic curvature, in the formation of single-walled aluminosilicate nanotubes is reported. The structural and compositional evolution of molecular and nanoscale species over a length scale of 0.1−100 nm, are characterized by electrospray ionization (ESI) mass spectrometry, and nuclear magnetic resonance (NMR) spectroscopy. DFT calculations revealed the intrinsic curvature of nanoscale intermediates with bonding environments similar to the structure of the final nanotube product. It is shown that curved nano-intermediates form in aqueous synthesis solutions immediately after initial hydrolysis of reactants at 25 ˚C, disappear

from the solution upon heating to 95 ˚C due to condensation, and finally rearrange to form ordered single-walled aluminosilicate nanotubes. Integration of all results leads to the construction of the first molecular-level mechanism of single-walled metal oxide nanotube formation, incorporating the role of monomeric and polymeric aluminosilicate species as well as larger nanoparticles.

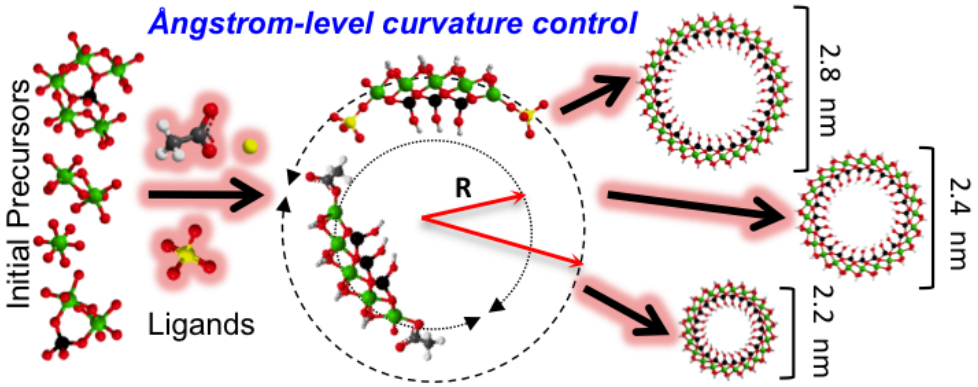

Chapter 3 – It is shown that different kinds of anionic species can be used to exert control over the shapes of nanotube-forming precursors, and that these shapes assemble into nanotubes with precisely-controlled diameter that correlate strongly with the curvature of the 'shaped' precursors [2].

Then, in Chapter 3, new molecular-level concepts for constructing nanoscopic metal oxide objects are demonstrated. The diameters of metal oxide nanotubes are shaped with Ångstrom-level precision by controlling the shape of nanometer-scale precursors. The subtle relationships between precursor shape and structure and final nanotube curvature are measured (at the molecular level). Anionic ligands (both organic and inorganic) are used to exert fine control over precursor shapes, allowing assembly into nanotubes whose diameters relate directly to the curvatures of shaped precursors.

Having obtained considerable insight into aluminosilicate nanotube formation, in Chapter 4 the complex aqueous chemistry of nanotube-forming aluminogermanate solutions are examined. The aluminogermanate system is particularly interesting since it forms ultra-short nanotubes of lengths as small as ~20 nm. Insights into the underlying important mechanistic differences between aluminogermanate and aluminosilicate nanotube growth as well as structural differences in the final nanotube dimensions are provided. Furthermore, an experimental example of control over nanotube length is shown, using the understanding of the mechanistic differences, along with further suggestions for possible ways of controlling nanotube lengths.

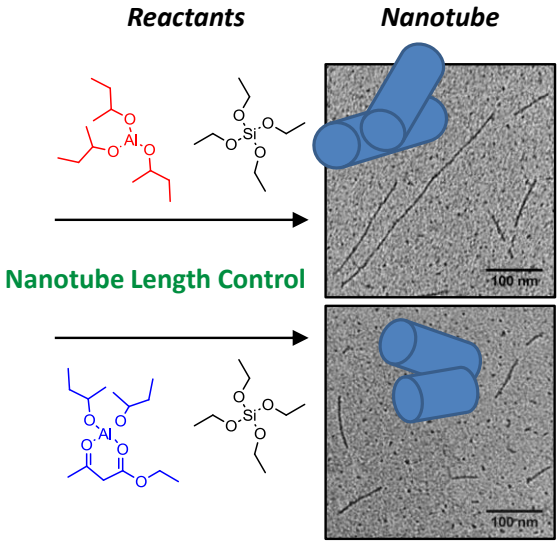

Chapter 4 – Mechanistic differences between aluminogermanate and aluminosilicate nanotube formation and growth are discussed. An experimental example that uses different reactants is given as a possible way to achieve control over nanotube lengths.

Ultimately, it is desired to produce the single-walled aluminosilicate nanotubes on a larger scale (e.g., kilogram or ton scales) for technological application. However, a quantitative multiscale understanding of nanotube growth via a detailed growth model, is

critical to be able to predict and control key properties such as the length distribution and concentration of the nanotubes. Such a model can then be used to design liquid-phase reactors for scale-up of nanotube synthesis. In Chapter 5, a generalized kinetic model is formulated to describe the reactions leading to formation and growth of single-walled metal oxide nanotubes. This model is capable of explaining and predicting the evolution of nanotube populations as a function of kinetic parameters. It also allows considerable insight into meso/microscale nanotube growth processes. For example, it shows that two different mechanisms operate during nanotube growth: (1) growth by precursor addition, and (2) by oriented attachment of nanotubes to each other.

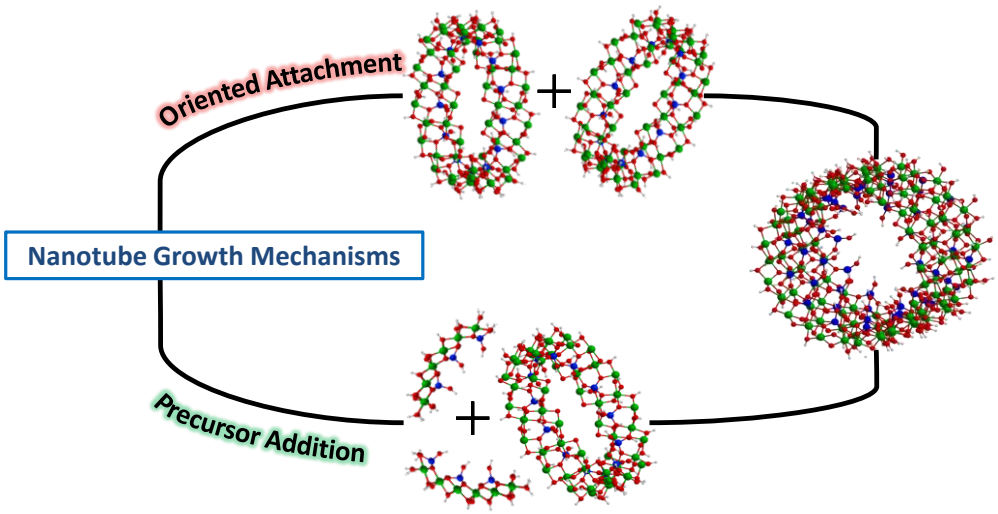

Chapter 5 – A generalized kinetic model is formulated to describe the reaction stages leading to formation and growth of single-walled metal oxide nanotubes that is capable of explaining and predicting experimental nanotube length populations obtained by TEM at defined synthesis times. The model shows that two different mechanisms are effective in the process of nanotube growth: (1) precursor addition and (2) oriented attachment.

In Chapter 6, a study of the structure of the nanotube walls is presented. It has usually been assumed in the literature that the nanotube wall is free of defects. A detailed

investigation of the defect structures in aluminosilicate single-walled nanotubes via multiple advanced solid-state NMR techniques is reported. A combination of ^{1}H-^{29}Si and ^{1}H-^{27}Al FSLG-HETCOR, ^{1}H CRAMPS, and ^{1}H-^{29}Si CP/MAS NMR experiments were employed to evaluate the proton environments around Al and Si atoms during nanotube synthesis and in the final structure. The HETCOR experiments allowed to track the evolving Si and Al environments during the formation of the nanotubes from precursor species, and relate them to the Si and Al coordination environments found in the final nanotube structure. The ^{1}H CRAMPS spectra of dehydrated aluminosilicate nanotubes revealed the proton environments in great detail. Integration of all the NMR results allows the structural assignment of all the chemical shifts and the identification of various types of defect structures in the aluminosilicate nanotube wall. In particular, five main types of defect structures are identified arising from specific atomic vacancies in the nanotube structure. It is estimated that ~16% of Si atoms in the nanotube inner wall are involved in a defect structure. The characterization of the detailed structure of the nanotube wall is expected to have significant implications for its chemical properties and applications.

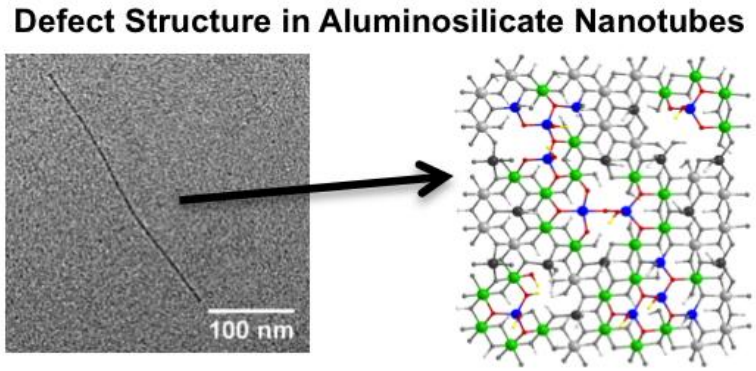

Chapter 6 – Integration of all NMR findings resulted in the first comprehensive molecular model of defect structures and associated proton environments in aluminosilicate single-walled nanotubes.

Chapter 7 contains concluding remarks, as well as suggestions for future directions in the engineering of single-walled nanotube materials.

CHAPTER 1

INTRODUCTION

1.1 Nanotubes

Nanomaterials, notable for their extremely small feature size in the range of 1-100 nanometers (nm), have been the subject of enormous interest and have a major influence on the rapidly advancing nanotechnology industry. The number and the variety of nanomaterials are immense, and they have the potential for wide-ranging industrial, biomedical, and electronic applications. The discovery of carbon nanotubes by S. Iijima in 1991 [3] attracted enormous interest and excitement in the field of nanomaterials over the last two decades [4]. Carbon nanotubes are described as rolled hollow structures of graphene sheets [3]. They exhibit unusual mechanical strength, electronic properties and heat conductivity providing potential technological applications as field emitters [5], reinforcing [6] and conductive fillers [7], electrodes [8], passive or active electronic components [9]. On the other hand, methods for preparing carbon nanotubes are not only expensive, but may also fail to yield large-scale, high-quality carbon nanotubes with controlled structural features [10]. “Curved” nanostructures are not exclusive to carbon; R. Tenne [11] reported the first synthesis of inorganic WS_2 nanotubes in 1992, just one year after the discovery of carbon nanotubes. However, their importance was not fully realized for nearly a decade [12].

1.2 Inorganic Nanotubes

Inorganic nanotube materials, such as MoS_2, WS_2, BN, V_2O_5, TiO_2, and NbS_2, offer a wide range of physicochemical properties that are quite different from those of carbon nanotubes. They are attractive candidates to be used in a variety of applications including biosensors, drug delivery, nanoreactors [13], reinforcing fibers, sensors, in photoconversion of solar energy and in nanoelectronics [12].

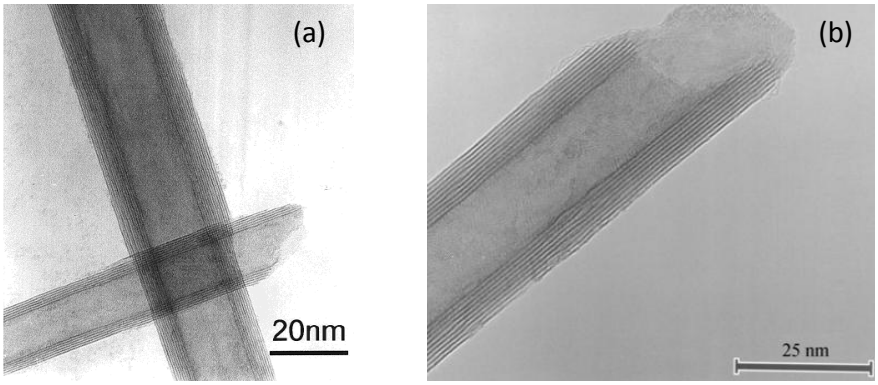

Figure 1-1. (a) Multi-walled WS_2 nanotubes which are around 15−25 nm in diameter. Taken from [14]. (b) HRTEM image of MoS_2 nanotubes with outer diameters of 30 nm. Taken from [15].

MoS_2 and WS_2 nanotubes (band gap of ~1.2 eV) have electronic properties similar to silicon but they are much more resistant to oxidation and humidity, making them attractive materials for nanoelectronics [12]. MoS_2 and WS_2 nanotubes show superior tribological properties to all known lubricants under high loads [16]. They are composed of layers that are analogous to graphene sheets that is capable of curving into a tubular shape as shown in Figure 1-1. BN nanotubes are shown to exhibit a Young's modulus as high as carbon nanotubes (1.2 TPa) [12]. They are structural analogues [17]

to carbon nanotubes having inner diameters of 1−3 nm, external diameters of 6−8 nm and lengths up to 200 nm [18]. BN and MoS_2 nanotubes are shown to exhibit hydrogen storage capabilities [19, 20]. NbS_2 nanotubes are predicted to be superconductors [21]. Most inorganic nanotubes are grown in the form of multi-walled nanotubes by various methods that requires high-temperatures such as directly from vapor phase, template processes, sulfurization [22].

There also exist metal oxide nanotubes that can be synthesized by "soft chemistry" methods including soft-gel processes and hydrothermal synthesis such as multi-walled titania (TiO_2) [23, 24] and vanadium oxide (V_2O_5) [25, 26] nanotubes. TiO_2 nanotubes have an external diameter of 10 nm and lengths up to ~400 nm [24, 27]. TiO_2 nanotubes have hydrogen storage capabilities [28] and are possible anode materials for lithium-ion batteries [27]. Vanadium oxide (V_2O_5) nanotubes attracted the interest of many researchers due to their potential applications in catalysis, photocatalytical activities, and as sensors [25, 26]. Although much speculation still exists on the formation mechanism of inorganic nanotubes, it was suggested that unsaturated bonds at the edges of the layers drive the formation of hollow tubular structures in order to condense these unsaturated bonds [29].

1.3 Single-Walled Metal Oxide Nanotubes

Despite the considerable progress in nanoscale materials processing, it is increasingly acknowledged that a vast potential for constructing nanoscopic materials of unprecedented complexity and functionality remains almost entirely unexplored, due to

current limitations in our understanding of nanoscopic molecular assembly processes. Specifically, the difficulty in engineering nanoscopic objects of complex structure, morphology, and composition increases dramatically as one or more dimensions of the nanoscale object drop to 10 nm or 1 nm length scales, and also when the desired structural complexity deviates from that of simple crystals (e.g., cubic, hexagonal). There are currently no generalizable approaches that provide the basis for generating complex nanoscopic objects such as hollow cylinders (nanotubes) and hollow nanospheres, with nanometer/subnanometer control over their dimensions as well as composition and atomic structure. Although micro/nanoparticles of relatively simple materials (e.g., carbon, or oxides such as ZnO and TiO_2) can be now produced through techniques that build upon existing catalytic or nucleation-and-growth (including templating) methods, the currently available approaches fail when materials of greater structural complexity are desired. There are many attractive technological and scientific reasons to pursue the creation of such "next-generation" nanoscopic objects. A large number of different theoretical and computational predictions show that they would be attractive for achieving many properties that define the full potential of nanotechnology –ballistic transport of charge/mass/heat, drastically tunable electronic structure, confinement phenomena, and extremely high surface areas.

1.3.1 Structure and Synthesis

In order to develop generalizable engineering approaches for single-walled nanotube materials, unique model systems are of particular interest that offer mechanistic insights into the assembly of nanoscale objects and which could lead to a more

generalized synthetic strategy. This model system is based on synthetic versions of naturally occurring aluminosilicate minerals such as imogolite. The synthetic aluminosilicate nanotube (whose natural analogue is referred to as imogolite) has the empirical formula of $[(OH)_3Al_2O_3SiOH]$. It has an outer wall that is made up of curved gibbsite $[Al(OH)_3]$ sheet with attachment of orthosilicate groups $[O_3SiOH]$ on inner face of the wall [30, 31]. The structural "repeat unit" of the nanotube is composed of six aluminum oxide octahedra arranged in a hexagonal ring and coordinated to a silicate tetrahedron via three oxygen bridges (μ_3-O) (Figure 1-2). There are 24 aluminum atoms in the circumference and aluminum octahedra are linked by μ_2-OH groups at shared edges. It is believed that the attachment of the orthosilicate group causes the shortening of O-O distances from 0.32 nm in gibbsite to ~0.27 nm, appropriate for the edge of a SiO_4 tetrahedron. Therefore, the curvature of the nanotube may be determined by the mismatch between the bond lengths on the inner and outer walls. The external diameter of the tube is ~2.2 nm and internal diameter is around 1.0 nm [30, 32]. Average nanotube length is ~100 nm [33].

The silicate units can be completely or partially replaced with germanate tetrahedra leading to the formation of aluminogermanate (AlGeOH) or aluminosilicogermanate (AlSiGeOH) nanotubes [33-36]. With increasing Ge-substitution, the diameter of the tube increases to 3.3 nm and the length decreases such that nanotubes as short as 20 nm can be synthesized [34].

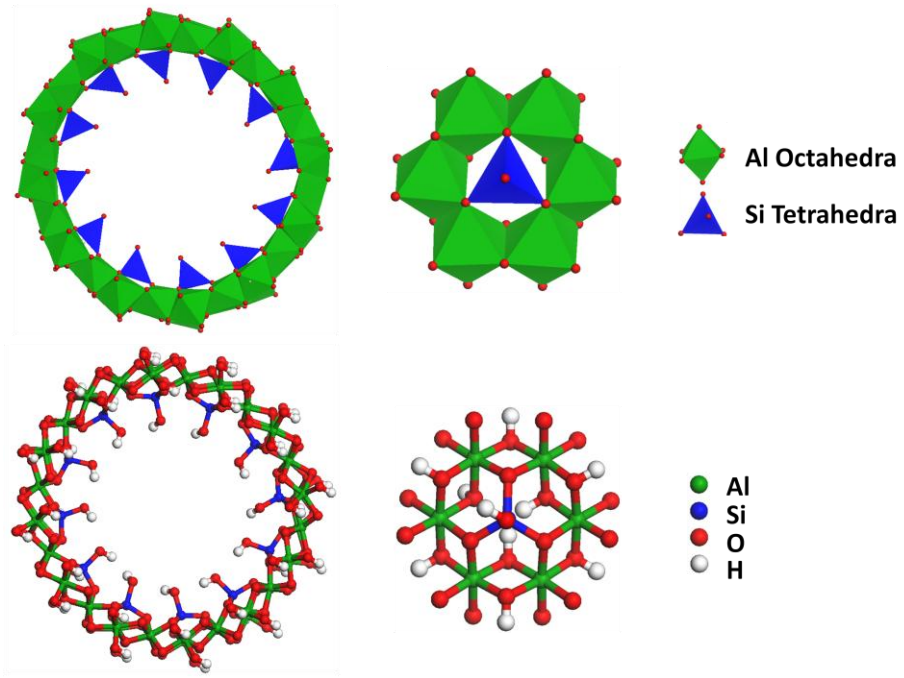

Figure 1-2. Ball-and-stick and polyhedron models of (left) the aluminosilicate nanotube, and (right) a section of the wall showing the hexagonal aluminosilicate repeat units.

Synthesis of aluminosilicate nanotubes was first reported in 1977 by Farmer et al. [37] at low temperatures (95 ˚C) from mildly acidic (pH∼4) solutions of hydroxyl-aluminum and orthosilicic acid [$Si(OH)_4$] species. The reactants are inexpensive [$AlCl_3$, or $Al(C_4H_9O)_3$, or $Al(ClO_4)_3$ as aluminum source and $Si(OC_2H_5)_4$ as silicon source] and easily accessible. Recognized synthesis involves a simple hydrolysis step of millimolar (mM) range starting materials (atomic ratio of Si/Al 0.5) with subsequent basification to pH∼5 and acidification (pH∼4) steps followed by heating of the reaction solution to 95 ˚C for 5 days. Purification is achieved with dialysis of the collected nanotube-gel and retentate is then dried in air [37]. This process yields 0.1 g of imogolite within a volume of 1 L reaction solution [38]. On the other hand, many other synthesis conditions were studied and classified [32] based on their outcome with optimum yields of aluminosilicate nanotubes achieved (~2g/10L) when tetraethyl orthosilicate/aluminum

tri-sec-butoxide/perchloric acid were mixed at a molar concentration ratio of 1:2:1 [32, 39, 40].

1.3.2 Properties and Emerging Applications

The intriguing properties of single-walled metal oxide nanotubes give them significant potential for use in diverse applications. Recently, significant progress has been made in functionalizing the interior of the nanotube with organic groups, by both post-synthesis modification as well as through direct synthesis [41, 42]. These developments create a basis for the use of these nanotubes in molecular transport, separation, encapsulation, and catalytic applications. For example, a defect-free molecular separation membrane containing single-walled aluminosilicate nanotubes embedded in a polymeric matrix, has recently been demonstrated [43]. Single-walled metal oxide nanotubes are well-known insulators. They may possess a wide band gap (~4-10 eV), independent of their size and chirality [44]. Aluminosilicate nanotubes are proposed to be used as an insulating sheath material in carbon nanotube core based nanocables, based on results of molecular dynamic simulations showing geometrical and electronic compatibility in between two materials [45]. Electric current flow through aluminosilicate nanotubes was observed experimentally only when they are exposed to water due to existence of protons as current carriers (H^+) on the outer surface [46]. It is also possible to introduce electrical conductivity by coating the nanotube surface with conducting polymers such as polypyrrole [47]. Reported field emission current density values are 103.8 and 129.1 μAcm^{-2} for single-walled aluminosilicate and carbon nanotubes at a field of 4 V/μm, respectively. Therefore, field emission current densities

of aluminosilicate nanotubes are comparable to single-walled carbon nanotubes (SWCNT) making them excellent electron emitters [48]. The mechanical properties of single-walled metal oxide nanotubes have only been investigated by few theoretical studies. Calculated Young's modulus (E) of aluminosilicate nanotubes are in the range of 175 – 390 GPa [44, 49]. This value is in the same range as for MoS_2 and GaS nanotubes whereas smaller than their carbon analogues [44, 45]. Due to their mechanical properties, these nanotubes have been largely considered to be used as nanofillers in polymer matrix nanocomposites [44, 50]. For example, transparent aluminosilicate nanotube and poly (vinyl alcohol) PVA films have been prepared by in situ synthesis and shows superior mechanical properties compared to PVA [51]. Functionalizable hydroxyl groups on the outer surface of imogolite allow the possibility of their incorporation in nanotube/polymercomposites together with enhanced interface characteristics [52, 53].

Due to their well-defined structure and porosity, hydrophilic surface, and functionalizability of outer and inner hydroxyl-groups (e.g., Si-OH, Al-OH), single-walled metal oxide nanotubes have a number of important applications, one of which involves fast mass transport through their engineered channels. Recent molecular dynamics (MD) simulation studies showed high water diffusivity (10^2-10^3 mol m^2s^{-1}) in single-walled metal oxide nanotubes with 15 to 100 nm tube length even at low pressure differentials of the order of 25 mm Hg [54]. Moreover, the inherent hydrophilicity of the nanotubes due to present hydroxyl groups and the chemically modifiable interior surface by different functional groups that have the ability to specifically adsorb and/or immobilize different target molecules, makes them attractive for the fabrication of nano-

devices or nano-machines, that achieves sensing [48], encapsulation, separation and storage [55] at molecular level. It has been reported, based on simulations, that the adsorption selectivity of water over methanol in aluminosilicate nanotubes is larger than 100, and that these materials may be attractive candidates for applications involving the dehydration of organic/water mixtures [56]. Besides, due to their well-defined structures, ultra-short (~20 nm) aluminogermanate nanotubes might be used as artificial ion-channels in biomolecular sensing devices based on variation in the ion conductance of the channel, with a single-molecule resolution [33, 44]. The use of imogolite in shape-selective catalysis has also been investigated [40, 57-59]. Tubular configuration of the nanotube was determined to retain up to 750 ˚C and the calcination of imogolite at 400-500 ˚C results in the formation of a large amount of acid sites required for the catalytic activity [58]. In addition, a more recent study [40] showed a phase transition to a lamellar phase at 500 ˚C which has stronger catalytic properties. Furthermore, silanol protons on the interior surface of the nanotube could be exchanged with different metal cations resulting in metal-loaded imogolite that could be used as a catalyst. Such a copper-based catalyst has been experimentally demonstrated [57] to have higher catalytic activity than unloaded imogolite for molecules that are smaller than the nanotube diameter and thus can diffuse inside the tubular structure, such as *tert*-butyl hydroperoxide.

1.4 Research Objectives and Strategy

1.4.1 Elucidating the Role of Molecular and Nanoparticle Species

Experimental studies have been carried out by Nair et al. to understand the aluminogermanate nanotube growth mechanism [33, 34]. XRD and TEM results showed that nanotubes are formed in aqueous solutions as early as 10 hours and the amount of nanotubes increases as a function of reaction time. Moreover, DLS and UV-Vis analysis revealed the existence of amorphous nanoparticles with a size of ~6 nm that appeared immediately upon heating. DLS data also pointed out that length of nanotubes practically stays constant throughout the synthesis time indicating a self-assembly rather than an inorganic polymerization in which length increases by the addition of precursors. Therefore, the conclusion was drawn that short, ordered single-walled metal-oxide nanotubes form by a condensation and molecular self-assembly process as illustrated in the Figure 1-3. Figure 1-3 shows, amorphous nanoparticles (~6 nm) formed by a reversible reaction possibly from monomeric or oligomeric precursors. Once nanoparticles formed, they might be evolving irreversibly into ordered nanotubes through self-assembly. Recently published work, based on molecular dynamics simulations, by our group members also shows there is a unique strain energy minimum that controls the diameter of nanotubes [35]. On the other hand, it was suggested that processes such as aggregation could also have a role in determining the final tube dimensions. In this thesis one of the aims is to identify the molecular composition and dimensions of molecular precursors and clusters, and to elucidate their role in nanotube formation and growth as they might be determining the final diameter and length of the nanotubes.

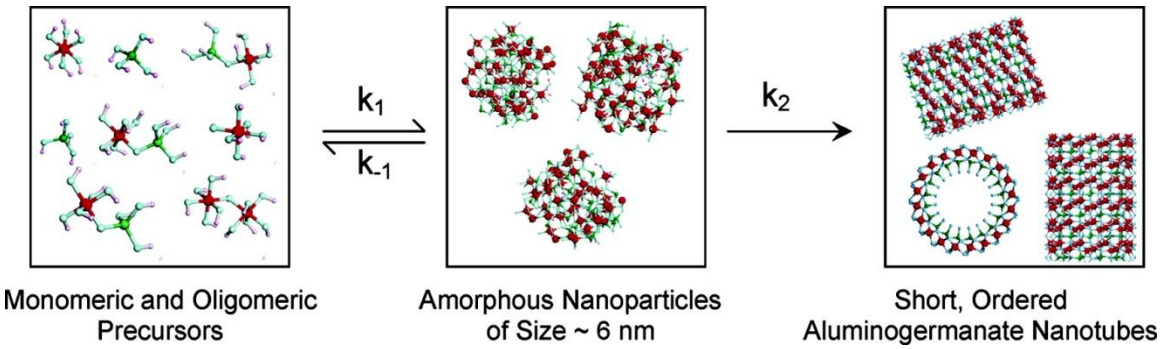

Figure 1-3. Summary of the aluminogermanate nanotube formation mechanism hypothesized by Mukherjee et al. in 2007 [60].

Farmer et al. [37, 61] speculated that formation of imogolite occurs from sheet-like precursors called "proto-imogolite" which has the same local atomic arrangement as imogolite and is formed by the interaction of hydroxy-aluminum cations with orthosilicic acid in reaction solutions. Although its existence was never proved experimentally (until the work described in this thesis) but rather assumed based on the composition of the final product, proto-imogolite has been considered as a precursor which forms earlier in the reaction and then polymerizes to form nanotubes ("proto-imogolite theory") [62]. However, such inorganic polymerization of proto-imogolite to imogolite can only be explained by a kinetically controlled growth, whereas studies suggest thermodynamic self-assembly of precursors into tubes [60]. One of the objectives of this thesis is to investigate the existence of "proto-imogolite" structures and their role in nanotube formation using multiple characterization techniques. Since so far the existence of proto-imogolite structures had been only speculated, their experimental discovery and explanation in this thesis is a significant contribution to knowledge in nanotube chemistry.

Several liquid phase conditions may affect the formation of metal oxide structures and their morphology, such as pH, temperature, interactions with anions (ClO_4^-, Cl^-, OH^-, etc.) together with inherent thermodynamic criteria. Although early experimental data [61] showed that anions inhibited nanotube formation ($Cl^- > NO_3^- > ClO_4^-$) and the largest yields of synthetic imogolite are obtained by heating hydrolyzed aluminium sec-butoxide and silicon tetraethoxide in perchloric acid solutions, no further progress was made regarding possible interactions of anions with nanotube precursors. In their ^{27}Al NMR studies, Akitt and Farthing [63] concluded that anions such as Cl^-, ClO_4^- interact with colloidal dispersions in aluminum solutions. They carried out experiments using solutions of $AlCl_3$ and $Al(ClO_4)_3$, and observed that hydrolysis takes place equally easily, however, differences manifest only in the tendencies of the solutions to form precipitates, for example solutions containing Cl^- formed a precipitate in 4 months, while for solutions containing ClO_4^-, almost no precipitate had formed after one year. Wada et al. [36] speculated that the shortening of the nanotube length, observed via Ge-substitution of Si by using $GeCl_4$ as a source of Ge, might be a result of an increase in Cl^- concentration in reaction solutions. Moreover, another study suggested that citric acid reacts with hydroxy-aluminosilicates and/or hydroxy-Al ions, and the interaction with such organic ligands might be important in terms of understanding the formation of natural imogolite in soils. It was shown that without the addition of citric acid, imogolite solutions generate a colloidal precipitate [64].

Based on the above discussion, it can be concluded that effect of anions such as chloride, perchlorate etc. is not clear, but is believed to have importance in determining

the size and structure of precursor species. In order to reveal the underlying formation mechanism of single-walled metal oxide nanotubes, the role of reactive anions should be understood as they might be involved in determining the final nanotube length and diameter. It is surprising that only a few researchers paid any attention to the anion effect on formation of single-walled metal oxide nanotubes. Therefore, in this thesis, the aim is to uncover the role of anions and their interaction with precursor species in nanotube synthesis solutions by partially and completely replacing $HClO_4$ in reaction solutions with other mineral acids as well as organic acids.

As proposed by Cradwick et al. [30], the imogolite wall unit consists of a curved single sheet of gibbsite wherein three out of six OH groups of the internal vacant sites are replaced with O_3SiOH groups [Q^3(3Al)]. It is believed that the attachment of orthosilicate group causes shortening of O-O distances around internal vacant site from 0.32 nm in gibbsite to less than 0.3 nm, appropriate for an edge of a SiO_4 tetrahedron. Therefore, the curvature of the imogolite wall might be determined by the misfit between the Al dioctahedral vacant site and silicon tetrahedron [30]. This theory might also explain larger diameter of AlGeOH nanotubes because O-O distance in Ge tetrahedron is larger than that of Si tetrahedron resulting in smaller curvature [36]. On the other hand, it does not provide insights into the causes of the nanotube length shortening induced by Ge-substitution of Si in imogolite structure. One of the objectives is to understand the underlying mechanism of growth of the AlGeOH and AlSiOH nanotubes from nanoscale precursors and intermediates. The acquired knowledge then can explain the role of the

nanoscale intermediates and their relationship to the nanotube dimensions. Such understanding is required in an attempt to achieve control over nanotube dimensions.

1.4.2 Shaping Nanotube Structure and Dimensions

In order to enable the applications of single-walled metal oxide nanotube materials, it is required to not only design inexpensive, low-temperature, high-purity synthesis processes; but also achieve control over the structure, dimensions, and composition of these nanoscale objects. The engineering of single-walled metal oxide nanotubes is of particular interest. Metal oxides offer a vast range of compositions, structures, and resultant properties. The capability to engineer metal oxides into single-walled tubular materials would lead to a large number of diverse applications in areas such as catalysis, separations, optoelectronics, and biotechnology. These applications would exploit the novel electronic, transport, mechanical, and surface properties of such materials.

There are only a few examples of single-walled metal oxide nanotubes currently known [33, 65]. There is currently no framework of design principles (based on mechanistic investigations) available for the engineering of such objects. The class of aluminosilicate/germanate nanotubes (referred to here as "AlSiOH, AlGeOH") are of particular interest to us, and serve as the exemplar materials for single-walled metal oxide nanotubes. These nanotubes can be synthesized in pure form and with monodisperse dimensions at low temperatures (95 ˚C) from aqueous solutions. The synthesis occurs on a time-scale of hours to days, making them an ideal model system to study the nanotube

formation mechanism. The growth process is slow (on a time scale of hours) enough to allow step by step characterization that would provide information on the evolution of species in aqueous solution. Once the underlying mechanistic picture of their formation and growth is determined, one can develop a more general framework that is designed to engineer an entirely new class of single-walled metal oxide nanotube by using a number of experimental "handles" (e.g., reaction composition, concentration, pH, temperature, energy source, and time). Therefore, a clear mechanistic framework at molecular (and larger) scale is necessary in order to engineer their dimensions and design high-yield synthesis processes.

The synthesis procedures employed frequently by researchers yield small quantities of nanotubes in relation to the desired industrial-scale synthesis of single-walled metal-oxide nanotubes. Design of high-yield processes is difficult without the knowledge of molecular-level reaction pathways leading from the reactants to final nanotube products. Thus, the synthesis, engineering, and applications of single-walled metal oxide nanotubes can be greatly advanced by a good understanding of the effects of processing parameters which controls the nanotube structure and properties. A molecular model of the growth mechanism will provide understanding of the nanoscale assembly and structural evolution that is taking place in aqueous phase, and provide a basis for engineering of processing conditions in order to produce desired tubular features.

1.4.3 Understanding Nanotube Growth

Mukherjee [34] suggested that the aluminogermanate nanotube length is pre-determined to a large extent by the precursor particle size and thus, self-assembly of the precursors could explain the final tube length. Meanwhile, length distributions of aluminosilicate nanotubes as a function of reaction time were studied [66], and it was suggested that final tube length is determined by a kinetically controlled growth mechanism in which the tube length increases with reaction time by the addition of precursors to the growing ends of the tubes. Another recent study based on SAXS data, has proposed that growth occurs by edge-to-edge aggregation of shorter nanotubes [38]. On the other, such kinetically controlled mechanisms alone cannot explain the low-polydispersity index values [66] of lengths of single-walled metal-oxide nanotubes. Therefore, the true growth mechanism of the nanotubes remained a mystery. In this thesis, one of the objectives is to understand the mechanism governing nanotube growth.

Proposed mechanisms for other type of inorganic nanotube growths in literature should also be mentioned. The growth of boehmite (AlOOH) nanotubes with an internal diameter of 2−5 nm and a length of ~170 nm has been achieved from fresh precipitates of aluminum hydroxide using soft chemistry route (aqueous phase at 120˚C) [67]. Uniform length and diameter of these nanotubes has been attributed to the slow (1−6 days) "Ostwald Ripening" process that controls the overall growth of beohmite nanostructures. In Ostwald Ripening process, there is a critical radius, r_c, of small particles which is determined by experimental conditions and if $r>r_c$, the particle grows, if $r<r_c$ particle shrinks and therefore, larger crystallites grow at the expense of smaller

crystals, driving force being the reduction in surface energy. On the other hand, some researchers suggested "Oriented Attachment Growth Mechanism" [68]. In this mechanism, bigger particles are grown from small primary particles through an oriented attachment mechanism, in which adjacent particles self-assembled by sharing a common crystallographic orientation. Moreover, recent studies on MoO_3 nanotubes suggest a possible "Cluster-based Self-Assembly" growth mechanism which is based on self assembly of polyatomic ions such as Keggin structure. Any of the mentioned mechanisms might also be affecting single-walled metal oxide nanotube growth at some point during the synthesis, and will be taken into consideration while explaining the growth of single-walled nanotube materials.

CHAPTER 2

FORMATION OF SINGLE-WALLED ALUMINOSILICATE NANOTUBES FROM MOLECULAR PRECURSORS AND CURVED NANOSCALE INTERMEDIATES

2.1 Introduction

Apart from emerging applications, the fundamental importance of single-walled metal oxide nanotubes lies in their use as a model system for developing a mechanistic model of self-assembly phenomena that lead to the formation of a "curved" nanostructure. The capability to engineer metal oxides into single-walled tubular materials with desired characteristics could be achieved through a detailed molecular-level understanding of their formation and growth mechanisms in the liquid phase. Such a model has not previously been available. Experimental studies so far have not been able to reveal the molecular structure of the precursors and intermediate species, which is a key step in understanding their evolution into nanotubes. However, due to the combined efforts of multiple authors, mechanistic information is available at larger length scales regarding both the initial formation of nanotubes as well as their subsequent growth. The formation of the aluminosilicate nanotubes has been proposed to occur from a sheet-like intermediate called "proto-imogolite" which is suggested to have an atomic arrangement similar to the final nanotube product [37, 62]. However, its existence has not been proven experimentally. The existence of nanoparticle precursors with a size of ~6 nm has also been shown in previous [33, 60] studies of the closely related aluminogermanate

nanotube system. Based on inferences from DLS data and synthetic variations, it was proposed that these nanoparticles, which form by condensation of molecular precursors, self-assemble irreversibly into ordered nanotubular particles of ~20 nm length. Another study by small-angle X-ray scattering (SAXS) has further assigned a specific structure for this precursor nanoparticle, in particular an aluminogermanate sheet-like structure [38]. However, the uniqueness of this assignment is not known, especially considering previous debates on the unique interpretation of SAXS data from zeolite synthesis solutions [69, 70]. Recent work on the synthesis of single-walled MoO_3 nanotubes [65] also suggests a cluster-based self-assembly of nanoscale precursors into nanotubes. Other studies have focused on the growth of the aluminosilicate nanotubes after their initial formation [66]. Based upon TEM, electron diffraction, and DLS observations, it was previously shown that large numbers of nanotubes form continuously in the synthesis solution by a self-assembly process, but that their subsequent growth is relatively much slower, thereby leading to an almost constant average length of the nanotubes as a function of synthesis time [60]. Similarly, it was shown that a 100-fold increase in the reactant concentration in the aluminogermanate nanotube synthesis had little effect on the average dimensions of the self-assembled nanotubes [71]. Nevertheless, the growth processes somewhat broaden the length distribution of the nanotubes, and may occur by one or more proposed mechanisms such as end-to-end aggregation of short nanotubes [38] and precursor addition to the nanotube ends [66]. It has also been suggested that the length distribution of the nanotubes is influenced by a slow Ostwald ripening process [38, 67].

The elucidation of the molecular precursors and intermediates in the nanotube synthesis is clearly a key "missing link" in describing the nanotube assembly. This work focuses on identifying the structure, composition, dimensions, and shapes of molecular precursors and clusters involved in the nanotube formation, and tracking the evolution of these characteristics during the synthesis process. This objective is achieved by the collection and detailed analysis of ESI−MS, and NMR spectra from the evolving nanotube synthesis solution; and is supported with quantum chemistry calculations on several key species of interest. This chapter concludes by integrating the observations into the first molecular-scale description of the initial events in the nanotube formation process.

2.2 Experimental Details

2.2.1 Single-Walled Aluminosilicate Nanotube Synthesis

TEOS (tetraethoxysilane) and Al(sec-butoxide)$_3$ were mixed in a glove box filled with nitrogen, and added dropwise to ~0.05 M aqueous solution of $HClO_4$ in the molar ratios Si:Al:$HClO_4$ = 1:2:1 at 25 ˚C. The solution was vigorously stirred and aged for 18 h at 25 ˚C, and then diluted to 0.02 M in Al. Immediately after dilution, the temperature was increased to 95 ˚C, and kept constant under vigorous stirring for 4 days (96 h). Please see Figure 2-1 for illustration of nanotube synthesis process. Samples for liquid-state NMR and ESI–MS experiments were directly taken from synthesis solutions during 18 h aging (25 ˚C) and subsequent 96 h heating steps (95 ˚C). Samples were immediately used for characterization. All characterizations were carried out at room temperature (25 ˚C).

To perform solid-state NMR experiments, the samples were immersed into liquid nitrogen at various stages of the aging and heating steps, and then freeze-dried at −50 ˚C for 5 days. At the end of the reaction sequence, the nanotubes were first precipitated by dropwise addition of a 30 *wt* % ammonia solution; the resulting gel was centrifuged, the supernatant was discarded and 10 N HCl was added dropwise to re-disperse the nanotubes. Finally, the dispersion was dialyzed for 4 days against de-ionized water using a 15 kiloDalton membrane to obtain a pure nanotube dispersion for liquid-state ^{27}Al NMR studies. Pure nanotube powder samples for solid-state NMR experiments were obtained by drying the dialyzed nanotube solution at 60˚C in an oven.

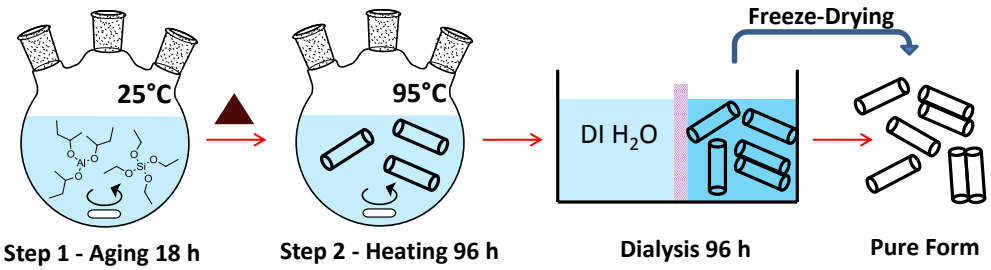

Figure 2-1. Single-walled aluminosilicate nanotube synthesis process

2.2.2 ^{27}Al Liquid-State NMR Spectroscopy

Liquid samples of volume 600 μL were placed in 5 mm glass NMR tubes and diluted with a 90% H_2O/10% D_2O mixture, which acted as a field frequency lock. Single-pulse ^{27}Al liquid-state NMR spectra were collected on a Bruker DMX 400 at a frequency of 104.2 MHz. 10k free induction decays were recorded with a repetition time of 0.1 sec. The pulse width and acquisition time were 7.5 μsec and 0.25 sec respectively. The spectra

were carefully corrected for background signals due to aluminum-containing ceramics in the probe, by subtracting a spectrum obtained from a "blank" H_2O/10% D_2O solution. Chemical shifts are referenced to a 0.1 M $AlCl_3$ solution.

2.2.3 ^{29}Si Solid-State CP−MAS NMR spectroscopy

^{29}Si solid-state CP−MAS NMR spectra were recorded on a Bruker DSX 300 spectrometer with a 7-mm rotor at a spinning rate of 6 kHz. ^{1}H and ^{29}Si frequencies were 300.2 MHz and 59.6 MHz respectively. Chemical shifts were referenced relative to 3-(trimethylsilyl)-1-propanesulfonic acid sodium salt. The standard cross-polarization ^{1}H-^{29}Si pulse sequence was performed with 5 s recycle delay between pulses, and 3 msec contact time. The 90° pulse length was 5 μs. The data represent 2048 transients processed with a 5-Hz line broadening.

2.2.4 ESI−Mass Spectrometry

A Quattro LC (quadrupole-hexapole-quadrupole) mass spectrometer with an orthogonal Z-spray electrospray interface was used. The temperature of the surface block was $100^{\circ}C$ and temperature of the desolvation gas was 150˚C. Samples were injected into the ESI−MS immediately after they were taken from nanotube synthesis reactor. The samples were not diluted. Capillary voltages of 3.3 kV for negative scan mode and 3.5 kV for positive scan mode were used. The optimum cone voltage was determined as 50 V via control experiments on aluminate and silicate samples. Information on species present in these solutions was difficult to extract from spectra obtained at lower cone voltages,

and higher cone voltages were not used to avoid the possibility of fragmentation of the species. Nitrogen was used as the drying gas and nebulizing gas, at flow rates of 500 and 100 L/h, respectively.

2.2.5 Molecular Modeling

The DFT calculations were performed using the DMol^3 package in the Materials Studio molecular modeling software (Accelrys). Energies are calculated using the generalized gradient approximation (GGA) and the BLYP functional to model exchange and electron correlation effects. Thermal smearing is applied to accelerate convergence. Many of the species identified by ESI−MS already possess an explicit first hydration shell of water and hydroxyl groups. Longer-range solvent effects are also included using the conductor-like screening model (COSMO) [72]. Since some of the species contain Cl atoms, spin-unrestricted ground-state energy calculations were performed in all cases for consistency. A double-numerical plus d functions (DND) effective core potential basis set was employed in all calculations. The effect of using a highly accurate double-numerical basis set with polarization functions (DNP) effective core potential basis set was then studied using a few test species. In all cases, there was very little change in the optimized geometries from the DND basis set calculations. Vibrational frequency calculations were then used to verify convergence to energy minima. To accelerate the tedious vibrational frequency calculations, this step was performed using a double-numerical (DN) basis set.

2.3 Results and Discussion

2.3.1 Characterization of Synthesis Solution by Liquid-State NMR

Liquid-state ^{27}Al, and solid-state ^{29}Si NMR spectroscopy are used to examine aluminosilicate nanotube formation from the precursors aluminum sec-butoxide (ASB) and tetraethoxysilane (TEOS) in mildly acidic aqueous solutions as a function of aging time (up to 18 h at 25 ˚C) and subsequent heating at elevated temperature (up to 96 h at 95 ˚C). Attempts to perform liquid-state ^{29}Si NMR studies on nanotube solutions were unsuccessful due to the low isotopic abundance and low sensitivity of ^{29}Si nuclei. Signal enhancement methods that depend on polarization transfer from ^{1}H (e.g., INEPT) [73] were also unsuccessful. Hence, all ^{29}Si NMR studies were performed in the solid state.

The ^{27}Al liquid-state NMR spectra show two sharp and distinct resonances corresponding to the six-coordinated octahedral monomer $[Al(H_2O)_6]^{3+}$ *($\delta_{Al(VI)} \approx 0$ ppm)* and a four-coordinated aluminum environment *($\delta_{Al(IV)} = 63.3$ ppm)* which begins to disappear upon heating, as well as a broader peak near 6 ppm that falls in the six-coordinated chemical shift region (Figure 2-2). The peak at 63.3 ppm is due to a tetrahedral Al unit at the center of a highly symmetric (Al_{13}) $[AlO_4Al_{12}(OH)_{24}(H_2O)_{12}]^{7+}$ species [74]. The nanoscale Keggin-like species is well-known to be present in acidic aluminate solutions [63], and contains a central tetrahedral Al coordinated with 12 surrounding Al octahedra via four oxygen atoms at each vertex of the tetrahedron (Figure 2-3). The ^{27}Al NMR line from the surrounding octahedral aluminums is nearly invisible due to quadrupolar broadening, and was only revealed at 12 ppm [75] after deconvoluting

the spectra obtained during aging stage (Figure 2-4). The inset in Figure 2-2 shows the single ^{27}Al NMR resonance *($\delta_{Al(VI)} \approx \sim 6$ ppm)* from a pure nanotube suspension after dialysis. Therefore, the broad peak centered around 6 ppm that was observed throughout the synthesis, is assigned to six-coordinated Al species with a bonding environment very similar to that found in the nanotube structure (i.e., hexagonal aluminosilicate repeat units as shown in Figure 1-2). As evident from Figure 2-2, this environment, corresponding to the "nanotube-like" structure exists throughout the synthesis together with the monomeric Al species.

The evolution of local environment around the Al atoms is examined by tracking the chemical shifts, line widths, and integrated areas of the measured resonances (Figures 2-4, 2-5, and 2-6). The NMR spectra collected at various stages of the synthesis were fit with a series of Lorentzian peaks to obtain the position, full width at half-maximum (fwhm) and area of each peak (Figure 2-4). In particular, tracking the 6 ppm resonance provides information regarding the evolution of Al configurations that resemble the nanotube wall structure. Moreover, the line widths of ^{27}Al NMR resonances are strongly dependent on the symmetry (i.e., electric field gradient) of the species [76].

The peak chemical shift of the broad octahedral ^{27}Al NMR signal decreases from 8.5 ppm to 5.5 ppm and its fwhm decreases from 13 ppm to 8 ppm (Figure 2-5a,b) during aging stage, likely due to local atomic ordering around Al in the nanotube-like configuration. After 7 h aging at 25 ˚C, these values become stable, indicating that stable species with an ordered nanotube-like configuration of the octahedral Al has been formed

in the aging process. Moreover, the integrated intensities of this peak, as well as that of the Al_{13} species (63.3 ppm), increases as a function of aging time but nearly reach a plateau after 18 h of aging (Figure 2-5c,d). Concurrently, the integrated area of the monomer peak at ~0 ppm decreases during the aging step (Figure 2-5e). Thus, the nanotube-like species and Keggin ions increase at the expense of the monomer species as equilibrium is established.

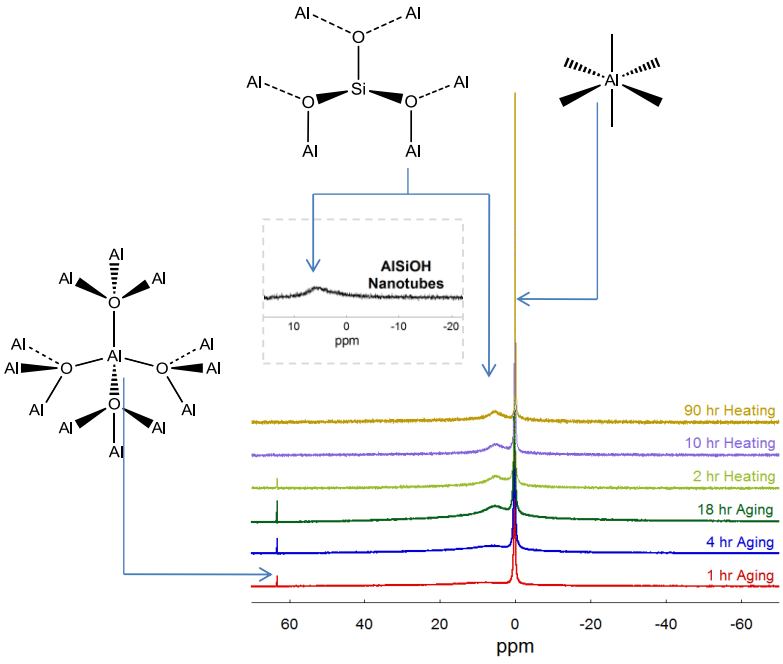

Figure 2-2. ^{27}Al liquid-state NMR spectra of nanotube solutions at various stages of aging (25 ˚C) and heating (95 ˚C). The inset shows ^{27}Al NMR resonance of dialyzed aluminosilicate nanotube solution *($\delta_{Al(VI)}$ ≈6 ppm)*. Spectra were collected at 25 ˚C. The species assigned to each NMR signal are shown by 2D ChemDraw representations. The peak at 63.3 ppm is observed during aging of nanotube synthesis solutions at 25 ˚C and is assigned to the tetrahedral aluminum at the center of a Keggin polycation. This peak disappears within 7 h of heating. The peak near 6 ppm is assigned to octahedral aluminum in a nanotube-like coordination environment. The sharp peak near 0 ppm represents octahedral monomer aluminate units.

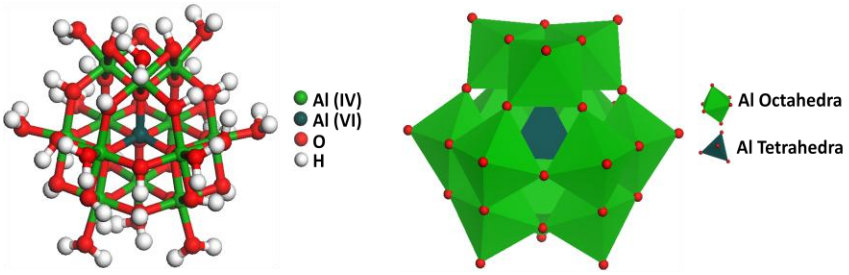

Figure 2-3. Ball-and-stick model (left) and polyhedron model (right) of the Keggin cation $[AlO_4Al_{12}(OH)_{24}(H_2O)_{12}]^{7+}$. The Keggin cation consists of a tetrahedral aluminate $[AlO_4]^{5-}$ center surrounded by four octahedral aluminate $[Al_3(OH)_6(H_2O)_3]^{3+}$ trimer units [75, 77].

Upon heating of the aged solution to 95 ˚C, the signal at 63.3 ppm disappears within 7 h (Figure 2-2 and 2-5e). A previous study of pure aluminate solutions suggests that the disappearance of the 63.3 ppm signal above 90 ˚C is due to clustering and rearrangement of the Keggin clusters to hexameric rings, which are appropriate precursors for gibbsite (layered $Al(OH)_3$) and boehmite (layered AlOOH) formation [78]. Such rearrangements should result in the broadening of the 63.3 ppm resonance [74] due to a breaking of the tetrahedral symmetry but is not observed in this study. The chemical shift of the monomer decreases from 0.3 ppm to 0.1 ppm within 24 hrs of heating, and its fwhm also decays and levels off in a similar manner (Figure 2-6a,b). These small changes can be explained by a shift in the equilibrium between aluminate monomers: [74, 78] $[Al(H_2O)_6]^{3+} \leftrightarrow [Al(H_2O)_5(OH)]^{2+} + [H]^{+}$. As explained later in this thesis, this equilibrium shift is clearly seen as a change of pH of the evolving nanotube synthesis solution.

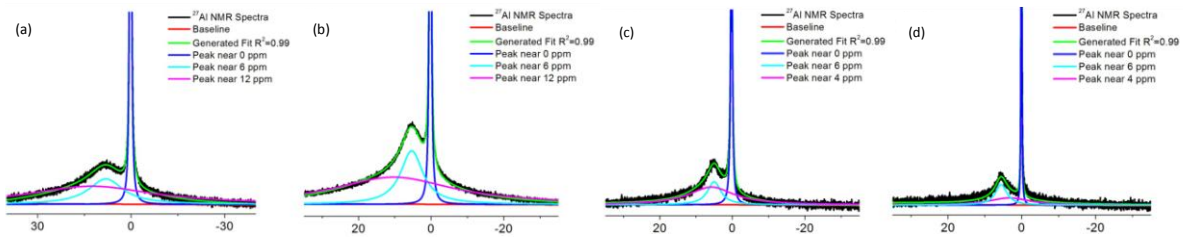

Figure 2-4. Lorentzian deconvolution of octahedral region in obtained ^{27}Al liquid NMR spectra of nanotube solutions at various synthesis times: (a) 1st h aging, (b) 18th h aging, (c) 2nd h heating, and (d) 92nd h heating.

No significant changes are observed in the chemical shift, integrated area, and line width of broad octahedral peak near 6 ppm during the heating step (Figure 2-6c,d,g). This result strongly indicates that no significant new Al coordination environments are formed during the heating step, and that the same Al-containing species formed in the aging step are participating in nanotube formation, albeit with some minor structural changes. The precursors necessary for nanotube formation should therefore already be in the solution prior to heating, and would be used in the formation of nanotubes during the heating stage.

Deconvolution of the heating stage spectra (Figure 2-3) also revealed a new broad peak at 3-5 ppm in the octahedral coordination region, whereas the 12 ppm peak detected during aging belonging to octahedral units of the Keggin ion have disappeared after 1 h of heating. These simultaneous events suggest a change in equilibrium between two species or breakdown of Al_{13} into species represented by the 3-5 ppm peak upon heating. Moreover, the changes in chemical shift of the 3-5 ppm peak are strongly correlated to that of the monomer peak (Figure 2-4f,g and Figure 2-5c). This may also indicate an equilibrium between these two species during heating stage. The ^{27}Al NMR peak near 3-5 ppm might be attributed to dimeric [76] or trimeric [79] aluminate species. According to

Akitt [63], there is an equilibrium between three species in hydrolyzed acidic aluminate solutions:

$$[Al(H_2O)_6]^{3+} \leftrightarrow [Al_2(OH)_2(H_2O)_8]^{4+} \leftrightarrow [AlO_4Al_{12}(OH)_{24}(H_2O)_{12}]^{7+}$$

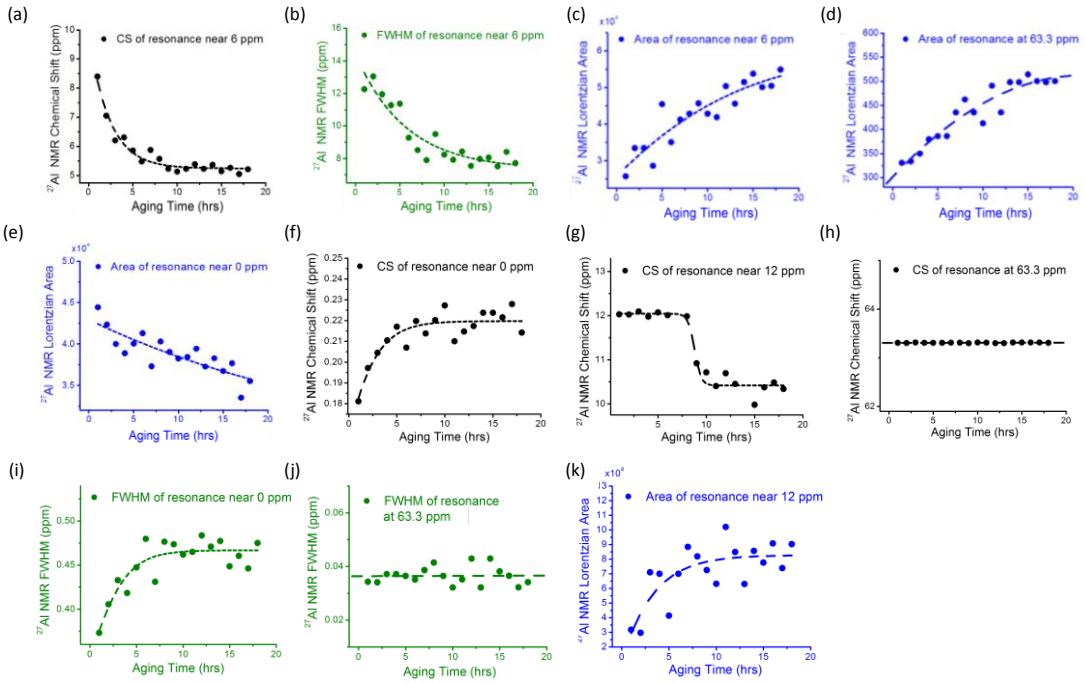

Figure 2-5. Chemical shift (CS), fwhm, and integrated areas (arbitrary units) of resonances in ^{27}Al liquid-state NMR spectra of evolving nanotube synthesis solution during aging stage. The lines are least-squares fits to guide the eye.

A similar equilibrium between Al_1Si_x, Al_2Si_x, Al_3Si_x species and a Keggin-like $Al_{13}Si_x$ metastable complex [63, 80] can explain the above observed behavior of the 0 ppm and 3-5 ppm peaks, together with the disappearance of the Keggin signal at 12 ppm. Another possibility is that the 12 ppm peak may have disappeared due to the increased quadrupolar broadening caused by condensation of Keggin molecules, although clear evidence for this speculation was not found in this study. In summary, liquid-state ^{27}Al NMR experiments and analysis provide substantial information on the species formed

and on their evolution. For the first time, Keggin species were identified clearly in the nanotube synthesis solution.

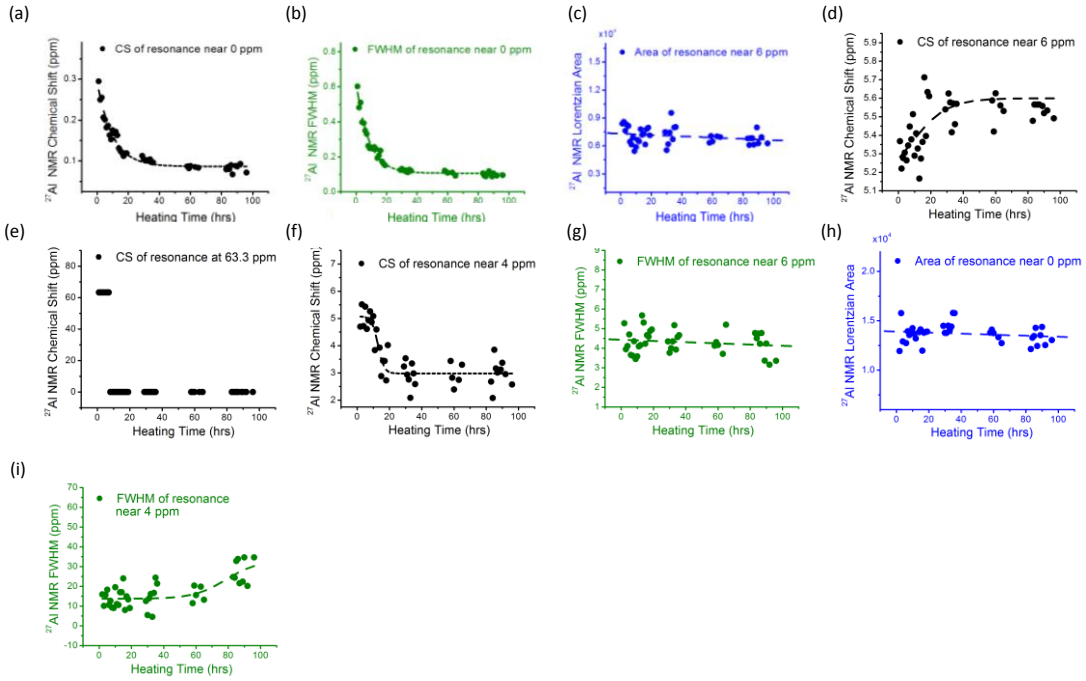

Figure 2-6. Chemical shift (CS), fwhm, and integrated areas (arbitrary units) of resonances in ^{27}Al liquid-state NMR spectra of evolving nanotube synthesis solution during heating stage. The lines are least-squares fits to guide the eye.

Figure 2-7 shows the change in pH as a function of aging and heating time. After initial mixing of reactants at 25 ˚C, the pH drops from ~3.7 to 3.3 within 7 h. The pH further drops precipitously to ~1.7 immediately after the onset of heating to 95 ˚C and thereafter stays nearly constant throughout the reaction. The large drop in pH denotes a precursor condensation [61, 62, 79] leading to a release of protons. Therefore, it is concluded that the combined observations in the aging step – decrease in linewidth, increase in integrated area, and decrease in chemical shift of the peak near 6 ppm; decrease in monomer peak intensity; increase in the Keggin signal; and slight decrease in

pH − clearly indicate an equilibrium established between the monomers, Keggin ions, and species with "nanotube-like" coordination environment, at 25 ˚C. Upon increasing the temperature to 95 ˚C, a condensation and rearrangement process takes place. The equilibrium between species shifts, and the Keggin ion decomposes. Trimeric and dimeric species are likely to be formed in addition to the monomers and the species with nanotube-like coordination. These events are also supported by ESI−MS study, discussed later.

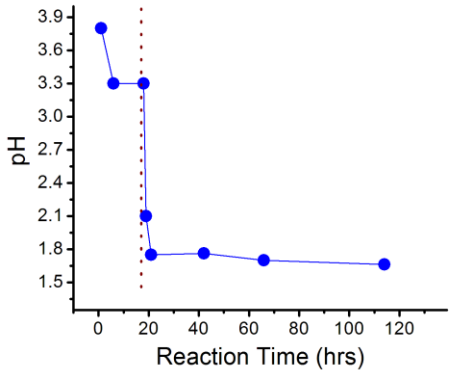

Figure 2-7. pH change of the nanotube synthesis solution as a function of reaction time. The dotted line separates the aging (left) (25 ˚C) and heating (right) (95 ˚C) stages.

2.3.2 Characterization of Synthesis Solutions by Solid-State NMR

The ^{29}Si CP−MAS NMR spectra of freeze-dried aluminosilicate nanotube solutions at various stages of the synthesis are shown in Figure 2-8. In aluminosilicate materials, ^{29}Si chemical shifts and line widths are affected by coordination with aluminum and the aluminum distribution in the lattice [Si(nAl)] with number n being the next-nearest neighbor Al atoms [81]. The ^{29}Si CP−MAS NMR spectra exhibit a broad resonance centered near −90 ppm (limits range from −75 to −110 ppm) and a sharp peak

at −80 ppm. Tetrahedral silicon groups attached to three Al atoms in a Q^3(6Al) coordination are known to give rise to a sharp resonance near −80 ppm [82]. These results indicate the existence of Q^3(6Al) coordination throughout the synthesis, as also confirmed by ^{27}Al NMR studies due to the peak near 6-7 ppm. The broad line width of the other resonance (centered at −90 ppm) is assigned to variation in the local silicon coordination arising from the individual Si(nAl) [n=1−5] coordination environments and their characteristic ^{29}Si NMR chemical shifts separated approximately by 5 ppm and known to resonate within the range of −75 to −110 ppm [83-85].

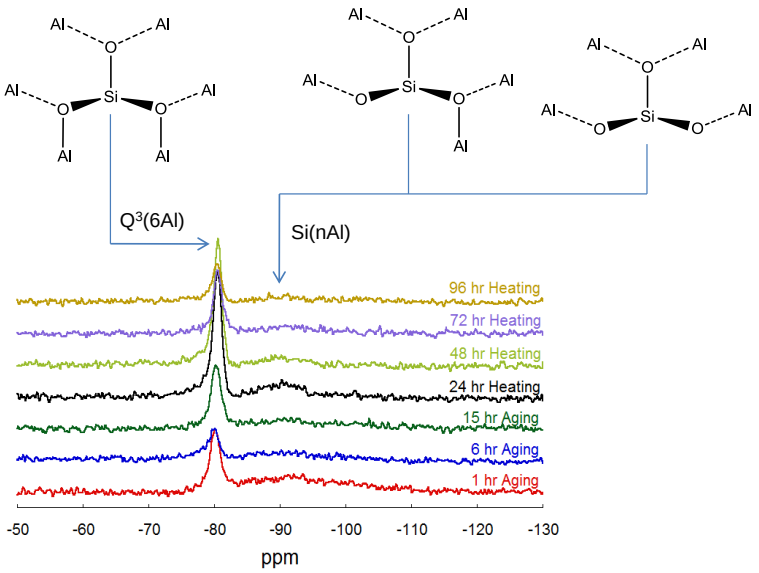

Figure 2-8. ^{29}Si CP-MAS NMR spectra of freeze-dried nanotube solutions as a function of synthesis time. Measurements are done at 25 ˚C. The peak at −80 ppm is due to the characteristic Q^3(6Al) configuration of Si in the aluminosilicate nanotube. The broad peak centered near −90 ppm is assigned to silicon tetrahedra surrounded by n=1−5 aluminum atoms. Tentative representations of Si(5Al) and Si(4Al) are shown above the NMR spectra.

As shown in Figure 2-9, the integrated area % of the −90 ppm peak (relative to the total integrated area) gradually decreases, whereas that of the −80 ppm peak

increases. This indicates the transformation of disordered Si environments to ordered Q^3(6Al) nanotube-like configurations. On the other hand, from ^{27}Al liquid NMR results it is known that the fraction of species with nanotube-like configuration (peak near 6 ppm) does not increase to a significant extent as a function of reaction time. Therefore, it is believed that the increase in relative intensity of the −80 ppm peak is a result of ordering (e.g., lattice formation) of aluminum atoms that are already in a nanotube-like coordination with the Si species [Si(nAl)→Si(6Al)], and not due to significantly new formation of Q^3(6Al) configurations. The ^{29}Si chemical shift near −80 ppm of the evolving solutions does not change, showing that the Si(6Al) chemical environment of silicon remains stable throughout the synthesis. The chemical shift of the peak centered at −90 ppm also remains constant, but it gradually diminishes during the reaction.

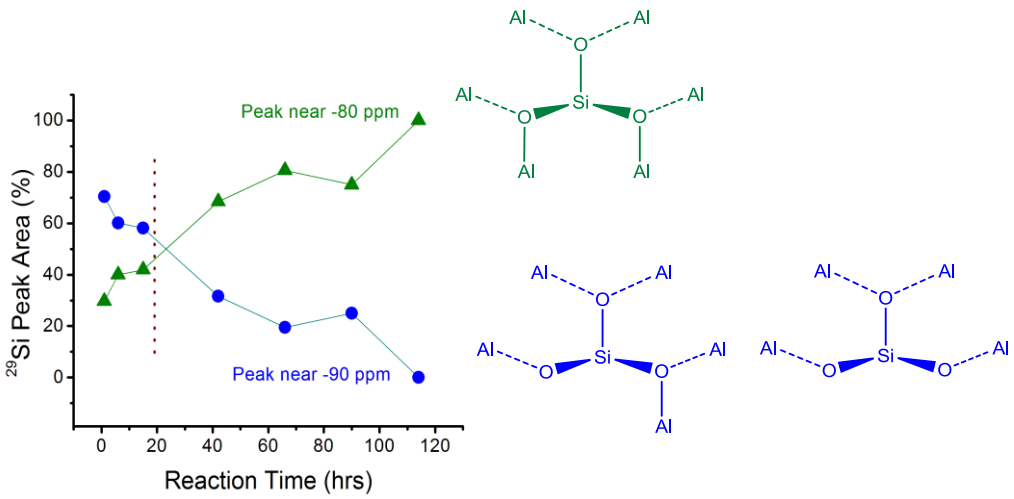

Figure 2-9. Integrated areas (relative to the total area) of the two resonances (peaks centered at −80 ppm and −90 ppm) in the ^{29}Si CP−MAS NMR spectra versus reaction time (18 h aging at 25 ˚C followed by 96 h heating at 95 ˚C). The dotted line separates the aging (left side of the line) and heating (right side of the line) stages. Spectra was collected at 25 ˚C.

2.3.3 Aluminum and Silicon Speciation

Before examining the nanotube synthesis solution, first electrospray ionization mass spectrometry (ESI−MS) experiments on ASB (0.1 M, pH 3.5, at 25 ˚C) and TEOS (0.05 M, pH 3.2, at 25 ˚C) solutions hydrolyzed in perchloric acid are conducted to understand aluminum and silicon speciation in mildly acidic aqueous solutions. The ESI−MS technique has the ability to "gently" vaporize and transfer ions directly from solutions to the gas phase in the mass spectrometry column, thereby allowing rapid and highly sensitive characterization of molecular species and larger complexes [86, 87]. The ESI−MS spectra of TEOS and ASB solutions after 1 h of hydrolysis at 25 ˚C are shown in Figure 2-10 and 2-11, respectively. The structural identification of hydrolysis products is carried out based on the detected mass-to-charge ratio (m/z), isotopic ratios, and "water (H_2O) series", which are signals with incremental differences of m=18 units (corresponding to the same species with different numbers of attached water molecules in the vaporized state). Therefore, the m/z separation between the signals will be 9 units for doubly charged species and 6 units for triply charged species [88-90]. Peaks that do not belong to a water series cannot be identified immediately, as their charge cannot be inferred *a priori*. Care is required in order to extract the relevant information from the large mass of ESI−MS data [91]. A detailed quantitative approach was adopted. A computer code was written in order to scan through all possible molecular formulae that match every detected peak (m/z ratio) above noise level. The code considers all elemental combinations (including all chemically significant isotopes) of Al, Si, H, O, C, and Cl, as well as every ligand (–OH, –Cl, $-OCl^{35}O_3$, $-OCl^{37}O_3$, $-OC_2H_5$, $-OC_4H_9$). This produced a list of arithmetically possible molecular formulae, of which the vast majority

are easily eliminated as being chemically impossible. The final lists of aluminate and silicate species in Table 2-1 and Table 2-2 were assigned to the experimental m/z ratios based on their full agreement with the interpreted charge, isotope separation, and structural consistency throughout the spectra. Moreover, the last m/z ratio of a "water series" should not exceed the number of available coordination sites for water in the identified structure. On the other hand, the chlorine isotopic distribution patterns in the m/z 400−900 region indicate several complexes with overlapping m/z values. In this region, it is much more difficult to identify the large number of isotope peaks and to correlate the isotope peak ratios to the amount of chlorine in the structure. For example, the isotopic peak intensity ratio should be 9:6:1 for species containing two $OClO_3^-$ ions, but because of overlapping of signals from different species, this ratio is not easily identified [92]. Finally, solvated DFT calculations were used to optimize the geometry of selected hydrolysis products.

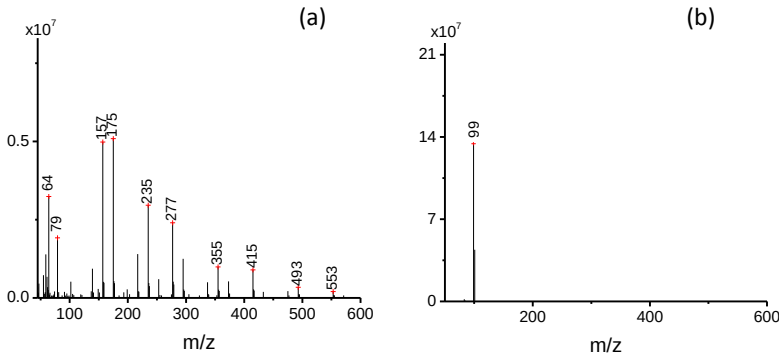

Figure 2-10. ESI−MS spectra of hydrolyzed 0.05 M TEOS at mildly acidic solutions (pH~3.2) obtained after 1 h aging at 25 ˚C: (a) ESI(+) and (b) ESI(−). Peak separations of 18 u (such as m/z 157 to 175 or m/z 355 to 373) might be due to dehydroxylation of silicate species [93].

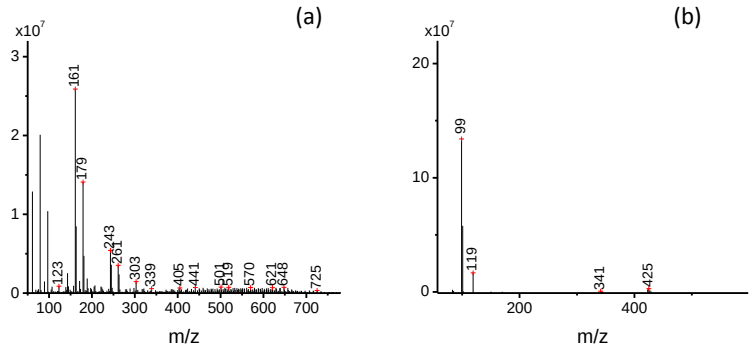

Figure 2-11. ESI−MS spectra of hydrolyzed 0.1 M ASB at mildly acidic solutions (pH∼3.4) obtained after 1 h aging at 25 ˚C: (a) ESI(+), and (b) ESI(−).

Table 2-1. Aluminate complexes identified from positive and negative charge scan modes of ESI–MS (m/z 20–900) in mildly acidic solutions (pH ∼3.4) after 1 h of hydrolysis of ASB at 25 ˚C.

Chemical Formula of *Al* Species	**Peak Series (m/z)**
***ESI*(+)**	
$[Al(OH)_2(H_2O)_n]^+$	61+18n (n=0-2)
$[Al(OH)(H_2O)_n(ClO_4)]^+$	143+18n (n=0-3)
$[Al(H_2O)_n(ClO_4)_2]^+$	225+18n (n=0-3)
$[Al_2(OH)_4(ClO_4)(H_2O)_n]^+$	221+18n (n=0-5)
$[Al_2(OH)_3(H_2O)_n(ClO_4)_2]^+$	303+18n (n=0-5)
$[Al_2(OH)_2(H_2O)_n(Cl^{35}O_4)_2(Cl^{37}O_4)]^+$	387+18n (n=0-4)
$[Al_5(OH)_9(H_2O)_{n+5}(ClO_4)_4]^{2+}$	387+9n (n=0-6)
$[Al_7(OH)_{17}(H_2O)_{7+n}(Cl^{35}O_4)_2]^{2+}$	401+9n (n=0-4)
$[Al_{10}(OH)_{22}(H_2O)_n(Cl^{35}O_4)_5(Cl^{37}O_4)]^+$	420+18n (n=0-2)
$[Al_6(OH)_{17}(H_2O)_n]^+$	451+18n (n=0-2)
$[Al_7(OH)_{15}(H_2O)_{n+5}(ClO_4)_4]^+$	465+18n (n=0-3)
$[Al_8(OH)_{17}(H_2O)_n(Cl^{35}O_4)_4(Cl^{37}O_4)]^{2+}$	501+9n (n=0-4)
$[Al_8(OH)_{17}(H_2O)_{n+2}(Cl^{35}O_4)_2(Cl^{37}O_4)]^{2+}$	515+9n (n=0-4)
$[Al_9(OH)_{22}(H_2O)_{n+8}(Cl^{35}O_4)_3]^{2+}$	529+9n (n=0-2)
$[Al_9(OH)_{20}(H_2O)_{n+9}(Cl^{35}O_4)_4(Cl^{37}O_4)]^{2+}$	621+9n (n=0-4)
$[Al_{13}O_4(OH)_{24}(H_2O)_{n+2}(Cl^{35}O_4)_4(Cl^{37}O_4)]^{2+}$	678+9n (n=0-5)
$[Al_8(OH)_{22}(H_2O)_{n+2}(Cl^{35}O_4)]^+$	707+18n (n=0-2)
$[Al_{12}O_4(OH)_{20}(H_2O)_{n+4}(Cl^{35}O_4)_5(Cl^{37}O_4)]^{2+}$	698+9n (n=0-5)
***ESI*(−)**	
$[Cl(O)_{n+3}]^-$	83+16n (n=0-1)
$[Al_2O_3(OH)]^-$	m/z 119
$[Al(ClO_4)_4]^-$	m/z 425
$[Al(OH)(ClO_4)_3]^-$	m/z 341

Several aluminate species of varying sizes, containing 1−13 aluminum atoms (Al_1−Al_{13} species), were identified (Table 2-1). Small molecules were observed in

various forms, ranging from monomeric complexes $[Al(OH)_2(H_2O)_n]^+$ (n=0−2), $[Al(OH)(H_2O)_n(ClO_4)]^+$ (n=0−3), $[Al(H_2O)_n(ClO_4)_2]^+$ (n=0−3), $[Al(OH)(ClO_4)_3]^-$, $[Al(ClO_4)_4]^-$, $[Al(OH)_3(H_2O)_n(ClO_4)_3]^-$; dimers $[Al_2(OH)_4(ClO_4)(H_2O)_n]^+$ (n=0−5), $[Al_2(OH)_3(H_2O)_n(ClO_4)_2]^+$ (n=0−5), $[Al_2(OH)_2(H_2O)_n(Cl^{35}O_4)_2(Cl^{37}O_4)]^+$ (n=0−4), $[Al_2O_3(OH)]^-$; and trimers $[Al_3O_3(OH)(H_2O)_n(ClO_4)_3]^-$ (n=0−4). As seen in the geometry-optimized structures (Figure 2-12) of singly or multiply-charged $[Al_6]^+$ and $[Al_8]^{2+}$ polymeric aluminate complexes, there are complete or incomplete aluminate rings in which octahedral aluminum centers are bridged with bis(μ_2-hydroxo) groups. Such complexes are immediately recognized as precursors for the formation of structures such as gibbsite $[Al(OH)_3]$, whose basic unit is the Al_6 ring. Larger complexes such as Al_9, Al_{10}, Al_{12} containing Al_6 ring units, and Al_{13} (Keggin ion) are also observed. In a further confirmation of results, a Al_{13}^{2+} Keggin ion [89] was also observed previously. Complexation between aluminum and perchlorate ($-OClO_3$) species was evident from the chlorine isotopic peak separations. The species contain various numbers of $-OClO_3$ ions. Although the Al_6 ring motif is always present, there are clearly several isomeric arrangements of perchlorate anions, hydroxyl groups, and water molecules on the edges of these complexes. The structures shown in Figure 2-11 depict only individual isomers of these species.

These structures are clearly shown to have planar minimum-energy configurations by the DFT calculations. Based on overall observations of the structural patterns in the identified monomer and dimer complexes, it is found that variations in the number of attached perchlorate ions are primarily caused by the replacement of outer −OH groups

with $-OClO_3$ groups. Bidentate ($=O_2ClO_2$) complexation of perchlorate anions with aluminates can potentially also occur. However, quantitative analysis of the low-molecular weight species clearly indicated that the molecular formulae are only consistent with monodentate complexation in the form of $-OClO_3$. A very recent ESI study on aluminum speciation in aqueous $AlCl_3$ solutions containing the ClO_4^- anion has suggested that the perchlorate anion might also help bridge two aluminum ions [88]. Other recent findings indicated denser, "brucite-like" aluminate complexes in hydrolyzed aluminum solutions that did not contain perchlorate ions [77, 94], whereas the results in this thesis clearly indicate species with a gibbsite (six-membered ring) structure (m/z = 519 in Figure 2-12) and also confirm previous SAXS studies [95]. The observed complexation of perchlorate ions with almost all the aluminate species (Table 2-1) may indicate their role in stabilizing species whose basic unit is the six-membered gibbsite ring, and inhibiting formation of brucite-like clusters. The complexation of aluminate species by perchlorate anions may also prevent further condensation of species larger than Al_{13}. Therefore, it is believed that complexation of aluminosilicate species with perchlorate anions is important in understanding the mechanism of nanotube formation. Species larger than Al_{13} was not detected, but previous studies on aluminate solutions indicated the possible existence of Al_{30} [75] and Al_{26} [96] structures that might be formed by condensation of more than one Keggin unit.

Next, silicon speciation in mildly acidic solutions is studied by ESI$-$MS$(+)$ and ESI$-$MS$(-)$ after 1 h of TEOS hydrolysis at 25 ˚C. Distances between the isotopic patterns (^{28}Si, ^{29}Si) are observed to be 1 m/z, showing that the species have 1 unit of

charge. Hydrolysis of TEOS predominantly resulted in the formation of small silicate species such as the dimer (m/z = 175) and cyclic trimer (m/z = 235) [93]. The silicate monomer was not detected in either scan mode. Complete hydrolysis occurred, and no ethoxy ($-OC_2H_5$) ligands were detected in the structures. Tetramer and pentamer silica species were also found at m/z = 277 and 373, respectively. The solution also contains cage-like polymeric ions. Signals at m/z = 415 and m/z = 533 were assigned to T6 and T8 cages, respectively. Previous studies also reported cage structures of silicates [86, 97]. No complexation with perchlorate anions (ClO_4^-) was detected. As expected, no silicon species were detected in the negative scan mode. Figure 2-13 shows DFT-optimized geometries of the species identified in the silicate solution, which are predominantly cyclic in structure. Previous computational works using density functional theory and free energy calculations [97, 98] also report that cyclic silicate species are very stable and are highly likely to be formed.

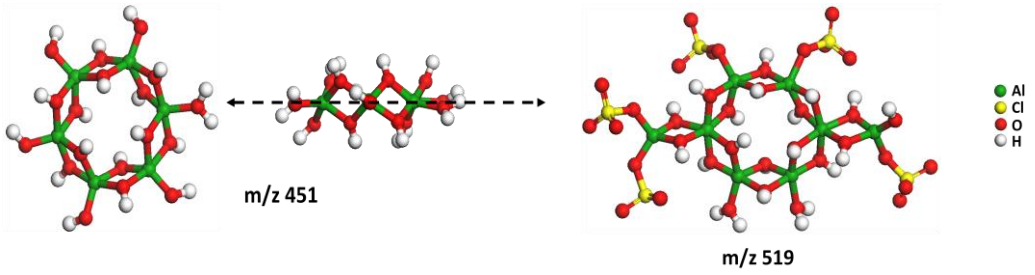

Figure 2-12. DFT-optimized geometries of selected planar complexes identified in a mildly acidic aqueous aluminate solution at 25 ˚C. For illustration, the upper structure (Al_6) with m/z = 451 is shown in two orientations: top view (on left), and side view (on right). As indicated by the dashed line, the complex is planar.

Table 2-2. Silicate complexes identified from positive and negative charge scan modes of ESI–MS (m/z 20–900) in mildly acidic solutions (pH~3.2) after 1 h of hydrolysis of TEOS at 25 ˚C.

Chemical Formula of *Si* Species	Peak (m/z)
$ESI(+)$	
$[Si_2O(OH)_5(H_2O)]^+$	m/z 175
$[Si_3O_3(OH)_5(H_2O)]^+$	m/z 235
$[Si_4O_6(OH)_3(H_2O)]^+$	m/z 277
$[Si_5O_6(OH)_7(H_2O)]^+$	m/z 355
$[Si_6O_9(OH)_5(H_2O)]^+$	m/z 415
$[Si_7O_{10}(OH)_7(H_2O)]^+$	m/z 493
$[Si_8O_{12}(OH)_7(H_2O)]^+$	m/z 553
$ESI(-)$	
$[Cl(O)_{n+3}]^-$	83+16n (n=0-1)

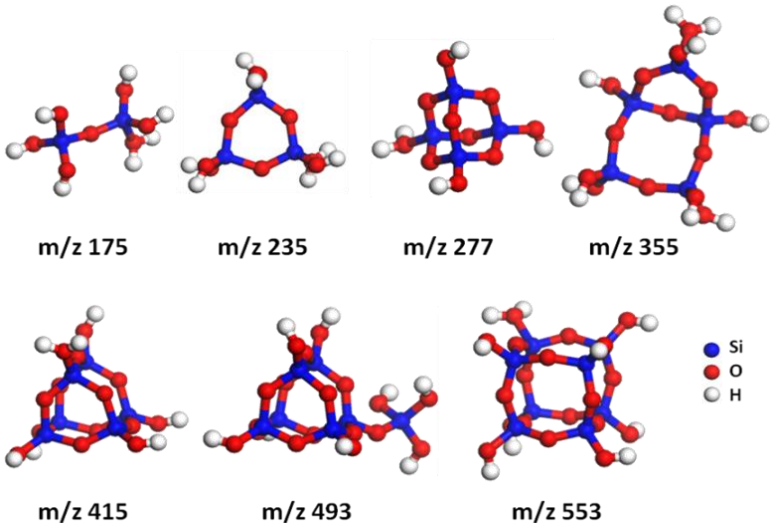

Figure 2-13. DFT-optimized geometries of selected complexes identified in a mildly acidic aqueous silicate solution at 25 ˚C.

2.3.4 Aluminosilicate Speciation

Having confirmed the reliability of ESI−MS measurements and analysis techniques, ESI−MS spectra from nanotube synthesis solutions at various stages are then obtained. The spectra collected throughout the aging stage did not show significant differences in peak positions. Therefore, it is concluded that the main species in the

synthesis solution do not change during the aging stage. Figure 2-14 shows a ESI−MS spectra of the nanotube synthesis solution (taken after 1 h of aging at 25 ˚C), and Table 2-3 shows the chemical composition of species identified by exhaustive quantitative procedure. It is clear that the nanotube synthesis is controlled by aluminate speciation. No signals from silicate species were detected. As in the pure aluminate solution, the distribution of aluminosilicate species in solution ranged from having 1−13 aluminum atoms in their structures, the differences being only in the number of attached silicon tetrahedra and perchlorate anions [i.e., $Al_1Si_x(ClO_4)_y - Al_{13}Si_x(ClO_4)_y$]. Keggin ions with attached silicate groups were also identified.

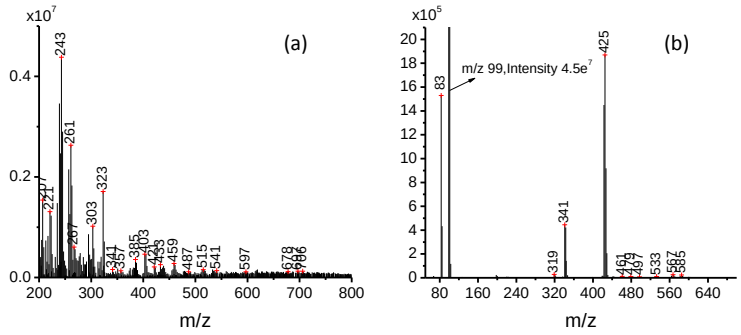

Figure 2-14. ESI−MS spectra of nanotube solutions after 1 h of aging at 25 ˚C: (a) ESI(+), and (b) ESI(−).

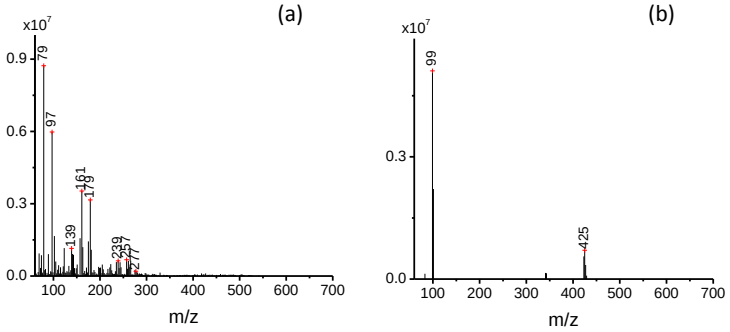

Figure 2-15. ESI−MS spectra of solutions after 3 h heating: (a) ESI(+), and (b) ESI(−). ESI−MS spectra of solutions after 96 h heating: (c) ESI(+), and (d) ESI(−).

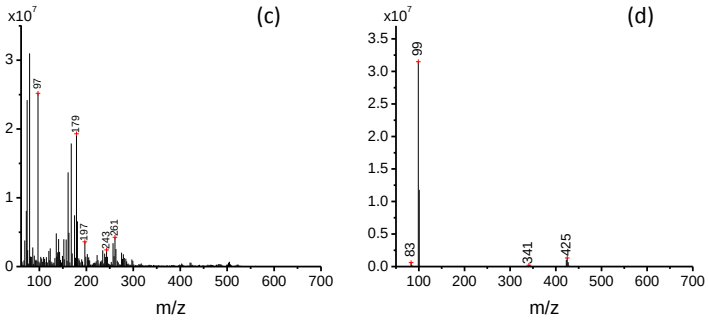

Figure 2-15 continued.

Table 2-3. Aluminosilicate complexes identified from positive and negative charge scan modes of ESI−MS (m/z 20−900) in the nanotube synthesis solution after 1 h of aging.

Chemical Formula of *AlSi* Species	**Peak Series (m/z)**
***ESI*(+)**	
$[Al(OH)_2(H_2O)_n]^+$	61+18n (n=0-2)
$[Al(OH)(H_2O)_n(ClO_4)]^+$	143+18n (n=0-3)
$[Al(H_2O)_n(ClO_4)_2]^+$	225+18n (n=0-3)
$[Al_2(OH)_5(H_2O)_n]^+$	139+18n (n=0-2)
$[Al_2(OH)_4(ClO_4)(H_2O)_n]^+$ / $[AlSiO(OH)_3(ClO_4)(H_2O)_n]^+$	221+18n (n=0-3)
$[Al_2SiO_2(OH)_5(H_2O)_{n+1}]^+$ / $[Al_3O(OH)_6(H_2O)_{n+1}]^+$	217+18n (n=0-3)
$[Al_3SiO_2(OH)_6(H_2O)_n(ClO_4)]^{2+}$	171+9n (n=0-5)
$[Al_3SiO_2(OH)_8(H_2O)_n]^+$ / m/z 277: $[Si_4O_6(OH)_3(H_2O)]^+$	277+18n (n=0-2)
$[Al_7Si_2O_5(OH)_{13}(H_2O)_{n+3}(ClO_4)_3]^{3+}$	299+6n (n=0-4)
$[Al_2(OH)_3(H_2O)_n(ClO_4)_2]^+$	303+18n (n=0-5)
$[Al_7Si_2O_5(OH)_{12}(H_2O)_n(Cl^{35}O_4)_3(Cl^{37}O_4)]^{3+}$	309+6n (n=0-10)
$[Al_8Si_2O_6(OH)_{13}(H_2O)_n(Cl^{35}O_4)_3(Cl^{37}O_4)]^{3+}$	329+6n (n=0-7)
$[Al_2(OH)_2(H_2O)_n(ClO_4)_3]^+$	385+18n (n=0-4)
$[Al_2(OH)_2(H_2O)_n(Cl^{35}O_4)_2(Cl^{37}O_4)]^+$	387+18n (n=0-4)
$[Al_2SiO(OH)_5(H_2O)_n(ClO_4)_2]^+$	381+18n (n=0-3)
$[Al_4SiO_3(OH)_8(H_2O)_{n+1}(ClO_4)]^+$	437+18n (n=0-2)
$[Al_2SiO(OH)_4(H_2O)_n(ClO_4)_3]^+$	463+18n (n=0-4)
$[Al_5SiO_3(OH)_{12}(H_2O)_{n+1}]^+$ / $[Al_4Si_2O_4(OH)_{11}(H_2O)_{n+1}]^+$	433+18n (n=0-6)
$[Al_5Si_2O_5(OH)_{12}(H_2O)_{n+1}]^+$	493+18n (n=0-3)
$[Al_6SiO_3(OH)_{15}(H_2O)_n]^+$	493+18n (n=0-3)
$[Al_4Si_2O_4(OH)_{10}(H_2O)_n(ClO_4)]^+$ / $[Al_5SiO_3(OH)_{11}(H_2O)_n(ClO_4)]^+$	497+18n (n=0-4)
$[Al_{10}SiO_3(OH)_{22}(H_2O)_n(ClO_4)_3(ClO_4)]^{2+}$	559+9n (n=0-4)
$[Al_8Si_2O_5(OH)_{15}(H_2O)_{n+5}(Cl^{35}O_4)_4(Cl^{37}O_4)]^{2+}$	597+9n (n=0-4)
$[Al_{10}Si_3O_9(OH)_{18}(H_2O)_{n+1}(Cl^{35}O_4)_3(Cl^{37}O_4)]^{2+}$	610+9n (n=0-5)
$[Al_{12}Si_3O_9(OH)_{27}(H_2O)_{n+6}(Cl^{35}O_4)]^{2+}$	609+9n (n=0-4)
$[Al_{12}Si_3O_9(OH)_{25}(H_2O)_n(Cl^{35}O_4)_2(Cl^{37}O_4)]^{2+}$	638+9n (n=0-6)
$[Al_{13}Si_2O_{10}(OH)_{22}(H_2O)_{n+1}(Cl^{35}O_4)_2(Cl^{37}O_4)]^{2+}$	638+9n (n=0-6)
$[Al_{12}Si_3O_9(OH)_{26}(H_2O)_{n+1}(ClO_4)_2]^{2+}$	605+9n (n=0-7)
$[Al_{12}Si_5O_{12}(OH)_{29}(H_2O)_{n+3}(ClO_4)]^{2+}$	678+9n (n=0-4)
$[Al_{13}O_4(OH)_{24}(H_2O)_{n+2}(Cl^{35}O_4)_4(Cl^{37}O_4)]^{2+}$	678+9n (n=0-4)
$[Al_{12}Si_4O_{10}(OH)_{29}(H_2O)_{n+6}(Cl^{35}O_4)]^{2+}$	648+9n (n=0-4)
$[Al_{12}Si_7O_{16}(OH)_{30}(H_2O)_{n+5}]^{2+}$	688+9n (n=0-5)
$[Al_{12}Si_4O_{10}(OH)_{28}(H_2O)_{n+8}(Cl^{35}O_4)_2]^{2+}$	707+9n (n=0-4)

Table 2-3 (continued).

$[Al_{12}Si_7O_{13}(OH)_{35}(H_2O)_{n+5}(ClO_4)]^{2+}$	756+9n (n=0-3)
$[Al_{13}Si_6O_{10}(OH)_{40}(H_2O)_{n+3}(ClO_4)]^{2+}$	756+9n (n=0-3)
$\boldsymbol{ESI(-)}$	
$[Cl(O)_{n+3}]^-$	83+16n (n=0-1)
$[Al(OH)(ClO_4)_3]^-$	m/z 341
$[Al(ClO_4)_4]^-$	m/z 425
$[Al_3O_3(OH)(H_2O)_n(ClO_4)_3]^-$	443+18n (n=0-3)
$[Al_2SiO_2(OH)_4(H_2O)_3(ClO_4)_3]^-$ / $[Al_3O(OH)_5(H_2O)_3(ClO_4)_3]^-$	m/z 533
$[Al_4Si_2O_4(OH)_{12}(H_2O)_{n+2}(ClO_4)]^-$	567+18n (n=0-1)

There are several important points to be highlighted at this stage. First, it is significant that nearly all species could be explained with the same basic structural characteristics as found in the aluminate solution, such as the octahedral aluminum units linked by μ_2-OH groups at shared edges, the existence of aluminosilicate gibbsite-like units with a Q^3(6Al) configuration of Si, the binding of perchlorate ions to the edges of the aluminosilicate complexes, and the existence of end-groups consisting of highly distorted tetra-coordinated aluminum sites (with Al−OH or $Al-OClO_3$ bonds). The silicate species are attached to aluminate complexes that are already in a nanotube-like configuration, most notably the Al_6 rings with silicon attached in a Q^3(6Al) configuration as well as larger sheet-like structures in which this structural motif is repeated. These complexes constitute the first direct evidence of "proto-nanotube" species existing in the solution. Second, these ESI−MS findings are directly supported by NMR results. Third, the aluminosilicate, aluminate, and silicate speciation arises naturally from the arithmetic analysis of the ESI−MS data and does not involve any structural assumptions other than the list of elements, isotopes, ligands, and reasonably expected coordination environments (e.g., octahedral Al, tetrahedral Al and Si). Fourth, the conversion of tetrahedral aluminum to octahedral aluminum was proposed as being necessary prior to proto-imogolite formation [62] and was interpreted as being a result of silicate species

bridging two aluminate species. On the other hand, it appears here that such a conversion more likely occurs due to rearrangement of tetrahedral aluminum (found on the edges of the proto-nanotube sheets) into octahedral aluminum during the assembly of the nanotube, by condensation of these proto-nanotube complexes.

Solvated DFT-based geometry optimizations performed on selected key species revealed the *inherent curvature* of identified aluminosilicate precursors (Figure 2-16) in comparison to the *planar* precursors found in aluminate solutions (Figure 2-12). The precursors with m/z = 547 consist of a hexagonal ring of aluminate octahedra, and tetrahedra, with a silanol group attached to it. This structure is closely related to the structure of the final nanotube material, and its radius of curvature is almost identical to that of the final nanotube material. Larger precursors such as m/z = 595 and 733 also show the existence of the same structural motif as the precursor with m/z = 547. The present study therefore indicates the potential for engineering the curvature of nanostructured materials (such as nanotubes and nanoshells) by controlling the speciation of the molecular and nanoscale precursors.

The species identified in the subsequent heating step at 95 ˚C are listed in Table 2-4. Upon heating the aged solution to 95 ˚C to induce nanotube assembly, it is observed that all proto-nanotube species in the m/z 500−800 region of the ESI−MS spectra disappear within 3 h, but the species identified in the m/z 50−500 region remain nearly constant throughout the reaction (Figure 2-15). This is consistent with the condensation of the proto-nanotube precursors into larger nanoparticles which then rearrange into short

nanotubes, a mechanism proposed by us previously [60]. New Al_3Si species (Table 2-4) (highlighted in bold) appeared within 24 h of heating. Therefore, the new 3-5 ppm peak appearing in the ^{27}Al NMR spectra are tentatively assigned to these Al_3Si species.

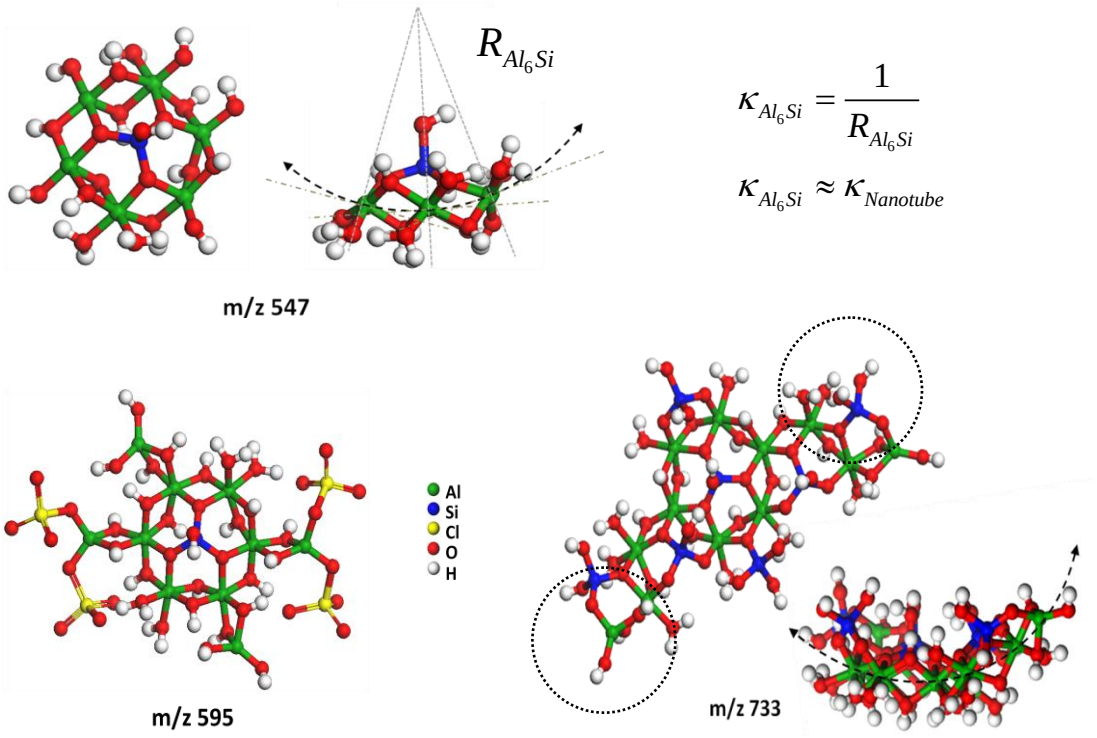

Figure 2-16. DFT-optimized geometries of selected aluminosilicate "proto-nanotube" precursors identified by ESI−MS. The species m/z = 547, 595, and 733 are shown in two orientations: top view (left) and side view (right). Dotted circles show example locations of Al tetrahedra adjoined by Si atoms in Si(nAl) coordination. The dashed lines follow the inherent curvature (κ) of these species, as measured from their radii of curvature (R). As shown, $\kappa_{Al_6Si} \approx \kappa_{Al_{12}Si_7} \approx \kappa_{Nanotube}$.

Table 2-4. Aluminosilicate complexes identified from positive and negative charge scan modes of ESI−MS (m/z 20−900) in the nanotube synthesis solution during 96 h reaction.

Chemical Formula of *AlSi* Species	**Peak Series (m/z)**
***ESI*(+)**	
$[Al(OH)_2(H_2O)_n]^+$	61+18n (n=0-2)
$[Al(OH)(H_2O)_n(ClO_4)]^+$	143+18n (n=0-3)
$[Al(H_2O)_n(ClO_4)_2]^+$	225+18n (n=0-3)
$[Al_2(OH)_5(H_2O)_n]^+$	139+18n (n=0-2)
$[Al_2(OH)_4(ClO_4)(H_2O)_n]^+$ / $[AlSiO(OH)_3(ClO_4)(H_2O)_n]^+$	221+18n (n=0-3)
$[Al_2SiO_2(OH)_5(H_2O)_{n+1}]^+$ / $[Al_3O(OH)_6(H_2O)_{n+1}]^+$	217+18n (n=0-3)
$[Al_3SiO_2(OH)_6(H_2O)_n(ClO_4)]^{2+}$	171+9n (n=0-5)
$[Al_3SiO_2(OH)_8(H_2O)_n]^+$ / m/z 277: $[Si_4O_6(OH)_3(H_2O)]^+$	277+18n (n=0-2)
$[Al_7Si_2O_5(OH)_{13}(H_2O)_{n+3}(ClO_4)_3]^{3+}$	299+6n (n=0-4)
$[Al_2(OH)_3(H_2O)_n(ClO_4)_2]^+$	303+18n (n=0-5)
$[Al_7Si_2O_5(OH)_{12}(H_2O)_n(Cl^{35}O_4)_3(Cl^{37}O_4)]^{3+}$	309+6n (n=0-10)
$[Al_8Si_2O_6(OH)_{13}(H_2O)_n(Cl^{35}O_4)_3(Cl^{37}O_4)]^{3+}$	329+6n (n=0-7)
$[Al_2(OH)_2(H_2O)_n(ClO_4)_3]^+$	385+18n (n=0-4)
$[Al_2(OH)_2(H_2O)_n(Cl^{35}O_4)_2(Cl^{37}O_4)]^+$	387+18n (n=0-4)
$[Al_2SiO(OH)_5(H_2O)_n(ClO_4)_2]^+$	381+18n (n=0-3)
$[Al_4SiO_3(OH)_8(H_2O)_{n+1}(ClO_4)]^+$	437+18n (n=0-2)
$[Al_2SiO(OH)_4(H_2O)_n(ClO_4)_3]^+$	463+18n (n=0-4)
$[Al_5SiO_3(OH)_{12}(H_2O)_{n+1}]^+$ / $[Al_4Si_2O_4(OH)_{11}(H_2O)_{n+1}]^+$	433+18n (n=0-6)
$[Al_5Si_2O_5(OH)_{12}(H_2O)_{n+1}]^+$	493+18n (n=0-3)
$[Al_6SiO_3(OH)_{15}(H_2O)_n]^+$	493+18n (n=0-3)
$[Al_4Si_2O_4(OH)_{10}(H_2O)_n(ClO_4)]^+$ / $[Al_5SiO_3(OH)_{11}(H_2O)_n(ClO_4)]^+$	497+18n (n=0-4)
$[Al_3SiO_2(OH)_7(H_2O)_{n+6}]^{2+}$	**184+9n (n=0-1)**
$[Al_3SiO_2(OH)_5(H_2O)_{n+6}(ClO_4)_2]^{2+}$	**266+9n (n=0-1)**
$[Al_3SiO_2(OH)_8(H_2O)_{n+2}]^+$	**313+18n (n=0-2)**
***ESI*(−)**	
$[Cl(O)_{n+3}]^-$	83+16n (n=0-1)
$[Al(OH)(ClO_4)_3]^-$	m/z 341
$[Al(ClO_4)_4]^-$	m/z 425
$[Al_3O_3(OH)(H_2O)_n(ClO_4)_3]^-$	443+18n (n=0-4)
$[Al_2SiO_2(OH)_4(H_2O)_3(ClO_4)_3]^+$ / $[Al_3O(OH)_5(H_2O)_3(ClO_4)_3]^+$	m/z 533

2.3.5 Overall Mechanism of Nanotube Formation

On the basis of the detailed insights from ESI−MS and NMR investigations, a molecular-level mechanism of single-walled aluminosilicate nanotube formation is constructed (Figure 2-17). Stable proto-nanotube intermediates with intrinsic curvature form within 1 h of aging and remain essentially unchanged throughout this step. Within 7

h of the initial mixing of reactants, a dynamic equilibrium between “small”, “medium”, and “large” aluminosilicate precursors is established.

The equilibria involving some main species detected by ESI−MS is depicted as follows:

$$2[Al_2SiO_2(OH)_5(H_2O)]^+ \leftrightarrow [Al_4Si_2O_4(OH)_{11}(H_2O)]^{2+} + [H]^+$$

$$3[Al_4SiO_3(OH)_8(H_2O)(ClO_4)]^+ \leftrightarrow [Al_{12}Si_3O_9(OH)_{26}(H_2O)(ClO_4)_2]^{2+} + 2[H]^+ + ClO_4^-$$

$$[Al_{12}Si_4O_{10}(OH)_{28}(H_2O)_8(ClO_4)_2]^{2+} + [Al(ClO_4)_4]$$
$$\leftrightarrow [Al_{13}Si_4O_{16}(OH)_{18}(H_2O)_5(ClO_4)_3]^{2+} + 2[H]^+ + ClO_4^- + 7H_2O$$

The experimental findings that support such equilibria are summarized as follows: (1) there is a slight decrease in pH from 3.7 to 3.3 during aging; (2) there is an increase in the integrated area of Keggin peaks at 63.3 ppm, 12 ppm, and 6 ppm peak in liquid-state ^{27}Al NMR that represents species in nanotube-like configuration; (3) there is a decrease in line width and chemical shift of the 6 ppm peak in liquid-state ^{27}Al NMR; (4) there is slight decrease in area % of −90 ppm peak in ^{29}Si MAS NMR spectra as a function of aging time; and (5) ESI-MS showed that main species remained essentially similar throughout the aging, but NMR peaks showed minor changes in terms of their chemical shift, integrated area and fwhm values.

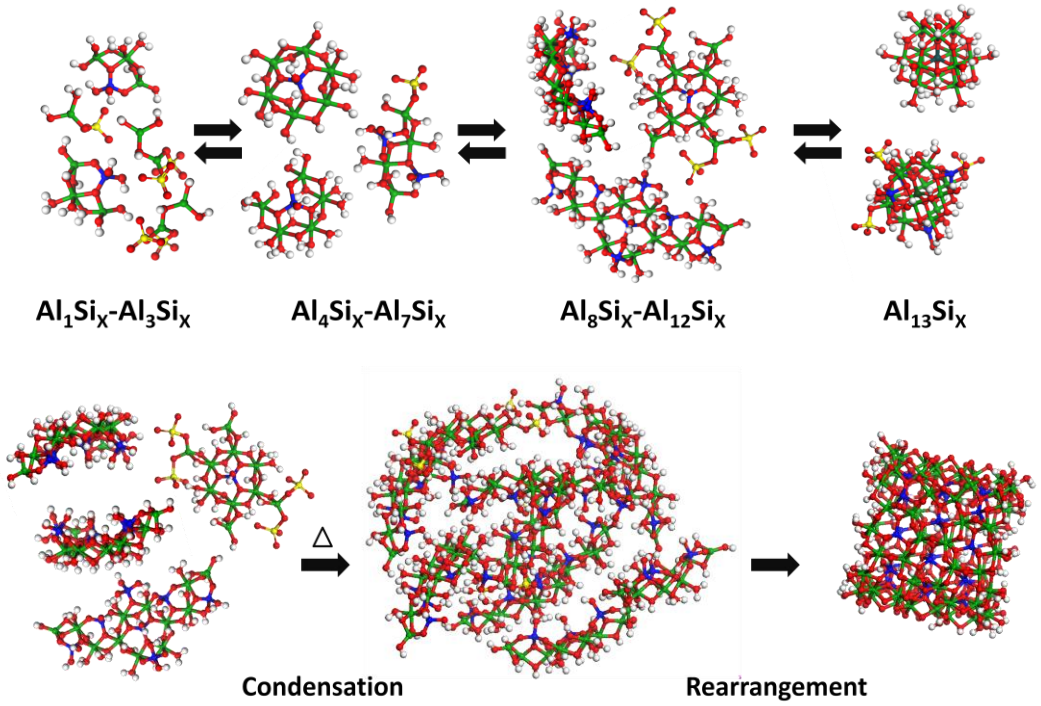

Figure 2-17. Formation mechanism of aluminosilicate nanotubes. The upper section of the figure shows the equilibrium established between aluminosilicate species during the aging stage at 25 ˚C. The lower section shows the condensation and rearrangement of $Al_8Si_x-Al_{12}Si_x$ species upon heating.

The DFT simulations revealed that the $Al_6Si_x-Al_{12}Si_x$ aluminosilicate species have intrinsically curved structures, in contrast to the planar structures observed in the aluminate solutions. Upon heating the aged nanotube synthesis solution, the nanoscale aluminosilicate intermediate species represented by the ESI−MS region m/z 500−800 (i.e., $Al_8Si_x-Al_{13}Si_x$) disappear from the ESI−MS spectra. Those species are hence condensing into larger nanoparticle aggregates and then rearrange into the initial nanotubes and subsequently grow by a variety of processes (e.g., precursor attachment, end-to-end aggregation). The experimental findings that support such a mechanism are summarized as follows: (1) an abrupt decrease in pH immediately upon heating to 95 ˚C and nearly constant pH throughout the remaining 95 h of reaction; (2) nearly constant

area of liquid-state ^{27}Al NMR 6 ppm peak that represents the nanotube-like aluminum bonding environment; and (3) rearrangement detected by increase in area % of −80 ppm and decrease in −90 ppm peak in solid-state ^{29}Si NMR.

The role of the aluminosilicate Keggin-like ions remains unclear. The literature on aluminate solutions suggests the transformation of aluminate Keggin ions into planar gibbsite-like layered structures. Such a rearrangement in the aluminosilicate solution was not observed. In contrast, the aluminosilicate solution contains a richer variety of species, many of which are complexed with perchlorate ions. On the basis of observations as discussed above, whether the $Al_{13}Si_x$ Keggin species participate in the condensation and rearrangement of the nanoscale species into nanotubes, or whether they decompose into smaller species such as the Al_3Si_x units that appear upon heating the nanotube synthesis solution cannot be distinguished.

CHAPTER 3

SHAPING SINGLE-WALLED METAL OXIDE NANOTUBES FROM PRECURSORS OF CONTROLLED CURVATURE

3.1 Introduction

Nanoscopic objects, such as nanotubes and nanowires, are important building block materials for nanoscale science and engineering. Despite the considerable progress in nanoscale materials processing, the difficulty in constructing nanoscopic objects of complex structure, morphology, and composition increases dramatically as one or more dimensions of the object drop to 10 or 1 nm length scales and also when the desired structural complexity deviates from that of simple crystals [99]. Such objects would be extremely interesting for achieving properties, such as fast transport of charge/mass/heat, drastically tunable electronic structure, confinement phenomena, and very high-surface areas [4]. Carbon nanotubes and their analogues continue to be extensively studied [16, 100]. Metal oxide nanotubes have emerged as attractive nanoscale materials due to their potentially vast range of tunable compositions and properties accessible by low-temperature solution-phase chemistry [22, 25]. Conventional routes for metal oxide nanoparticle growth involve either gas-phase catalytic or liquid-phase templated approaches to produce polydisperse, multiwalled nanotubes or nanowires several tens of nanometers in diameter (e.g., ZnO and TiO_2) [25]. However, examples of single-walled metal oxide nanotubes are available, such as aluminosilicate/germanate ($Al_2SiO_3(OH)_4/Al_2GeO_3(OH)_4$) and molybdenum oxide ($MoO_3$) nanotubes [33, 65]. Their unique wall structure and porosity, tunable dimensions, and chemically modifiable

interior and exterior surfaces cannot be obtained by scaling down the size of bulk porous materials [71]. The unique structure and tunable length of the aluminosilicate nanotube channel allow very high fluxes of water, alcohols, and potentially of charged species [54, 56, 101], thereby offering a self-assembled alternative to nanopores fabricated by top-down methods [102, 103]. The confinement of molecules and ions in the channel, and their interactions with species (including organic groups) [40-42, 104] on the inner wall of the nanotubes, offers potential for controlling molecular recognition phenomena relevant to applications, such as catalysis, separation, encapsulation, controlled release, and sensing. These nanotubes can be synthesized by low-temperature solution-phase processes with inexpensive reactants and without a catalyst [105-107].

Generalizable ‘design rules’ for nanoscopic metal oxide objects have not been available. In this work, two important steps toward this objective are demonstrated. First, it is shown that the diameter of a metal oxide nanotube can be shaped with angstrom-level precision by engineering the structure and composition of molecular- and nanometer-scale precursors responsible for nanotube formation, without disturbing the structure or composition of the final nanotube material. Second, the relationships between subtle alterations of the reactant composition, their effect on the structure and shape of the molecular and nanoscale precursors, and the curvature of the final nanotube were characterized at the molecular level. Although the findings have significant implications for nanoscale metal oxide systems in general, single-walled aluminosilicate (“AlSiOH”) nanotubes, which are synthetic analogues of the naturally occurring single-walled nanotubular mineral imogolite, are the main focus here on. Recent works have provided mechanistic information on the formation and growth of these nanotubes. It is now

known that their formation occurs by the condensation of nanoscale precursors into nanoparticle aggregates that subsequently assemble into ordered nanotubular structures and then continue to grow in length by a variety of mechanisms [38, 66]. These mechanisms have some similarities, but also fundamental differences, with those operating in the assembly of bulk porous materials such as zeolites [71, 108]. A molecular-level understanding of the nanotube assembly processes holds quantitative promise for rationally 'shaping' nanoscopic metal oxide objects in solution.

Figure 3-1 depicts the key principles underlying this work. It is hypothesized that there is a specific relationship between the precursor shapes and the resulting nanotube shapes; and furthermore that the precursor shape could be engineered precisely via the reactant composition. To demonstrate the Ångstrom-level control over precursor shape and the resulting nanotube shape, it is shown here that the binding of different anions to the nanoscale precursors can be exploited rationally to alter their curvature and thereby form nanotubes of precisely controlled diameters. Through a combination of nanotube synthesis, molecular mass spectrometry, cryo-electron microscopy, NMR spectroscopy, and quantum chemistry computations, the relationship between the type of binding anion, the shape and structure of the precursors, and the final nanotube curvature is shown explicitly. The findings clearly reveal a deliberate molecular-level approach to shaping nanoscale objects with a precision that is difficult to attain by conventional approaches.

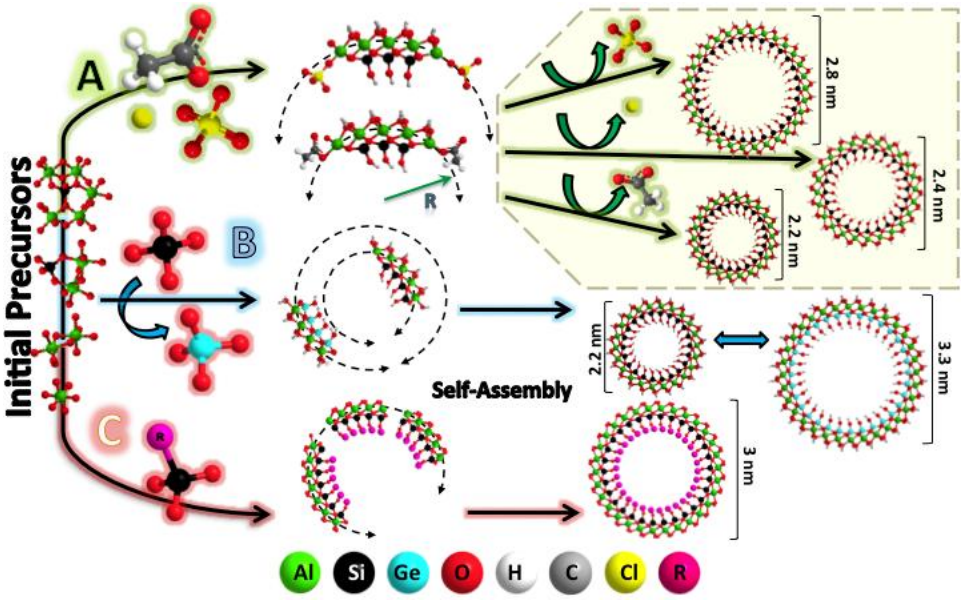

Figure 3-1. Shape control of metal oxide nanotubes. **A:** *Anion Complexation.* Use of different anions (e.g., acetate, chloride, perchlorate) that complex with the precursors and alter their curvature. The anions are released during condensation of the precursors, leaving the nanotube structure unaffected but allowing control of curvature, as shown in this work. Other methods for altering nanotube structure (not investigated here) may also follow similar but yet-unexplained mechanisms, such as **B:** *Substitution*. The silicate tetrahedra can be substituted with other tetrahedra (e.g., germanate), or **C:** *Functional Groups*. The silicate tetrahedra can be replaced by organosilicate ($Si-R$) tetrahedra; in both cases leading to a change in diameter as well as composition.

3.2 Experimental Details

TEOS (tetraethoxysilane) and Al(sec-butoxide)$_3$ were mixed in a glove box under inert conditions, and added to a 0.05 M aqueous solution of a protic acid X (where X = $HClO_4$, HCl, CH_3COOH) in the molar ratios Si:Al:X = 1:2:1 at 25 ˚C. The solution was stirred for 18 h, and then diluted to 0.02 M in Al. Immediately after dilution, the solution was heated to 95 ˚C and maintained under vigorous stirring for 4 days. Finally, the solution was dialyzed for 4 days against deionized water and then freeze-dried to obtain the final nanotube product for solid-state characterizations. Samples for cryo-electron microscopy were taken directly from the aqueous nanotube dispersion.

Powder X-ray diffraction (XRD) was performed on a PAnalytical X'pert Pro diffractometer operating with a Cu Kα source. The high-resolution diffraction data were collected with a diffracted beam collimator and a proportional detector, scanning from 2 to 30° two theta with a step size of 0.05°. Nitrogen physisorption measurements were carried out on a Micromeritics Tristar IIat 77 K. The sample was placed in an analysis tube and degassed under 15 mTorr vacuum at 200 ˚C for 12 hours before the physisorption measurement. Cryo-electron microscopy was performed at the Emory University Robert P. Apkarian Integrated Electron Microscopy Core. Nanotube aliquots were flash-frozen (plunge-frozen) onto glow-discharged, 200 mesh, holey carbon-coated copper grids in liquid ethane using a Vitrobot Mark III system (FEI, Hillsboro, Oregon). Images were collected using a JEOL JEM-2200FS 200 kV field emission transmission electron microscope with an in-column Omega energy filter (operated at 200 kV). The images were energy filtered with a slit width of 20 eV. Images were collected under low dose conditions with the sample maintained at a temperature of ~−177 ˚C Celsius. Images were captured on a high sensitivity Gatan 4k x 4k Ultrascan CCD camera at close to focus (i.e. minimal defocus applied).

^{27}Al and ^{29}Si solid-state NMR spectra were recorded on a Bruker AV 400 at 104.2 MHz and 79 MHz respectively, using 4-mm rotor and a sample spinning rate of 10 kHz. For the ^{27}Al NMR spectra, single-pulse excitation was employed with a pulse delay of 2 s and a pulse width of 3.20 μs, and 2048 free induction decays were recorded. $Al(NO)_3$ was used for calibration. For the ^{29}Si NMR spectra, a standard ^{1}H-^{29}Si cross-polarization sequence was used with a 5-μs ^{1}H 90° pulse length, 2-ms contact time, 5-s delay between

^{1}H excitation pulses, and 2048 scans were acquired. The spectra were calibrated with the sodium salt of 3-(trimethylsilyl)-1-propanesulfonic acid. Details of the ESI-MS and DFT experiments are described in Chapter 2.

3.3 Results and Discussion

3.3.1 X-ray Diffraction

Figure 3-2 shows the measured X-ray diffraction (XRD) patterns of aluminosilicate nanotubes synthesized using protic acids with different anions at 0.05 M concentration. The XRD patterns exhibit an intense low-angle peak, an accompanying shoulder, and a series of other peaks, corresponding to the scattering from bundles of tubes in monoclinic or hexagonal packing configurations. Detailed XRD studies show that the low-angle peak position is most strongly correlated with the external diameter of the nanotube, with the spacing between the nanotubes playing only a minor role [109]. As seen in Figure 3-2a, the low-angle peak, as well as the remaining peaks, show systematic shifts as a function of the anion(s) present in the synthesis solution, indicating systematic changes in the nanotube diameter. Aluminosilicate nanotubes synthesized using acetate anions have the smallest external diameters, whereas the use of perchlorate anions produces nanotubes with the largest external diameters. Figure 3-2b shows simulated XRD patterns of nanotube bundles in a hexagonal packing arrangement, showing the clear correlation of the peak shifts to the number of repeat units (N = 11−16) in the circumference. Since the structure of the nanotube wall is the same in all cases (as verified by multiple techniques described in this work), the pore size (internal diameter) should also exhibit the same trend as the outer diameter.

3.3.2 Nitrogen Physisorption

N_2 physisorption measurements were made to investigate the change in pore size due to the different anions in aluminosilicate nanotube synthesis and corroborate the XRD data. Figure 3-3a shows pore-size distribution plots determined using the Horvath-Kawazoe model with the Saito-Foley modification for cylindrical pores [110, 111]. Pore sizes centered at 0.80±0.02 nm, 0.93±0.05 nm, and 0.99±0.06 nm are obtained for nanotubes synthesized using 0.05 M HCl, 0.05 M 50%HCl-50%$HClO_4$, and 0.05 M $HClO_4$, respectively. The pore size of nanotubes synthesized with 0.05 M CH_3COOH is smaller than 0.8 nm and could not be resolved by N_2 physisorption analysis. The original adsorption curves are also provided in the Figure 3-3b.

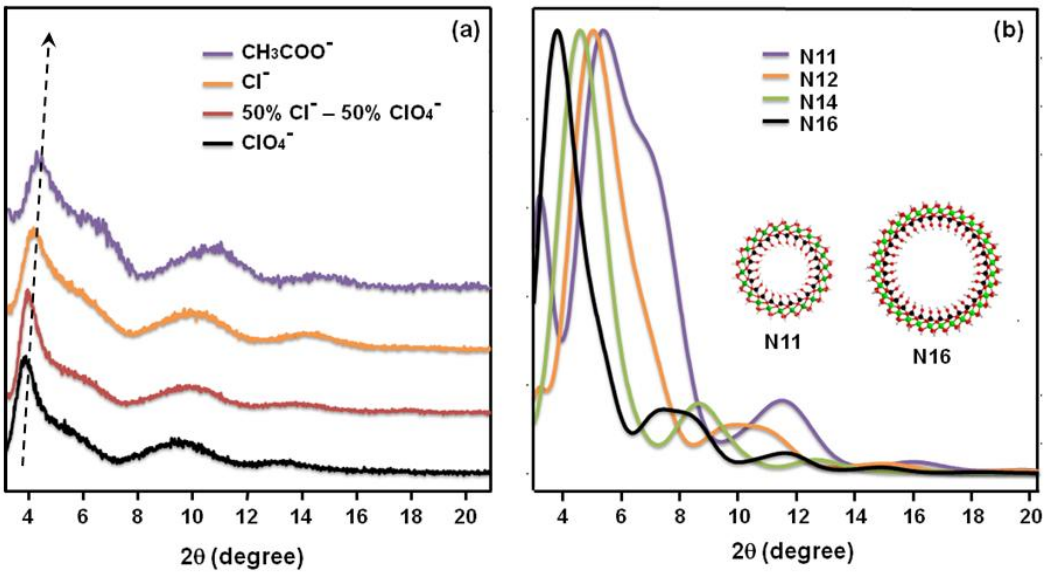

Figure 3-2. (a) Experimental XRD patterns of single-walled aluminosilicate nanotubes synthesized in acidic solutions containing different anions, showing a shift in the low-angle scattering peak with variation of the anion; and (b) Simulated XRD patterns of hexagonally-packed nanotubes, revealing the monotonic relationship between the location of the low-angle peak and the nanotube diameter. *N* represents the number of aluminosilicate repeat units in the nanotube circumference.

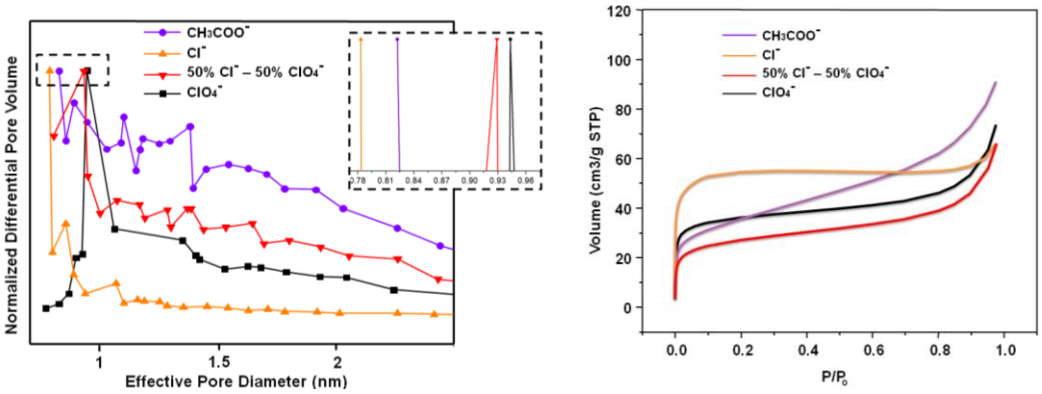

Figure 3-3. (a) Differential pore size distributions of aluminosilicate nanotubes synthesized in acidic solutions in the presence of different anions. Inset shows magnified range of pore diameters. (b) Nitrogen adsorption curves of aluminosilicate nanotubes synthesized from different acids.

3.3.3 Cryo-electron Microscopy

Although the nanotube dimensions derived from XRD and nitrogen physisorption analysis strongly indicate that the nanotube diameter can be controlled by the use of anionic ligands, high-resolution cryo-electron microscopy (cryo-EM) conclusively demonstrates the principle of nanotube shaping. Individual nanotubes can rarely be imaged by conventional TEM techniques because they aggregate upon solvent evaporation during sample preparation. Cryo-EM specimens were prepared by pipetting dialyzed nanotube solutions on to an EM grid, blotting away excess solution, and then rapidly plunge-freezing the grid in liquid ethane. Image processing and analysis was done with the ImageJ software [112]. The nanotube diameter distribution in each material was determined based on measurement of the diameter of 50 individual nanotubes in several high-resolution cryo-EM micrographs. Representative cryo-EM images are shown in Figure 3-4a-h. Image analysis revealed remarkably sharp diameter distributions in all the materials. Moreover, these distributions changed significantly depending upon the anion

used in the synthesis. The average nanotube diameters were found to be 2.8±0.2 nm (NTs synthesized in $HClO_4$), 2.5±0.2 nm (50% $HClO_4$ - 50% HCl), 2.4±0.2 nm (HCl), and 2.2±0.2 nm (CH_3COOH). Cryo-EM counts for nanotube diameters are shown in Figure 3-5. While these precisely determined diameters fully follow the trends indicated by the XRD and physisorption analysis, an exact agreement of the latter two methods with the cryo-EM results cannot be expected. Previous studies suggest that the pore size derived from nitrogen physisorption tends to be an underestimate [113]. Existing models for translating physisorption isotherms into pore size distributions asusme a uniform packing of nitrogen molecules into the channels [114], which is likely to be an approximation in materials with pore sizes smaller than 1 nm [115].

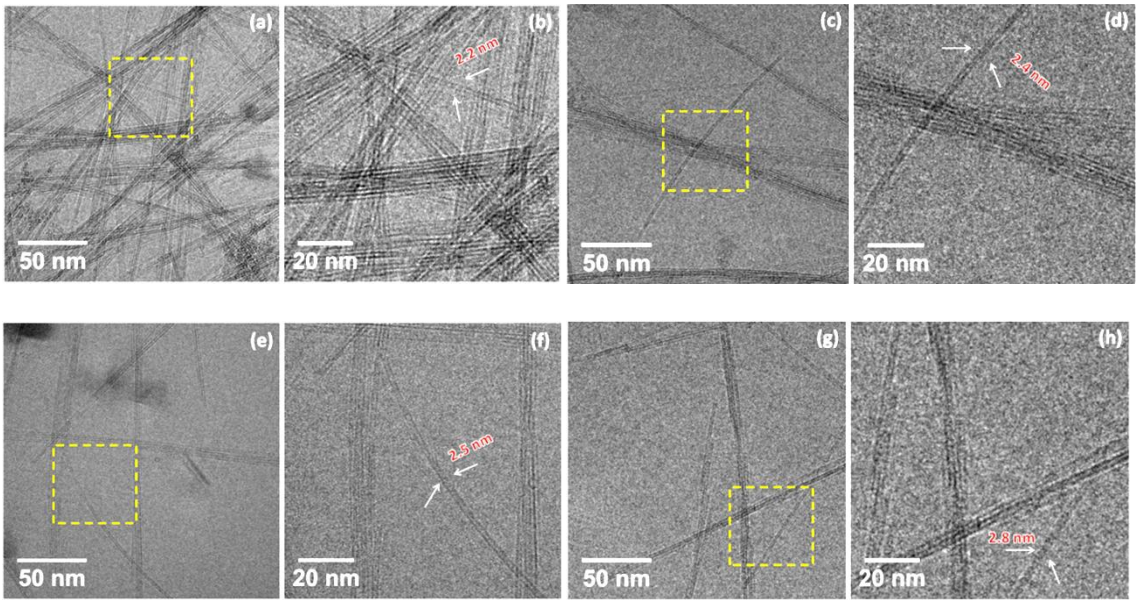

Figure 3-4. Representative low-magnification and high-magnification cryo-EM images of single-walled aluminosilicate nanotubes synthesized in 0.05 M: (a, b) CH_3COOH; (c, d) HCl; (e, f) 50%HCl−50%$HClO_4$; and (g, h) $HClO_4$. The yellow squares indicate the magnified areas shown in the right-hand images.

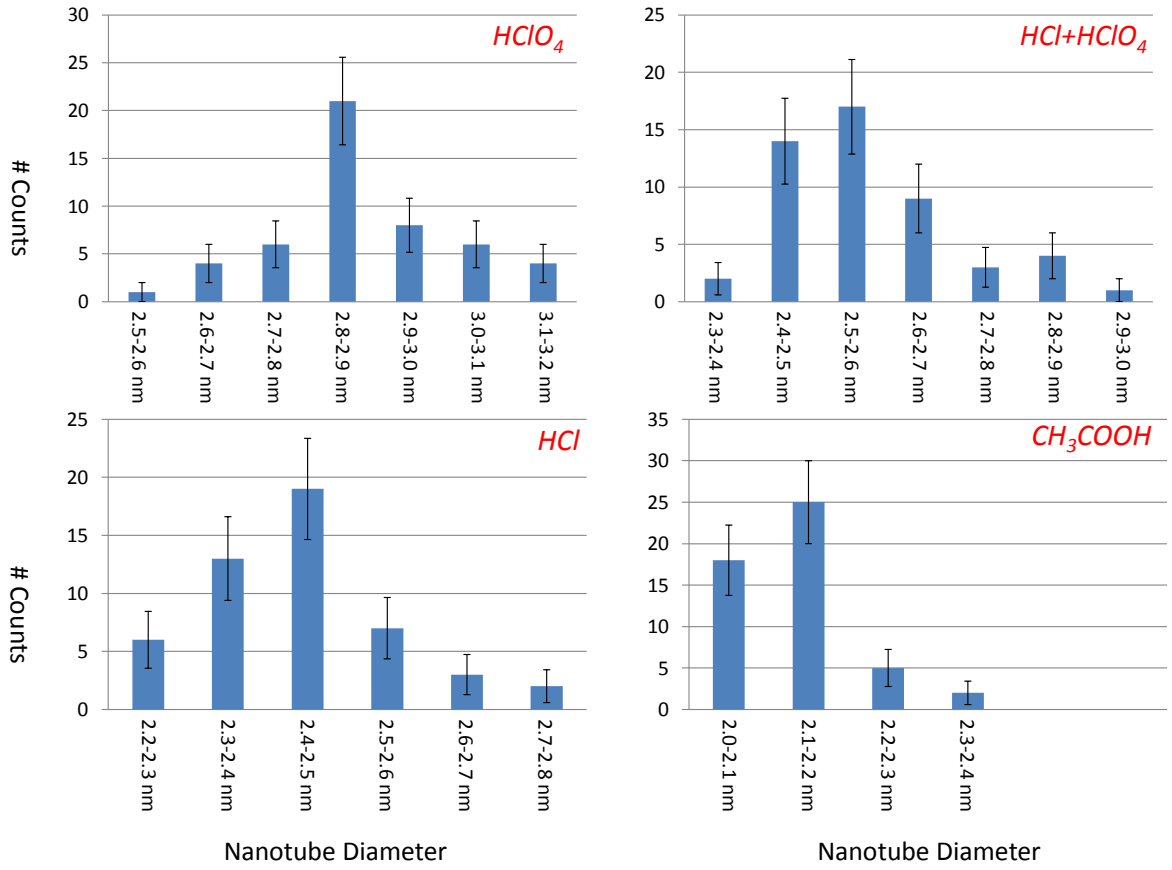

Figure 3-5. Cryo-EM diameter counts with Poisson error bars for nanotubes synthesized using different acids.

Figure 3-6 depicts the range of diameters of the nanotubes synthesized using different anions, along with the corresponding number of aluminosilicate repeat units in the circumference. Given the experimental nanotube diameter, the number of repeat units in the circumference of the nanotube can be ascertained using a previously developed geometrical relation [116] obtained from geometry-optimized nanotube models of various diameters. The use of perchlorate anions resulted in the largest diameter with 15 repeat units in the circumference, whereas the use of chloride and acetate anions resulted in nanotubes possessing 12 and 11 repeat units, respectively.

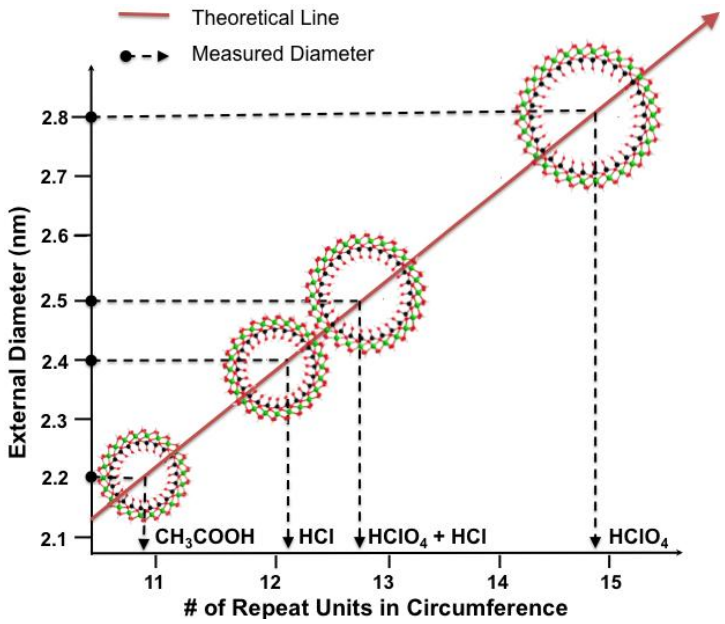

Figure 3-6. Average external nanotube diameters measured from cryo-EM micrographs and the corresponding number of aluminosilicate repeat units in the circumference, for each type of anion used in the synthesis. The structures of the nanotubes are also shown. Theoretical diameters or line is obtained from geometry optimized nanotube models and were used to calculate the # of repeating units as indicated by the experimental cryo-EM data.

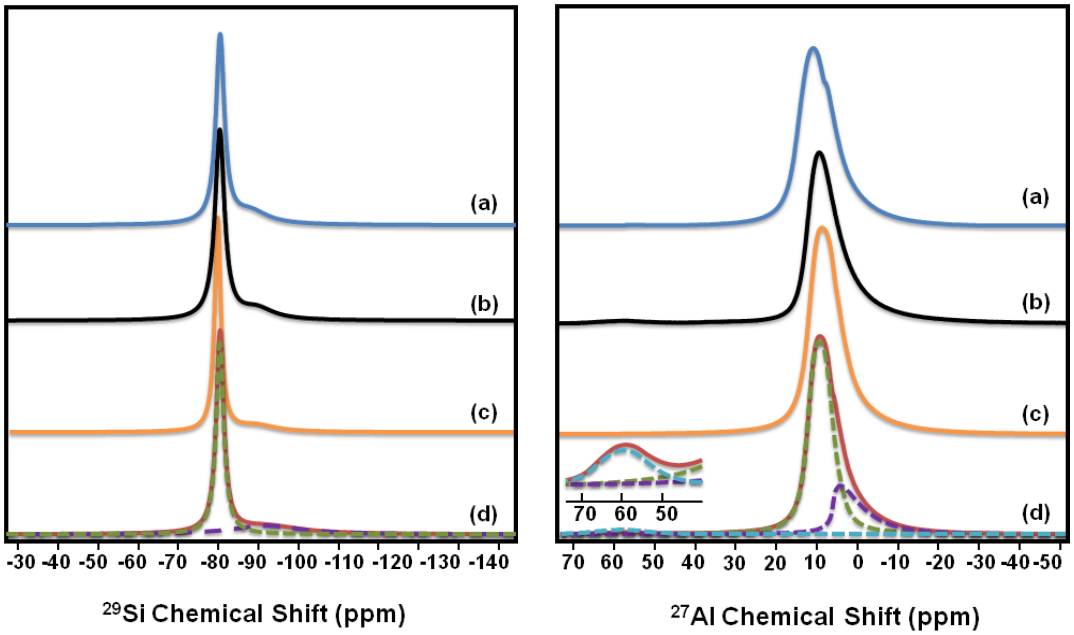

Figure 3-7. ^{29}Si and ^{27}Al MAS solid-state NMR spectra of aluminosilicate nanotubes synthesized from aqueous solutions of 0.05 M: (a) CH_3COOH, (b) HCl, (c) 50%HCl-50%$HClO_4$, and (d) $HClO_4$. Lorentzian deconvolution of peaks is depicted by dashed lines in the bottom set of spectra.

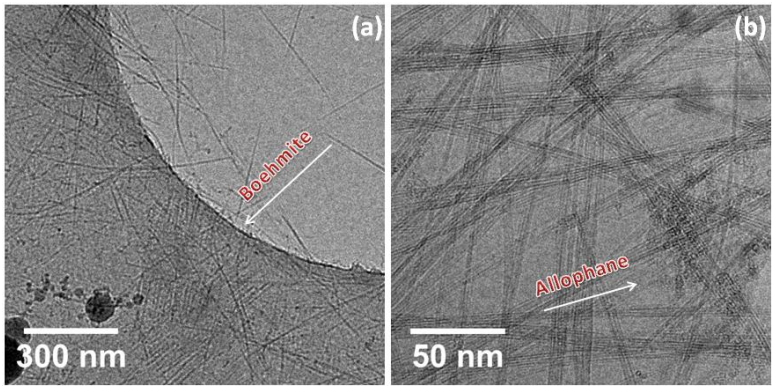

Figure 3-8. Cryo-EM micrographs of synthesis byproducts (a) boehmite byproducts in nanotube synthesis solutions of HCl, (b) CH_3COOH synthesized nanotubes together with allophane, an aluminosilicate shell structure around 3-5 nm in diameter.

3.3.4 ^{27}Al and ^{29}Si MAS NMR

All the nanotubes have the same structure, as shown by high-resolution ^{29}Si and ^{27}Al MAS NMR spectra (Figure 3-7). In all cases, the ^{29}Si NMR spectra show a sharp resonance at −80 ppm from silanol units (Si−OH) on the internal nanotube wall in a well-defined Q^3(6Al) configuration (dashed green line in Figure 3-7a). Small amounts of impurities or defects are indicated by a broad resonance in the range of −70 to −110 ppm (dashed purple line), indicative of less well-ordered silicon environments with 0−5 next-nearest neighbor aluminum atoms [1]. The ^{27}Al NMR spectra for all the materials are also essentially identical. All the spectra have a main peak at 8−10 ppm that represents six-coordinated structural units of aluminum hydroxide on the external nanotube wall (dashed green line in Figure 3-7b). There is also a small contribution from a broad peak centered at 3 ppm with an average quadrupolar coupling constant of 3.8 MHz, suggesting the presence of less ordered six-coordinated aluminum environments (dashed purple line). A more pronounced shoulder in the ^{27}Al NMR spectrum of acetic acid synthesized

nanotubes is probably due to the coexistence of small amount of less ordered allophones with aluminosilicate nanotubes (Figure 3-8). A small amount (~1%) of tetrahedral aluminum (at ~60 ppm) is also observed. This feature is likely due to defects in nanotube structure.

3.3.5 ESI−Mass Spectrometry

Having shown that nanotubes of the same structure but variable diameters can be produced by introducing different anionic species in the synthesis, the molecular composition of the precursor solution is now examined. As shown in Chapter 2, via identification of nanotube precursors by ESI−MS and structural optimization of the precursors with solvated DFT calculations, aluminosilicate nanotube-forming synthesis solutions contain precursors with intrinsic curvature; whereas solutions that do not form nanotubes contain only planar precursors [1]. Mass spectrometry has also proven very useful in investigating precursor speciation at the early stages of zeolite formation [117]. Here it is shown that the intrinsic curvature of the precursors depends on the type of anion present in the synthesis solution. The details of ESI−MS data interpretation to identify aluminate, silicate, and aluminosilicate speciation in $HClO_4$ containing nanotube synthesis solutions has been described by us recently [1]. First, all possible molecular formulae was determined consistent with the ESI−MS spectra, up to a mass/charge ratio (m/z) of 900, covering the nanometer and sub-nanometer size precursors of interest. Of the molecular formulae thus obtained, the vast majority can be eliminated as chemically impossible. The remaining structures are then examined in detail, leading to a final set of

precursor structures that can be subjected to structural optimization by solvated DFT calculations.

Comprehensive results of the ESI−MS investigation of precursors in HCl and CH_3COOH solutions are given in the Figures 3-9 to 3-16 and Tables 3-1 to 3-8, and data for $HClO_4$ solutions is available in Chapter 2 of this thesis [1]. Comparative investigation revealed clear differences in the interactions of the anions with the nanoscale precursors. Initial experiments with solutions containing only silicate precursors (and no aluminum) showed that perchlorate anions (ClO_4^-) did not complex silicate species. On the other hand, small amounts of silicate species complexed with Cl^- and CH_3COO^- ligands were detected. Another set of experiments with solutions containing only aluminate precursors (and no silicon) showed that the structure of aluminate species was strongly affected by the ligands. In $HClO_4$ and CH_3COOH solutions, the structures of all detected nanoscale aluminate species, both cationic and anionic, contained the motif of six-membered aluminate (Al_6) units that contain Al atoms bridged by μ_2-OH groups. The ClO_4^- and CH_3COO^- anions complexed Al^{3+} only by ligand exchange (replacement of pendant −OH groups) and exclusively in monodentate coordination. In HCl solutions, complexes are formed by the direct bonding of Cl^- to Al^{3+}. Such coordination complexes promoted the formation of brucite-like clusters (Table 3-4), which contain edge-shared Al octahedra and are building units of boehmite (AlOOH). This observation explains the boehmite byproducts observed in small amounts in HCl-containing solutions (Figure 3-8). Details of the ESI−MS analysis of the nanotube-forming aluminosilicate solutions are given in Tables 3-5 to 3-8. All solutions containing different acids displayed a limited set of sub-

nanometer and nanometer sized precursors containing $Al_1Si_x-Al_{14}Si_x$ ($x = 0-7$) atoms and anionic ligands. The ESI−MS spectra contains a number of peak series, within which the same precursor appears with different numbers of water molecules. The correct assignment of these peak series in every precursor solution also corroborates the overall validity and uniqueness of the precursors identified by ESI−MS data analysis. Upon heating of these solutions, the nanoscale clusters ($Al_8Si_x-Al_{14}Si_x$) disappeared from the ESI spectra in all cases. At the same time, nanoparticles of size ~5 nm appear in dynamic light scattering spectra [33]. As discovered in previous chapter [33, 60], these events are key to the process of nanotube nucleation, which occurs by temperature-induced condensation of precursors into nanoparticle clusters followed by rearrangement into a nanotubular structure. Based on all the above observations, it is concluded that the processes driving the nucleation of the nanotubular structure remain the same in all the acidic solutions and that the nanotube curvature must therefore be intrinsically dictated by the anion-complexed nanoscale precursors themselves.

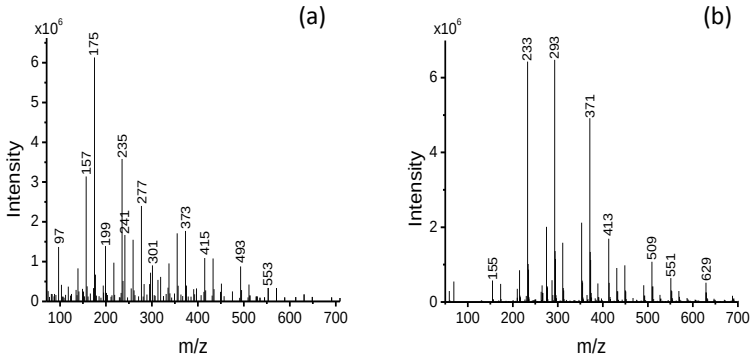

Figure 3-9. Cationic (a) and anionic (b) ESI mass spectrum of mildly acidic aqueous solutions of 0.05 M acetic acid at a pH of ~3.5 after 18 h hydrolysis of 0.05 M $Si(OC_2H_5)_4$ at 25 ˚C.

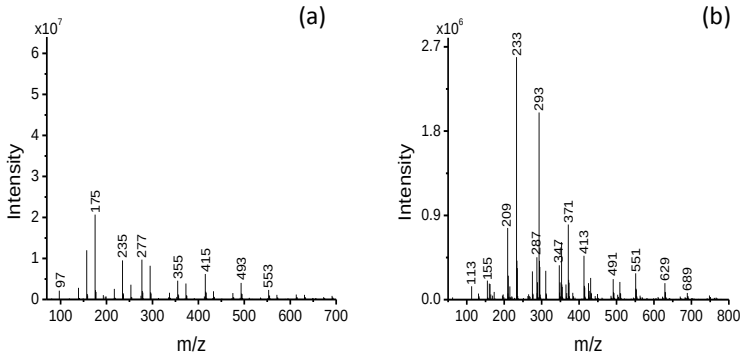

Figure 3-10. Cationic (a) and anionic (b) ESI mass spectrum of mildly acidic aqueous solutions of 0.05 M hydrochloric acid at a pH of ~3.5 after 18 h hydrolysis of 0.05 M $Si(OC_2H_5)_4$ at 25 ˚C.

Table 3-1. Chemical formula of silicate species detected by ESI−MS in mildly acidic aqueous solutions of 0.05 M acetic acid at a pH of ~3.5 after 18 h hydrolysis of 0.05 M $Si(OC_2H_5)_4$ at 25 ˚C.

Chemical Formula of *Si* Species	**Peak Series (m/z)**
***ESI*(+)**	
$[SiO(OH)(H_2O)]^+$	79+18n (n=0-1)
$[Si_2O_3(OH)(H_2O)]^+$	139+18n (n=0-2)
$[Si_2O_3(H_2O)(CH_3COO)]^+$	181+18n (n=0-2)
$[Si_3O_4(OH)_3(H_2O)]^+$	217+18n (n=0-1)
$[Si_3O_5(H_2O)(CH_3COO)]^+$	241+18n (n=0-1)
$[Si_4O_6(OH)_3(H_2O)]^+$	277+18n (n=0-2)
$[Si_3O_4(OC_2H_5)_3]^+$	283+18n (n=0-2)
$[Si_5O_8(OH)_3(H_2O)]^+$	337+18n (n=0-2)
$[Si_6O_9(OH)_5(H_2O)]^+$	415+18n (n=0-2)
$[Si_7O_{10}(OH)_7(H_2O)]^+$	493+18n (n=0-1)
$[Si_8O_{12}(OH)_7(H_2O)]^+$	553+18n (n=0-1)
***ESI*(−)**	
$[Si_2O_3(OH)_3]^-$	155+18n (n=0-1)
$[Si_3O_5(OH)_3]^-$	215+18n (n=0-2)
$[Si_4O_7(OH)_3]^-$	275+18n (n=0-2)
$[Si_5O_8(OH)_5]^-$	353+18n (n=0-2)
$[Si_6O_{10}(OH)_5]^-$	413+18n (n=0-2)
$[Si_7O_{11}(OH)_7]^-$	491+18n (n=0-2)
$[Si_8O_{13}(OH)_7]^-$	551+18n (n=0-2)
$[Si_9O_{14}(OH)_9]^-$	629+18n (n=0-1)

Table 3-2. Chemical formula of silicate species detected by ESI−MS in mildly acidic aqueous solutions of 0.05 M hydrochloric acid at a pH of ~3.5 after 18 h hydrolysis of 0.05 M $Si(OC_2H_5)_4$ at 25 ˚C.

Chemical Formula of *Si* Species Detected	**Peak Series (m/z)**
***ESI*(+)**	
$[Si(OH)_3(H_2O)]^+$	97
$[Si_2O_3(OH)(H_2O)]^+$	139+18n (n=0-2)
$[Si_3O_4(OH)_3(H_2O)]^+$	217+18n (n=0-1)
$[Si_4O_6(OH)_3(H_2O)]^+$	277+18n (n=0-1)
$[Si_5O_8(OH)_3(H_2O)]^+$	337+18n (n=0-2)
$[Si_6O_9(OH)_5(H_2O)]^+$	415+18n (n=0-2)
$[Si_7O_{11}(OH)_5(H_2O)]^+$	475+18n (n=0-2)
$[Si_8O_{12}(OH)_7(H_2O)]^+$	553+18n (n=0-1)
$[Si_9O_{14}(OH)_7(H_2O)]^+$	613+18n (n=0-1)
***ESI*(−)**	
$[SiO(OH)_2Cl]^-$	113
$[SiO(OH)Cl_2]^-$	131
$[Si_2O_3(OH)_3]^-$	155+18n (n=0-2)
$[Si_4O_7(OH)_3]^-$	275+18n (n=0-2)
$[Si_5O_8(OH)_5]^-$	353+18n (n=0-1)
$[Si_4O_5(OH)_5Cl_2]^-$	347
$[Si_4O_5(OH)_4Cl_3]^-$	365
$[Si_6O_{10}(OH)_5]^-$	413+18n (n=0-2)
$[Si_7O_{11}(OH)_7]^-$	491+18n (n=0-1)
$[Si_8O_{13}(OH)_7]^-$	551+18n (n=0-1)
$[Si_{10}O_{17}(OH)_7]^-$	671+18n (n=0-1)
$[Si_2O_2(OH)_3Cl_2]^-$	209
$[Si_3O_3(OH)_5Cl_2]^-$	287
$[Si_5O_6(OH)_7Cl_2]^-$	425+18n (n=0-2)
$[Si_6O_8(OH)_7Cl_2]^-$	485
$[Si_7O_9(OH)_{10}Cl]^-$	545+18n (n=0-2)

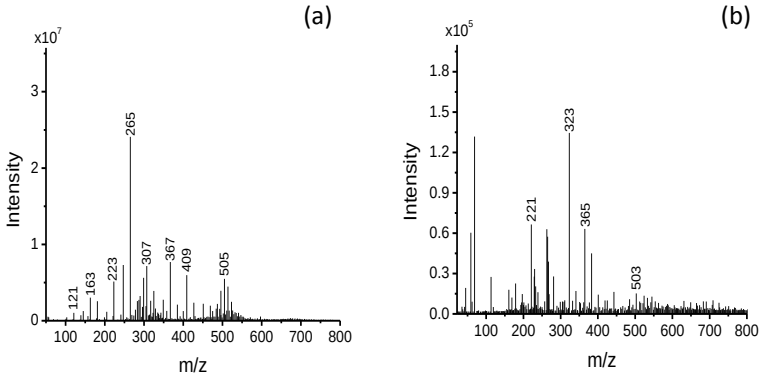

Figure 3-11. Cationic (a) and anionic (b) ESI mass spectrum of mildly acidic aqueous solutions of 0.05 M acetic acid at a pH of ~3.5 after 18 h hydrolysis of 0.1 M $Al(OC_4H_9)_3$ at 25 ˚C.

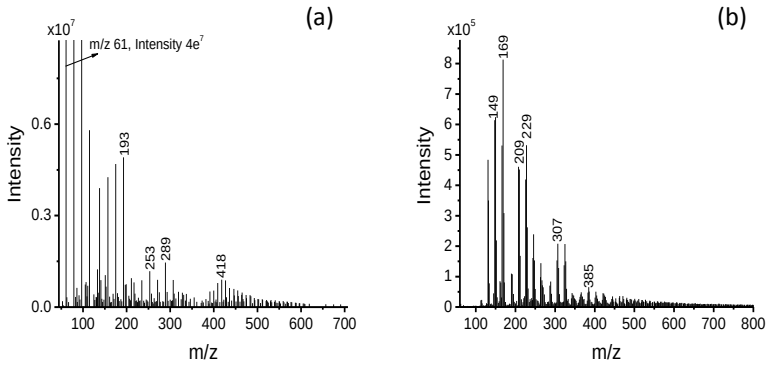

Figure 3-12. Cationic (a) and anionic (b) ESI mass spectrum of mildly acidic aqueous solutions of 0.05 M hydrochloric acid at a pH of ~3.5 after 18 h hydrolysis of 0.1 M $Al(OC_4H_9)_3$ at 25 ˚C.

Table 3-3. Chemical formula of aluminate species detected by ESI−MS in mildly acidic aqueous solutions of 0.05 M acetic acid at a pH of ~3.5 after 18 h hydrolysis of 0.1 M $Al(OC_4H_9)_3$ at 25 ˚C.

Chemical Formula of *Al* Species	**Peak Series (m/z)**
$\boldsymbol{ESI(+)}$	
$[Al(OH)(CH_3COO)]^+$	103+18n (n=0-2)
$[Al(CH_3COO)_2]^+$	145+18n (n=0-3)
$[Al_2(OH)_3(CH_3COO)_2]^+$	223+18n (n=0-1)
$[Al_2(OH)_2(CH_3COO)_3]^+$	265+18n (n=0-1)
$[Al_2(OH)(CH_3COO)_4]^+$	307+18n (n=0-2)
$[Al_2(OH)(C_4H_9O)_3(CH_3COO)]^+$	349+18n (n=0-2)
$[Al_4(OH)_{10}(H_2O)_4(CH_3COO)]^+$	409+18n (n=0-2)
$[Al_9(OH)_{19}(H_2O)_4(CH_3COO)_6]^{2+}$	496+9n (n=0-6)
$[Al_{14}(OH)_{29}(H_2O)_{13}(CH_3COO)_{14}]^{3+}$	565+6n (n=0-4)
$[Al_{15}(OH)_{30}(H_2O)_{10}(CH_3COO)_{12}]^{3+}$	601+6n (n=0-7)
$[Al_{16}(OH)_{27}(H_2O)_{11}(CH_3COO)_{15}]^{3+}$	649+6n (n=0-10)
$\boldsymbol{ESI(-)}$	
$[Al(OH)_4(H_2O)]^-$	113
$[AlO(CH_3COO)]^-$	161+18n (n=0-2)
$[Al_2(OH)_2(CH_3COO)_6]^{2-}$	221+9n (n=0-2)
$[Al_2(OH)_6(C_4H_9O)]^-$	229
$[Al(CH_3COO)_4]^-$	263+18n (n=0-2)
$[Al_2O(OH)(CH_3COO)_4]^-$	323+18n (n=0-1)
$[Al_2O(CH_3COO)]^-$	365+18n (n=0-3)
$[Al_3O_2(OH)_2(C_4H_9O)_3(CH_3COO)]^-$	425+18n (n=0-1)
$[Al_5(OH)_{15}(H_2O)(CH_3COO)]^-$	467+18n (n=0-1)
$[Al_8(OH)_{18}(H_2O)_3(CH_3COO)_8]^{2-}$	551+9n (n=0-2)
$[Al_8(OH)_{19}(H_2O)_4(CH_3COO)_7]^{2-}$	512+9n (n=0-1)
$[Al_8(OH)_{17}(H_2O)_3(CH_3COO)_9]^{2-}$	545+9n (n=0-3)
$[Al_9(OH)_{19}(H_2O)_2(CH_3COO)_{10}]^{2-}$	596+9n (n=0-2)
$[Al_4(OH)_7(H_2O)_2(C_4H_9O)(CH_3COO)_5]^-$	631+18n (n=0-2)
$[Al_5(OH)_{12}(H_2O)_5(CH_3COO)_4]^-$	665+18n (n=0-1)
$[Al_5(OH)_{10}(C_4H_9O)(CH_3COO)_5]^-$	673+18n (n=0-2)

Table 3-4. Chemical formula of aluminate species detected by ESI−MS in mildly acidic aqueous solutions of 0.05 M hydrochloric acid at a pH of ~3.5 after 18 h hydrolysis of 0.1 M $Al(OC_4H_9)_3$ at 25 ˚C.

Chemical Formula of *Al* Species	**Peak Series (m/z)**
***ESI*(+)**	
$[Al(OH)_2]^+$	61+18n (n=0-6)
$[Al_2(OH)_5]^+$	139+18n (n=0-4)
$[Al_3O(OH)_6(H_2O)]^+$	217+18n (n=0-5)
$[Al_{10}O_8(OH)_{10}Cl_2]^{2+}$	319+9n (n=0-14)
$[Al_{10}O_8(OH)_9(H_2O)_{12}Cl_3]^{2+}$	437+9n (n=0-3)
$[Al_5O_3(OH)_5(H_2O)_4Cl_3]^+$	447+18n (n=0-3)
$[Al_7O_5(OH)_{10}(H_2O)]^+$	457+18n (n=0-6)
$[Al_{14}O_{13}(OH)_{13}(H_2O)_7Cl]^+$	484+18n (n=0-5)
$[Al_7O_5(OH)_7Cl_3]^+$	495+18n (n=0-4)
***ESI*(−)**	
$[Al(OH)Cl_3]^-$	151+18n (n=0-1)
$[Al(OH)_2Cl_2]^-$	131+18n (n=0-2)
$[Al_2O_2Cl_3]^-$	191+18n (n=0-4)
$[Al_3O_3(OH)(H_2O)_2Cl_3]^-$	289+18n (n=0-3)
$[Al_4O_2(OH)_6(H_2O)Cl_3]^-$	367+18n (n=0-3)
$[Al_5O_3(OH)_5Cl_5]^-$	445+18n (n=0-2)
$[Al_{14}O_{15}(OH)_{11}(H_2O)_5Cl_3]^{2-}$	501+9n (n=0-3)

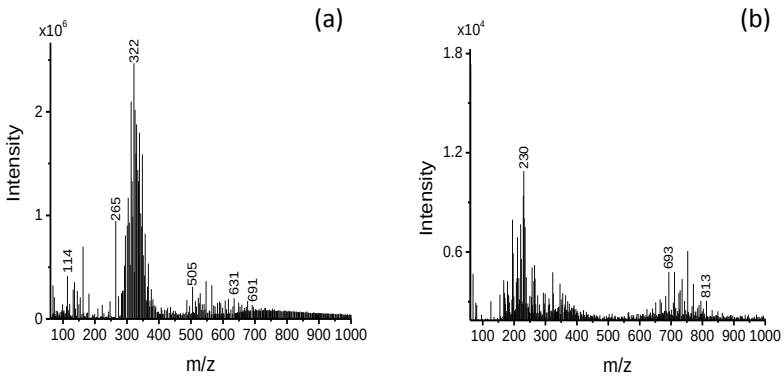

Figure 3-13. Cationic (a) and anionic (b) ESI mass spectrum of mildly acidic aqueous solutions of 0.05 M acetic acid at a pH of ~3.5 after 18 h hydrolysis of 0.1 M $Al(OC_4H_9)_3$ and 0.05 M $Si(OC_2H_5)_4$ at 25 ˚C.

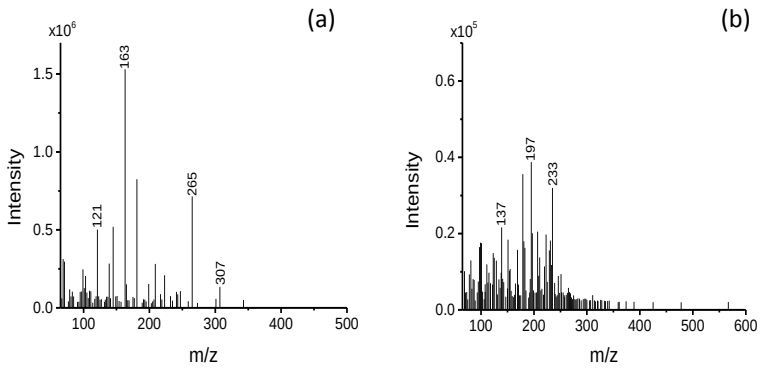

Figure 3-14. Cationic (a) and anionic (b) ESI mass spectrum of mildly acidic aqueous solutions of 0.05 M acetic acid at a pH of ~2.2 after 3 h heating of hydrolyzed 0.1 M $Al(OC_4H_9)_3$ and 0.05 M $Si(OC_2H_5)_4$ at 95 ˚C.

Table 3-5. Chemical formula of aluminosilicate species detected by ESI−MS in mildly acidic aqueous solutions of 0.05 M acetic acid at a pH of ~3.5 after 18 h hydrolysis of 0.1 M $Al(OC_4H_9)_3$ and 0.05 M $Si(OC_2H_5)_4$ at 25 ˚C.

Chemical Formula of *AlSi* Species	**Peak Series (m/z)**
$\boldsymbol{ESI(+)}$	
$[Al(OH)_2]^+$	61+18n (n=0-2)
$[Al(OH)(CH_3COO)]^+$	103+18n (n=0-2)
$[Al_2(OH)_5]^+$	111+18n (n=0-1)
$[Si_2O_2(H_2O)(C_2H_5O)(CH_3COO)]^{2+}$	96+9n (n=0-2)
$[Al_3O(OH)_3(H_2O)_5]^{2+}$	136+9n (n=0-2)
$[Al(CH_3COO)_2]^+$	145+18n (n=0-3)
$[Al_2SiO(OH)_2(H_2O)_2(C_2H_5O)(CH_3COO)_3]^{2+}$	195+14n (n=0-2)
$[Al_2(OH)_2(CH_3COO)_3]^+$	365+18n (n=0-2)
$[Al_6SiO_3(OH)_{13}(H_2O)_3(CH_3COO)]^{2+}$	286+9n (n=0-5)
$[Al_5SiO_3(OH)_7(CH_3COO)_4]^{2+}$	283+9n (n=0-3)
$[Al_7SiO_3(OH)_{15}(H_2O)(CH_3COO)_2]^{2+}$	328+9n (n=0-4)
$[Al_2(OH)(CH_3COO)_4]^+$	307+18n (n=0-3)
$[Al_6SiO_3(OH)_{11}(H_2O)_3(C_2H_5O)(CH_3COO)_2]^{2+}$	321+9n (n=0-5)
$[Al_6Si_2O_5(OH)_{13}(H_2O)_3(C_2H_5O)]^{2+}$	309+9n (n=0-4)
$[Al_{10}Si_2O_6(OH)_{19}(H_2O)_2(CH_3COO)_4]^{3+}$	339+6n (n=0-9)
$[Al_7Si_2O_5(OH)_{17}(H_2O)_4]^{2+}$	343+14n (n=0-4)
$[Al_{13}O_4(OH)_{23}(H_2O)_0(CH_3COO)_5]^{3+}$	367+6n (n=0-3)
$[Al_{10}SiO_3(OH)_{18}(H_2O)(CH_3COO)_8]^{2+}$	571+9n (n=0-5)
$[Al_8SiO_3(OH)_{16}(H_2O)(CH_3COO)_4]^{2+}$	409+9n (n=0-5)
$[Al_8SiO_3(OH)_{14}(H_2O)_4(CH_3COO)_6]^{2+}$	478+9n (n=0-4)
$[Al_{10}Si_2O_6(OH)_{20}(H_2O)(CH_3COO)_4]^{2+}$	508+9n (n=0-3)
$[Al_{10}Si_2O_6(OH)_{19}(H_2O)_3(CH_3COO)_5]^{2+}$	547+9n (n=0-4)
$[Al_6SiO_3(OH)_{14}(H_2O)_2(C_2H_5O)]^+$	557+18n (n=0-2)
$[Al_6SiO_3(OH)_{13}(H_2O)_3(CH_3COO)_2]^+$	631+18n (n=0-4)
$[Al_6SiO_3(OH)_{12}(H_2O)_3(CH_3COO)_3]^+$	673+18n (n=0-2)
$\boldsymbol{ESI(-)}$	
$[Si_2O_4(OH)]^-$	137+18n (n=0-2)

Table 3-5 (continued).

$[AlO(CH_3COO)]^-$	161+18n (n=0-2)
$[Al_2SiO(OH)_8(H_2O)(C_2H_5O)_2]^{2-}$	171+14n (n=0-1)
$[Al_2(OH)_5(C_4H_9O)_2(CH_3COO)]^{2-}$	172+9n (n=0-1)
$[Al_2SiO_4(OH)_5(C_2H_5O)_2]^{2-}$	174+9n (n=0-1)
$[Al_2SiO(OH)_7(H_2O)(OC_2H_5)(CH_3COO)_2]^{2-}$	199+9n (n=0-1)
$[Si_3O_5(OH)_3]^-$	215+18n (n=0-1)
$[Al_3SiO_3(OH)_6(H_2O)(C_2H_5O)(CH_3COO)_2]^{2-}$	220+9n (n=0-1)
$[Al_2(OH)_2(CH_3COO)_6]^{2-}$	221+9n (n=0-2)
$[Al(CH_3COO)_4]^-$	263+18n (n=0-2)
$[Al_4Si_2O_5(OH)_{11}(H_2O)_2(OC_2H_5)]^{2-}$	256+9n (n=0-2)
$[Si_4O_7(OH)_3]^-$	275+18n (n=0-2)
$[Al_2O(OH)(CH_3COO)_4]^-$	323+18n (n=0-1)
$[Si_5O_8(OH)_5]^-$	353+18n (n=0-1)
$[Al_2O(CH_3COO)]^-$	365+18n (n=0-3)
$[Al_3SiO_4(OH)_4(H_2O)_3(C_2H_5O)_2(CH_3COO)]^{2-}$	222+9n (n=0-2)
$[Al_6SiO_3(OH)_{15}(H_2O)_2(C_2H_5O)(CH_3COO)_2]^{2-}$	346+9n (n=0-2)
$[Al_6SiO_3(OH)_{11}(C_2H_5O)(CH_3COO)_6]^{2-}$	412+9n (n=0-2)
$[Al_9Si_3O_9(OH)_{14}(H_2O)_4(C_2H_5O)_3(CH_3COO)_7]^{3-}$	443+6n (n=0-3)
$[Al_4SiO_3(OH)_9(H_2O)_6(CH_3COO)_2]^-$	437+18n (n=0-2)
$[Al_8(OH)_{19}(H_2O)(CH_3COO)_7]^{2-}$	485+9n (n=0-3)
$[Al_8(OH)_{18}(H_2O)_3(CH_3COO)_8]^{2-}$	524+9n (n=0-2)
$[Al_9(OH)_{19}(H_2O)_3(CH_3COO)_{10}]^{2-}$	605+9n (n=0-2)
$[Al_5(OH)_{12}(H_2O)_5(CH_3COO)_4]^-$	665+18n (n=0-2)
$[Al_5SiO_3(OH)_{10}(H_2O)_2(C_2H_5O)(CH_3COO)_3]^-$	633+18n (n=0-4)
$[Al_7(OH)_{19}(H_2O)(CH_3COO)_3]^-$	707+18n (n=0-2)
$[Al_6SiO_3(OH)_{13}(H_2O)_3(C_2H_5O)(CH_3COO)_3]^-$	735+18n (n=0-2)
$[Al_8SiO_3(OH)_{20}(C_2H_5O)(CH_3COO)_2]^-$	795+18n (n=0-3)

Table 3-6. Chemical formula of aluminosilicate species detected by ESI−MS in mildly acidic aqueous solutions of 0.05 M acetic acid at a pH of ∼2.2 after 3 h heating of hydrolyzed 0.1 M $Al(OC_4H_9)_3$ and 0.05 M $Si(OC_2H_5)_4$ at 95 ˚C.

Chemical Formula of *AlSi* Species	**Peak Series (m/z)**
$\boldsymbol{ESI(+)}$	
$[Al(OH)_2]^+$	61+18n (n=0-2)
$[Al(CH_3COO)_2]^+$	145+18n (n=0-3)
$[Al(OH)(CH_3COO)]^+$	103+18n (n=0-2)
$[Al_2SiO(OH)_2(H_2O)_2(C_2H_5O)(CH_3COO)_3]^{2+}$	195+14n (n=0-2)
$[Al_2(OH)(CH_3COO)_4]^+$	307+18n (n=0-3)
$[Al_2O(CH_3COO)_3]^+$	247+18n (n=0-1)
$\boldsymbol{ESI(-)}$	
$[Si_4O_7(OH)_3]^-$	275+18n (n=0-2)
$[AlO(CH_3COO)]^-$	161+18n (n=0-2)
$[Si_2O_4(OH)]^-$	137+18n (n=0-2)
$[Si_3O_5(OH)_3]^-$	215+18n (n=0-2)
$[Al_2(OH)_2(CH_3COO)_6]^{2-}$	221+9n (n=0-2)
$[Al(CH_3COO)_4]^-$	263+18n (n=0-2)
$[Al_3SiO_3(OH)_6(C_2H_5O)(CH_3COO)_2]^{2-}$	211+9n (n=0-2)
$[Al_2(OH)_5(C_4H_9O)_2(CH_3COO)]^{2-}$	172+9n (n=0-1)
$[Al_2SiO_4(OH)_5(C_2H_5O)_2]^{2-}$	174+9n (n=0-1)
$[Al_2SiO(OH)_8(H_2O)(C_2H_5O)_2]^{2-}$	171+14n (n=0-1)

Table 3-6 (continued).

$[Al_2SiO_2(OH)_7(H_2O)(CH_3COO)]^{2-}$	155+14n (n=0-3)
$[Al_4SiO_4(OH)_8(H_2O)(C_2H_5O)_2]^{2-}$	231+9n (n=0-1)

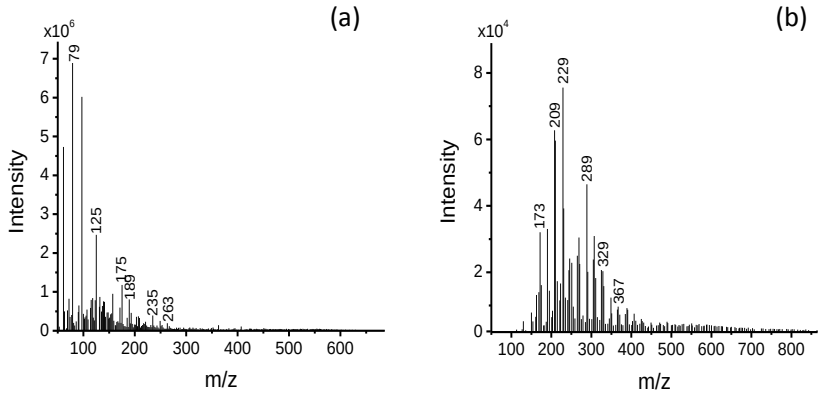

Figure 3-15. Cationic (a) and anionic (b) ESI mass spectrum of mildly acidic aqueous solutions of 0.05 M hydrochloric acid at a pH of ~3.3 after 18 h hydrolysis of 0.1 M $Al(OC_4H_9)_3$ and 0.05 M $Si(OC_2H_5)_4$ at 25 ˚C.

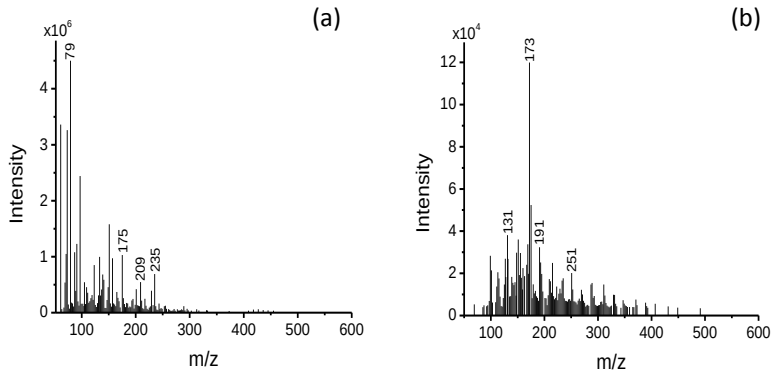

Figure 3-16. Cationic (a) and anionic (b) ESI mass spectrum of mildly acidic aqueous solutions of 0.05 M hydrochloric acid at a pH of ~2.0 after 3 h heating of hydrolyzed 0.1 M $Al(OC_4H_9)_3$ and 0.05 M $Si(OC_2H_5)_4$ at 95 ˚C.

Table 3-7. Chemical formula of aluminosilicate species detected by ESI−MS in mildly acidic aqueous solutions of 0.05 M hydrochloric acid at a pH of ~3.3 after 18 h hydrolysis of 0.1 M $Al(OC_4H_9)_3$ and 0.05 M $Si(OC_2H_5)_4$ at 25 ˚C.

Chemical Formula of *AlSi* Species	**Peak Series (m/z)**
***ESI*(+)**	
$[Al(OH)_2]^+$	61+18n (n=0-3)
$[Al_2(OH)_5]^+$	139+18n (n=0-3)
$[AlSiO(H_2O)_3Cl_3]^{2+}$	126+9n (n=0-3)
$[Al_6SiO_3(OH)_{11}Cl_2]^{3+}$	165+6n (n=0-7)
$[Al_3SiO(OH)_6Cl_3]^{2+}$	167+9n (n=0-6)
$[Si_3O_4(OH)_3(H_2O)]^+$	217+18n (n=0-2)
$[Al_2(OH)_2(H_2O)_2Cl_3]^+$	231+18n (n=0-2)
$[Al_3O(OH)_3Cl_2]^{2+}$	109+18n (n=0-1)
$[Al_2SiO(OH)_3Cl_3]^{2+}$	128+9n (n=0-3)
$[Al_7SiO_3(OH)_{13}(H_2O)_2Cl_3]^{3+}$	209+6n (n=0-3)
$[Al_8Si_2O_6(OH)_{15}Cl_2]^{3+}$	231+6n (n=0-5)
$[Al_5SiO_3(OH)_7Cl_4]^{2+}$	236+9n (n=0-7)
$[Al_9Si_2O_6(OH)_{17}Cl_3]^{3+}$	263+6n (n=0-3)
$[Si_4O_6(OH)_3(H_2O)]^+$	277+18n (n=0-2)
$[Al_2O(H_2O)_3Cl_3]^+$	231+18n (n=0-4)
$[Al_3O(OH)_3Cl_3]^+$	255+18n (n=0-3)
$[Al_{12}Si_2O_{12}(OH)_{15}(H_2O)_3Cl_2]^{3+}$	317+6n (n=0-5)
$[Al_{13}O_4(OH)_{25}(H_2O)_2Cl_3]^{3+}$	327+6n (n=0-5)
$[Al_8SiO_3(OH)_{15}(H_2O)_6Cl_5]^{2+}$	407+9n (n=0-2)
***ESI*(−)**	
$[Al(OH)_2Cl_2]^-$	131+18n (n=0-2)
$[Al(OH)Cl_3]^-$	151+18n (n=0-1)
$[Si_2O_3(OH)_3]^-$	155+18n (n=0-1)
$[Al_2O_2Cl_3]^-$	191+18n (n=0-4)
$[Al_2SiO_2(OH)_5Cl_2]^-$	269+18n (n=0-2)
$[Al_2SiO_2(OH)_4Cl_3]^-$	289+18n (n=0-2)
$[Al_3SiO_3(OH)_6Cl_2]^-$	329+18n (n=0-1)
$[Al_3SiO_3(OH)_5Cl_3]^-$	349+18n (n=0-2)
$[Al_4SiO_4(OH)_8Cl]^-$	371+18n (n=0-2)
$[Al_4SiO_4(OH)_6Cl_3]^-$	409+18n (n=0-2)
$[Al_5SiO_4(OH)_{12}]^-$	431+18n (n=0-2)
$[Al_6O_6(OH)_4(H_2O)Cl_3]^-$	451+18n (n=0-2)
$[Al_{14}O_{15}(OH)_{11}(H_2O)_5Cl_3]^{2-}$	501+18n (n=0-3)

Table 3-8. Chemical formula of aluminosilicate species detected by ESI−MS in mildly acidic aqueous solutions of 0.05 M hydrochloric acid at a pH of ~2.0 after 3 h heating of hydrolyzed 0.1 M $Al(OC_4H_9)_3$ and 0.05 M $Si(OC_2H_5)_4$ at 95 ˚C.

Chemical Formula of *AlSi* Species	**Peak Series (m/z)**
***ESI*(+)**	
$[Al(OH)_2]^+$	61+18n (n=0-6)
$[Al_2(OH)_5]^+$	139+18n (n=0-4)
$[Si_3O_4(OH)_3(H_2O)]^+$	217+18n (n=0-2)
$[Al_{10}O_8(OH)_{10}(H_2O)_{10}Cl_2]^{2+}$	409+9n (n=0-4)

Table 3-8 (continued).

$[Al_3SiO_2(OH)_8]^+$	277+18n (n=0-2)
$[Al_3O(OH)_3Cl_3]^+$	295+18n (n=0-3)
$[Si_5O_8(OH)_3(H_2O)]^+$	255+18n (n=0-3)
$[Al_6SiO_3(OH)_{11}(H_2O)_4Cl_2]^{3+}$	189+6n (n=0-3)
$[Al_7SiO_3(OH)_{13}(H_2O)Cl_3]^{3+}$	203+6n (n=0-4)
$\boldsymbol{ESI(-)}$	
$[Al(OH)_2Cl_2]^-$	131+18n (n=0-2)
$[Si_2O_3(OH)_3]^-$	155+18n (n=0-1)
$[Al_2O_2Cl_3]^-$	191+18n (n=0-1)
$[Al_3O(OH)_8]^-$	233+18n (n=0-4)
$[Al_2SiO_2(OH)_4Cl_3]^-$	289+18n (n=0-2)
$[Al_3SiO_3(OH)_6Cl_2]^-$	329+18n (n=0-1)
$[Al_4SiO_4(OH)_8Cl]^-$	371+18n (n=0-2)
$[Al_5SiO_4(OH)_{12}]^-$	431+18n (n=0-2)
$[Al(OH)Cl_3]^-$	151+18n (n=0-1)
$[Al_2O_2(H_2O)_2Cl_3]^-$	229+18n (n=0-2)

3.3.6 Solvated Density Functional Theory Calculations

Solvated density-functional theory (DFT) calculations were performed on a set of structurally similar aluminosilicate nano-intermediate species detected in acidic solutions of $HClO_4$, CH_3COOH, and HCl, and in which Al atoms are complexed with different ligands (Cl^-, ClO_4^- and CH_3COO^-). These precursors form a fully representative set of key nanoscale intermediates involved in the formation of single-walled aluminosilicate nanotube materials. All the nanoscale precursors examined were found to exhibit intrinsic curvature. To accurately estimate the curvature, a cylindrical radius was fitted by least-squares to the Cartesian coordinates of Al atoms in the DFT-optimized nanoscale intermediates. Figures 3-18 to 3-20 show detailed results of DFT optimization and curvature estimation of several precursors detected in the nanotube synthesis solutions containing each of the three different acids. Although the curvature forms due to the bond length differences of the Al-O and Si-O bonds (0.19 nm and 0.16 nm respectively), it is clear that it can be controlled precisely by the complexation of anions to the precursors.

The effect of anion complexation on precursor curvature is further investigated by performing DFT optimizations after replacing the complexed anions by hydroxyl groups (Figure 3-21). The ligand-complexed precursors were hydroxyl-substituted to obtain the $[Al_{10}SiO_3(OH)_{26}(H_2O)_4]^{2+}$, $[Al_{10}Si_2O_6(OH)_{24}(H_2O)_4]^{2+}$, $[Al_9Si_2O_6(OH)_{20}(H_2O)_3]^{3+}$ structures. The coordination of CH_3COO^- ions to the hydroxylated precursor $[Al_{10}Si_2O_6(OH)_{24}(H_2O)_4]^{2+}$ significantly increases its curvature from 1.37 nm^{-1} to 1.43 nm^{-1} (the radius R changes from 0.73 nm to 0.70 nm), whereas Cl^- complexation to the hydroxylated precursor $[Al_9Si_2O_6(OH)_{20}(H_2O)_3]^{2+}$ significantly decreases the curvature from 0.71 nm^{-1} to 0.66 nm^{-1} (R changes from 1.4 nm to 1.5 nm). However, the largest effect is seen upon ClO_4^- coordination, which decreases the curvature of the hydroxylated precursor $[Al_{10}SiO_3(OH)_{26}(H_2O)_4]^{2+}$ from 0.71 nm^{-1} to 0.44 nm^{-1} (R changes from 1.4 nm to 2.3 nm). Figure 3-17 compares the curvatures calculated for twelve representative nanoscale precursors. For clarity, the precursor structures are arranged around the horizontal dashed lines corresponding to the nanotube diameters as determined by cryo-EM. The curvatures of the precursors are clustered in different ranges, depending upon the type of anion complexing the precursors. Furthermore, there is a clear correlation between the clustered precursor curvatures and the diameters of the nanotubes obtained. The precursor curvatures follow the trend of $HClO_4$<HCl<CH_3COOH, and the nanotube diameters correspondingly follow the inverse trend.

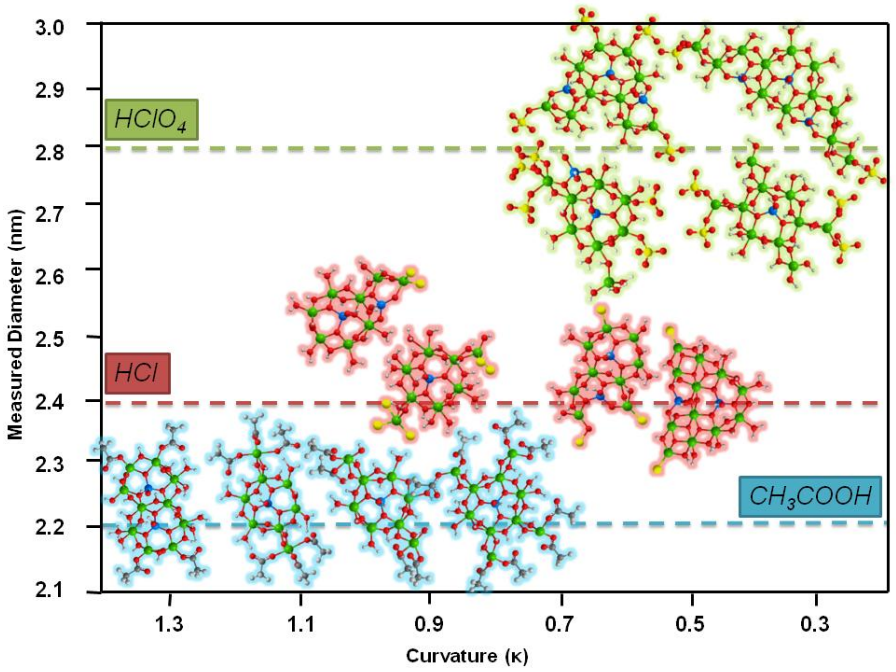

Figure 3-17. Structures and curvatures of DFT-optimized nanoscale intermediates detected by ESI−MS, arranged versus the measured nanotube diameters from cryo-EM analysis.

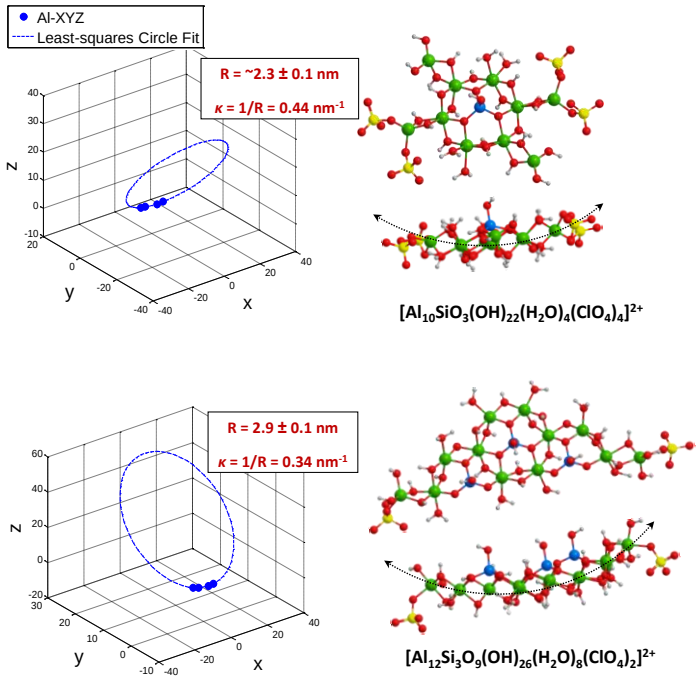

Figure 3-18. MATLAB plots on the left demonstrate the least-squares fitting of cylindrical radii to *xyz* Cartesian aluminum atom coordinates of DFT optimized aluminosilicate precursors detected in mildly acidic aluminosilicate nanotube synthesis solutions of 0.05

M $HClO_4$ by ESI−MS(+) and thus calculated molecular curvature (κ). Top and side view of the molecule is shown on the right side and inherent curvature of the molecule is indicated with a dotted line. Atom colors representing green: aluminum, yellow: chloride, blue: silicon, white: hydrogen, red: oxygen respectively.

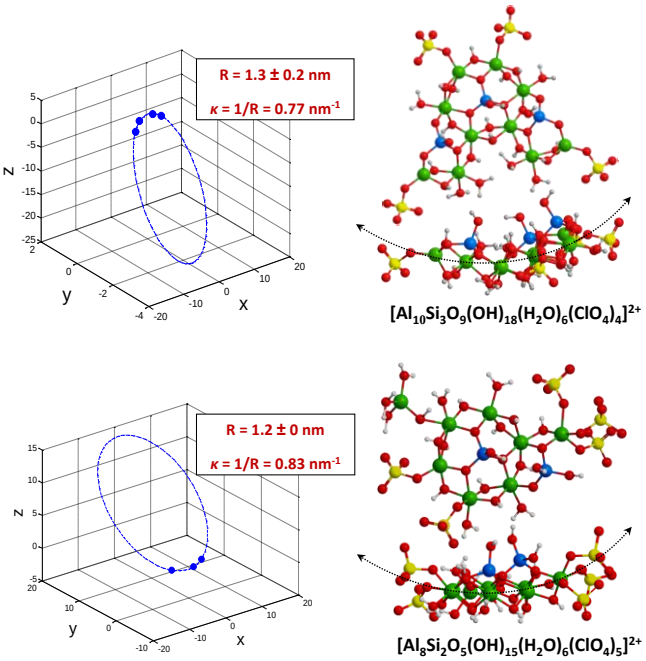

Figure 3-18 continued.

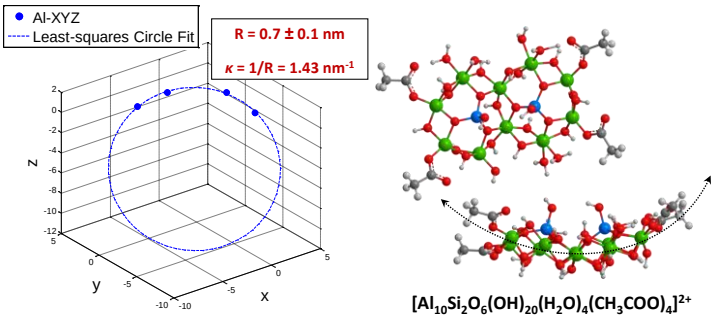

Figure 3-19. MATLAB plots on the left demonstrate the least-squares fitting of cylindrical radii to *xyz* Cartesian aluminum atom coordinates of DFT optimized aluminosilicate precursors detected in mildly acidic aluminosilicate nanotube synthesis solutions of 0.05 M CH_3COOH by ESI-MS(+) and thus calculated molecular curvature (κ). Top and side view of the molecule is shown on the right side and inherent curvature of the molecule is indicated with a dotted line. Atom colors representing green: aluminum, gray: carbon, blue: silicon, white: hydrogen, red: oxygen respectively.

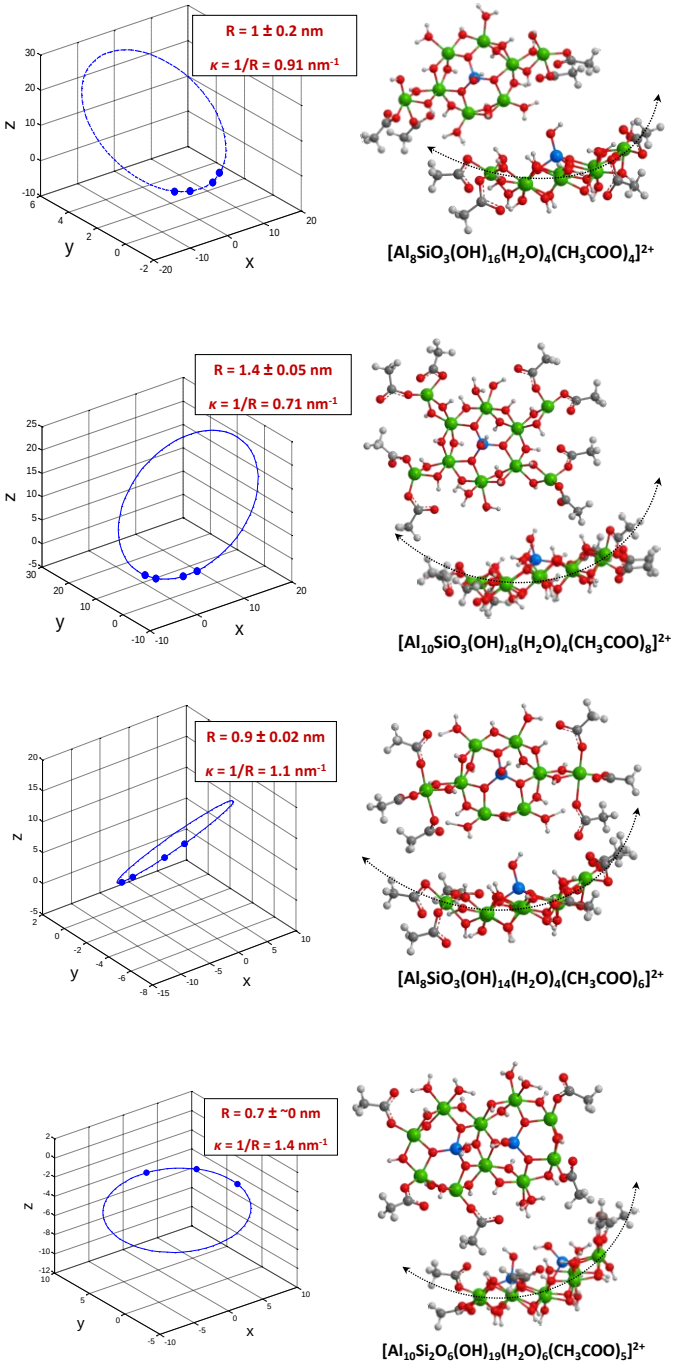

Figure 3-19 continued.

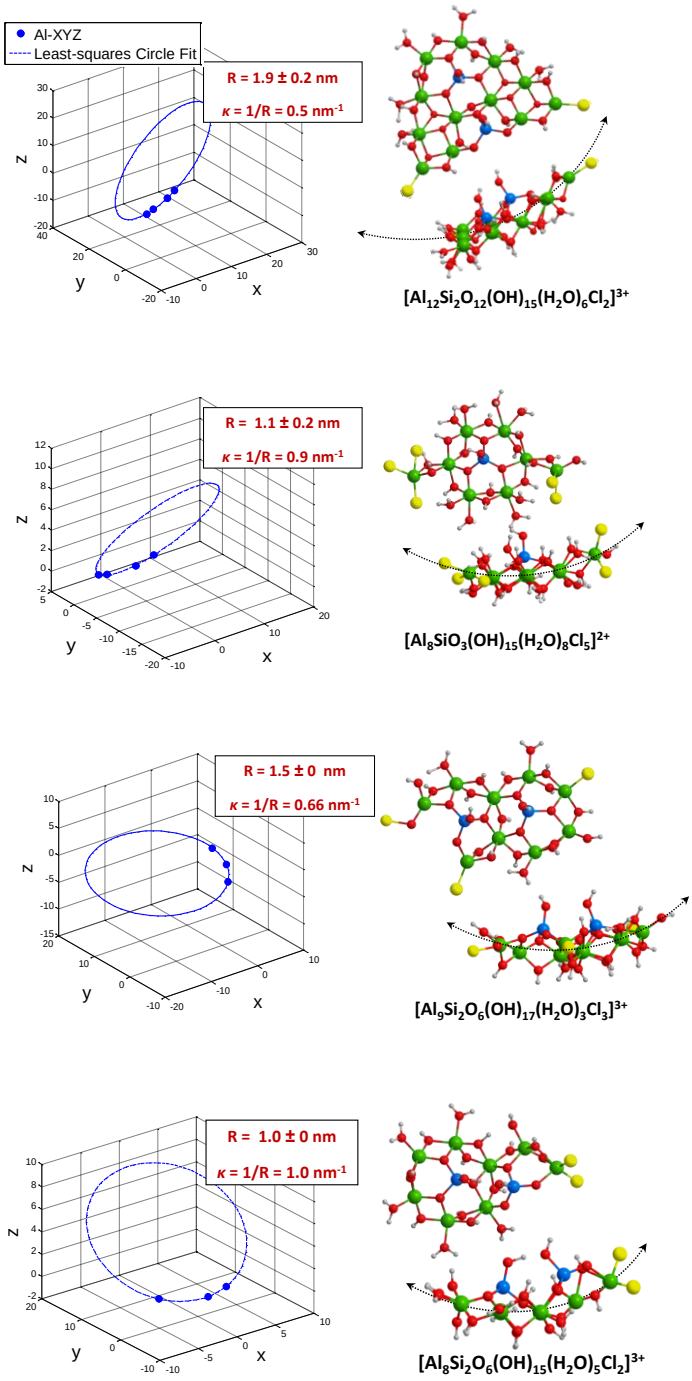

Figure 3-20. MATLAB plots on the left demonstrate the least-squares fitting of cylindrical radii to *xyz* Cartesian aluminum atom coordinates of DFT optimized aluminosilicate precursors detected in mildly acidic aluminosilicate nanotube synthesis solutions of 0.05 M HCl by ESI−MS(+) and thus calculated molecular curvature (κ). Top and side view of the molecule is shown on the right side and inherent curvature of the molecule is indicated with a dotted line. Atom colors representing green: aluminum, yellow: chloride, blue: silicon, white: hydrogen, red: oxygen respectively.

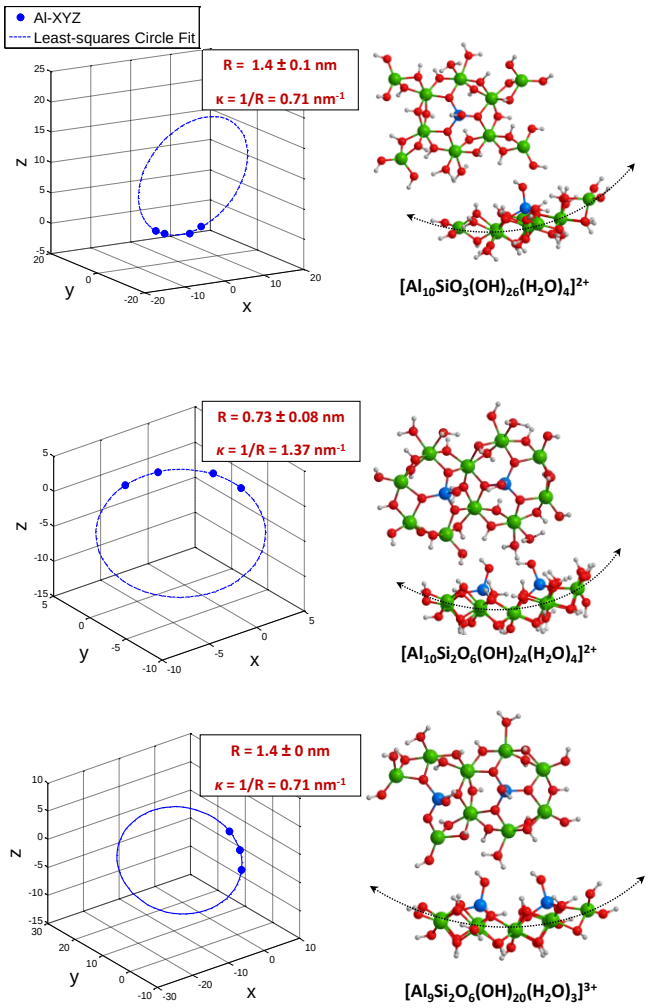

Figure 3-21. MATLAB plot on the left demonstrates the least-squares fitting of a cylindrical radius to xyz Cartesian aluminum atom coordinates of DFT optimized aluminosilicate precursor and calculated molecular curvature (κ). Top and side view of the molecule is shown on the right side and inherent curvature of the molecule is indicated with a dotted line. Atom colors representing green: aluminum, yellow: chloride, blue: silicon, white: hydrogen, red: oxygen respectively.

3.4 Conclusion

The findings presented in this thesis provide clear evidence of the remarkable role of ligand complexation in altering the curvature of nanotube-forming metal oxide precursors that otherwise possess essentially similar topology in terms of the arrangement of the framework atoms (Al and Si). This has been conclusively demonstrated by a

combination of nanotube synthesis variations, cryo-EM, ESI-MS, NMR, XRD, and DFT methods to reveal and control the relationships between precursor geometry and resulting nanotube geometry. The present findings provide a rational and quantitative framework for Ångstrom-scale shaping and structuring of nanoscopic metal oxide objects in solution for a variety of possible applications, by creating precursors of well-defined and controlled molecular structure and shape.

CHAPTER 4

FORMATION OF ALUMINOGERMANATE NANOTUBES AND POSSIBLE ROUTES TO CONTROLLING METAL OXIDE NANOTUBE LENGTH

4.1 Introduction

In the last two decades, nanotubes have been a core focus of nanomaterials science and technology, owing to the remarkable surface and structural properties associated with their low dimensionality [3, 4, 11, 12]. Low-temperature synthesis procedures are sought that allow fine control over chemical composition, size, shape, and uniformity to make widespread technological use of nanotube materials. Single-walled metal-oxide nanotubes, namely aluminosilicate (AlSiOH) [1, 37] and aluminogermanate (AlGeOH) nanotubes [38, 60, 118], can be efficiently synthesized [105] from aqueous phase at low-temperatures (95 ˚C) within a short period of few days [37]. Consequently, they are emerging as candidates for a variety of applications including catalysis [40], molecular transport [101, 104], storage [55] and separation [56, 101].

As described in detail in previous chapters, AlSiOH nanotubes are made up of a curved gibbsite [$Al(OH)_3$] sheet with inner silicate [O_3SiOH] groups located on each vacant sites of the continuous gibbsite wall [30]. An external diameter of 2.0−2.8 nm, an inner diameter of 0.9−1 nm, and lengths ranging from several hundered nanometers to a few micrometers have been reported for AlSiOH nanotubes [2, 30, 36, 119]. [O_3SiOH] groups can be completely replaced by [O_3GeOH] tetrahedra yielding their AlGeOH

analogues [36], which have larger diameter of 3.3 nm and much shorter average lengths (~20 nm) [38, 60]. Figure 4-1 summarizes the key structural and physical differences between AlSiOH and AlGeOH nanotubes.

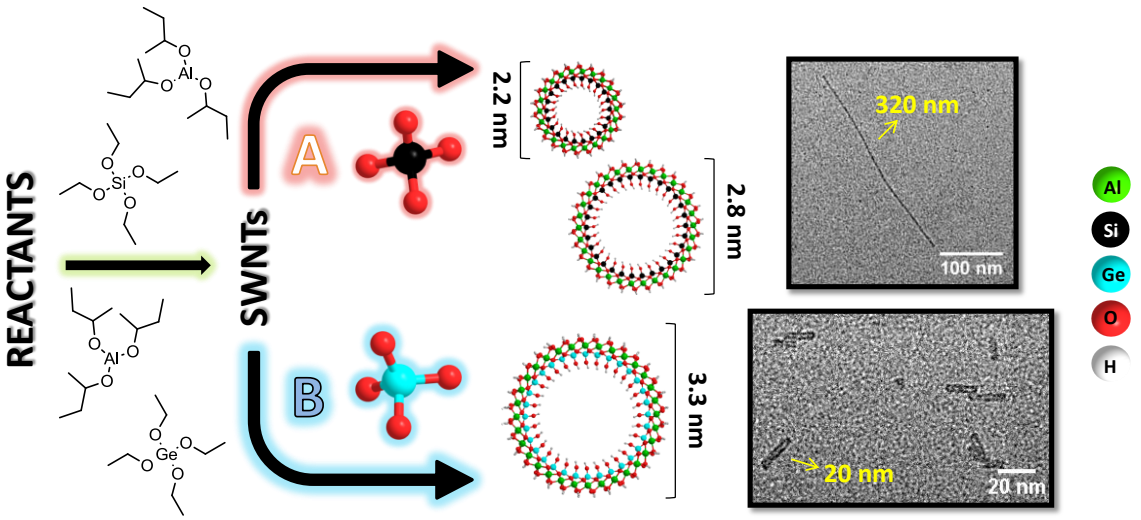

Figure 4-1. A) Aluminum-tri-sec-butoxide [$Al(OC_4H_9)_3$] and tetraethyl orthosilicate [$Si(OC_2H_5)_4$] are precursors used to synthesize AlSiOH nanotubes [1]. B) Complete replacement of the [$Si(OC_2H_5)_4$] source with germanium ethoxide [$Ge(OC_2H_5)_4$] results in AlGeOH nanotubes which are larger in diameter but smaller in length. TEM images of final nanotubes showing the differences in length between AlSiOH and AlGeOH nanotubes. How this similar reaction conditions cause structural changes in nanotubes is still not clear. Mechanistic understanding of this difference would lead to achieving control over nanotube dimensions.

More widespread use of single-walled metal-oxide nanotubes is possible through the development of synthesis procedures that provide guidelines for achieving desired pore dimensions as well as lengths. Such tailoring of nanotube features for specific applications are challenged by the lack of knowledge of the formation and growth mechanisms. Significant progress has been made in recent years that provided insights into the self-assembly and growth mechanism of AlSiOH [1] and AlGeOH [38, 60]

nanotubes in aqueous phase. It is now known that nanotube-like curved nanointermediates, having the same nanotube composition, exist very early in synthesis solutions at 25 ˚C [1, 38]. Upon heating to 95 ˚C, nanointermediate precursors condense and rearrange into short nanotubes [1, 33, 60]. The curvature of the precursors defines the final pore size of the nanotube [2]. Infact, recently, diameter control of AlSiOH nanotubes was achieved through the modifications of precursor curvature due to complexation with solution anions without any necessary modifications to chemical compositions [2]. This finding also explained the differences in reported diameters (2.0−2.8 nm) of AlSiOH nanotubes. Growth mechanism of the nanotubes is still not known. They grow either by proposed edge-edge aggregation [38] or nutrient addition [66] mechanism.

This Chapter has two objectives. The first is to investigate of AlGeOH nanotube formation through time-resolved NMR and ESI−MS analysis of AlGeOH synthesis solutions. A similar study was previously reported by us for AlSiOH nanotubes [1], as described in Chapter 2. Secondly, similarities and differences detected between AlSiOH and AlGeOH nanotube formation are discussed by comparing the results of the present study with those pertaining to aluminosilicate nanotube formation [1]. The presented work in this Chapter is a first attempt to explain the structural and physical differences observed between AlSiOH and AlGeOH nanotubes, and to gain understanding of the factors affecting the shortening of AlGeOH nanotube lengths. To the best of our knowledge, no previous attempts have been made to explain these differences. Here some examples of nanotube length control is also provided.

4.2 Experimental Details

4.2.1 Aluminogermanate Nanotube Synthesis

Synthesis details of AlSiOH nanotubes are given in Chapter 2 and elsewhere [1]. For synthesis of AlGeOH nanotubes, 0.05 M germanium ethoxide (TEOG) is mixed with 0.1 M Al sec-butoxide in a glove box under nitrogen gas. This mixture is then introduced into acidic solution of 0.05 M $HClO_4$. The obtained solution is kept under vigourous strirring for 18 h at 25 ˚C ("Aging Stage"). The solution is then diluted to 0.02 M Al to slow down the condensation kinetics and subsequently temperature is increased to 95 ˚C. The reaction lasts for 4 days (96 h). Experiments are performed in liquid phase and the samples were directly taken from the reactors without any further modification directly used in ESI−MS and NMR experiments at various stages of the synthesis.

4.2.2 TEM, NMR, and DFT Calculations

A JEOL JEM-1400 transmission electron microscope (TEM) that is operating at 120kV was used to characterize nanotube lengths. Samples were screened with an Orius SC1000 CCD and an UltraScan1000 CCD camera. Details of the ^{27}Al liquid-state NMR measurements and Density Functional Theory calculations are described in Chapter 2.

4.2.3 ESI−Mass Spectrometry

All mass spectrometric measurements were acquired utilizing electrospray ionization with a Q-TOF mass spectrometer (Bruker micrOTOF-QII; Bremen, Germany). Optimal settings were determined in advance with representative silicate and germanate

samples. Capillary voltages of -3.0 kV and $+3.5$ kV were used for positive-ion and negative-ion modes, respectively. The endplate offset was -500 V for both acquisition modes. Nitrogen was employed as the drying gas at a flow rate of 4 L min^{-1} and nebulizing gas at a pressure of 2.0 bar. The drying gas temperatures were 150 ˚C and 250 ˚C for positive-ion and negative-ion modes, respectively. Spectra were acquired at 1.0 Hz in the m/z 35 – 1000 for positive-ion and m/z 35 – 1500 range for negative-ion mode. The instrument was mass calibrated before conducting experiments using a solution of sodium formate. Mass spectral data processing, signal averaging, and background subtraction were performed using DataAnalysis 4.0, the built-in mass spectrometer software.

4.3 Results and Discussion

4.3.1 ^{27}Al Liquid-State NMR Spectroscopy

^{27}Al NMR spectra of aluminogermanate nanotube synthesis solutions at different reaction times during aging (25 ˚C) and heating stages (95 ˚C) are shown in Figure 4-2. Three chemical environments of Al were identified after performing spectrum deconvolution with Lorentzian peak shapes. As seen in Figure 4-2, spectra displays a sharp peak at 0 ppm originating from octahedrally coordinated Al_1 monomers [63]. Two other components were also observed: a broad peak near 8 ppm, and, a relatively sharp peak again at 8 ppm. Both signals are due to Al configurations exist in pure nanotube structure or possibly nanotube-like less organized structure (such as precursors, defects, or end groups). Thus, the broad signal near 8 ppm, observed at aging and heating stages of synthesis, could originate from Al in less-ordered areas of nanotube-like precursors

that are evolving and rearranging into nanotubes. The broad peak could also overlapping resonances due to small units such as aluminate [63] or aluminogermanate dimers, and/or trimers. Rather sharper signal at 8 ppm represents more-ordered Al environments in nanotubes and/or nanotube building units. It should be noted that "more-ordered" Al environments do not necessarily mean a long range order in the detected structure due to the reason that linewidth of ^{27}Al NMR resonances are more sensitive to order in first coordination sphere of an aluminum atom [120, 121]. No tetrahedrally coordinated aluminum present in synthesis solutions of aluminogermanate nanotubes. The absence of tetrahedral Al in this material has previously been reported [38].

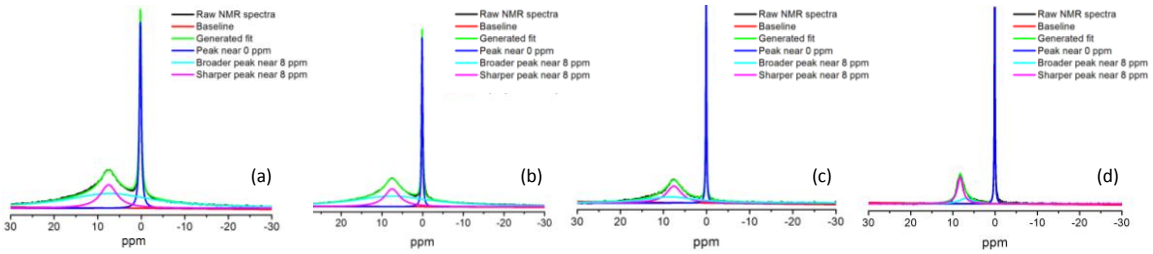

Figure 4-2: ^{27}Al liquid NMR spectra of aluminogermanate nanotube synthesis solutions at various reaction times: (a) 2nd h aging at 25˚C, (b) 18th h aging at 25˚C, (c) 1st h heating at 95˚C, and (d) 96th h heating at 95˚C. Deconvoluted peaks are plotted simultaneously.

The evolution of each ^{27}Al NMR signal was tracked in terms of its chemical shift, linewidth, and area% throughout the AlGeOH nanotube synthesis procedure as shown in Figure 4-3. As clearly seen from Figure 4-2, at all stages of nanotube formation and growth, species represented by 0 ppm peak is observed. During the aging stages at 25 ˚C, the monomeric species represented by this peak is consumed in favor of forming AlGeOH nanotube precursors and/or small aluminogermanate species like dimers or

trimers (Figure 4-3a). Equilibrium is reached, within as quickly as 2 h, between species represented by the peaks near 8 ppm and the monomeric units (Figure 4-3a, c, and e). After 2 h aging at 25 ˚C, no further structural rearrangement around Al atoms (Figure 4-3e) takes place in the synthesis solutions and no further increases in the amount of AlGeOH precursors were detected (Figure 4-3a); indicating that the reaction between Al- and Ge-containing species has reached equilibrium.

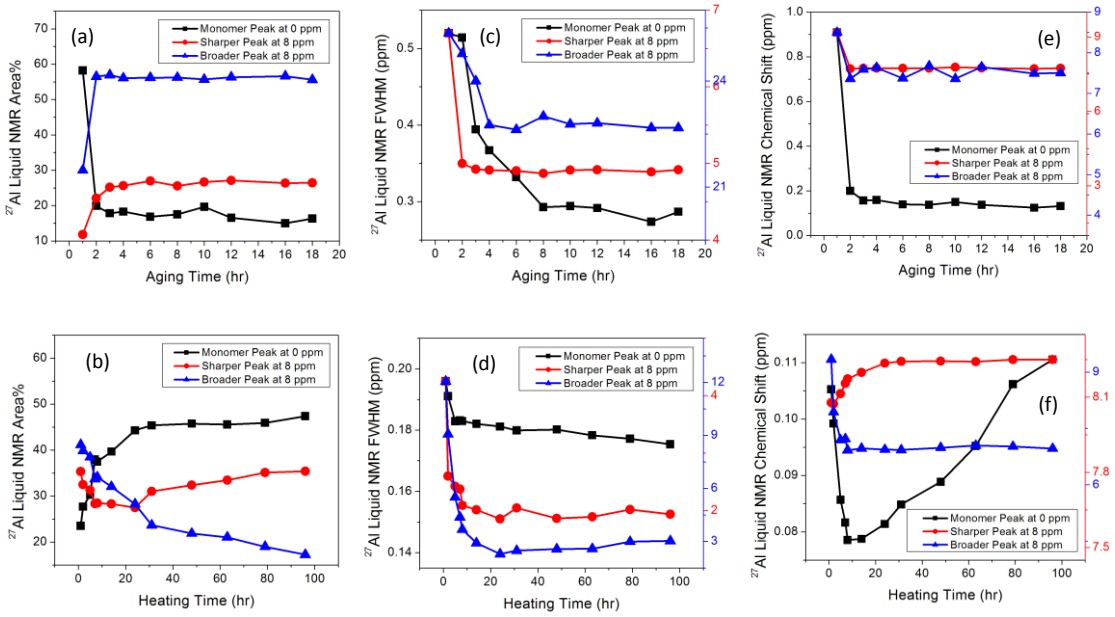

Figure 4-3. Changes in ^{27}Al liquid NMR areas% (a and b), FWHMs (c and d), and chemical shifts (d and e) of three octahedrally coordinated Al environment (represented by relatively sharper 8 ppm peak, broader 8 ppm peak, and 0 ppm peak) observed in spectra of AlGeOH nanotube synthesis solutions as a function of 18 h aging at 25 ˚C (a, c, and e) and 96 h heating at 95 ˚C (b, d, and f).

After 18 h aging at 25 ˚C, the synthesis solution is heated to 95 ˚C. Based on studies of the AlSiOH nanotube system, it is known that the precursors condense and rearrange upon heating to form nanotubes [1, 60]. Changes in the area %, linewidth, and chemical shift of ^{27}Al NMR signals during 4 days of heating of the AlGeOH system are

shown in Figure 4-3. The area% of the Al signal belonging to ordered nanotube-like configurations stays nearly constant throughout the heating (see the behavior of relatively sharp 8 ppm peak in Figure 4-3b). However, the area% of monomeric species (Figure 4-3b) increases up until 24 h of heating, whereas the area% of the broader 8 ppm signal continuously decreases. The overall decrease in the amount of species represented by the broad 8 ppm peak could be associated with the rearrangement of precursors and also with dissolution of dimeric or trimeric aluminogermanate species to monomeric species. A decrease in the full width at half maximum (FWHM) of each of the three peaks is observed within the first 24 h (Figure 4-3d). As discussed before, this suggests a more symmetrical/ordered rearrangement of atoms in the first coordination sphere around aluminum [122]. The most dramatic decrease in FWHM (from 12 to 3 ppm) is observed for the ~8 ppm peak. This is also accompanied by a change in its chemical shift (Figure 4-3f) that is attributed to the rearrangement of precursors into an ordered configuration approaching the final nanotube structure. The relatively sharper peak, in the meanwhile, has experienced only a 2 ppm decrease in FWHM. Slight changes in chemical shift (Figure 4-3f) and FWHM of the sharper 8 ppm peak are expected, due to a increase in structural strain in the first coordination shell around Al when the precursors rearrange into nanotubes. The slight decrease in FWHM of the monomer signal is due to the equilibrium shift between aluminate monomers [1]. This is likely also be the reason for the observed increase in the 0 ppm signal, because of a more symmetric environment forming around Al [122] and hence increasing the detectable Al signal (Figure 4-3b).

4.3.2 ESI−Mass Spectrometry

To determine the interaction between aluminum and germanium species and to study the speciation and structural characterization of aluminogermanate hydrolysis products, nanotube synthesis solutions were analyzed by high-resolution ESI-MS up to a mass/charge (m/z) ratio of 1500. The positive and negative ESI-MS mass spectra of nanotube synthesis solutions collected at various aging (1st and 18th h) and heating stages (3th, 24th and 96th h) are given in Figures 4-4 and 4-5. The resulting ESI-MS spectra were characterized by wide distribution of aluminate and aluminogermanate species ranging from approximately m/z 200 to 1000. Molecular formulae of identified species are listed in Tables 4-1 to 4-5.

Germanium has a characteristic isotopic distribution pattern [^{70}Ge (20.5%), ^{72}Ge (27.4%), ^{73}Ge (7.8%), ^{74}Ge (36.5%), ^{76}Ge (7.8%)] [123]. Thus, the spectra were crowded by germanium-containing isotope clusters. The isotopic patterns of germanium allowed determination of the number of germanium atoms in species [123, 124]. To ensure the accuracy of interpreted molecular formula, recorded spectra was compared to calculated isotopic pattern and the mass tolerance was set to 0.05 Da. Further details of data analysis can be found in Chapter 2 and Ref. [1].

Hydrolysis products observed at aging stages of nanotube synthesis solutions are listed in Tables 4-1 and 4-2. The aluminogermanate species comprises of various amounts of Al and Ge ranging from containing a single Al atom ($AlGe_x$) up to ten Al

($Al_{10}Ge_x$) (x=0−4). A variety of ligands are complexed with aluminogermanate species ($-OC_2H_5$, $-OC_4H_9$, $-OClO_3$).

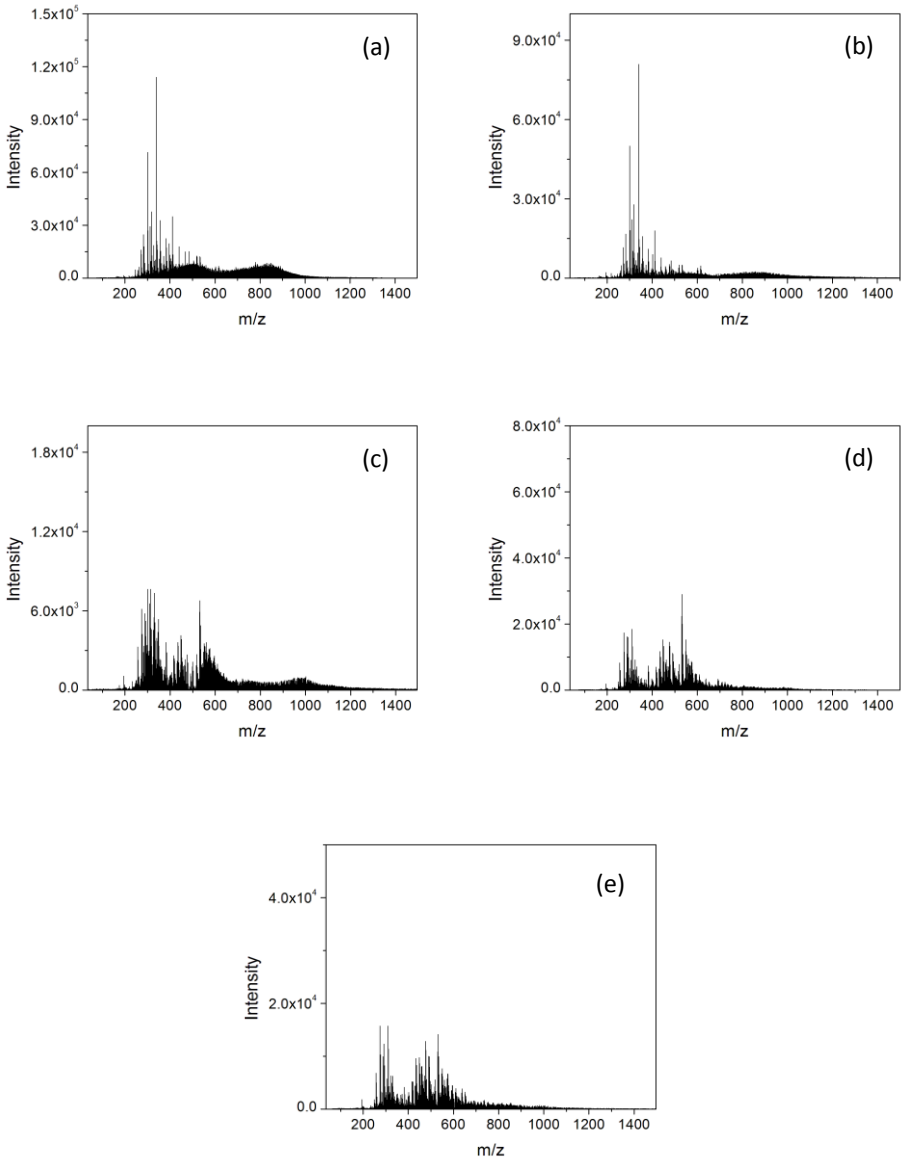

Figure 4-4. ESI−MS(+) spectra of AlGeOH nanotube synthesis solutions after (a) 1 h aging and (b) 18 h aging at 25 ˚C, (c) 3 h heating, (d) 24 h heating, and (e) 96 h heating at 95 ˚C.

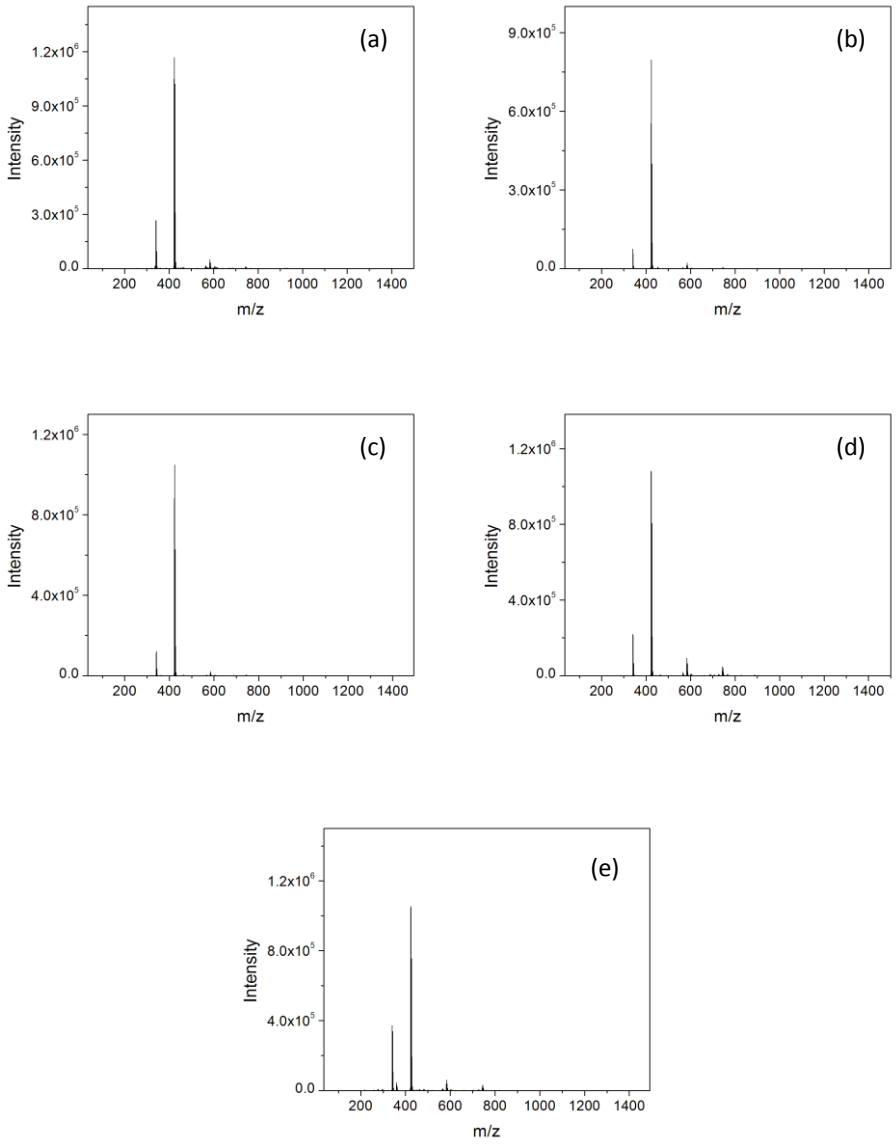

Figure 4-5. ESI−MS(−) spectra of AlGeOH nanotube synthesis solutions after (a) 1 h aging and (b) 18 h aging at 25 ˚C, (c) 3 h heating, (d) 24 h heating, and (e) 96 h heating at 95 ˚C.

Table 4-1. Molecular formula of aluminogermanate species detected by high-resolution ESI−MS in AlGeOH nanotube synthesis solutions after 1 h aging at 25 ˚C.

m/z (observed)	m/z (exact)	Molecular Formula
	$ESI(+)$	
260.93	260.90	$[Al(H_2O)_2(ClO_4)_2]^+$
283.02	283.02	$[Al_3(OH)_3(H_2O)_5(C_4H_9O)_2(ClO_4)_2]^{2+}$
301.03	300.94	$[Al_3O_3(C_4H_9O)(ClO_4)]^+$
319.04	318.95	$[Al_3O_3(C_4H_9O)(H_2O)(ClO_4)]^+$
329.06	329.09	$[Al_3O(OH)_4(H_2O)(C_4H_9O)_2]^+$
337.18	337.10	$[Al_4(OH)_5(H_2O)_5(C_4H_9O)_4(ClO_4)]^{2+}$

Table 4-1 (continued).

341.16	341.15	$[Al_2(OH)_3(H_2O)_5(C_4H_9O)_2]^+$
345.06	345.07	$[Al_3O(OH)_5(H_2O)_5(C_4H_9O)]^+$
382.98	383.01	$[Al_6(OH)_{11}(C_4H_9O)_3(ClO_4)_2]^{2+}$
397.06	397.08	$[Al_6(OH)_{11}(H_2O)_6(C_4H_9O)_4(ClO_4)]^{2+}$
403.19	403.16	$[Al_3(OH)_5(H_2O)(C_4H_9O)_3]^+$
403.19	403.11	$[Al_5Ge(OH)_{10}(H_2O)(C_2H_5O)_3(C_4H_9O)_4]^{2+}$
412.10	412.12	$[Al_5(OH)_8(H_2O)_9(C_4H_9O)_4(ClO_4)]^{2+}$
441.11	441.11	$[Al_2(OH)_2(H_2O)_6(C_4H_9O)_2(ClO_4)]^+$
485.14	485.11	$[Al_3(OH)_4(H_2O)(C_4H_9O)_3(ClO_4)]^+$
518.95	518.87	$[Al_3(OH)_4(C_4H_9O)(ClO_4)_3]^+$
532.96	532.96	$[Al_2(C_4H_9O)_2(H_2O)_2(ClO_4)_3]^+$
602.91	602.92	$[Al_8(OH)_{14}(H_2O)_2(C_4H_9O)_3(ClO_4)_5]^+$
616.91	616.90	$[Al_3GeO_2(OH)_3(H_2O)(C_2H_5O)_2(C_4H_9O)(ClO_4)_2]^+$
624.90	624.89	$[Al_3GeO_2(OH)_4(H_2O)_3(C_2H_5O)(C_4H_9O)(ClO_4)_2]^+$
634.92	634.91	$[Al_3GeO_2(OH)_3(H_2O)_2(C_2H_5O)_2(C_4H_9O)(ClO_4)_2]^+$
644.91	644.90	$[Al_5(OH)_{12}(H_2O)_6(ClO_4)_2]^+$
652.91	652.93	$[Al_3GeO_2(OH)_3(H_2O)_3(C_2H_5O)_2(C_4H_9O)(ClO_4)_2]^+$
656.91	656.92	$[Al_6GeO_3(OH)_{14}(H_2O)_5(C_2H_5O)]^+$
662.91	662.91	$[Al_5GeO_3(OH)_9(H_2O)_2(C_2H_5O)(C_4H_9O)(ClO_4)]^+$
666.90	666.89	$[Al_6Ge_3O_3(OH)_{14}(H_2O)_8(C_2H_5O)_5(ClO_4)_3]^{2+}$
670.91	670.90	$[Al_5Ge_3O_4(OH)_5(H_2O)_3(C_2H_5O)_7(C_4H_9O)(ClO_4)_4]^{2+}$
674.91	674.89	$[Al_5Ge_3O_3(OH)_8(H_2O)_4(C_2H_5O)_6(C_4H_9O)(ClO_4)_4]^{2+}$
678.90	678.89	$[Al_5GeO_4(OH)_8(H_2O)_7(C_2H_5O)(ClO_4)]^+$
686.90	686.92	$[Al_4Ge_2O_4(OH)_9(H_2O)_7(C_2H_5O)_2]^+$
686.90	686.88	$[Al_5GeO_3(OH)_{11}(H_2O)_8(ClO_4)]^+$
686.90	686.92	$[Al_3GeO_2(OH)_5(H_2O)_8(C_4H_9O)(ClO_4)_2]^+$
702.90	702.88	$[Al_5Ge_2O_5(OH)_9(C_2H_5O)_3(H_2O)_3]^+$
710.90	710.91	$[Al_8Ge_4O_9(OH)_{13}(H_2O)_7(C_2H_5O)_4(C_4H_9O)_2(ClO_4)]^{2+}$
716.90	716.87	$[Al_6Ge_3O_3(OH)_{13}(H_2O)_9(C_2H_5O)_5(ClO_4)_4]^{2+}$
724.90	724.89	$[Al_8Ge_2O_3(OH)_{15}(H_2O)_9(C_2H_5O)_5(ClO_4)_4]^{2+}$
730.91	730.92	$[Al_8Ge_2O_5(OH)_{11}(H_2O)_7(C_2H_5O)_2(C_4H_9O)_3(ClO_4)_4]^{2+}$
762.88	762.86	$[Al_5GeO_3(OH)_8(H_2O)_3(C_2H_5O)(C_4H_9O)(ClO_4)_2]^+$
780.90	780.91	$[Al_7Ge_3O_5(OH)_9(H_2O)_6(C_2H_5O)_6(C_4H_9O)_2(ClO_4)_4]^{2+}$
830.88	830.89	$[Al_8Ge_4O_7(OH)_{14}(H_2O)_6(C_2H_5O)_4(C_4H_9O)_3(ClO_4)_3]^{2+}$
848.89	848.90	$[Al_8Ge_4O_7(OH)_{14}(H_2O)_8(C_2H_5O)_4(C_4H_9O)_3(ClO_4)_3]^{2+}$
857.89	857.89	$[Al_9Ge_3O_7(OH)_{13}(H_2O)_{11}(C_2H_5O)_4(C_4H_9O)_2(ClO_4)_4]^{2+}$
872.86	872.88	$[Al_4Ge_2O_4(OH)_4(H_2O)_2(C_2H_5O)_4(C_4H_9O)(ClO_4)_2]^+$
882.86	882.87	$[Al_4GeO_3(OH)_5(H_2O)_{11}(C_4H_9O)(ClO_4)_3]^+$
889.87	889.85	$[Al_9Ge_3O_7(OH)_{12}(H_2O)_{10}(C_2H_5O)_4(C_4H_9O)_2(ClO_4)_5]^{2+}$
899.87	899.88	$[Al_9Ge_3O_7(OH)_{11}(H_2O)_8(C_2H_5O)_4(C_4H_9O)_3(ClO_4)_5]^{2+}$
910.87	910.84	$[Al_{10}Ge_3O_7(OH)_{15}(H_2O)_9(C_2H_5O)_4(C_4H_9O)_2(ClO_4)_4]^{2+}$
919.87	919.84	$[Al_{10}Ge_3O_7(OH)_{15}(H_2O)_9(C_2H_5O)_4(C_4H_9O)_2(ClO_4)_5]^{2+}$
916.86	916.85	$[Al_5GeO_3(OH)_7(H_2O)_7(C_2H_5O)(C_4H_9O)(ClO_4)_3]^+$
924.85	924.84	$[Al_5GeO_3(OH)_7(H_2O)_9(C_2H_5O)_2(ClO_4)_3]^+$
934.84	934.86	$[Al_5GeO_3(OH)_7(H_2O)_8(C_2H_5O)(C_4H_9O)(ClO_4)_3]^+$
942.84	942.87	$[Al_{10}Ge_3O_7(OH)_{15}(H_2O)_{10}(C_2H_5O)_3(C_4H_9O)_3(ClO_4)_5]^{2+}$
951.85	951.87	$[Al_{10}Ge_3O_7(OH)_{15}(H_2O)_{11}(C_2H_5O)_3(C_4H_9O)_3(ClO_4)_5]^{2+}$
960.84	960.88	$[Al_{10}Ge_3O_7(OH)_{15}(H_2O)_{12}(C_2H_5O)_3(C_4H_9O)_3(ClO_4)_5]^{2+}$
968.84	968.84	$[Al_6GeO_3(OH)_{10}(H_2O)_4(C_4H_9O)_2(ClO_4)_3]^+$
976.82	976.83	$[Al_6GeO_3(OH)_{10}(H_2O)_6(C_4H_9O)(C_2H_5O)(ClO_4)_3]^+$
988.82	988.78	$[Al_6Ge_2O_5(OH)_{12}(H_2O)_7(C_4H_9O)(ClO_4)_2]^+$
		ESI $(-)$
340.84	340.83	$[Al(OH)(ClO_4)_3]^-$

Table 4-1 (continued).

424.78	424.77	$[Al(ClO_4)_4]^-$
464.76	464.75	$[AlGeO(OH)_3(ClO_4)_3]^-$
564.72	564.72	$[Al_7Ge_2O_8(OH)_{10}(ClO_4)_5]^{2-}$
584.71	584.71	$[Al_2(OH)_2(ClO_4)_5]^-$
614.71	614.70	$[Al_6GeO_4(OH)_8(ClO_4)_8]^{2-}$
623.71	623.70	$[Al_6GeO_4(OH)_8(ClO_4)_8(H_2O)]^{2-}$
633.71	633.70	$[Al_8GeO_6(OH)_{11}(ClO_4)_7]^{2-}$
642.73	642.71	$[Al_8GeO_6(OH)_{11}(ClO_4)_7(H_2O)]^{2-}$
658.67	658.65	$[Al_7Ge_3O_{10}(OH)_9(ClO_4)_6]^{2-}$
667.66	667.65	$[Al_7Ge_3O_{10}(OH)_9(ClO_4)_6(H_2O)]^{2-}$
676.67	676.66	$[Al_7Ge_3O_{10}(OH)_9(ClO_4)_6(H_2O)_2]^{2-}$
685.67	685.66	$[Al_7Ge_3O_{10}(OH)_9(ClO_4)_6(H_2O)_3]^{2-}$
694.67	694.67	$[Al_7Ge_3O_{10}(OH)_9(ClO_4)_6(H_2O)_4]^{2-}$
706.65	706.64	$[AlGe_2O_2(OH)_4(ClO_4)_4(H_2O)_2]^-$
726.64	726.63	$[Al_5Ge_2O_7(OH)_8(ClO_4)_2]^-$
744.65	744.64	$[Al_3(OH)_4(ClO_4)_6]^-$
766.62	766.62	$[Al_2Ge_2O_3(OH)_5(ClO_4)_4(H_2O)_2]^-$

Table 4-2. Molecular formula of aluminogermanate species detected by high-resolution ESI−MS in AlGeOH nanotube synthesis solutions after 18 h aging at 25 ˚C.

m/z (observed)	m/z (exact)	Molecular Formula
	ESI (+)	
195.15	195.04	$[Al_2(OH)_4(C_4H_9O)]^+$
233.10	233.09	$[Al_2O(OH)(C_4H_9O)_2]^+$
301.03	300.94	$[Al_3O_3(C_4H_9O)(ClO_4)]^+$
312.14	312.18	$[Al_3(OH)_2(H_2O)_8(C_4H_9O)_5]^{2+}$ / $[Al_5(OH)_9(H_2O)(C_4H_9O)_3(ClO_4)]^{2+}$
341.16	341.15	$[Al_2(OH)_3(H_2O)_5(C_4H_9O)_2]^+$
357.11	356.90	$[Al_2(OH)_3(H_2O)_3(ClO_4)_2]^+$
373.04	372.99	$[Al_3(OH)_6(H_2O)(C_4H_9O)(ClO_4)]^+$
382.98	383.12	$[Al_3(OH)_6(H_2O)_3(C_4H_9O)_2]^+$
403.19	403.16	$[Al_3(OH)_5(H_2O)(C_4H_9O)_3]^+$
353.96	353.98	$[Al_4Ge_2O_4(OH)_6(C_2H_5O)_4(H_2O)_6]^{2+}$
399.06	398.88	$[Al_2GeO_3(OH)_2(ClO_4)(H_2O)_5]^+$
412.10	412.12	$[Al_5(OH)_8(C_4H_9O)_4(H_2O)_9(ClO_4)]^{2+}$
417.19	417.19	$[Al_5(OH)_8(C_4H_9O)_5(H_2O)_{11}]^{2+}$
419.13	419.14	$[Al_3(OH)_6(H_2O)_5(C_4H_9O)_2]^+$
428.09	428.09	$[Al_7(OH)_8(C_4H_9O)_4(H_2O)_9(ClO_4)]^{2+}$
439.10	439.04	$[Al_4(OH)_{11}(H_2O)_8]^+$
441.11	441.11	$[Al_2(OH)_2(H_2O)_6(C_4H_9O)_2(ClO_4)]^+$
458.90	458.85	$[Al_3GeO_2(OH)_7(ClO_4)(H_2O)_3]^+$
458.90	458.85	$[Al_2(OH)_2(H_2O)_4(ClO_4)_3]^+$
476.91	476.86	$[Al_2(OH)_2(H_2O)_5(ClO_4)_3]^+$
476.91	476.87	$[Al_3GeO_2(OH)_7(ClO_4)(H_2O)_4]^+$
485.15	485.11	$[Al_3(OH)_4(C_4H_9O)_3(ClO_4)(H_2O)]^+$
490.93	490.95	$[Al_3(OH)_5(C_4H_9O)(ClO_4)_2(H_2O)_3]^+$
520.94	520.98	$[Al_4GeO_3(OH)_7(H_2O)_3(C_2H_5O)(C_4H_9O)]^+$
532.96	532.92	$[Al_4(OH)_8(H_2O)(C_4H_9O)(ClO_4)_2]^+$
542.92	542.95	$[Al_3GeO(OH)_6(H_2O)_2(C_2H_5O)_3(ClO_4)]^+$
560.90	560.96	$[Al_3GeO(OH)_6(H_2O)_3(C_2H_5O)_3(ClO_4)]^+$
602.91	602.93	$[Al_4GeO_3(OH)_6(H_2O)_3(C_2H_5O)(C_4H_9O)(ClO_4)]^+$

Table 4-2 (continued).

616.91	616.90	$[Al_4Ge_2O_4(OH)_7(C_2H_5O)_4]^+$
634.91	634.92	$[Al_4Ge_2O_4(OH)_7(H_2O)(C_2H_5O)_4]^+$
686.87	686.92	$[Al_4Ge_2O_5(OH)_8(H_2O)_8(C_4H_9O)]^+$
704.86	704.81	$[Al_4Ge_2O_5(OH)_7(H_2O)_6(C_2H_5O)(ClO_4)]^+$
722.85	722.82	$[Al_4Ge_2O_5(OH)_7(H_2O)_7(C_2H_5O)(ClO_4)]^+$
734.83	734.83	$[Al_5GeO_3(OH)_9(H_2O)_3(C_4H_9O)(ClO_4)_2]^+$
744.83	744.85	$[Al_5GeO_3(OH)_8(H_2O)_2(C_4H_9O)(C_2H_5O)(ClO_4)_2]^+$
752.83	752.84	$[Al_5GeO_3(OH)_9(H_2O)_4(C_4H_9O)(ClO_4)_2]^+$
764.83	764.79	$[Al_4GeO_3(OH)_5(H_2O)_6(C_2H_5O)(ClO_4)_3]^+$
782.82	782.80	$[Al_4GeO_3(OH)_5(H_2O)_7(C_2H_5O)(ClO_4)_3]^+$
798.81	798.82	$[Al_4Ge_3O_4(OH)_{14}(H_2O)_7(C_2H_5O)]^+$
808.81	808.80	$[Al_5Ge_2O_5(OH)_{11}(H_2O)_9(ClO_4)]^+$
794.81	794.81	$[Al_6GeO_3(OH)_{12}(H_2O)_2(C_4H_9O)(ClO_4)_2]^+$
804.82	804.83	$[Al_6GeO_3(OH)_{11}(H_2O)(C_4H_9O)(C_2H_5O)(ClO_4)_2]^+$
820.81	820.81	$[Al_6GeO_3(OH)_{12}(H_2O)_5(C_2H_5O)(ClO_4)_2]^+$
814.81	814.84	$[Al_9Ge_4O_8(OH)_{17}(H_2O)_4(C_4H_9O)_2(C_2H_5O)_3(ClO_4)_3]^{2+}$
835.80	835.85	$[Al_9Ge_4O_8(OH)_{17}(H_2O)_8(C_4H_9O)_3(C_2H_5O)_2(ClO_4)_3]^{2+}$
840.80	840.79	$[Al_5Ge_3O_5(OH)_{15}(H_2O)_6(C_2H_5O)]^+$
858.79	858.80	$[Al_5Ge_3O_5(OH)_{15}(H_2O)_7(C_2H_5O)]^+$
876.79	876.81	$[Al_5Ge_3O_5(OH)_{15}(H_2O)_8(C_2H_5O)]^+$
846.79	846.81	$[Al_7Ge_2O_5(OH)_{18}(H_2O)_7]^+$
848.80	848.78	$[Al_5Ge_3O_5(OH)_{16}(H_2O)_8]^+$
868.78	868.81	$[Al_9Ge_4O_8(OH)_{15}(H_2O)_7(C_4H_9O)(C_2H_5O)_5(ClO_4)_4]^{2+}$
877.79	877.82	$[Al_9Ge_4O_8(OH)_{15}(H_2O)_8(C_4H_9O)(C_2H_5O)_5(ClO_4)_4]^{2+}$
896.78	896.81	$[Al_6Ge_2O_4(OH)_{15}(H_2O)_7(C_2H_5O)(ClO_4)]^+$
890.78	890.74	$[Al_5Ge_2O_2(OH)_{16}(H_2O)_6(ClO_4)_2]^+$
908.76	908.76	$[Al_5Ge_2O_2(OH)_{16}(H_2O)_7(ClO_4)_2]^+$
		ESI $(-)$
340.84	340.83	$[Al(OH)(ClO_4)_3]^-$
424.78	424.77	$[Al(ClO_4)_4]^-$
566.70	566.70	$[Al_2O(ClO_4)_5]^-$
584.71	584.71	$[Al_2(OH)_2(ClO_4)_5]^-$
602.72	602.72	$[Al_2(OH)_2(ClO_4)_5(H_2O)]^-$
744.65	744.64	$[Al_3(OH)_4(ClO_4)_6]^-$

Table 4-3. Molecular formula of aluminogermanate species detected by high-resolution ESI−MS in AlGeOH nanotube synthesis solutions after 3 h heating at 95 ˚C

m/z (observed)	m/z (exact)	Molecular Formula
		ESI $(+)$
195.15	195.04	$[Al_2(OH)_4(C_4H_9O)]^+$
233.10	233.09	$[Al_2O(OH)(C_4H_9O)_2]^+$
256.91	256.94	$[Al_2(OH)_4(ClO_4)(H_2O)_2]^+$
274.92	274.95	$[Al_2(OH)_4(ClO_4)(H_2O)_3]^+$
292.93	292.96	$[Al_2(OH)_4(ClO_4)(H_2O)_4]^+$
312.91	312.90	$[AlGeO(OH)_2(C_2H_5O)(ClO_4)(H_2O)]^+$
330.91	330.91	$[AlGeO(OH)_2(C_2H_5O)(ClO_4)(H_2O)_2]^+$
348.92	348.92	$[AlGeO(OH)_2(C_2H_5O)(ClO_4)(H_2O)_3]^+$
341.15	341.15	$[Al_2(OH)_3(C_4H_9O)_2(H_2O)_5]^+$
358.95	358.94	$[AlGeO(OH)(C_2H_5O)_2(ClO_4)(H_2O)_2]^+$
434.85	434.89	$[Al_3(OH)_6(ClO_4)_2(H_2O)_3]^+$

Table 4-3 (continued).

448.87	448.87	$[Al_2(OH)(C_2H_5O)(ClO_4)_3(H_2O)_2]^+$
466.87	466.88	$[Al_2(OH)(C_2H_5O)(ClO_4)_3(H_2O)_3]^+$
476.91	476.86	$[Al_4(OH)_9(ClO_4)_2(H_2O)]^+$
490.92	490.95	$[Al_3(OH)_5(OC_4H_9)(ClO_4)_2(H_2O)_3]^+$
500.80	500.82	$[Al_3(OH)_5(ClO_4)_3(H_2O)_2]^+$
518.80	518.83	$[Al_3(OH)_5(ClO_4)_3(H_2O)_2]^+$
532.82	532.81	$[Al_2(C_2H_5O)(ClO_4)_4(H_2O)_2]^+$
550.82	550.82	$[Al_2(C_2H_5O)(ClO_4)_4(H_2O)_3]^+$
560.84	560.84	$[Al_2(C_4H_9O)(ClO_4)_4(H_2O)]^+$
568.82	568.83	$[Al_2(C_2H_5O)(ClO_4)_4(H_2O)_4]^+$
576.84	576.82	$[Al_3GeO_2(OH)_6(ClO_4)_2(H_2O)_5]^+$
596.82	596.82	$[Al_4(OH)_8(ClO_4)_3(H_2O)_3]^+$
610.82	610.84	$[Al_2GeO(OH)(C_2H_5O)_3(ClO_4)_3(H_2O)]^+$
624.83	624.83	$[Al_2Ge_3O_3(OH)_{10}(C_2H_5O)(H_2O)_5]^+$
638.84	638.83	$[Al_3(OH)_3(C_4H_9O)(ClO_4)_2(H_2O)_5]^+$
650.84	650.86	$[Al_5GeO_3(OH)_{11}(ClO_4)(H_2O)_6]^+$
692.76	692.80	$[Al_3Ge_3O_3(OH)_{14}(H_2O)_6]^+$
720.79	720.83	$[Al_3Ge_3O_3(OH)_{13}(C_2H_5O)(H_2O)_6]^+$
746.78	746.82	$[Al_3Ge_2O_3(OH)_6(C_2H_5O)(C_4H_9O)(ClO_4)_2(H_2O)_3]^+$
950.67	950.65	$[Al_5Ge_3O_7(OH)_9(C_2H_5O)(ClO_4)_2(H_2O)_5]^+$
966.68	966.70	$[Al_5Ge_2O_4(OH)_{10}(C_2H_5O)(ClO_4)_3(H_2O)_6]^+$
972.67	972.69	$[Al_5Ge_2O_4(OH)_{11}(ClO_4)_3(H_2O)_8]^+$
980.67	980.64	$[Al_5GeO_3(OH)_7(ClO_4)_5(H_2O)_6]^+$
1002.68	1002.72	$[Al_5Ge_2O_4(OH)_{10}(C_2H_5O)(ClO_4)_3(H_2O)_8]^+$
1008.67	1008.63	$[Al_{12}Ge_5O_{11}(OH)_{27}(ClO_4)_5(H_2O)_{11}]^{2+}$
1014.68	1014.66	$[Al_7Ge_3O_7(OH)_{17}(ClO_4)(H_2O)_6]^+$
1018.66	1018.64	$[Al_{10}Ge_2O_6(OH)_{24}(ClO_4)]^+$
1022.67	1022.68	$[Al_{14}Ge_3O_9(OH)_{28}(ClO_4)_6(H_2O)_{13}]^{2+}$
1032.67	1032.67	$[Al_7Ge_3O_7(OH)_{17}(ClO_4)(H_2O)_7]^+$
1048.65	1048.69	$[Al_6Ge_4O_6(OH)_{21}(H_2O)_8]^+$
1058.65	1058.61	$[Al_{12}Ge_5O_{12}(OH)_{24}(ClO_4)_6(H_2O)_{13}]^{2+}$
1064.65	1064.65	$[Al_{15}Ge_4O_{12}(OH)_{30}(ClO_4)_5(H_2O)_{13}]^{2+}$
1073.64	1073.66	$[Al_{15}Ge_4O_{12}(OH)_{30}(ClO_4)_5(H_2O)_{14}]^{2+}$
1078.65	1078.60	$[Al_5Ge_3O_5(OH)_{13}(ClO_4)_3(H_2O)_7]^+$
1095.62	1095.63	$[Al_{13}Ge_4O_{10}(OH)_{26}(ClO_4)_7(H_2O)_{14}]^{2+}$
1106.58	1106.61	$[Al_{13}Ge_5O_{11}(OH)_{29}(ClO_4)_6(H_2O)_{13}]^{2+}$
		ESI $(-)$
342.83	342.83	$[Al(OH)(ClO_4)_3]^-$
424.78	424.77	$[Al(ClO_4)_4]^-$
584.72	584.71	$[Al_2(OH)_2(ClO_4)_5]^-$
744.65	744.64	$[Al_3(OH)_4(ClO_4)_6]^-$
766.62	766.61	$[Al_2(ClO_4)_7(H_2O)]^-$

Table 4-4. Molecular formula of aluminogermanate species detected by high-resolution ESI−MS in AlGeOH nanotube synthesis solutions after 24 h heating at 95 ˚C.

m/z (observed)	m/z (exact)	Molecular Formula
	ESI $(+)$	
256.91	256.94	$[Al_2(OH)_4(ClO_4)(H_2O)_2]^+$
274.92	274.95	$[Al_2(OH)_4(ClO_4)(H_2O)_3]^+$
292.93	292.96	$[Al_2(OH)_4(ClO_4)(H_2O)_4]^+$

Table 4-4 (continued).

310.94	310.98	$[Al_2(OH)_4(ClO_4)(H_2O)_5]^+$
288.93	289.01	$[Al_3(OH)_8(H_2O)_4]^+$
324.95	325.03	$[Al_3(OH)_8(H_2O)_6]^+$
330.97	331.02	$[Al_2(OH)_2(C_2H_5O)_2(ClO_4)(H_2O)_3]^+$
338.97	338.89	$[Al_2(OH)_3(ClO_4)_2(H_2O)_2]^+$
338.97	338.90	$[AlGeO(OH)_3(ClO_4)(H_2O)_4]^+$
382.98	383.01	$[Al_2GeO(OH)_4(C_2H_5O)_3(H_2O)_2]^+$
416.84	416.88	$[Al_3(OH)_6(ClO_4)_2(H_2O)_2]^+$
416.84	416.89	$[Al_2GeO(OH)_6(ClO_4)(H_2O)_4]^+$
434.85	434.90	$[Al_2GeO(OH)_6(ClO_4)(H_2O)_5]^+$
448.87	448.87	$[Al_2Ge_2O_2(OH)_8(C_2H_5O)(H_2O)_2]^+$
462.88	462.93	$[Al_2GeO(OH)_5(C_2H_5O)(ClO_4)(H_2O)_5]^+$
476.89	476.91	$[Al_2Ge_2O_2(OH)_7(C_2H_5O)_2(H_2O)_2]^+$
490.90	490.96	$[Al_2GeO(OH)_4(C_2H_5O)_2(ClO_4)(H_2O)_5]^+$
532.81	532.81	$[Al_2(C_2H_5O)(ClO_4)_4(H_2O)_2]^+$
550.82	550.82	$[Al_2(C_2H_5O)(ClO_4)_4(H_2O)_3]^+$
560.85	560.84	$[Al_3GeO_2(OH)_4(C_2H_5O)_2(ClO_4)_2(H_2O)]^+$
574.85	574.90	$[Al_4GeO_3(OH)_7(C_4H_9O)(ClO_4)(H_2O)_3]^+$
592.85	592.91	$[Al_4GeO_3(OH)_7(C_4H_9O)(ClO_4)(H_2O)_4]^+$
610.82	610.84	$[Al_2GeO(OH)(C_2H_5O)_3(ClO_4)_3(H_2O)]^+$
638.84	638.83	$[Al_4GeO_3(OH)_5(C_2H_5O)_2(ClO_4)_2(H_2O)_2]^+$
692.75	692.75	$[Al_4GeO_3(OH)_5(C_2H_5O)(ClO_4)_3(H_2O)_2]^+$
710.76	710.76	$[Al_4GeO_3(OH)_5(C_2H_5O)(ClO_4)_3(H_2O)_3]^+$
722.78	722.74	$[Al_2Ge_2O_2(OH)_4(C_2H_5O)_2(ClO_4)_3(H_2O)_2]^+$
734.79	734.79	$[Al_6(OH)_{14}(ClO_4)_3(H_2O)_2]^+$
752.79	752.80	$[Al_6(OH)_{14}(ClO_4)_3(H_2O)_3]^+$
806.73	806.76	$[Al_4(OH)_5(C_2H_5O)(ClO_4)_5(H_2O)_4]^+$
		ESI $(-)$
340.84	340.83	$[Al(OH)(ClO_4)_3]^-$
424.78	424.77	$[Al(ClO_4)_4]^-$
584.72	584.71	$[Al_2(OH)_2(ClO_4)_5]^-$
744.65	744.64	$[Al_3(OH)_4(ClO_4)_6]^-$
766.63	766.61	$[Al_2(ClO_4)_7(H_2O)]^-$

Table 4-5. Molecular formula of aluminogermanate species detected by ESI−MS in AlGeOH nanotube synthesis solutions after 96 h heating at 95 ˚C

m/z (observed)	m/z (exact)	Molecular Formula
	ESI $(+)$	
256.91	256.94	$[Al_2(OH)_4(ClO_4)(H_2O)_2]^+$
274.92	274.95	$[Al_2(OH)_4(ClO_4)(H_2O)_3]^+$
292.93	292.96	$[Al_2(OH)_4(ClO_4)(H_2O)_4]^+$
310.93	310.98	$[Al_2(OH)_4(ClO_4)(H_2O)_5]^+$
324.95	325.03	$[Al_3(OH)_8(H_2O)_6]^+$
330.97	331.02	$[Al_2(OH)_2(C_2H_5O)_2(ClO_4)(H_2O)_3]^+$
382.97	383.01	$[Al_2GeO(OH)_4(C_2H_5O)_3(H_2O)_2]^+$
416.84	416.88	$[Al_3(OH)_6(ClO_4)_2(H_2O)_2]^+$
416.84	416.89	$[Al_2GeO(OH)_6(ClO_4)(H_2O)_4]^+$
434.85	434.90	$[Al_2GeO(OH)_6(ClO_4)(H_2O)_5]^+$
448.87	448.87	$[Al_2Ge_2O_2(OH)_8(C_2H_5O)(H_2O)_2]^+$
476.89	476.91	$[Al_2Ge_2O_2(OH)_7(C_2H_5O)_2(H_2O)_2]^+$

Table 4-5 (continued).

490.90	490.96	$[Al_2GeO(OH)_4(C_2H_5O)_2(ClO_4)(H_2O)_5]^+$
532.81	532.81	$[Al_2(C_2H_5O)(ClO_4)_4(H_2O)_2]^+$
550.82	550.82	$[Al_2(C_2H_5O)(ClO_4)_4(H_2O)_3]^+$
560.84	560.84	$[Al_3GeO_2(OH)_4(C_2H_5O)_2(ClO_4)_2(H_2O)]^+$
574.86	574.90	$[Al_4GeO_3(OH)_7(C_4H_9O)(ClO_4)(H_2O)_3]^+$
610.82	610.84	$[Al_2GeO(OH)(C_2H_5O)_3(ClO_4)_3(H_2O)]^+$
638.83	638.83	$[Al_4GeO_3(OH)_5(C_2H_5O)_2(ClO_4)_2(H_2O)_2]^+$
652.84	652.81	$[Al_3GeO_2(OH)_3(C_2H_5O)(C_4H_9O)(ClO_4)_3]^+$
708.78	708.77	$[Al_4Ge_3O_6(OH)_{10}(C_2H_5O)(H_2O)_4]^+$
722.78	722.74	$[Al_2Ge_2O_2(OH)_4(C_2H_5O)_2(ClO_4)_3(H_2O)_2]^+$
736.79	736.80	$[Al_3Ge_2O_3(OH)_6(C_2H_5O)_2(ClO_4)_2(H_2O)_4]^+$
752.79	752.80	$[Al_6(OH)_{14}(ClO_4)_3(H_2O)_3]^+$
		ESI $(-)$
340.84	340.83	$[Al(OH)(ClO_4)_3]^-$
424.78	424.77	$[Al(ClO_4)_4]^-$
584.72	584.71	$[Al_2(OH)_2(ClO_4)_5]^-$
744.65	744.64	$[Al_3(OH)_4(ClO_4)_6]^-$
766.63	766.61	$[Al_2(ClO_4)_7(H_2O)]^-$
340.84	340.83	$[Al(OH)(ClO_4)_3]^-$

The first mass spectrum was collected one hour after adding the aluminum and germanium sources into the synthesis solution. Hydrolysis reactions of Al sec-butoxide and TEOG already have taken place at this early stage. For the next 18 h of aging at 25 ˚C, no change is observed in the type of species identified and new formations were not detected. However, time-resolved NMR analysis of prenucleating nanotube solutions (Figure 4-3a, c, and e) indicated structural changes and possible rearrangements occur up until the 2nd h after initial mixing of the reactants. Thus, these changes can be interpreted as an established equilibrium between small, medium, and large aluminogermanate species [1]. The major species in analyzed prenucleating solutions (at 1st and 18th h aging) can be explained with same structural units correspond to nanotube-like solid-state configurations. Representative molecular structure of identified aluminogermanate species are given in Figure 4-6.

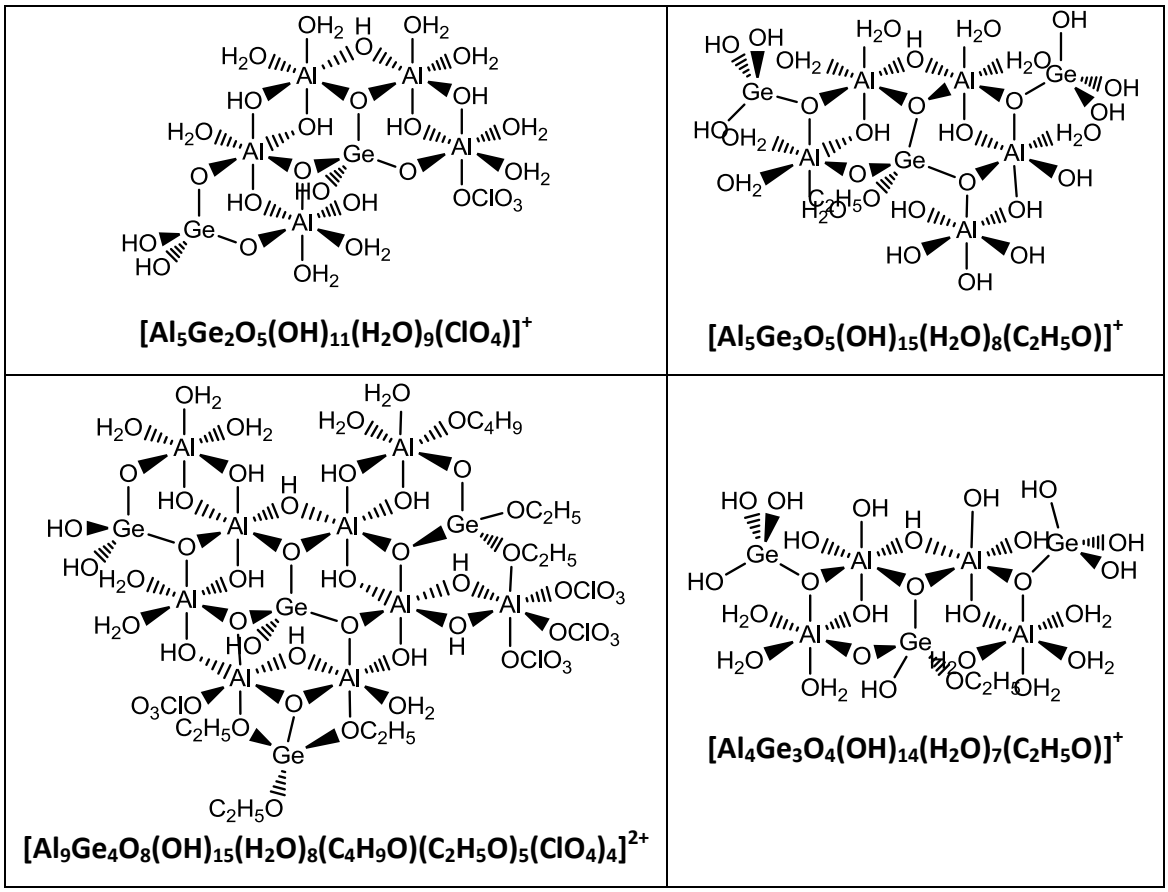

Figure 4-6. 2D ChemDraw illustrations of representative AlGeOH structures identified during aging in nanotube synthesis solutions.

Analysis of prenucleating solutions by ESI−MS yield insights into the hydrolysis and condensation behavior of germinate and aluminate species. Such understanding is crucial since polymerization/depolymerization reactions of germanate species are believed to play a major role in the shortening of aluminogermanate nanotube lengths [105, 107]. However, in this study, pure germanate species were *not* detected, either in negative or positive ESI−MS scan modes. On the other hand, small aluminate species such as $[Al_5(OH)_8(H_2O)_9(C_4H_9O)_4(ClO_4)]^{2+}$, or $[Al_3(OH)_6(H_2O)_5(OC_4H_9)_2]^{+}$ were detected after hydrolysis reactions took place not only during the aging process but also throughout reaction. This indicates that, due to differences in hydrolysis and

condensation rates of Al sec-butoxide and TEOG sources, aluminate and aluminogermanate species (but not germanate species) were able to form in nanotube reaction solutions. As soon as the hydrolysis reaction of TEOG occurs, the released Ge^{4+} ions are stabilized by reacting with Al, thereby inhibiting germanate condensation.

After 3 h of heating the reaction mixture at 95 ˚C larger condensates such as $[Al_{15}Ge_4O_{12}(OH)_{30}(ClO_4)_5(H_2O)_{13}]^{2+}$ or $[Al_{14}Ge_3O_9(OH)_{28}(ClO_4)_6(H_2O)_{13}]^{2+}$ were detected in AlGeOH nanotube synthesis solutions (Table 4-3). Figure 4-7 depicts the molecular structure of $[Al_{15}Ge_4O_{12}(OH)_{30}(ClO_4)_5(H_2O)_{13}]^{2+}$ species. However, with longer heating times (24^{th} and 96^{th} h) at 95 ˚C (Table 4-4 and 4-5), species of higher masses occur upon further condensation and rearrangement, and are undetectable to ESI−MS. Overall, aluminogermanate species larger than Al_5Ge_x disappear in synthesis solutions following the temperature increase, suggesting they are the precursors to nanotubes. Similar behavior was also observed for nucleating aluminosilicate nanotube solutions previously [1].

4.3.3 Solvated Density Functional Theory Calculations

Geometry optimization calculations by solvated DFT were performed on a set of AlGeOH species detected in nanotube synthesis solutions (Figure 4-8). All nanoscale precursors are found to exhibit intrinsic curvature. In order to quantify the curvature (κ), a cylindrical radius was fitted by least-squares to the Cartesian coordinates of at least three Al atoms (or O atoms) along the curvature in the DFT-optimized nanoscale intermediates. DFT studies showed AlGeOH precursors intrinsically have larger

curvatures compared to the species identified in AlSiOH nanotube solutions [2]. This is expected since it has long been suspected [36] that curvature differences between AlSiOH and AlGeOH nanotubes arise due to the larger O−O distance in GeO_4 compared to SiO_4 tetrahedra. Results presented in this Chapter experimentally prove this speculation, meanwhile providing another example that precursor curvature directly correlates with final nanotube diameter.

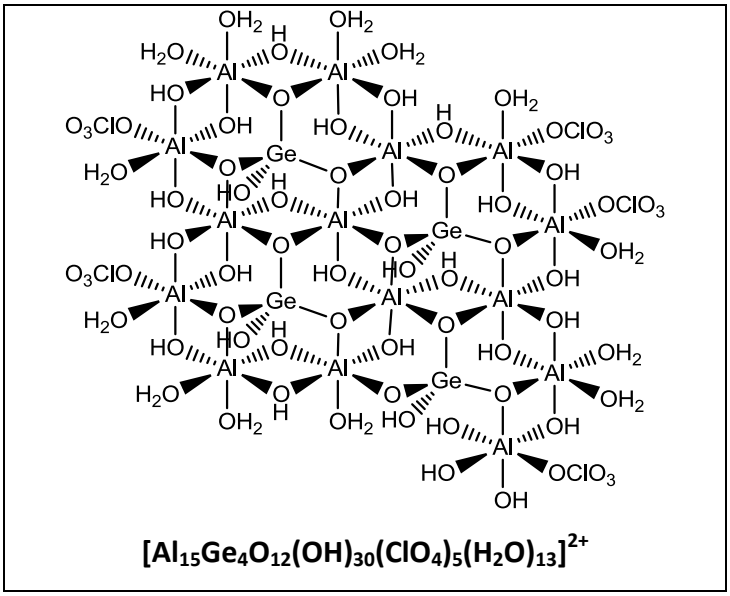

Figure 4-7. 2D ChemDraw illustration of representative AlGeOH structure identified during initial heating stage in nanotube synthesis solutions.

4.4 Differences Between AlSiOH and AlGeOH Nanotube Systems

4.4.1 Comparison of Silicon and Germanium Speciation

AlSiOH and AlGeOH nanotubes are synthesized using the same aluminum source (Al sec-butoxide). The only difference is the use of TEOS as Si source and TEOG as Ge source. Thus, to understand the mechanistic differences between the synthesis of AlSiOH

and AlGeOH nanotubes, differences and similarities between TEOS and TEOG hydrolysis were first investigated.

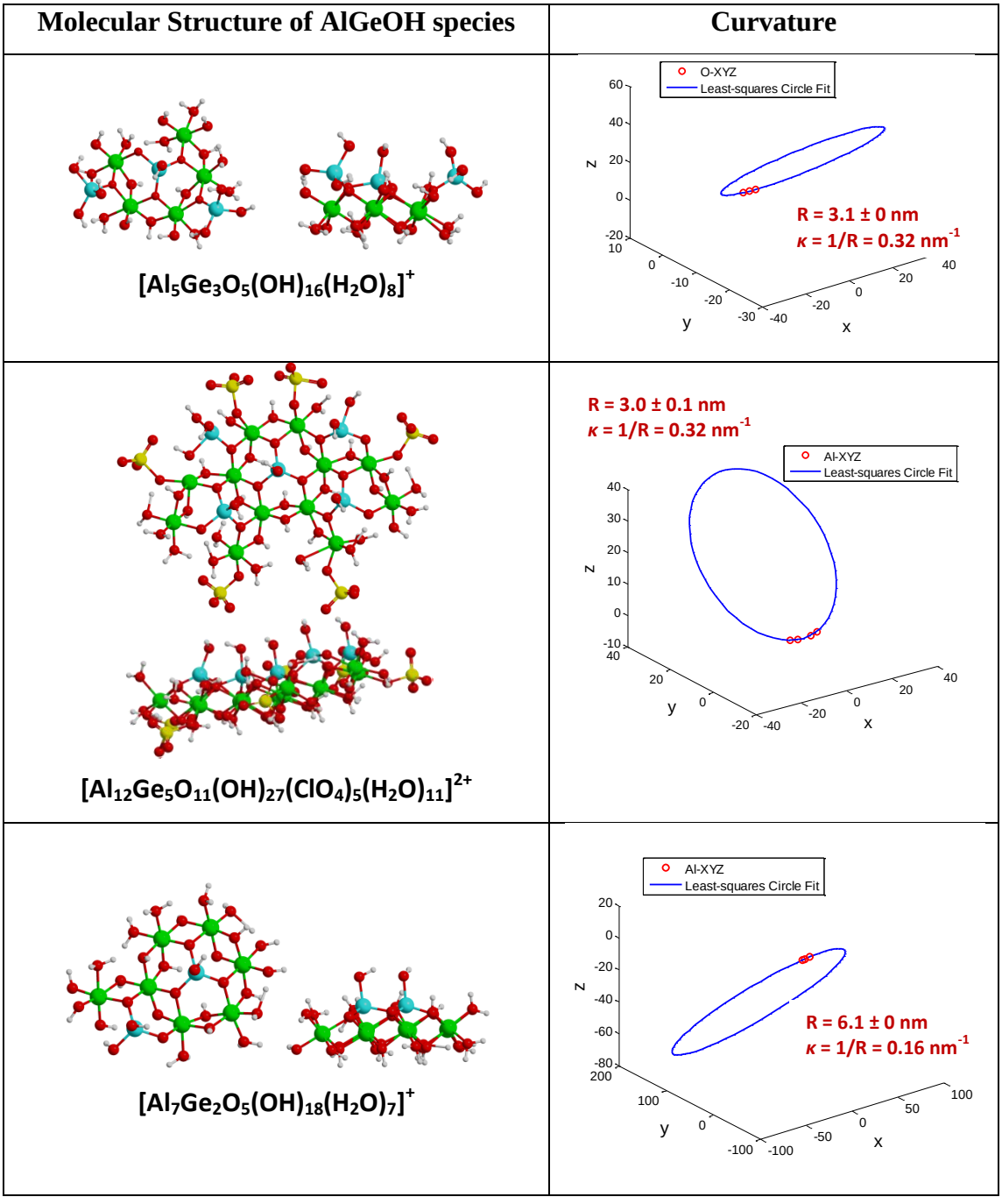

Figure 4-8. Molecular structure of AlGeOH species identified by ESI−MS in prenucleating and nucleating nanotube synthesis solutions after DFT optimization and their curvature (κ) estimation.

The nature of aqueous complexes formed by Si and Ge in 0.05 M $HClO_4$ solutions at 25 ˚C was investigated *via* mass spectrometry up to m/z = 1000. 0.05 M $Si(OC_2H_5)_4$ and 0.05M $Ge(OC_2H_5)_4$ are hydrolyzed in separate flasks to observe Si and Ge speciation, respectively after 18 h aging. Figure 4-9 gives the ESI−MS spectra of hydrolyzed TEOS and TEOG solutions. Tables 4-6 and 4-7 summarize the molecular composition of detected Si and Ge species in negative and positive scan mode. Tables show only the base peaks that belongs to an $\Delta m/z$ =18 (achieved by the elimination of water from the proposed structures) peak series.

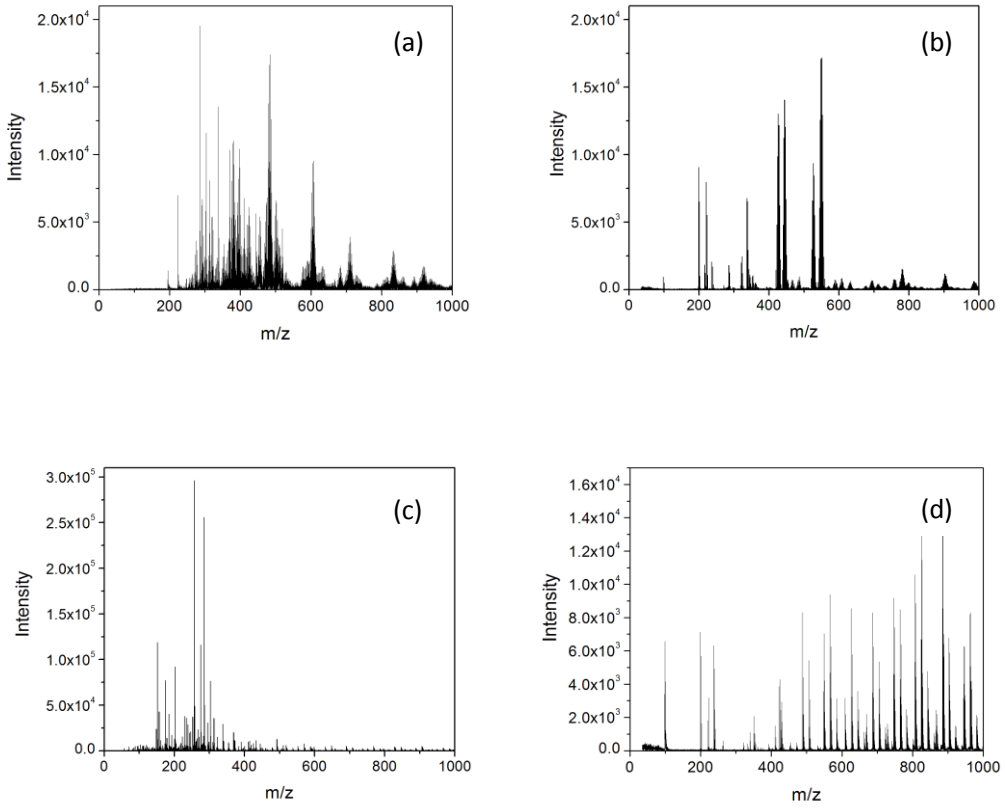

Figure 4-9. ESI−MS spectra of TEOG (a, b) and TEOS (c, d) in $HClO_4$ solutions: (a, c) ESI(+), and (b, d) ESI(−).

The only stable oxidation state for Ge and Si in aqueous solutions is IV [125]. The hydrated/hydroxylated ions exhibit tetrahedral coordination and form structurally similar cyclic network structures via hydrolysis and polycondensation reactions as seen in Figure 4-10 [1].

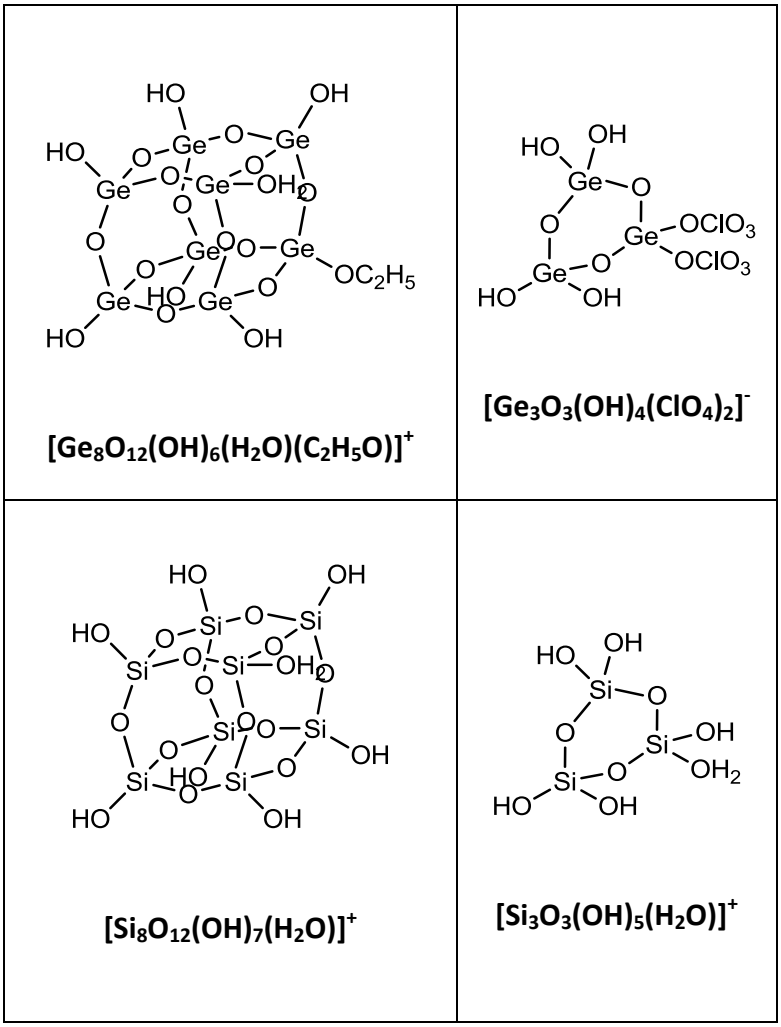

Figure 4-10. Representative cyclic molecular structure of silicate and germanate species detected in mildly acidic TEOG and TEOS solutions as identified by ESI−MS.

There has been no previous attempt made to explain the shortening of AlGeOH nanotubes. Wada speculated [36] that one reason could be the increased Cl^- concentration

due to the previous use of $GeCl_4$ as a germanium source in synthesis solutions, which inhibits the development of the nanotube structure. It is true that the existence of Cl^- promotes brucite-like arrangements of Al atoms rather than hexagonal gibbsite-like ring configurations [1]. However, the synthesis procedure used in our studies is different than Wada's [36] method of AlGeOH nanotube synthesis, since $GeCl_4$ is not used at all. Moreover, the reaction conditions (pH, temperature, type of acid, reactant amount and duration) were exactly the same for AlGeOH and AlSiOH nanotube synthesis. The only difference is that aqueous solutions were obtained by hydrolysis of $Si(OC_2H_5)_4$ or $Ge(OC_2H_5)_4$ sources in the presence of ClO_4^- ions. Although Cl^- anions were not present, the aluminogermanate nanotube lengths are still very short (~20 nm) (Figure 4-1), and are similar to those reported in a variety of different reaction procedures for AlGeOH nanotubes [38, 60, 107].

Table 4-6. Molecular formula of germanate species detected by high-resolution ESI−MS in TEOG solutions after 18 h aging at 25 ˚C.

m/z (observed)	m/z (exact)	Molecular Formula
	ESI $(+)$	
292.89	292.89	$[Ge_2O(OH)_4(H_2O)(C_2H_5O)]^+$
320.92	320.93	$[Ge_2O(OH)_3(H_2O)(C_2H_5O)_2]^+$
378.80	378.80	$[Ge_3O_3(OH)_4(C_2H_5O)]^+$
456.67	456.68	$[Ge_4O_6(OH)_3(H_2O)]^+$
484.71	482.71	$[Ge_4O_6(OH)_2(H_2O)(C_2H_5O)]^+$
576.60	576.60	$[Ge_5O_7(OH)_5(H_2O)]^+$
588.62	588.62	$[Ge_5O_7(OH)_4(C_2H_5O)]^+$
632.65	632.66	$[Ge_5O_7(OH)_3(H_2O)(C_2H_5O)_2]^+$
682.51	682.51	$[Ge_6O_9(OH)_5(H_2O)]^+$
710.54	710.54	$[Ge_6O_9(OH)_4(H_2O)(C_2H_5O)]^+$
788.42	788.42	$[Ge_7O_{11}(OH)_5(H_2O)]^+$
816.45	816.45	$[Ge_7O_{11}(OH)_4(H_2O)(C_2H_5O)]^+$
892.33	892.34	$[Ge_8O_{13}(OH)_5(H_2O)]^+$
938.37	938.38	$[Ge_8O_{12}(OH)_6(H_2O)(C_2H_5O)]^+$
	ESI $(-)$	
322.83	322.83	$[Ge(OH)_3(ClO_4)]^- + ClO_4^-$
426.74	426.74	$[Ge_2O_2(OH)_3(ClO_4)]^- + ClO_4^-$
444.75	444.75	$[Ge_2O(OH)_5(ClO_4)]^- + ClO_4^-$
466.72	466.72	$[Ge_3O_3(OH)_6]^- + ClO_4^-$
486.73	486.72	$[Ge(OH)(ClO_4)_3]^- + ClO_4^-$

Table 4-6 (continued).

526.70	526.69	$[Ge_2O(OH)_4(ClO_4)_2]^- + ClO_4^-$
550.66	550.66	$[Ge_3O_3(OH)_5(ClO_4)]^- + ClO_4^-$
588.64	588.64	$[Ge_4O_4(OH)_8]^- + ClO_4^-$
608.65	608.65	$[Ge_4O_3(OH)_{10}]^- + ClO_4^-$
632.61	632.61	$[Ge_3O_3(OH)_4(ClO_4)_2]^- + ClO_4^-$
676.54	676.54	$[Ge_5O_7(OH)_6]^- + ClO_4^-$
694.55	694.55	$[Ge_5O_6(OH)_8]^- + ClO_4^-$
710.56	710.56	$[Ge_5O_5(OH)_{10}]^- + ClO_4^-$
728.57	728.57	$[Ge_5O_4(OH)_{12}]^- + ClO_4^-$
758.48	758.48	$[Ge_5O_7(OH)_5(ClO_4)]^- + ClO_4^-$
780.45	780.45	$[Ge_6O_9(OH)_6]^- + ClO_4^-$
798.46	798.46	$[Ge_6O_8(OH)_8]^- + ClO_4^-$
902.37	902.37	$[Ge_7O_{10}(OH)_8]^- + ClO_4^-$

Table 4-7: Molecular formula of silicate species detected by high-resolution ESI−MS in TEOS solutions after 18 h aging at 25 ˚C.

m/z (observed)	m/z (exact)	Molecular Formula
	$\boldsymbol{ESI}(+)$	
184.99	184.99	$[Si_2O(OH)_4(C_2H_5O)]^+$
156.96	156.96	$[Si_2O(OH)_5]^+$
234.94	234.94	$[Si_3O_3(OH)_5(H_2O)]^+$
294.91	294.91	$[Si_4O_5(OH)_5(H_2O)]^+$
322.94	322.94	$[Si_4O_5(OH)_4(H_2O)(OC_2H_5)]^+$
382.90	382.90	$[Si_5O_7(OH)_4(H_2O)(OC_2H_5)]^+$
414.84	414.84	$[Si_6O_9(OH)_6]^+$
492.81	492.82	$[Si_7O_{10}(OH)_7(H_2O)]^+$
552.78	552.78	$[Si_8O_{12}(OH)_7(H_2O)]^+$
630.76	630.76	$[Si_9O_{13}(OH)_9(H_2O)]^+$
690.72	690.72	$[Si_{10}O_{15}(OH)_9(H_2O)]^+$
750.69	750.69	$[Si_{11}O_{17}(OH)_9(H_2O)]^+$
828.67	828.67	$[Si_{12}O_{18}(OH)_{11}(H_2O)]^+$
888.64	888.64	$[Si_{13}O_{20}(OH)_{11}(H_2O)]^+$
	$\boldsymbol{ESI}\ (-)$	
198.91	198.90	$[HCl_2O_8]^-$
350.90	350.89	$[Si_3O_2(OH)_8]^- + (ClO_4^-)$
410.86	410.86	$[Si_4O_4(OH)_8]^- + (ClO_4^-)$
488.84	488.84	$[Si_5O_5(OH)_{10}]^- + (ClO_4^-)$
548.81	548.80	$[Si_6O_7(OH)_{10}]^- + (ClO_4^-)$
626.79	626.78	$[Si_7O_8(OH)_{12}]^- + (ClO_4^-)$
686.76	686.75	$[Si_8O_{10}(OH)_{12}]^- + (ClO_4^-)$
746.72	746.71	$[Si_9O_{12}(OH)_{12}]^- + (ClO_4^-)$
824.70	824.69	$[Si_{10}O_{13}(OH)_{14}]^- + (ClO_4^-)$
884.66	884.66	$[Si_{11}O_{15}(OH)_{14}]^- + (ClO_4^-)$
962.64	962.63	$[Si_{12}O_{16}(OH)_{16}]^- + (ClO_4^-)$

Ge has been considered as a chemical analog of Si [126] and can substitute for Si in crystal lattices [127]. Data on the complexation of Si and Ge with anions (Cl^-, ClO_4^-) is

scarce. On the other hand, many studies exist that show Ge forming more stable complexes than Si with organic ligands [126]. These complexes are established through bidentate covalent bonds, and the coordination number of Ge can change from 4 to 6 as shown by EXAFS studies [128]. The ionic radius of Ge^{4+} (0.39 Å) is larger than that of Si^{4+} (0.26 Å). Unlike Ge, Si is reluctant to enlarge its coordination sphere to form stable complexes [128]. One of the significant differences observed in this work is that Ge can form stable complexes with perchlorate anion (ClO_4^-) as seen in Table 4-6. Ge^{4+} contains a completely full *d*-orbital unlike Si^{4+}, leading to a greater tendency towards covalent bonding that results in more stable chloride complexes [125]. While it is difficult to conclude with full certainty at the moment, it might be proposed that complexation (Ge-$OClO_3$), ongoing exchange between anions (ClO_4^- in our case or Cl^- in Wada's paper [36]) and hydroxyl ligands (OH^-), and the ability of Ge to increase its coordination number in complexes contribute to slowing down the growth kinetics of aluminogermanate nanotubes.

4.4.2 Comparison of Aluminosilicate and Aluminogermanate Speciation

No tetrahedrally coordinated aluminum is present in synthesis solutions of aluminogermanate nanotubes. This strikes us as one of the main differences between evolving ^{27}Al NMR spectra of AlSiOH and AlGeOH nanotube solutions [1]. Tetrahedral Al coordination in AlSiOH nanotube synthesis solutions arises from the presence of the Al_{13} Keggin complex $[Al_{13}O_4(OH)_{24}(H_2O)_{12}]^{7+}$ which is confirmed by both NMR and ESI−MS studies [1]. Tetrahedral Al coordination in pure AlSiOH nanotubes does also exists as a defect [1] which is believed to correspond to Al tetrahedra replacing Si

tetrahedra in the structure [129]. It is highly possible that the Keggin complex can rearrange to take part in the nanotube structure, while preserving its tetrahedral Al species. The Keggin complex does not form in AlGeOH solutions; its formation is somehow inhibited. Moreover, no tetrahedral Al coordination in the aluminogermanate nanotube structure itself is observed [38, 107].

The main reason for the absence of Keggin complex in AlGeOH and its existence in AlSiOH system is again believed to be the hydrolysis rate differences between TEOS/TEOG and Al sec-butoxide. The hydrolysis rate of Al sec-butoxide or other aluminum alkoxides is much higher than that of TEOS [130, 131]. Because of the difference between the hydrolysis rates of aluminum and silicon sources, the formation of aluminates (e.g. Keggin cation) cannot be avoided [130]. In fact, when TEOS is replaced with another silicon source such as TMOS, which has a higher hydrolysis rate than TEOS, more homogenous aluminosilicate networks are obtained [130-132]. Moreover, it is very well known that TEOG (or $GeCl_4$) [133] hydrolyzes much faster than TEOS [134]. Thus, Ge ions attack the aluminate species as soon as they are released by the hydrolysis of Al sec-butoxide preventing the polymerization of larger aluminate complexes such as the Keggin complex. In fact, no aluminate species bigger than Al_7 are detected in pre-nucleating AlGeOH nanotube solutions (Table 4-1 and 4-2). However, incomplete hydrolysis of TEOS results in formation of aluminates (including the Al-13 Keggin complex) in aluminosilicate nanotube-forming solutions [1].

Figure 4-11. Images of AlSiOH and AlGeOH nanotube synthesis solutions after 18 h of vigorous mixing at room temperature. The solutions were prepared by addition of Al sec-butoxide/TEOS and Al sec-butoxide/TEOG mixtures in $HClO_4$ solutions respectively.

A simple observation of solution transparency did also support the existence of large aluminates in aluminosilicate nanotube solutions. Figure 4-11 shows samples from AlSiOH and AlGeOH nanotube synthesis solutions after 18 h of aging at room temperature. The AlSiOH solution is cloudy due to the presence of large species that may form gel-like networks [135-138]. However, the AlGeOH solution is clear and transparent. Within a few hours of heating to 95 ˚C, the AlSiOH solution also becomes transparent. It is believed that in AlSiOH nanotube solutions, a precipitate or a gel containing separate aluminate and silicate phases or aluminate particles covered by silica, is present due to the lower hydrolysis rate of TEOS [131]. In fact, ESI−MS studies found Keggin-13 complexes surrounded by silicate units as described in Chapter 2 [1]. Other studies showed the possible existence of even bigger aluminate complexes like Al_{26} [96] or Al_{30} [139] that are said to be comprised of polymerized Keggin molecules. Heating of the solution to 95 ˚C promotes redissolution or rearrangement of Keggin complexes [1, 78] or larger polymerized complexes which provide a continuous precursor supply to the already nucleated nanotubes. This process is rather slow as evidenced by NMR studies [1]. It takes nearly 7 h for the Keggin signal to completely disappear upon heating.

Slower dissolution or rearrangement rate of the large aluminosilicate species assures the slow but ongoing resupply of precursors to the growing nanotubes after initial condensation and rearrangement process. Such a supply of aluminosilicate precursors in growing AlSiOH nanotubes could explain the previously reported *nutrient-addition growth mechanism* [66] that results in the observation of longer AlSiOH nanotubes (~100 nm) than AlGeOH nanotubes (~20 nm). The latter is suggested to grow by an *aggregative growth mechanism* [38]. The slow formation kinetics of AlSiOH nanotubes compared to AlGeOH nanotubes also received the attention of other researchers [107] who interpreted it in terms of differences in polymerization/depolymerization kinetics between Si and Ge species [105].

Here is should also be noted that an equilibrium is quickly established within 2 h aging of AlGeOH solutions [Figure 4-3a, c, and e], which cannot be reached for over 18 h in AlSiOH nanotube synthesis solutions [1] as indicated by detailed NMR studies. This can also support incomplete reaction and continuous ordering in prenucleating AlSiOH nanotube solutions between Al and Si units and/or an equilibrium is being established between bigger species throughout the aging stage compared to AlGeOH solutions in which no further increase in the amount of precursors (Figure 4-3c) is detected after 2 h, indicating that the reaction between Al and Ge atoms is complete and all available Al interacted with Ge atoms, thereby preventing the formation of larger aluminate complexes. Change in linewidth and chemical shifts of peaks in AlGeOH system (see Figure 4-3a, c and e) during the aging stage supports rather fast rearrangement and equilibrium that is established within a few hours into the synthesis as compared to AlSiOH system. As supported by ESI−MS experiments, although AlGeOH and AlSiOH

precursors can be chemically explained by the same structural configurations, the identified small and medium sized AlGeOH species contain three and even four germanium atoms whereas the number of Si atoms in similar-sized AlSiOH precursors is one or two [1]. This indicates that more Ge is available to interact with Al, resulting in a larger concentration of precursors in the AlGeOH nanotube solutions during aging as compared to the AlSiOH system. This is also supported by ^{27}Al NMR studies (Figure 4-12).

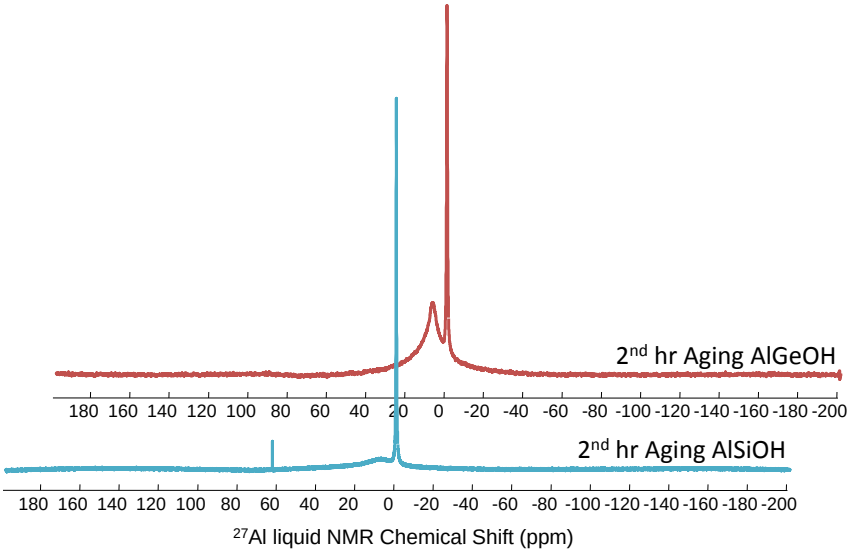

Figure 4-12. Comparison of ^{27}Al liquid-state NMR spectra of AlSiOH and AlGeOH solutions collected at 2nd aging h. The broad peak near 6 ppm in AlSiOH solutions [1] and 8 ppm peak in AlGeOH system is assigned to nanotube precursors. As seen from the ratio of monomer to precursor signal, precursor amount is much higher in AlGeOH solutions. Moreover as indicated by the linewidth of the precursor signal, first coordination environment of Al in AlGeOH precursors are much ordered. This again is an indication of a higher Ge/Al ratio in AlGeOH precursors compared to Si/Al ratio in AlGeOH precursors.

4.5 Controlling Single-Walled Metal Oxide Nanotube Lengths

The findings strongly indicate that hydrolysis rate differences between Al and Si/Ge reactants is a key factor in controlling single-walled metal-oxide nanotube length.

In order to synthesize short nanotubes, hydrolysis rate differences between the reactants should be minimized, i.e. the hydrolysis rates should be properly "matched". A combination of ESI−MS and NMR results suggest that this rate difference is relatively smaller between Al sec-butoxide and TEOG. Thus, shortened nanotube lengths and a smaller variety in precursor speciation (e.g., the absence of tetrahedral Al) are readily achieved for AlGeOH. As discussed before, the slower hydrolysis rate of TEOS limits the rate of precursor formation in AlSiOH solutions and also explains the observation of aluminate species. The number of nanotube-nucleating sites in AlSiOH solutions is therefore much smaller, and with the continuous supply of precursors during heating stage, the already formed nanotubes continue to grow by precursor addition, thereby resulting in longer nanotubes.

One can still shorten AlGeOH nanotubes by increasing the hydrolysis rate of TEOG slightly to match with the hydrolysis rate of Al sec-butoxide, thereby limiting the formation of even small aluminates, and further increasing the efficiency of Al and Ge complexation with each other. Exactly the opposite approach is also possible in order to grow longer AlGeOH nanotubes. To possibly obtain shorter AlSiOH nanotube lengths, the hydrolysis rate of the silicon source could be accelerated to match that of Al sec-butoxide. If TEOS is used, the hydrolysis rate can be accelerated by the addition of fluoride ions as a catalyst, or one may substitute TEOS with TMOS [140]. On the other hand, the hydrolysis rate of Al sec-butoxide can also be controlled by chelating agents [141, 142]. In this work, ethylacetoacetate-modified Al sec-butoxide (Alfa-Aesar) was used. This modification enables Al sec-butoxide to become less susceptible to attack by

water [141]. This Al source is mainly used to prevent aluminate formation in aluminosilicate sol-gel synthesis procedures and thereby allow increased complexation between Al and Si species [143]. The ^{27}Al liquid NMR spectra of such solutions show less Keggin and more precursor signal as compared to synthesis solutions with regular Al sec-butoxide (Figure 4-13). The amount of Keggin signal is used as an indication of the efficiency between Al and Si interaction, and is a direct measure of the amount of aluminate formation. When the Keggin signal is more predominant in AlSiOH nanotube solutions, it indicates that the hydrolysis rate difference between Al sec-butoxide and the Si source is large, leading to a lower yield of AlSiOH nanotube precursors and a higher number of aluminate species that do not directly participate in nanotube formation.

Figure 4-14 shows the length histograms of AlSiOH nanotubes synthesized using modified and non-modified Al sec-butoxide. The Figure includes TEM images of the nanotubes obtained from solutions at the final stage of the nanotube synthesis (96th h heating). Approximately 50 TEM images were collected, and the length distributions were obtained over 500 counts of individual nanotube lengths. It is clearly observed that nanotubes synthesized using the modified Al source are nearly two times shorter in average length (~83 nm) than nanotubes obtained with regular Al sec-butoxide (~167 nm). This remarkable change is entirely consistent with the hypothesis, and provides clear preliminary evidence of a rational route to control nanotube length in liquid-phase synthesis.

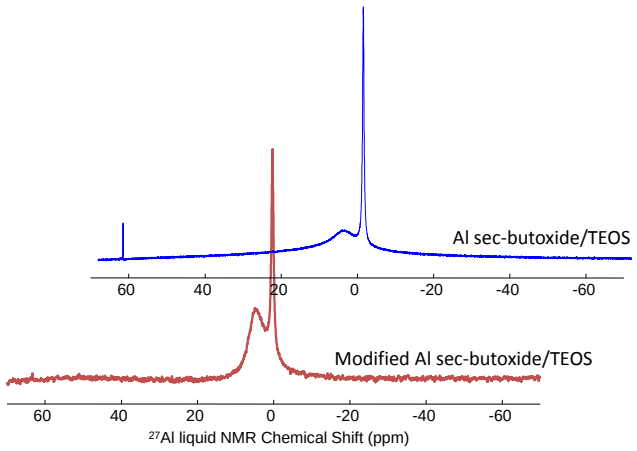

Figure 4-12. ^{27}Al liquid NMR spectra of 18 h aged AlSiOH nanotube forming solutions at 25 ˚C. The solution spectra shows less Keggin signal (63.3 ppm) but more precursor signal (6 ppm) [1] when modified Al sec-butoxide used as aluminum source.

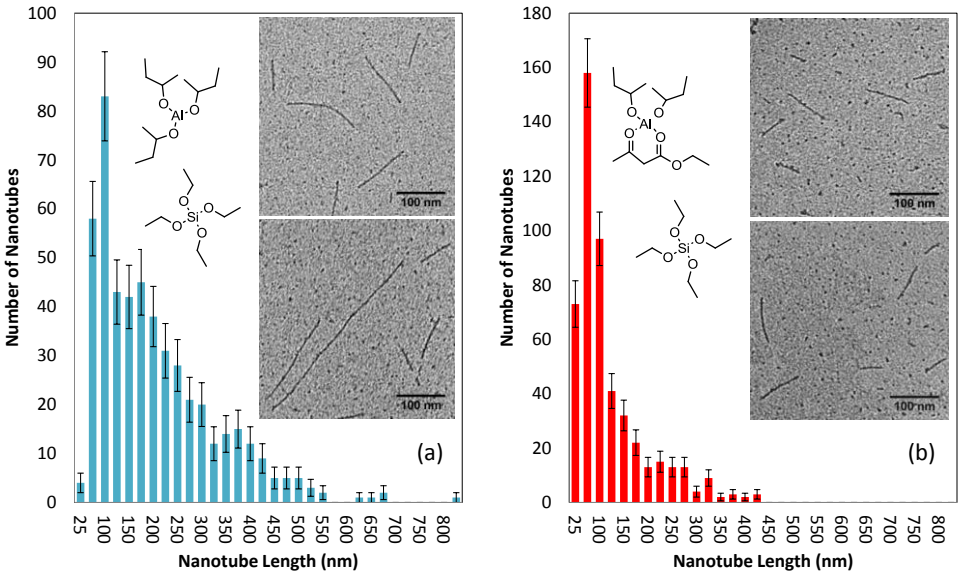

Figure 4-13. Histograms (with poisson counting errors) of AlSiOH nanotube lengths for nanotubes synthesized using (a) non-modified Al sec-butoxide and TEOS. The average length is 180 nm, (b) modified Al sec-butoxide and TEOS. The average length is 83 nm. Nanotube lengths are measured with segmented lines using ImageJ [112].

CHAPTER 5

A GENERALIZED KINETIC MODEL FOR THE FORMATION AND GROWTH OF SINGLE-WALLED METAL OXIDE NANOTUBES

5.1 Introduction

Solution-based methods are now being widely used for synthesizing a large number of nanostructures [67, 144-151]. This route offers superior control over morphology, structure and dimensions of the nanomaterials as it allows the modification of synthesis parameters such as duration, temperature, pH, and concentration of starting reactants. However, the mechanisms of nanomaterial formation and growth in solution are still yet to be understood. A few studies have been conducted on the kinetics of the synthesis reactions under hydrothermal conditions, including ZnO nanorods [146], V_2O_5 nanoribbons [151], SnO_2 [152] and CdSe nanocrystals [149]. The growth kinetics of nanomaterials are mainly governed by *Ostwald ripening* (OR) [153-155], *oriented attachment* (OA) [147, 151, 156, 157], or combination of both [158, 159]. OR mechanism is the growth of larger crystals at the expense of smaller crystals with a driving force to decrease the surface energy [154]. Meanwhile, OA may occur in two ways: (1) collision between aligned particles, or (2) coalescence of nonaligned particles in contact that undergo crystallographic rotation [151].

Only a few examples of single-walled metal oxide nanotubes are currently available, specifically aluminosilicate/germinate [33] [$(OH)_3Al_2O_3SiOH$,

$(OH)_3Al_2O_3GeOH$] and molybdenum oxide (MoO_3) nanotubes [65]. Since Farmer et al. [37] first reported the synthesis of aluminosilicate nanotubes, it has attracted enormous interest due to its distinctive physical and chemical properties [44, 160]. Over the years, they showed potent for various applications, ranging from nanocables [45] to high-flux membranes [54], based on experimental results and/or simulations that are taking the advantage of its well-defined open pores, and functionalizable inner and outer walls [41, 43]. Single-walled metal oxide nanotubes are synthesized via a facile and low cost solution-based method [161]. Industrial-scale processing of single-walled metal oxide nanotubes requires quantitative models describing the formation and growth mechanisms for desired engineering and high-yield production of such objects.

Several attempts have been made to develop qualitative and quantitative understanding of the formation and growth mechanism of single-walled metal oxide nanotubes [1, 33, 38, 60, 66, 162]. Mukherjee et al. [60] first proposed a two-step model to explain the kinetics of 20 nm long aluminogermanate nanotube formation based on dynamic light scattering, and UV-vis spectroscopy results. This model incorporates three main species in synthesis solutions. These are monomeric/oligomeric aluminogermanate precursors which are in reversible equilibrium with amorphous nanoscale condensates of ~ 6 nm having the ability to irreversibly *self-assemble and rearrange* into short aluminogermanate (AlGeOH) nanotubes when reaction solutions are heated. Levard et al. [38], on the other hand, observed the existence of rooftile-shaped precursors of size ~ 5 nm which assemble to ring segments that later form AlGeOH nanotubes with an *edge-to-edge assembly* process using XAS and SAXS techniques. The same research group also

proposed a kinetic model that assumed an *oriented aggregation* growth mechanism to explain the differences in final length distributions of single- and double-walled AlGeOH nanotubes [162]. A TEM study [66] proposed a kinetically controlled "nutrient addition" mechanism for aluminosilicate nanotubes (AlSiOH) that also supported early speculations [163] in which nanotubes are believed to grow with the addition of the precursors to growing nanotube ends. In detailed NMR, ESI−MS, and DFT study of AlSiOH nanotube formation shown in Chapter 2 [1], the existence of curved nanoscale intermediates of various sizes with nanotube-like bonding configurations was shown. These nanoscale intermediates were shown to *condense and self-assemble* into AlSiOH nanotubes upon heating.

It is seen that different mechanisms have been proposed to govern the nanotube formation and growth kinetics, thereby causing considerable confusion among researchers in this area. A more generalized quantitative model is needed to explain the formation and growth mechanisms of both single-walled aluminosilicate and aluminogermanate nanotubes, and it might even be generalizable to all single-walled nanotube objects prepared in solution. The objective of this Chapter is to develop a new quantitative model describing the formation and growth of single-walled metal oxide nanotubes. This model should also be able to *predict* size distribution and mean lengths of nanotubes at different experimental conditions. Such a model will be of high value in the design of nanotube reaction engineering processes.

5.2 Experimental Details

The synthesis of nanotubes was carried out as described previously in this thesis. Typically, 0.1 M Aluminum sec-butoxide (ASB) is mixed with 0.05 M tetraethoxysilane (TEOS) to synthesize AlSiOH nanotubes. In case of AlGeOH nanotube synthesis, the same amount of ASB is mixed with 0.05 M germanium ethoxide (TEOG). Reactant mixtures are dissolved in acidic aqueous solutions that are obtained by the addition of 0.05 M $HClO_4$ (20%) to 48 ml DI water. After 18 h vigorous mixing at room temperature, the reaction solutions are diluted to 0.02 M Al and the temperature is increased to 95 ˚C. Samples are withdrawn from the reactor at various reaction times (8, 14, 30, 48, 72, 85, 96, and 144 hrs).

Dispersed nanotube samples on TEM grids are prepared as follows: 10 μL of 20% $HClO_4$ is added to 10 ml of DI water in a small vial. Then, 10 μL acidic dispersions of nanotubes are directly taken from synthesis reactors at various reaction hours (8^{th} h, 14^{th} h, 30^{th} h, 48^{th} h, 72^{nd} h, 85^{th} h, 96^{th} h, and 144^{th} h). Whenever a sample is taken from the reactors at each defined time, it is added to the acidic water in the small vial. This way of diluting the nanotube solutions helps achieving a great dispersion of individual nanotubes over the TEM grid without the need to use any other difficult and/or time consuming techniques such as cryo-EM, grid drying in saturated ethanol atmosphere [66] or AFM [162]. As soon as the mixture is prepared, sample volumes of 2 μL were pipette onto thin carbon-coated 400-mesh copper grids and blotted with Whatman no. 4 filter paper immediately. A JEOL JEM-1400 transmission electron microscope (TEM) that is operating at 120kV is used to characterize nanotube length distributions. Samples are

screened with an Orius SC1000 CCD and an UltraScan1000 CCD camera. ImageJ software is used to characterize the length of nanotubes [112].

5.3 Results and Discussion

In the following sections, the formation and growth of single-walled metal oxide nanotubes under hydrothermal conditions are investigated experimentally and theoretically. A set of chemical reactions leading to nanotube formation and growth are proposed based on the experimental findings of this thesis and previous reports [1, 38, 60, 66]. A mathematical model is then derived to describe the time-dependent length distributions of nanotubes throughout the synthesis. The model is parameterized by fitting to experimental size distributions obtained from TEM micrographs of aluminosilicate and aluminogermanate nanotube samples collected at eight different times during synthesis. The model is shown to fully capture the features of evolving single-walled metal oxide nanotube length distributions. Finally, the predictive capability of the model is tested by comparision with experimental result at a different synthesis condition.

5.3.1 Quantitative Kinetic Model Formulation

There are three primary types of species known to coexist in synthesis solutions of single-walled metal oxide nanotubes, as evinced by multiple studies [1, 33, 60, 66, 162, 164]. These are nanotube-forming precursors (P), amorphous nanoparticles (A), and growing nanotubes (NT). In this thesis, a detailed kinetic model is formulated that governs the nucleation and growth kinetics in nucleating nanotube synthesis solutions

using the P, A, and NT species. It is now established that pre-nucleating aluminosilicate and aluminogermanate nanotube solutions contain curved precursors. These precursors form as soon as the hydrolysis of the starting reactants (e.g. ASB, $AlCl_3$, $Al(ClO_4)_3$, TEOS, TEOG, and/or $GeCl_4$ etc.) takes place in synthesis solutions at room temperature [1, 118]. Clearly, the model does not include the reaction steps leading to formation of these precursors. At the end of the aging step and at the start of the heating step, these precursors are already existing in solution and are ready to react and form nanotubes.

Nanotube synthesis and growth in nucleating solutions is assumed to be a four-step process. Molecular representations of the proposed reaction steps are depicted in Figure 5-1. Nanotube formation and growth involves the following elementary steps:

$$nP \overset{k_1}{\rightarrow} A \overset{k_2}{\rightarrow} NT_i \quad (i = a) \tag{1}$$

$$NT_i + P \overset{k_3}{\rightarrow} NT_{i+1} \quad (i \geq a) \quad i = a, a+1, a+2, \dots, N \tag{2}$$

$$NT_i + NT_j \overset{k_4}{\rightarrow} NT_{i+j} \quad (i, j \geq a) \quad i, j = a, a+1, a+2, \dots, N \tag{3}$$

where $a = n/4.\, n$ denotes the average number of precursors P forming an amorphous nanoparticle A via (1). The number n is a positive integer. At least n = 4 precursors (P) are necessary to form the smallest nanotube ring unit whose length is ~ 1 nm. Thus, the smallest nanotube length formed is assumed to be $(a = n/4)$. The index i denotes the length of nanotubes (e.g. NT_1 represents nanotubes that are 1 nm in length). Here, N is the size of the longest nanotube.

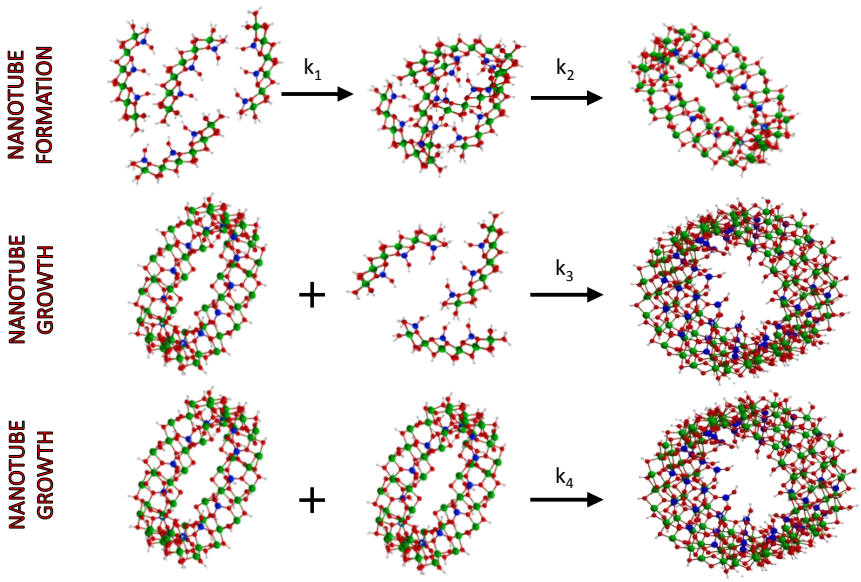

Figure 5-1. Molecular representations of the proposed reaction steps leading to nanotube formation and growth. Nanotube formation is two-step mechanisms occur by the precursor (P) condensation with a rate constant denoted as k_1 and rearrangement of the amorphous particles (A) with a rate constant denoted as k_2. Growth is permitted when rearrangement is complete and it occurs via two mechanisms: *precursor addition* and *edge-to-edge aggregation* with rate constants denoted as k_3 and k_4, respectively.

Upon heating to 95 ˚C, precursors already formed during aging condense to form amorphous nanoparticles in the first step of the reaction (1). k_1 is defined as the condensation ($P \rightarrow A$) rate constant. The size of these amorphous condensates is well known to be 3-6 nm according to DLS, TEM, and SAXS studies [38, 60, 66]. significant amounts of these particles were also observed in early-stage synthesis solutions (e.g., at 8 h of heating). TEM micrographs can be seen in Figure 5-2. The average particle size measured is 3.8±0.6 and 2.9±0.5 nm in AlSiOH and AlGeOH synthesis solutions, respectively. There is no experimental evidence to suggest that these particles directly contribute to nanotube growth such as adding to growing nanotube ends. The particles stay suspended in solution with no signs of aggregation. They are surrounded by charged ligands [2] that possibly prevents aggregation due to electrostatic repulsion. They are

possibly colloidally stable nanoparticles that are capable of transforming into short nanotubes as they tend to disappear at longer reaction times [66].

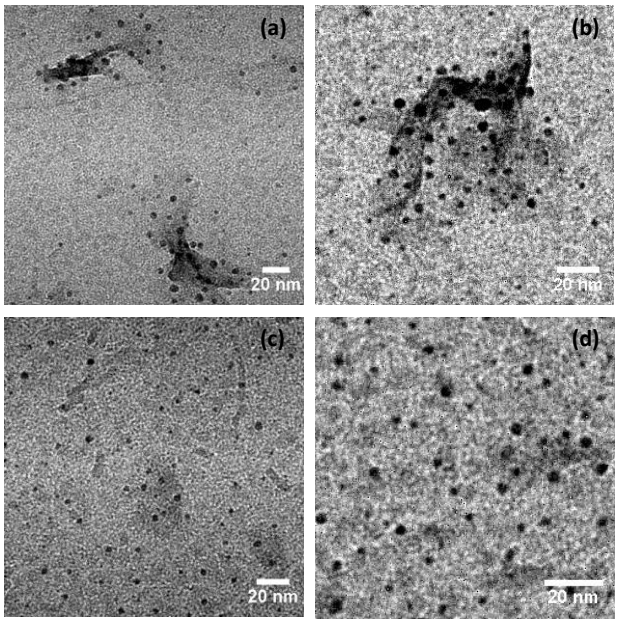

Figure 5-2. Representative TEM micrographs of amorphous nanoparticles (A) in nucleating aluminosilicate (a and b) and aluminogermanate (c) nanotube solutions at as early as 8th reaction hour. Average particle size is 3.8$\pm$0.6 and 2.9$\pm$0.5 nm for AlSiOH and AlGeOH nanotube solutions, respectively.

The formation of the smallest nanotube is treated as the result of two consecutive reactions, i.e., the condensation of precursor species (P) and the subsequent transformation of the condensate (A) to a nanotube nucleus, as depicted in Figure 5-1. The quantity k_2 represents the transformation rate constant for the formation of the smallest nanotube by the rearrangement of nanoparticles ($A \rightarrow NT_i$) via (1).

After irreversible transformation of amorphous particles to small nanotubes with a first order reaction, they continue to grow via mechanisms given in (2) and (3). The rate constant k_3 is defined for nanotube growth through the addition of precursors to the

growing nanotube ends. This mechanism was previously called *nutrient addition* [66], and has been the sole mechanism assumed to govern the growth kinetics of aluminosilicate nanotubes [62, 163]. An additional mechanism, with a rate constant k_4, is added to explain the experimentally obtained population trend. It is called the *oriented attachment* [38] mechanism which assumes that nanotubes increase in length by joining to each other (i.e., end-to-end attachment, which can be considered as a one-dimensional aggregation process). Previously k_4 was assumed to be nanotube length-dependent [$k_4 \sim L^{-\propto}$] [162] based on Brownian collision theory [147]. However, no difference was noticed in the model results upon keeping this parameter constant or defining it in a length-dependent manner. As previously noted, oriented attachment requires not only a collision between two nanotubes but also relative rotation until a thermodynamically favorable end-to-end configuration is achieved [165]. Moreover, random Brownian collisions usually result in branched aggregates [147]. Such branching was not observed in single-walled metal oxide nanotubes.

The rate equations for each of the three species are then written as follows for a batch synthesis reactor:

$$\frac{d[P]}{dt} = -nk_1[P]^m - k_3[P]\,[NT] \tag{4}$$

$$\frac{d[A]}{dt} = k_1[P]^m - k_2[A] \tag{5}$$

$$\frac{d[NT]}{dt} = k_2[A] - k_4[NT]^2 \tag{6}$$

Here, m is the order of the reaction in which the precursors condense to form amorphous particles ($P \rightarrow A$). Since multiple precursors are typically involved in the reaction, the reaction order is not known *a priori*. $[P]$, $[A]$, and $[NT]$ denote the concentrations of precursors, amorphous particles, and nanotubes in synthesis solutions, respectively. A population balance analysis then gives the set of balance equations for the nanotubes at different lengths. The aggregation (k_4) term is described by the Smoluchowski equation [147, 166].

$$\frac{d[NT]_i}{dt} = k_2[A] - k_3[P]NT_i - k_4 NT_i[NT] \quad (i = a) \tag{7}$$

$$\frac{d[NT]_k}{dt} = k_3[P][NT_{k-1} - NT_k] + \frac{1}{2}k_4\left(\sum_{\substack{i=a \\ j=k-i}}^{i=k-1} NT_i NT_j - 2NT_k \sum_{i=a}^{N} NT_i\right) \quad (k > a) \tag{8}$$

The Euler method is used to numerically solve the ordinary differential equations given by (4), (5), (7), and (8), with a step size of 0.01 h. Numerical simulations were performed using MATLAB. The initial concentrations (at $t = 0$) of amorphous particles and nanotubes are zero ($[A_0] = 0$, $[NT]_i = 0$ for $i \in [a, N]$). Typically, N ~ 800 for AlSiOH (~ 40 for AlGeOH) in order to cover all possible nanotube lengths and thereby fully describe the typical nanotube synthesis results. Thus, the population balance model requires the simultaneous solution of about 800 ordinary differential equations for AlSiOH nanotubes synthesis (40 for AlGeOH nanotube synthesis).

Synthesis solutions at $t = 0$ are not a pure suspension of nanotube-forming precursors (P particles). As shown in previous Chapters, smaller monomeric, dimeric $etc.$ units and many aluminates [Al_1, Al_2, or Al_{13}] are also present. Therefore, the starting *reactant* concentrations (e.g. 0.02 M ASB or 0.01 M TEOS) cannot directly represent the initial precursor concentration ($[P_0]$) in solutions, in fact the exact $[P_0]$ is very hard to determine experimentally or theoretically. Thus, $[P_0]$ should be one of the variables in the kinetic model.

5.3.2 Characterization of Nanotube Length Distributions

The dimensional evolution of aluminosilicate and aluminogermanate nanotubes throughout synthesis is studied by transmission electron microscopy (TEM). Over 20 electron micrographs, from different regions of the TEM grid, are recorded at 80K and 100K magnifications for each sample obtained at various times. Representative TEM micrographs of aluminosilicate and aluminogermanate nanotubes are presented in Figures 5-3 and 5-4, respectively. Direct observation of individual nanotubes using TEM has been a major problem because nanotubes tend to aggregate on the grid upon solvent evaporation, forming dense entangled networks [66]. To remove this difficulty, a previous work reported that aqueous dispersions of nanotubes were dried on the TEM grid under a saturated ethanol atmosphere [66]. This time consuming step is eliminated in this thesis, and acidic dispersions of nanotubes are directly used to achieve highly efficient individual dispersion of nanotubes over the grid. Some small AlGeOH nanotube clusters were still detected as seen in Figure 5-4, however, only individually observable nanotubes were used for measurements in this study. The lengths of 500 different

nanotubes are measured from the images collected at each reaction time to obtain a high-quality length distribution. Measurement of nanotube lengths were done with the ImageJ software [112], using its segmented line tool to outline the nanotube contour.

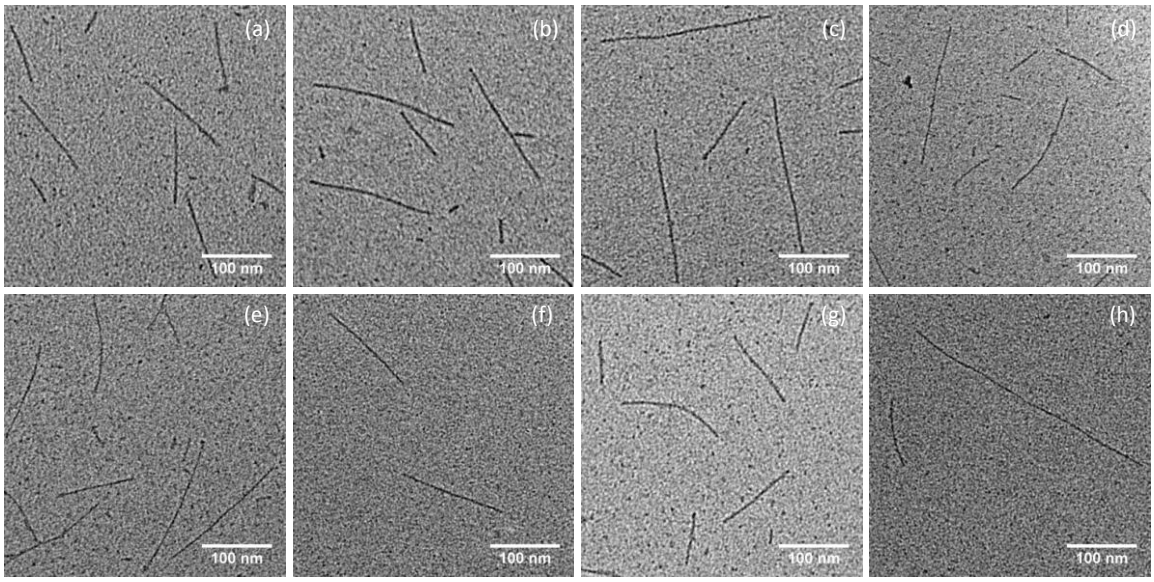

Figure 5-3. Representative transmission electron micrographs of individually dispersed aluminosilicate nanotubes at reaction times of (a) 8 h, (b) 14 h, (c) 30 h, (d) 48 h, (e) 72 h, (f) 85 h, (g) 96 h, and (h) 144 h.

5.3.3 Model Fitting and Validation

The model is parameterized to the extensive experimental data by combining the solution of the population balance equations with a nonlinear least squares fit to minimize residual error between experimental and simulated nanotube length distributions (NLDs) throughout the synthesis. The final values of the rate constants (k_1, k_2, k_3, and k_4), initial precursor concentration ($[P_0]$), order of reaction (m), and the number of precursors in amorphous particles (n) are summarized in Table 5-1.

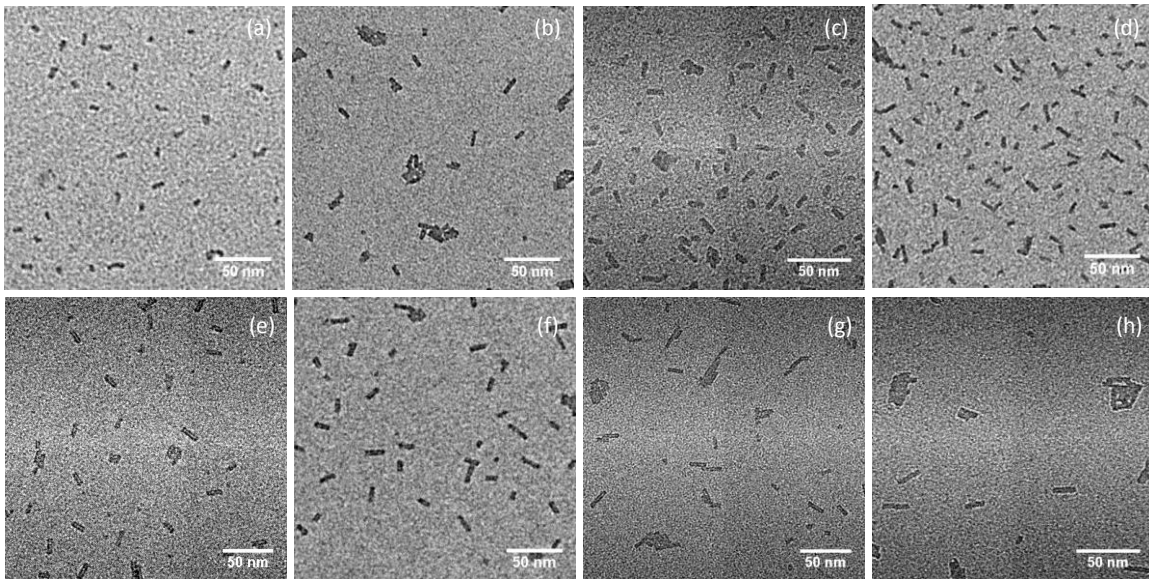

Figure 5-4. Representative transmission electron micrographs of individually dispersed aluminogermanate nanotubes at reaction time of (a) 8 h, (b) 14 h, (c) 30 h, (d) 48 h, (e) 72 h, (f) 85 h, (g) 96 h, and (h) 144 h.

Table 5-1: Summary of kinetic model fit parameters.

Reaction Constants	**AlSiOH NT Synthesis**	**AlGeOH NT Synthesis**
$k_1(M^{-m}s^{-1})$	1.4×10^{7}	9.7
$k_2(s^{-1})$	2.2×10^{-4}	2.7×10^{-4}
$k_3(M^{-1}s^{-1})$	2.8×10^{2}	13.8
$k_4(M^{-1}s^{-1})$	19.4	0.4
n	80	20
m	3.9	2.5
$P_0\ (M)$	8.0×10^{-5}	1×10^{-4}

The normalized experimental and simulated NLDs are given in Figures 5-5 and 5-6 for aluminosilicate and aluminogermanate nanotubes, respectively. As seen from the Figures, the proposed model fully captures all the features of the NLDs and the parameterization results in excellent agreement of the model with data collected from TEM experiments.

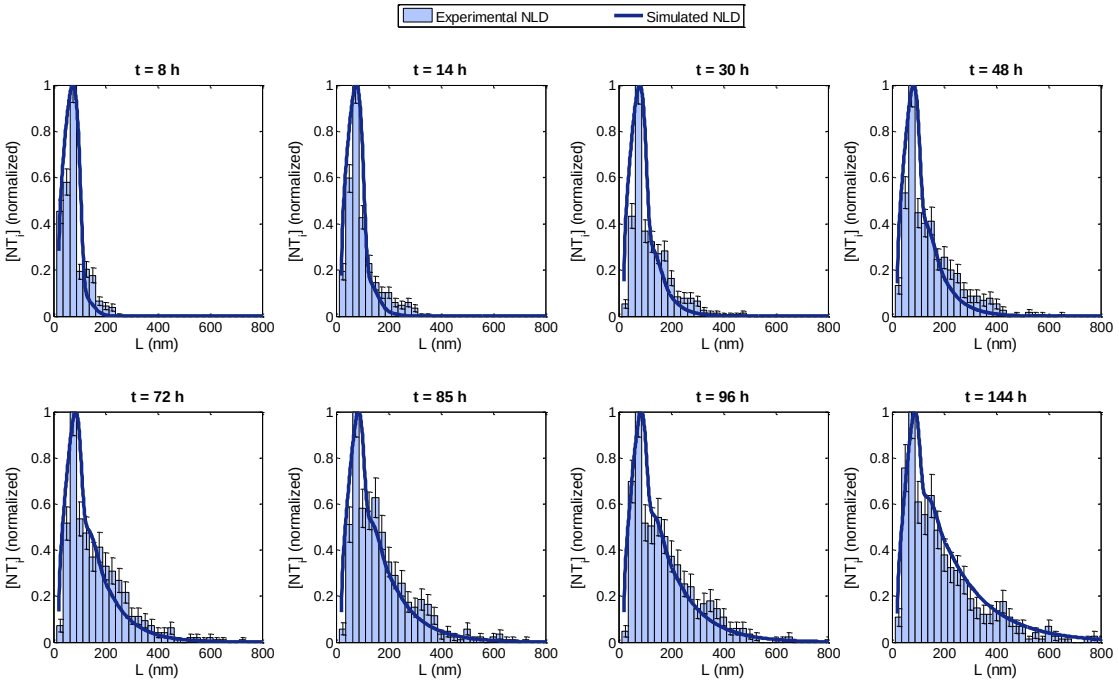

Figure 5-5. Normalized aluminosilicate nanotube length distributions (NLD) at defined reaction times (light-colored) with Poisson counting errors and fits of the proposed kinetic model (dark-colored line). Histogram bin size is 25 nm.

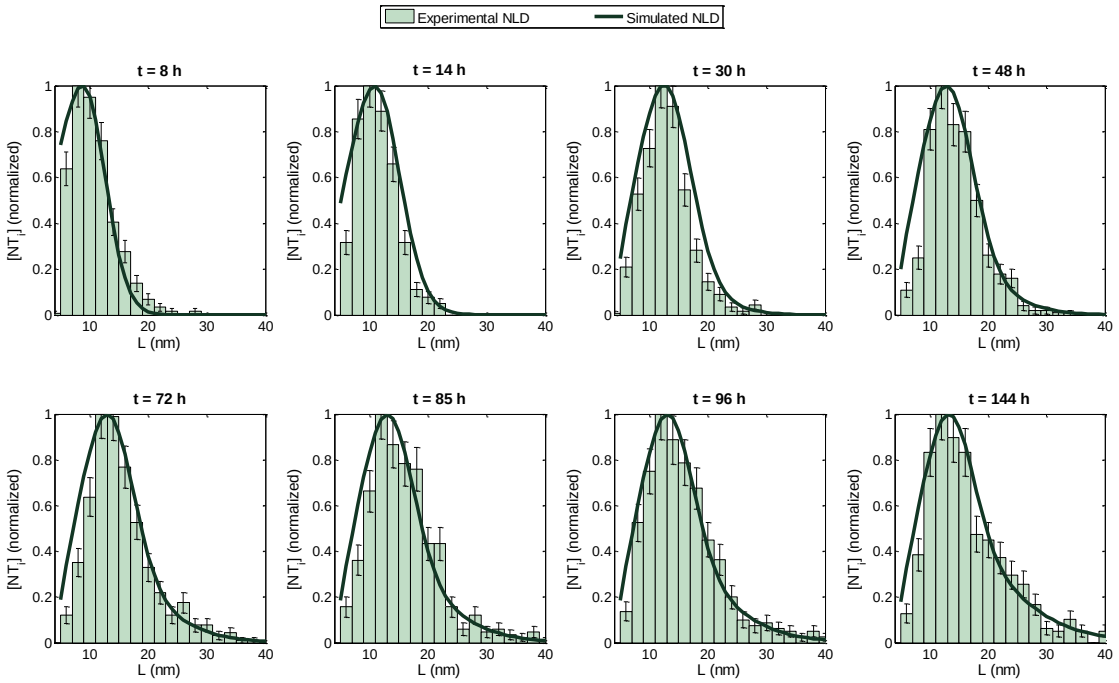

Figure 5-6. Normalized aluminogermanate nanotube length distributions (NLD) at defined reaction times (light-colored) with Poisson counting errors and fits of the proposed kinetic model (dark-colored line). Histogram bin size is 2 nm.

Average residual error values are ~10% and ~15% for aluminosilicate and aluminogermanate NLDs respectively. Slightly larger error values observed for aluminogermanate nanotube might be due to coexistence of single-walled and double-walled nanotubes. A recent study suggests that double-walled AlGeOH nanotubes may form in such reaction solutions and with different reaction growth kinetics compared to their single-walled analogues [162]. Double-walled nanotube populations could not be distinguished in this work. Therefore, although the proposed model was able to capture the general trend of experimentally observed NLDs, further studies (such as high-resolution cryo-TEM tracking) can be performed to discriminate between single-walled and double-walled nanotube populations [162] and model their formation kinetics in more detail.

The NLDs become broader as a function of reaction time as seen in Figures 5-5 and 5-6. Figure 5-5 shows that the maximum AlSiOH nanotube length observed at 8 h heated synthesis solutions is nearly 300 nm whereas it is up to 800 nm in the final reaction hours. The minimum nanotube length observed, on the other hand, remains around 20 nm throughout the reaction. Shorter nanotubes were never observed in the measurements, even though such objects are well within the resolution of the TEM imaging. This clearly suggests that the minimum AlSiOH nanotube length that can form by the rearrangement of amorphous particles is ~20 nm. To form a 20 nm length nanotube, ~ 10^2 precursors are needed. In fact, the best-fit *n* value from the model fitting is 80 for AlSiOH nanotubes as seen in Table 5-1. Therefore, one might not need to use *n* as one of the fitting parameters and can directly determine it from the value of minimum nanotube length observed. The minimum nanotube length observed in AlGeOH solutions

is about 5 nm throughout the synthesis. In this case, the best-fit *n* value is 20. This number is very well consistent with the number of precursors required to form a 5 nm nanotube. TEM image analysis shows that the amorphous particle size in AlSiOH synthesis solutions is approximately 1 nm larger than that of observed in AlGeOH solutions as seen in Figure 5-2. These results also suggest the importance of initial amorphous particle size in determining the minimum tube lengths in synthesis solutions. Thus, further studies should include the determination of the dependency of kinetic parameters to particle size and investigation of the reaction conditions that are effective in determining the condensed particle size. Especially, understanding and modeling of the factors controlling the precursor size and condensed particle size can allow us to explain the formation of different metal oxide morphologies such as allophanes, which are single-walled nanospheres of ~4 nm diameter [167] that form in alkaline solutions (e.g., this can be achieved by correlating solution pH with condensation rate constant).

To elucidate the role of aggregation phenomena, k_4 was set to 0 meanwhile keeping all other reaction parameters identical to their best-fit values. The resulting distributions are shown in Figure 5-7 and 5-8. When $k_4 = 0$, narrow nanotube length distributions are obtained throughout the synthesis. The mean length would stay almost constant after 8 h of the synthesis if oriented aggregation (OA) was not an effective mechanism. Therefore, nanotube-nanotube attachment/aggregation is responsible for the observed increase in polydisperity as a function of reaction time. At early stages of the growth, the dominant mechanism is precursor addition (PA), while OA has nearly no effect on nanotube populations. It is possible that nanotubes mainly grow by precursor

addition during the early stages of synthesis till a large fraction of the precursors are consumed. Then, OA becomes an important growth mechanism.

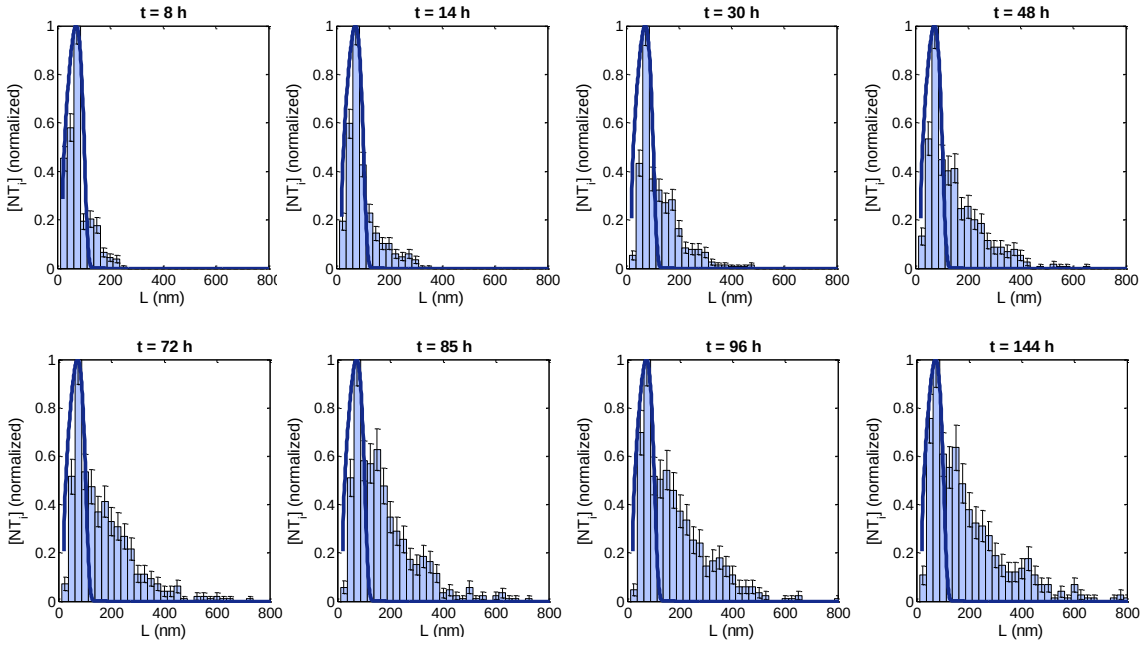

Figure 5-7. Normalized aluminosilicate nanotube length distributions (NLD) at defined reaction times (light-colored) with Poisson counting errors and fits of the proposed kinetic model when $k_4 = 0$ (dark-colored line).

Changes in the concentration of each species type ($P, A,$ and NT) obtained based on the kinetic model are shown in Figure 5-9. Precursors are consumed within the first day of synthesis, both due to formation of the amorphous particles as well as addition to the growing tube ends. Furthermore, the concentration of amorphous particles reaches a maximum within the first hour of reaction. The resulting nanotube concentrations are higher for AlGeOH nanotubes compared to AlSiOH nanotubes, clearly due to the higher starting precursor concentration $[P_0]$ values of AlGeOH system (see Table 5-1). However, the maximum nanotube concentration is achieved within the first day of synthesis and thereafter slightly but continuously decreases due to the OA mechanism.

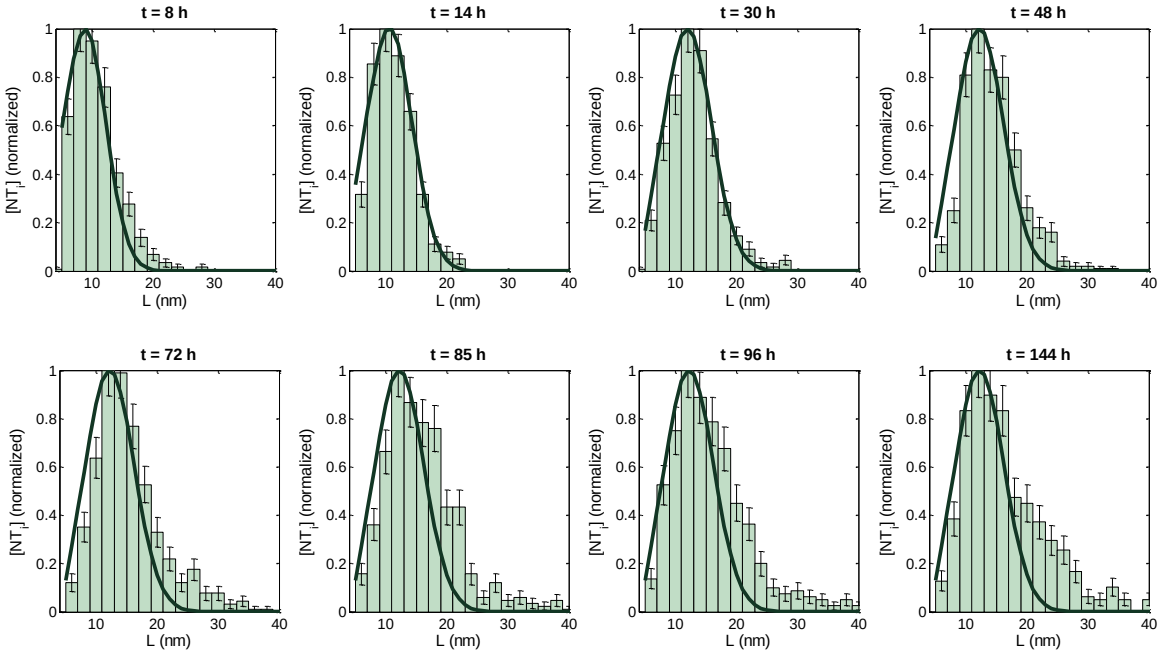

Figure 5-8. Normalized aluminogermanate nanotube length distributions (NLD) at defined reaction times (light-colored) with Poisson counting errors and fits of the proposed kinetic model when $k_4 = 0$ (dark-colored line).

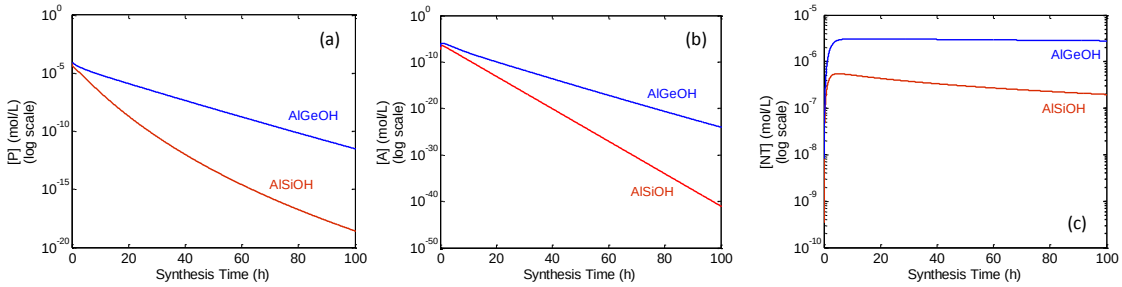

Figure 5-9. Changes in $P, A,$ and NT concentrations as a function of synthesis time based on the proposed kinetic model.

It should be noted that, in detail, many combinations of chemical entities and reaction steps were examined; such as direct transformation of precursors to nanotubes without intermediate formation of amorphous particles, or the absence of the OA mechanism, or the absence of the PA mechanism. The other proposed growth mechanism of oriented rotation (OR) was also modeled and studied. However, the model presently

discussed is the only one that properly captured all the features of the time-dependent length distributions. The model has 4 rate constants (k_1, k_2, k_3, and k_4) as listed in Table 5-1. It is found that in aluminosilicate and aluminogermanate nanotube synthesis, $k_1 \gg k_2$, i.e. precursor condensation reactions are much faster than rearrangement processes taking place upon heating reaction solutions. In fact, $k_2 \ll k_1, k_3, k_4$ suggesting that rearrangement process is the rate-limiting step.

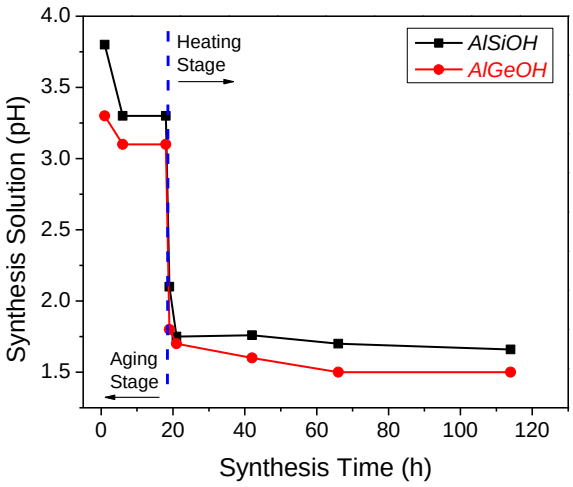

Figure 5-10. Change in pH as a function of synthesis time in AlSiOH and AlGeOH nanotube synthesis solutions.

The largest differences between AlSiOH and AlGeOH nanotube systems are seen to be the values of the condensation rate constant (k_1) and of n. The k_1 value of AlSiOH nanotube synthesis is six orders of magnitude higher than that of AlGeOH. Also, the number of precursors involved in formation of amorphous condensates is four times higher in AlSiOH nanotube solutions. Moreover, the kinetic parameters representing growth processes (k_3 and k_4) show that the AlGeOH nanotubes grow at a slower rate (about 1 order of magnitude slower than AlSiOH). As discussed in detail in Chapter 4,

TEOG hydrolysis much faster [133, 134] than TEOS, thereby allowing efficient complexation of Al and Ge species and hence increasing the number of nanotube precursors in aging solutions, or amorphous nanoparticles (A) in nucleating AlGeOH nanotube solutions compared to AlSiOH (as evident from Figure 5-9). This is also supported by pH measurements of the two systems throughout the synthesis, as seen in Figure 5-10. The pH trends of the two systems are slightly different, especially during the aging stage. An hour after the addition of reactants, the pH of the AlSiOH system is 3.7 where as it is 3.3 in AlGeOH. At the end of aging (18 h), the solution pHs are 3.3 and 3.1 respectively. The larger pH drop during the aging process in AlSiOH system could be due to the equilibrium established between many different type of species including small, medium-sized, and larger AlSiOH complexes $(9-11)$ [1]. Meanwhile, equilibrium is established within between small and medium species in AlGeOH system as there are no large complexes (e.g., Keggin):

$$2[Al_2SiO_2(OH)_5(H_2O)]^+ \leftrightarrow [Al_4Si_2O_4(OH)_{11}(H_2O)]^{2+} + [H]^+ \quad (9)$$

$$3[Al_4SiO_3(OH)_8(H_2O)(ClO_4)]^+ \leftrightarrow [Al_{12}Si_3O_9(OH)_{26}(H_2O)(ClO_4)_2]^{2+} + 2[H]^+ + ClO_4^- \quad (10)$$

$$[Al_{12}Si_4O_{10}(OH)_{28}(H_2O)_8(ClO_4)_2]^{2+} + [Al(ClO_4)_4]$$
$$\leftrightarrow [Al_{13}Si_4O_{16}(OH)_{18}(H_2O)_5(ClO_4)_3]^{2+} + 2[H]^+ + ClO_4^- + 7H_2O \quad (11)$$

It is very crucial to understand that larger AlSiOH complexes (e.g., $Al_{13}Si$) do not directly take part in nanotube formation upon condensation. However, within the first 7 h of heating, the large complexes redissolve or rearrange to supply additional precursors to

growing nanotubes. This can explain the faster growth kinetics in the AlSiOH system. Such complex reaction steps are not included in the presented model, but might be necessary for a more refined understanding of nanotube growth. Therefore, the P_o value for AlSiOH system might be slightly overestimated.

5.3.4 Model Predictions

From Figures 5-7 and 5-8, it is clearly observed that the model can explain the experimental length distributions quite well with $\sim 10-15\%$ average residual error. Next, the predictive capability of the model was tested by comparing its predictions to experimental data obtained for another synthesis condition. Specifically, the starting concentrations of reactants (ASB, TEOS, and TEOG) in aluminosilicate and aluminogermanate nanotube synthesis solutions are changed by ±50%. Since the nanotube synthesis solutions are dilute and are far below the thermodynamic solubility of Al, Si, and Ge species, a change in the reactant concentration is expected to result in a corresponding linear (~50%) change in the initial precursor concentrations (P_0). Representative TEM micrographs of obtained nanotubes at 96 h of synthesis are given in Figures 5-11 and 5-12. Simulations were performed to determine if the model can capture the essential features of evolving experimental NLDs at different P_o values. All model parameters (m, n, k_1, k_2, k_3, and k_4) determined in Table 5-1 are kept constant, and only the initial precursor concentration ($[P_0]$) is increased or decreased by 50 percent. Figures 5-13 and 5-14 compare the simulation results (at $0.5P_0$ and $1.5P_0$ initial precursor concentrations) to experimental NLDs obtained for aluminosilicate and

aluminogermanate nanotubes at 14 h and 96 h of the synthesis. The model is in remarkable agreement with experimental data.

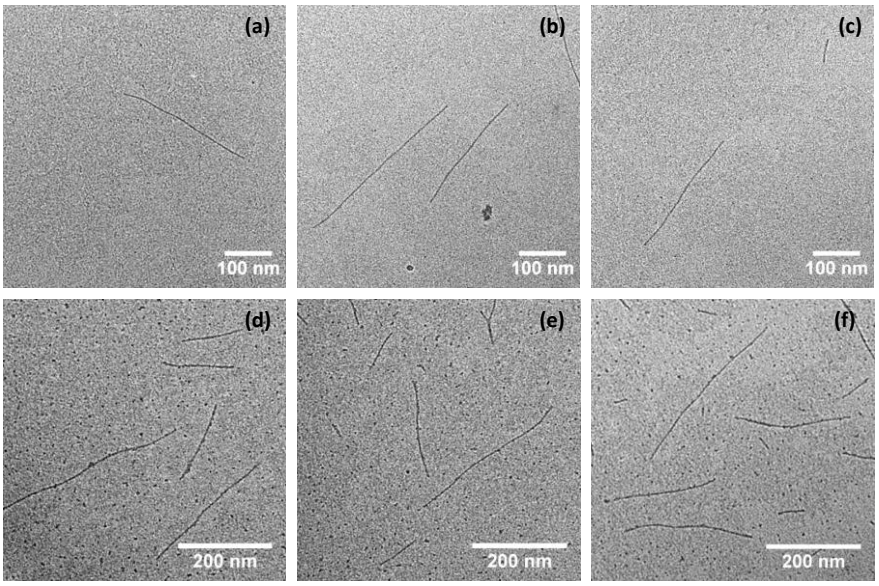

Figure 5-11. Representative TEM micrographs of aluminosilicate nanotubes synthesized from 0.05 M Al (a, b, and c) and 0.15 M Al (d, e, and f) collected at 96 h of reaction.

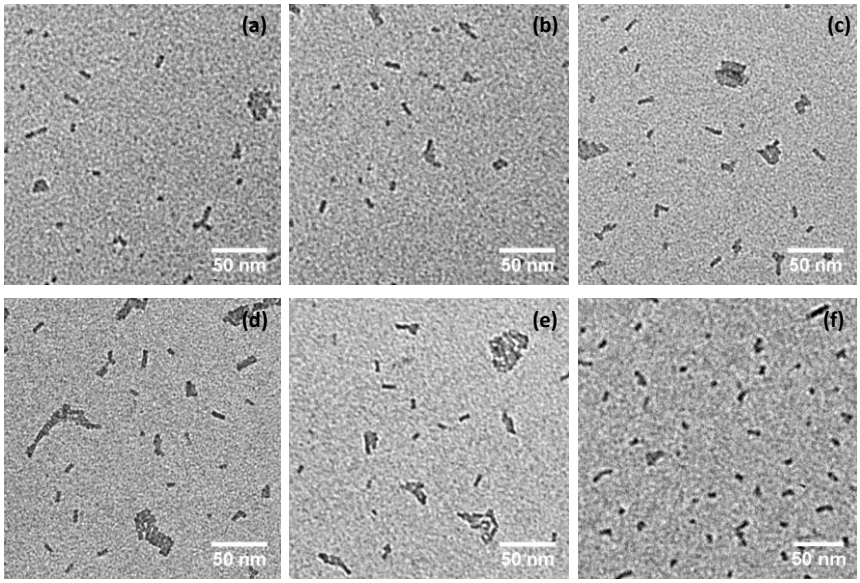

Figure 5-12. Representative TEM micrographs of aluminogermanate nanotubes synthesized from 0.05 M Al (a, b, and c) and 0.15 M Al (d, e, and f) collected at 96 h of reaction.

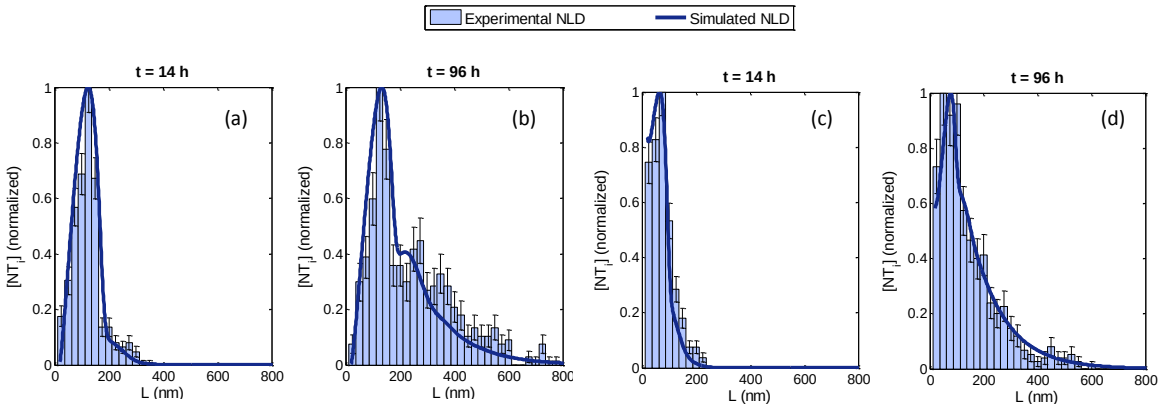

Figure 5-13. Comparisons of experimental aluminosilicate nanotube length distributions (NLDs) to simulated NLDs generated from fixed kinetic model parameters but different precursor concentrations: (a, b) $0.5P_0$, and (c, d) $1.5P_0$ at reaction times of 14 and 96 h.

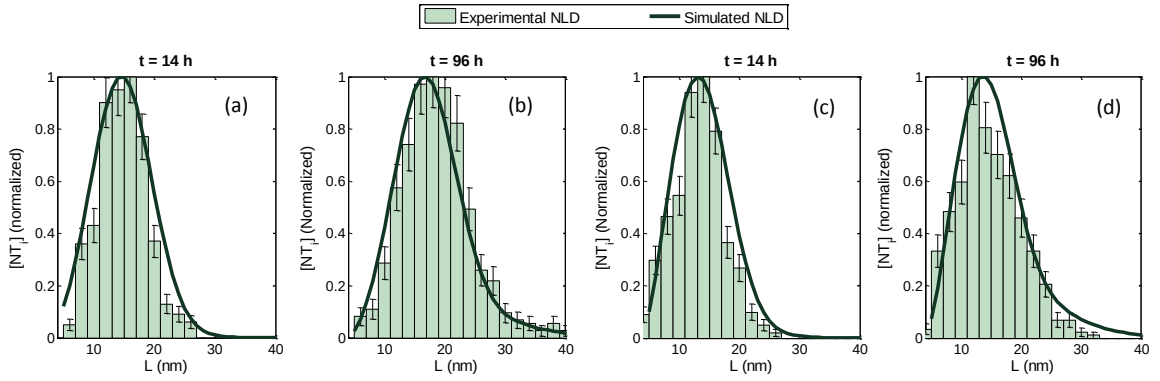

Figure 5-14. Comparisons of experimental aluminogermanate nanotube length distributions (NLDs) to simulated NLDs generated from fixed kinetic model parameters but different precursor concentrations: (a, b) $0.5P_0$, and (c, d) $1.5P_0$ at reaction times of 14 and 96 h.

Figure 5-15 shows that the average nanotube length (i.e., the mean value of the NLD) is very well predicted by the model at all three precursor concentrations. It is seen that the mean nanotube length is highly dependent on the precursor concentrations. It increases as the precursor concentration is decreased, and decreases when the precursor concentration is increased. The main reason for observed increase in nanotube length upon decrease in precursor concentration is the decrease in the number of amorphous

nanoparticles through reaction (1). This, in turn, leads to the formation of fewer nanotube nuclei, and hence the growth of fewer nanotubes to larger lengths. The final nanotube concentration/yield, on the other hand, decreases with decreasing precursor concentrations as shown in Figure 5-16. This result is also qualitatively seen in the TEM micrographs shown in Figure 5-11 and 5-12.

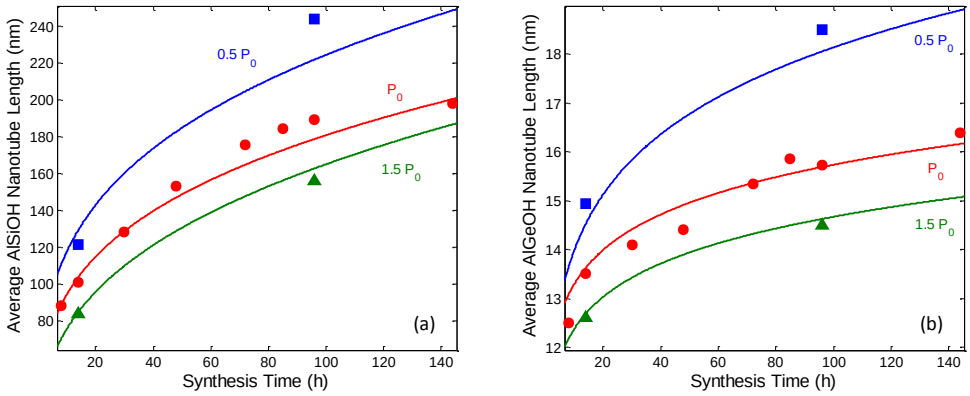

Figure 5-15. Comparison between experiments (symbols) and model predictions (curves) of the mean length of (a) aluminosilicate nanotubes, and (b) aluminogermanate nanotubes as a function of synthesis time and P_0.

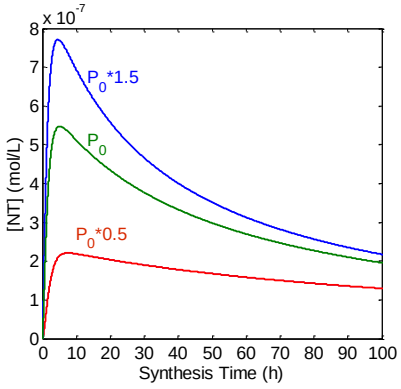

Figure 5-16. Change in concentration of aluminosilicate nanotubes as a function of P_0 and synthesis time.

In summary, the control of nanotube lengths through precursor concentrations at constant temperature, emerges as a predictable method for controlling nanotube lengths. Other hydrothermal synthesis parameters that can be controlled include the synthesis temperature (which would have a large effect on the rate constants).

CHAPTER 6

DEFECT STRUCTURES IN ALUMINOSILICATE SINGLE-WALLED NANOTUBES: A SOLID-STATE NUCLEAR MAGNETIC RESONANCE INVESTIGATION

6.1 Introduction

The model of the 'perfect' structure of the AlSiOH nanotube has been built up over the years *via* a combination of multiple techniques as depicted in Figure 1-2 [30, 168]. Although this structure is an accurate overall model of the nanotube material, several structural aspects remain to be fully understood and are critical to the surface properties and chemical reactivity of the nanotube, e.g., the location and dynamics of the protons on the inner and outer surfaces, and the types of structural defects existing in the nanotube [107]. So far, ^{29}Si and ^{27}Al MAS NMR (e.g., Figures 6-1a and 1b) [1, 81, 121] have been used to reveal the coordination environments of aluminum and silicon atoms. Only two ^{29}Si NMR chemical shifts have been discussed. The first is a sharp resonance at -80 ppm, and is conclusively ascribed to Q^3(6Al) coordination [109] of a silanol group connected to six Al wall atoms through bridging O atoms (Figure 6-1b). The second is a broad resonance at -90 ppm that extends up to -110 ppm, representing a small but significant fraction ($\sim$20% of total Si) of less ordered silicon environments. In one study, it has been speculated to originate from a more polymerized phase containing silicate or aluminosilicate units [121].

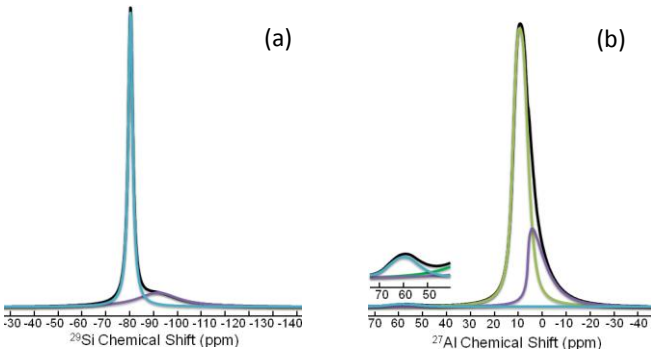

Figure 6-1. (a) 1D ^{29}Si CP MAS spectrum, and (b) 1D ^{27}Al MAS NMR spectrum of a purified nanotube sample [1].

This disordered phase was also assumed to be the source of a weak Al(IV) peak near 60 ppm [121] (Figure 6–1b and inset), which occurs in addition to the sharp peak at ~6 ppm from octahedrally coordinated Al(VI) in the nanotube wall (Figure 6–1b). The disordered phase was interpreted to contain Q^4 silicate tetrahedra, each connected to fewer than 3 Al atoms [Si(nAl), n<3], with the Al atoms also being in tetrahedral coordination [62, 121]. However, such a disordered phase has never been observed as an impurity phase in extensive TEM and cryo-EM imaging of the nanotubes [2, 66, 109]. In fact, more recently, Al(IV) has been proposed to exist as a part of the SWNT structure, either bound to the Al(VI) outer wall or substituting Si(IV) tetrahedral on the inner wall [129]. Other evidence also suggests that the aforementioned resonances [0 ppm and 60 ppm ^{27}Al, −90 ppm ^{29}Si] originate from the nanotube structure itself. For example, the terminal groups of the SWNTs could consist of relatively disordered Si and Al environments, and make up 2% of the Si and the Al atoms in a nanotube sample of ~100 nm average length. Secondly, the SWNTs form by rearrangement of a number of nanoscale precursors such that the complete absence of defects would be unexpected [1]. Thirdly, as mentioned earlier, cryo-EM studies show no impurity phases but only pure

nanotube products [109]. Finally, Si and Al species represented by similar chemical shifts are also observed in allophanes (single-walled aluminosilicate nanoshells of ~4 nm in diameter), and are modeled as being part of the nanoshell structure [169]. In view of all the above reasons, it is clear that the minority Si and Al species are indeed part of the SWNT structure and can be considered as defect sites existing in the mostly perfect SWNT structure.

In a defect-free nanotubes from which adsorbed water molecules have been evacuated, only two proton environments are identified: bridging outer surface hydroxyls (Al−*OH*−Al) and inner-wall silanols (Si−*OH*) (Figures 1-2). In this chapter of the thesis, the primary hypothesis is that the dynamics of protons near the defect structures can be used to interpret the local structure of the defect sites by means of advanced NMR techniques. In particular, high-resolution 1D ^{1}H MAS and ^{1}H CRAMPS NMR experiments can be used to obtain information about different hydroxyl groups present in the aluminosilicate SWNTs. To assign more precise structural locations to the ^{1}H signals, the hydroxyl groups were further distinguished on the basis of their heteronuclear coupling with ^{27}Al or ^{29}Si nuclei by means of 2D FSLG HETCOR NMR. ^{1}H→^{29}Si CP/MAS NMR experiments were used to distinguish Si signals that are coupled with protons. To elucidate the role of surface protons in the formation of nanotubes, the evolution of proton environments around Al and Si throughout the synthesis were also studied by correlation NMR studies. Overall, this chapter presents an updated model of the structure of the aluminosilicate SWNTs with a clearer understanding of its defect structures.

6.2 Experimental Details

The synthesis of aluminosilicate SWNTs was carrried out as described in previous Chapters [1]. Aluminosilicate nanotubes were synthesized from an aqueous solution of 0.1 M aluminium sec-butoxide and 0.05 M tetraethyoxysilane, with 0.05 M $HClO_4$ being used as the acid medium. The solution was aged at room temperature for 18 h, and the system evolved to an aluminosilicate colloid with a local structure close to that of the nanotube. Upon heating to 95 ˚C, nanotubes continuously form and grow by mechanisms elucidated in Chapter 5 [1, 33]. After 96 hours of heating, the obtained nanotube gel was dialyzed against DI water with a 15 kDa membrane to obtain a purified nanotube dispersion. Freeze-drying preserves the molecular structure of species in solution [170]. NMR experiments were performed on freeze-dried materials sampled from the reactor at various stages of the nanotube synthesis, and also on freeze-dried nanotube dispersions after dialysis. Dehydration of a pure freeze-dried nanotube sample was carried out in a Schlenk line at 250 ˚C for 24 h under vacuum. Samples were then transferred to zirconia rotors under a nitrogen atmosphere in a glove box, and sealed with an O-ring cap prior to NMR measurements.

All NMR spectra were collected at room temperature on a Bruker AV3-400 spectrometer operating at 400 MHz for ^{1}H and with a 10 kHz spinning frequency. The ^{27}Al chemical shifts are with respect to aluminum nitrate, whereas the ^{29}Si and ^{1}H chemical shifts are with respect to 3-(trimethylsilyl)-1-propanesulfonic acid sodium salt. $^{1}H \rightarrow {}^{29}Si$ CP/MAS NMR experiments were performed with a 5 s repetition rate, 1024 scans, and varying contact times. ^{1}H CRAMPS spectra were recorded using a windowed

Phase-Modulated Lee-Goldburg (wPMLG) pulse sequence with 2.8-μs $\pi/2$ pulses. ^{1}H CRAMPS spectra were calibrated using glycine. ^{1}H MAS NMR spectra were collected using single-pulse experiments with a 3-μs $\pi/2$ pulse, a 2-s repetition time, and 16 scans. Two-dimensional HETCOR (HETeronuclear CORrelation) experiments were initially hindered by ^{1}H-^{1}H dipolar coupling, which causes line-broadening in the ^{1}H spectra. Therefore, Frequency-Switched Lee-Goldburg (FSLG) decoupling was incorporated into the HETCOR sequence [171]. This pulse sequence is based on cross-polarization from one nucleus to another [172] and was adapted from the literature [173]. The ^{1}H $\rightarrow$^{29}Si experiments were recorded with a ramped-amplitude CP sequence using a contact time of 2 ms; 128 scans were collected. Spectra were acquired with 64 t_1 increments of 63 μs, a ^{1}H $\pi/2$ pulse of 3 μs, a dwell time of 20 μs and a recycle delay of 5 s. ^{1}H$\rightarrow$^{27}Al FSLG HETCOR experiments were performed with a ^{1}H $\pi/2$ pulse of 3 μs, a 200-μs contact time, and a 4-s ms repetition rate. A set of 64 free induction decays was obtained with a t_1 increment of 63 μs, States-TPPI (time proportional phase incrementation) phase cycling, [174] and a dwell time of 12 μs. The protons were decoupled from the nuclei of interest using a TPPM proton decoupling [175] [two pulse phase modulation] scheme.

6.3 Results and Discussion

First, ^{1}H$\rightarrow$^{29}Si FSLG-HETCOR and 2D ^{1}H$\rightarrow$^{27}Al experiments were performed to track the evolution of proton groups surrounding Al and Si species throughout the nanotube synthesis, and to identify Al-correlated or Si-correlated ^{1}H chemical shifts in the final nanotube structure. ^{29}Si NMR cross polarization contact time experiments were

also simultaneously carried out to identify previously unresolved Si chemical shifts in the nanotubes.

6.3.1 ^{1}H-^{29}Si FSLG-HETCOR and ^{29}Si CP NMR Experiments

A number of ^{1}H-^{29}Si FSLG-HETCOR correlation spectra collected at various stages of the synthesis are shown in Figures 6-2a−6-2d. Through the precursor solution aging step, Q^3(6Al) Si−OH are the main species seen in nanotube synthesis solutions [1]; however, the 2D spectra allow the identification of a wide range of relatively low-concentration Si environments as signified by signal in the range of *ca*. −80 to −106 ppm. On the other hand, there is only one proton resonance at *ca.* 10 ppm around all the Si environments indicating a single proton pool [such as Si-***OH***$\cdots OH_2$]. During the aging step at 25 ˚C, it was previously shown by ESI mass spectroscopy [1] that smaller aluminosilicate species evolve into proto-nanotube precursors ($Al_{8\text{-}12}Si_{1\text{-}2}$). At this stage, hydroxyl groups surrounding (Si-***OH***$\cdots OH_2$) species are progressively replaced by Al atoms through oxygen bridges (Al-O-Si) [1, 176]. This significantly changes the proton environment as aging progresses from 1 h to 18 h (Figures 6-2a, 6-2b). The ^{1}H chemical shift moves from 10 ppm to 8 ppm. After aging is complete, the chemical shift of protons surrounding Si atoms remains at *ca.* 8 ppm throughout the nanotube formation and growth. This indicates, in agreement with the previous investigations in this thesis by other techniques [1], that short-range ordering around Si atoms in nanotube precursors has taken place and that all precursors necessary for nanotube formation have already assembled during aging.

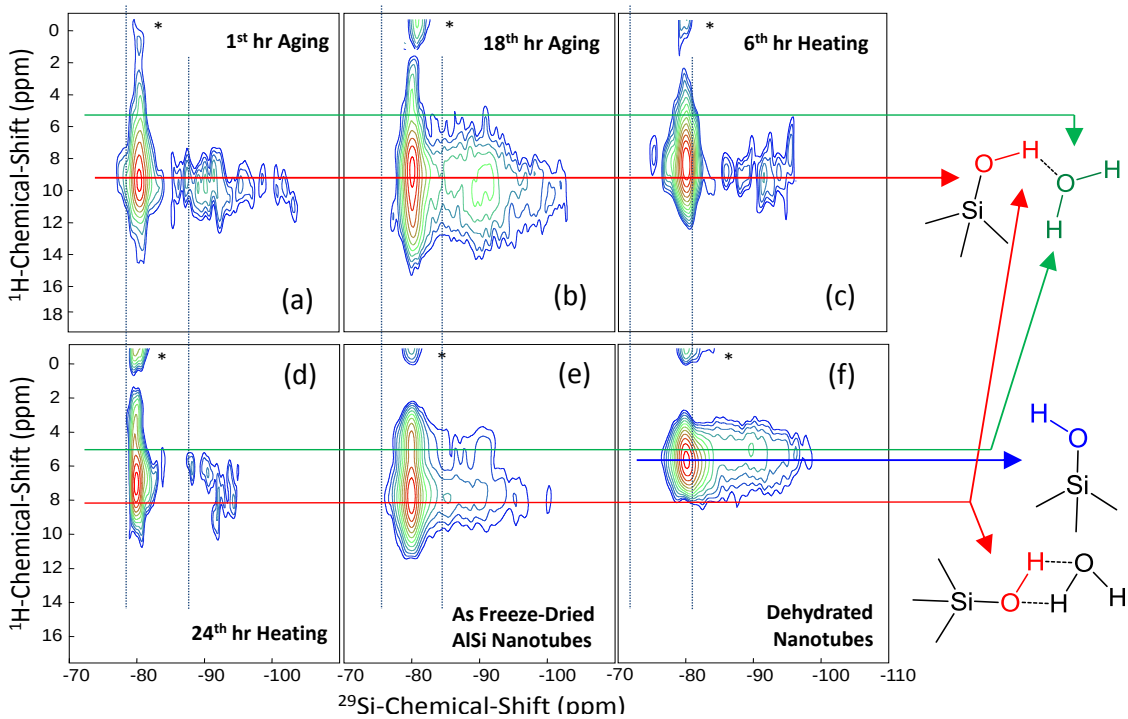

Figure 6-2. 2D ^{1}H-^{29}Si FSLG-HETCOR spectra of (a−d) freeze-dried samples collected at various times during nanotube synthesis, (e) freeze-dried nanotubes after purification by dialysis, and (f) nanotubes dehydrated *in vacuo* at 250 ˚C. Contact time is 2500 μs in all experiments. (*) indicates center spin-lock frequency.

As mentioned in the Introduction, it has been previously proposed that the broad ^{29}Si resonance could belong to polymerized Q^4 silicate or aluminosilicate environments [121], in which case the second coordination sphere of Si is occupied by Al or Si atoms, and not by −OH groups [62, 81, 121]. On the other hand, Figures 6-2a−6-2f show strong proton correlations with Si in the species represented by the broad peak centered around -90 ppm in ^{29}Si MAS spectra. This indicates the existence of −OH groups in the second coordination sphere of Si (i.e., Q^3 or Q^2 Si species) or structures that are more open than a polymerized unit, thereby allowing binding of water protons and resulting in the observed proton correlations. It should be noted again that the ^{1}H chemical resonance of the broad signals are exactly the same as the ^{1}H chemical resonance of the nanotube structural

configuration (Si-**O*H***$\cdots OH_2$) as depicted by red lines and arrows in Figure 6-2. After 18 hours of aging, the initial range of Si environments (*ca.* −86 to −106 ppm) converges into a sharper Si environment represented by a −90 ppm chemical shift (Figure 6-2b). Upon heating, the species represented by this ^{29}Si chemical shift are less exposed to solvent water molecules due to the condensation and rearrangement of the aluminosilicate precursors. As the synthesis progresses by assembly and ordering of the precursors, most of these species transform into ordered Q^3(6Al) Si-OH species at −80 ppm (Figures 6-2c−6-2d); however, a small number of 'defect' species are preserved in the final nanotube structure (Figures 6-2e−6-2f). In hydrated nanotubes (Figure 6-2e), two different proton environments were identified (*ca.* 5 ppm and 8 ppm), both of which belong to Q^3(6Al) Si-OH units (at −80 ppm). The resonance at *ca.* 8 ppm is assigned to silanol units that are hydrogen bonded to water oxygens (Si-**O*H***$\cdots OH_2$) as depicted on the right-hand side of Figure 6-2, whereas the ^{1}H resonance near 5 ppm represents the molecular water hydrogen-bonded to silanol groups (Si-OH$\cdots$***O*H*$_2$**). Previous multilayer adsorption simulations also showed that water molecules immobilized on the nanotube inner wall can form water layers by hydrogen bonding [41]. Moreover, Figure 6-2e indicates that the Si-***OH***$\cdots OH_2$ species is also found at a variety of different Si environments represented by *ca.* −90 ppm ^{29}Si NMR resonances that are different from the dominant Q^3(6Al) configurations. Molecular water is also bound to defect areas in nanotube as indicated by the red line in Figure 6-2e. Dehydration of the nanotubes at 250 ˚C under vacuum completely removes adsorbed water molecules and isolates the Si-OH structures that are at various Si chemical shifts including defects. The ^{1}H resonance belonging to Si-OH environments is present at 6 ppm (Figure 6-2f). For a successful

modification of interior nanotube walls, it was shown that adsorbed water molecules should be removed completely by an appropriate heat treatment condition [41]. Presented NMR study also confirms that heat treatment at 250 ˚C completely removes the water molecules while preserving the nanotube structure [41, 109].

As discussed before, the ^{29}Si NMR spectra of aluminosilicate nanotubes exhibit resonances from about −80 to −110 ppm. This indicates the presence of disordered ^{29}Si environments in addition to the perfectly ordered configuration [81]. In fact, 2D ^{1}H-^{29}Si FSLG-HETCOR studies indicates the existence of species with various ^{29}Si chemical shifts that appear in the ~ −80 to −110 ppm region. The grouping of Si atoms with hydroxyl groups (−OH) can be facilitated by the use of ^{1}H→^{29}Si cross-polarization (CP) between protons and silicon atoms that are within the van der Waals contact distance (0.33 nm) [170]. The application of CP enhances selectively the Si signals of atoms that are coupled with protons by internuclear ^{1}H→^{29}Si dipole interactions. ^{29}Si CP NMR contact-time experiments (*cf.* Figure 6-3) were carried out to clarify the dominant silicon species that are coupled with protons represented by the broad −90 ppm resonance and to identify the chemical shifts of unresolved silicon species under this broad peak. Each spectrum was deconvoluted with a minimum necessary number of Lorentzian peaks (also see magnified insets). CP experiments show that the number of detectable peaks depends on the contact time. There are five Si environments (at −80.4, −86.6, −92.1, −100, and −105.5 ppm) detected at a short contact time of 1 ms (Figure 6-3a), of which only three (at −80.4, −86.6, and −92.1 ppm) are seen at a higher contact time of 15 ms (Figure 6-3b).

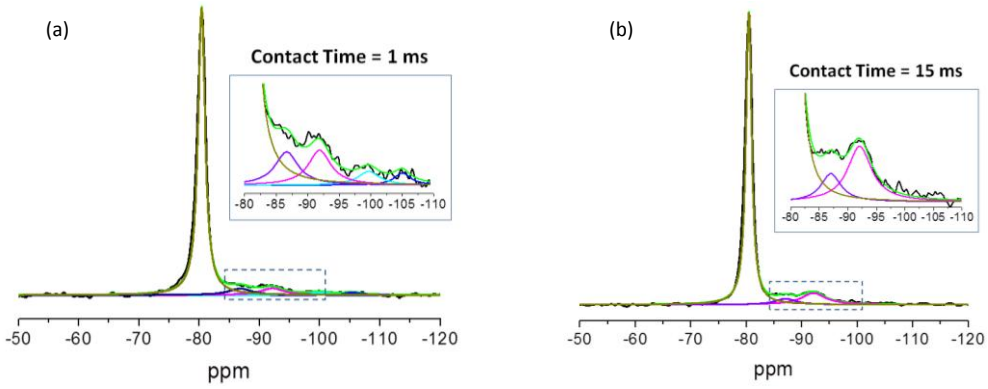

Figure 6-3. $^{1}H \rightarrow ^{29}Si$ CP/MAS NMR spectra of freeze-dried aluminosilicate nanotubes at contact times of (a) 1 ms, and (b) 15 ms.

Structural interpretation of chemical shifts in the −80 to −110 ppm region is complicated because this region is composed of overlapping signals from Q^4, Q^3, and Q^2 environments [81, 170, 177-179]. Both silicate and aluminosilicate environments [81] were reported for peaks included in this broad region. However, previous studies can provide guidelines in the interpretation of these peaks. ^{29}Si chemical shifts are highly sensitive to the second coordination sphere. For example, a 5.5 ppm chemical shift difference within pairs of ^{29}Si signals (−86.6 and −92.1, or −100 and −105.5 ppm) indicates aluminum deshielding in the second coordination sphere of Si atoms in a Q^4 aluminosilicate unit [180]. Moreover, when one or two hydroxyl groups are attached to Si atoms (i.e., Q^3 and Q^2) in a silica gel, chemical shifts of −99.8 and −90.6 ppm respectively are reported with a 10 ppm difference [178, 179]. The fact that the tail of the broad peak tail never reaches −110 ppm indicates that there is no Si(0Al) or pure polymerized silica in the sample [179].

Table 6-1 shows all the possible Si configurations consistent with the above discussion. It also shows likely configurations of water binding to the Q^3 Si(6Al)−OH units as suggested by 2D HETCOR studies described earlier in this report. As summarized in Table 6-1, the Si environments (−86.6 and −92.1 ppm, or −100 and −105.5 ppm) correspond to a range of Q^4 Si(*n*Al) units, where n = 1−4 is the number of Al atoms in the coordination sphere. However, the peaks at *ca.* −92.1 and −100 ppm could also be assigned to Q^2 and Q^3 silanols, respectively [170, 177]. The peak at −105.5 ppm is assigned to resonances arising from coordinations to 3 Si atoms (3Si, 1Al) [177, 181]. It should also be noted that the proton environments bound to the Si configurations are confirmed by ^{1}H NMR studies, as described later in this Chapter.

Table 6-1. Chemical environments detected by HETCOR and CP experiments.

δ (ppm)	**Peak Area (%)**	**Possible Chemical Environments**
-80.4	83	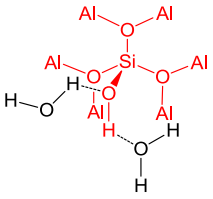
-86.6	6	

-92.1	6	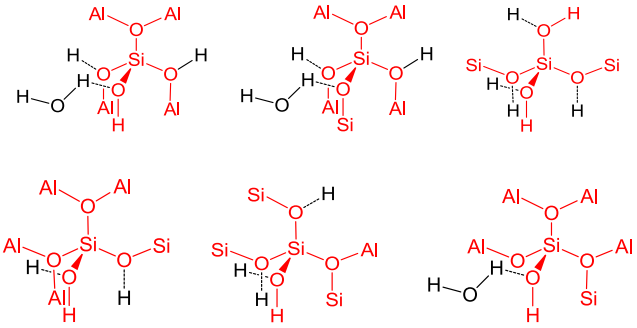
-100.0	2	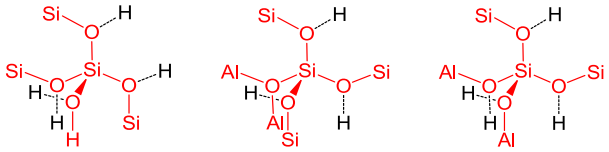
-105.5	2	

6.3.2 ^{1}H-^{27}Al FSLG-HETCOR Experiments

High-resolution heteronuclear ^{1}H-^{27}Al correlation NMR spectra are shown in Figure 6-4. The nature of the evolving proton species around Al at various stages of nanotube synthesis are demonstrated in Figures 6-4a−6-4d. Throughout the reaction (both during aging and heating), Al remains hexacoordinated with the same chemical shift as in the final nanotubes. However, the proton environment around hexacoordinated Al undergoes significant changes different from that of the protons around Si. Tetrahedrally coordinated Al atoms are not visible in ^{1}H-^{27}Al HETCOR spectra even though their presence is confirmed by 1D ^{27}Al spectra [1]. This does not necessarily preclude a correlation between proton and tetrahedral Al, which comprises less than 1%

of total detectable Al in the nanotube. Therefore, it likely does not appear above noise level at a contact time of 200 μs. Further studies may be necessary to reveal proton correlations of tetrahedral Al.

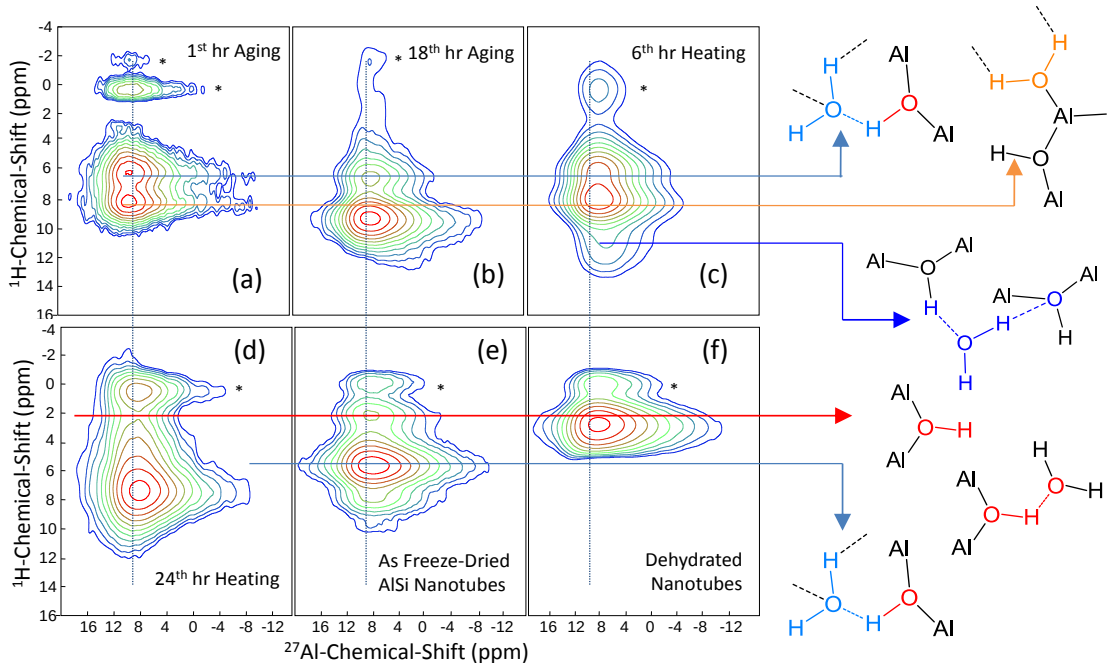

Figure 6-4. 2D ^{1}H-^{27}Al FSLG-HETCOR spectra of (a-d) freeze-dried samples collected at various times during the synthesis, (e) freeze-dried AlSiOH nanotubes, and (f) nanotubes dehydrated *in vacuo* at 250 ˚C. Contact time is 200 μs in all experiments. (*) indicates center spin-lock frequency and spinning side bands.

At the very early stages of synthesis, aluminosilicate intermediates are rapidly formed as the aluminum sec-butoxide and tetraethoxysilane precursors are hydrolyzed. Butoxy (-OC_4H_9) groups around the Al atoms are rapidly replaced by hydroxyl groups (Al-OH) and strongly bound water molecules (Al-OH_2) to produce octahedral sites. It is known that at 1 h of aging [1], hydroxylated aluminosilicate precursors of different sizes exist in synthesis solutions, as indicated by the orange arrow in Figure 6-4. A main cause of the broadening of the ^{27}Al negative chemical shift region at early stages of aging is the

asymmetric distribution of water and hydroxyl ligands around Al atoms in a variety of aluminosilicate species ($Al_{1-12}Si_X$) [1]. Thus, the peak near 9 ppm is attributed to water attached to Al atoms. The peak near 6 ppm is due to water molecules adsorbed to the bridging hydroxyl groups [$Al_2(OH)\cdots\boldsymbol{H_2O}$] as depicted by light blue in Figure 6-4. As aging proceeds, hydroxyl bridges between Al atoms are formed. This rearrangement is indicated by a decrease in the ^{27}Al linewidth (Figures 6-4b−6-4c). Upon heating, new proton environments arise around 12 ppm due to the condensation of the hydroxylated complexes as depicted by the dark blue arrow in Figure 6-4. Rearrangement takes place by elimination of water molecules and formation of hydroxyl bridges indicated by the red arrow in Figure 6-4. When the nanotubes are dehydrated, isolated bridging hydroxyl protons (Al_2-***OH***) are observed at a ^1H chemical shift of 3 ppm (Figure 6-4f).

6.3.3 ^1H MAS and ^1H CRAMPS NMR

High-resolution 1D ^1H MAS and ^1H CRAMPS NMR can give direct information about different hydroxyl groups and their environments in the aluminosilicate nanotubes. However, no previous study exists on this aspect, and very little ^1H chemical shift data are available for single-walled metal-oxide nanotubes [109]. The nanotubes are hydrated up to 20 *wt*% at room temperature after freeze-drying [109]. Due to the dominance of signal from water molecules, only a single peak is observed in ^1H MAS NMR spectra. Hence, ^1H MAS NMR has not been commonly employed as a method of characterizing the nanotubes. In this Chapter, the 2D HETCOR experiments described earlier, in conjunction with 1D ^1H MAS and ^1H CRAMPS NMR discussed in this section, allowed

us to assign accurate molecular environments to individual ^{1}H chemical shifts. These spectra are shown in Figure 6-5 with peak assignments summarized in Table 6-2.

Figure 6-5a displays the ^{1}H MAS NMR spectrum of the freeze-dried hydrated aluminosilicate nanotubes, which includes spinning side bands, showing how phase correction of spectra is done before spectral deconvolution. Figure 6-5b shows the main peak in the ^{1}H MAS NMR spectrum along with deconvolved peaks that were obtained by fitting with a combination of Lorentzian and Gaussian peaks using DMfit software [182]. The number of underlying peaks was selected based on the number of proton environments suggested by 2D HETCOR studies described earlier in this report. Thus, four fitted peaks are shown in Figure 6-5b at 4 ppm (area = 31% of total), 5 ppm (19%), 6 ppm (11%), and at 7 ppm (39%). The peaks at 5−6 ppm are due to water molecules hydrogen-bonded to surface hydroxyl groups at Si and Al sites in the intra-tube and inter-tube channels (*cf.* Table 6-2, left column). An intense broad peak centered at 7 ppm is due to the inner-wall silanol (Si-***OH***$\cdots OH_2$) groups with bound water molecules in a variety of possible configurations (*cf.* Table 6-1). The 4 ppm peak is assigned to bridging hydroxyl (Al_2-***OH***$\cdots OH_2$) groups with bound water molecules, as also suggested by the HETCOR measurements. For nanotubes dehydrated at 250 ˚C under vacuum for 24 h, two peaks (at 3 ppm and 5 ppm) were sufficient to deconvolute the ^{1}H MAS spectrum. The main peak (area = 60% of the total) of the ^{1}H MAS NMR spectrum shifts to 3 ppm (Figure 6-5c) and is due to the bridging hydroxyl (Al_2-***OH***) groups on the outer wall, whereas the 5 ppm peak (40%) is due to the inner-wall silanols (Si-***OH***).

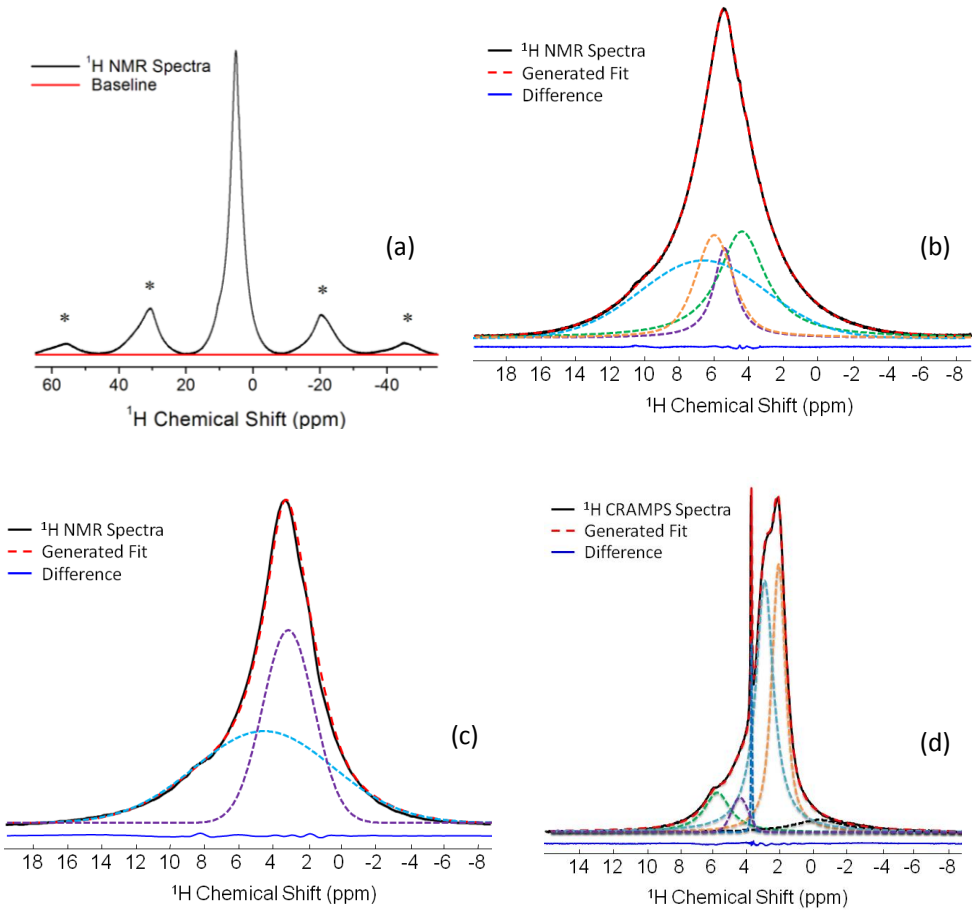

Figure 6-5. ^{1}H MAS NMR spectra of freeze-dried hydrated (20 *wt*% water) aluminosilicate nanotubes: (a) with indicated spinning side bands (*) showing phase correction before deconvolution, and (b) the center peak with deconvolved peaks. ^{1}H MAS NMR spectra of nanotubes dehydrated at 250 ˚C under vacuum for 24 h: (c) the center peak with deconvolved peaks, and (d) CRAMPS spectrum showing deconvolved peaks.

Without information on ^{1}H chemical shifts as obtained from 2D HETCOR spectra, it would have been difficult to reliably deconvolute and interpret the ^{1}H MAS NMR spectra. To assign more precise structural locations to ^{1}H signals, the hydroxyl groups can be distinguished by their coupling to Al or Si nuclei with the use of 2D FSLG-HETCOR NMR. However, the use of ^{1}H CRAMPS data allows us to accurately resolve and confirm the proton environments. ^{1}H CRAMPS increases the spectral

resolution of ^{1}H MAS NMR spectra by suppressing homonuclear dipolar interactions between protons. It was found that the technique was only successful with the complete elimination of water molecules. Six clearly distinguishable ^{1}H CRAMPS resonances were identified after the removal of bound water by *in vacuo* dehydration at 250 ˚C for 24 h (Figure 6-5d and Table 6-2, right column). In the solid form, the nanotubes are organized into a network of bundles within which the individual nanotubes are arranged in a monoclinic or hexagonal packing [40, 109]. The resonance near 3 ppm is assigned to *Al* bridging protons involved in hydrogen bonding to oxygen atoms on the outer wall of an adjacent nanotube (Al_2-*OH*···*O*). The peak at 2 ppm arises from protons in isolated bridging (Al_2-***OH***) groups on the outer nanotube circumference. The peak at 6 ppm is assigned to the protons associated with the isolated Si-OH groups on the inner walls. The ratio of the area percentages of Al bridging protons (36%) to silanol protons (10%) is about 3, further supporting the interpretation based on the chemical formula of the nanotube material [$(OH)_3Al_2O_3Si(OH)$].

Table 6-2. Structural representations of ^{1}H MAS and ^{1}H CRAMPS NMR peak assignments.

δ (ppm)	**Area (%)**	**^{1}H MAS NMR**	**δ (ppm)**	**Area (%)**	**^{1}H CRAMPS NMR**
4	31	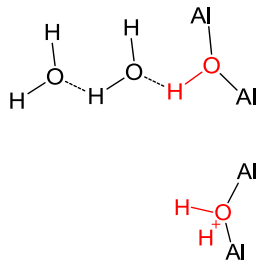	**-0.5**	2	
			2	36	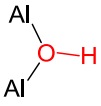

Table 6.2 (continued).

5-6	30	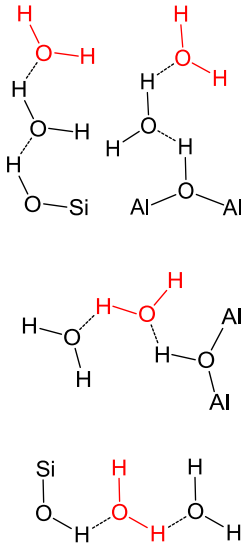	**3**	46	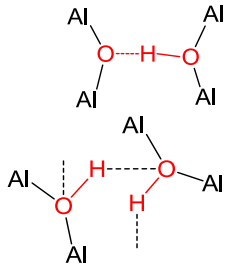
			3.7	2	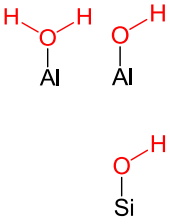 Extra-framework
7	39	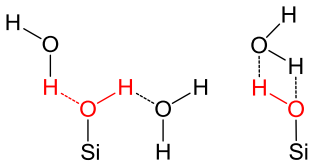	**4.5**	3	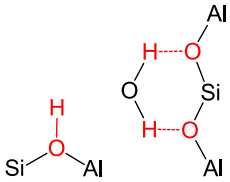
			6.0	10	

The above assignments cover the expected proton environments in the perfect nanotube structure. In addition, there is a sharp peak at 3.7 ppm which possibly belongs to mobile water or hydroxyl ligands in extra-framework Al or Si species such as those observed in zeolites [183]. A broad resonance near 4.5 ppm is assigned to hydroxyl protons that bridge Si and Al atoms (Al-***OH***-Si) in lattice defects (2% of total spectral area) [177, 184]. The −0.5 ppm peak is probably due to (Al-***OH***) protons in lattice defects at the outer nanotube wall or nanotube ends [176, 185]. In summary, ^{1}H CRAMPS spectra of dehydrated nanotube revealed the existence of a variety of proton

environments in the nanotube structure, and also confirmed that dehydration at 250 ˚C removes the bound water without any significant effect on the nanotube structure [109]. It is suggested that the simplicity of this method may render it very useful in studying structural transformations (e.g., induced by heating at higher temperatures) or chemical surface modifications of nanotube materials.

6.3.4 Proposed Defect Structures

As evinced by a combination of NMR techniques, several types of disordered regions exist in aluminosilicate nanotubes. By integrating NMR findings described previously in this Chapter, the defect structures likely to exist in the aluminosilicate nanotubes are depicted in Figure 6-6. As discussed before, any kind of defect would introduce lattice strain, which is a possible cause for the broadening of ^{27}Al NMR line shapes. ^{29}Si chemical shifts are more sensitive to changes in the surrounding atoms, and thereby provided more definite clues regarding the structure of the defects. The study presented in this Chapter confirm that the disordered regions are part of the nanotube walls, and not an impurity phase. The broad resonances seen in ^{27}Al, ^{29}Si, and ^{1}H NMR spectra may even originate from the same defective region which may constitute approximately up to ~10% of the overall nanotube structure based on their average NMR percentages. The most probable defect structures are those that incorporate species represented by the −80 to −90 ppm ^{29}Si chemical shift region, due to their dominance in the ^{29}Si NMR spectra over other defect peaks. Figure 6-6 illustrates the most frequent structural defects in nanotubes as deduced from NMR data, together with the corresponding chemical environments which are confirmed by the comprehensive ^{1}H,

^{27}Al and ^{29}Si NMR investigation. The remaining, less probable, defects are shown in Figure 6-8.

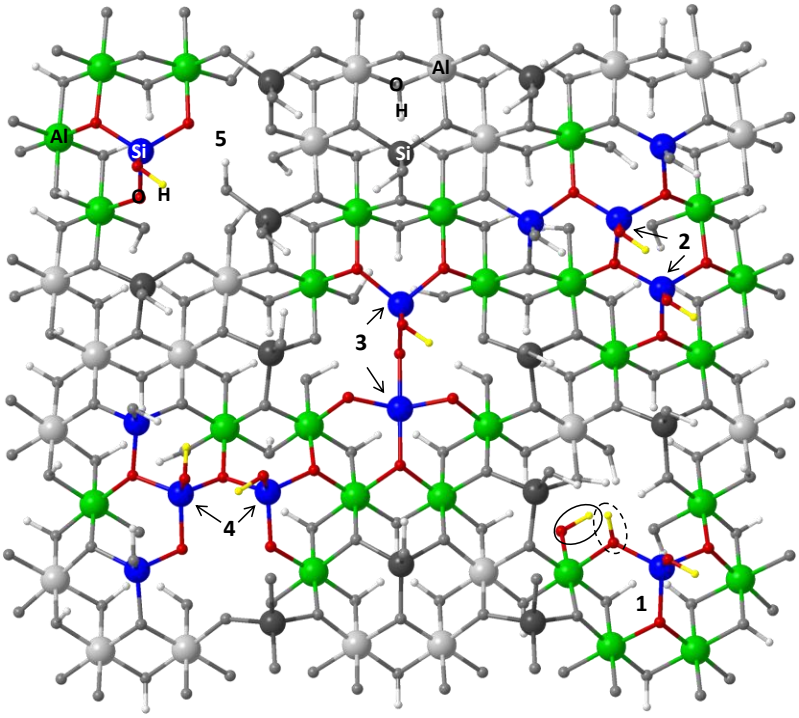

Figure 6-6. Cross-section of single-walled aluminosilicate nanotube inner wall. Colored areas indicate disordered Al, Si, and H environments created by defects (numbered 1 to 5 and discussed in the text). The NMR confirmation details are shown in Figure 6-8.

A brief discussion of each type of defect depicted in Figure 6-6 is given as follows: *Defect 1* involves the absence of an Al atom from the nanotube wall, resulting in voids similar to those observed in allophanes [121, 186, 187]. Such Al vacancy defects might be the source of dangling Al-OH bonds in an otherwise perfectly hydroxyl-bridged Al lattice [176, 185]. One such Al-OH bond is colored and circled with a solid line in Figure 6-6. It is the source of the ^{1}H NMR signal observed at −0.5 ppm [185]. This defect also leads to Si-OH-Al hydroxyls (^{1}H NMR signal at 4.5 ppm) bridging the inner and outer walls of the nanotubes, as indicated by a dashed circle in Figure 6-6. It should be noted that similar Al-OH and Si-OH-Al environments can be observed as a result of

nearly all defects depicted in Figure 6-6, and the resulting ^{1}H NMR signals are therefore not limited to Defect 1. Defect 1 results in a ^{29}Si NMR signal at around −86.6 ppm. *Defect 2* involves the presence of an additional Si atom in the inner wall, causing the formation of Si-O-Si bonds. This defect causes the formation of two irregular chemical environments around Si [(3Al, 3Si), (5Al, 1Si)] as indicated in Figure 6-6. Both can give rise to ^{29}Si NMR signal near −86.6 ppm. In any type of defect, as in this one, an asymmetric environment around aluminum emerge, possibly the cause for quadrupolar broadening. Moreover, the broadening of peaks centered around −90 ppm in ^{29}Si spectra is possibly due to such Defect 2 induced lattice strains. *Defect 3* indicates the absence of two Al atoms in the outer wall that could cause instability or lattice strain, compensated by the condensation between two adjacent silanols along the nanotube circumference. This results in the formation of defective Q^4 and Q^3 Si sites giving rise to ^{29}Si NMR signals near −92.1 ppm. *Defect 4* involves the absence of an Al atom and an extra Si atom in the framework, resulting again in the formation of Si-O-Si bonds. *Defect 5* depicts the formation of Q^3(4Al) Si-OH groups due to missing two Al atoms in the outer framework. Both Defect 4 and Defect 5 are evinced by the broad signal centered at −92.1 ppm. Please see Figure 6-8 for the chemical environments around each defect and NMR confirmation. Figure 6-6 shows each type of defect only once, but it is seen that vacancy-type defects result in multiple distorted chemical environments around the vacancy. This explains the observation of a high defect percentage in the nanotube structure (which involves as much as ~16% of the Si atoms). Most of the defects are due to vacancies/"holes" in the nanotube wall. The existence of such structures has interesting implications for the nanotube properties and potential applications [40, 107].

6	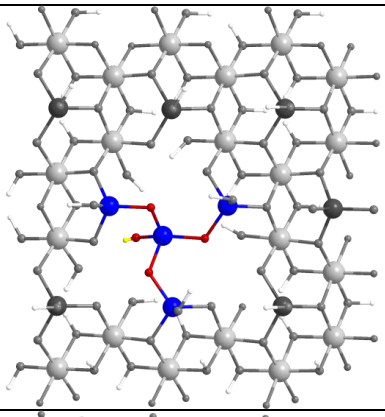	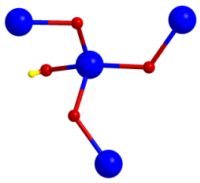 *^{29}Si/ca. -100 ppm*
7	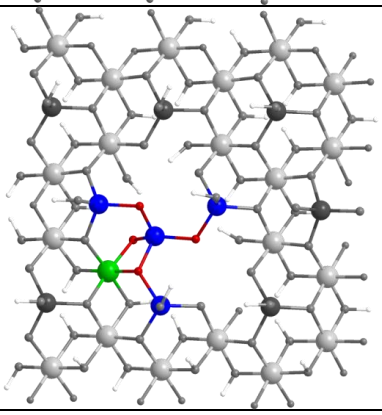	 *^{29}Si/ca. -105.5 ppm*
8	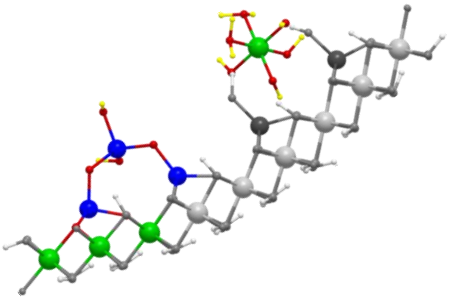	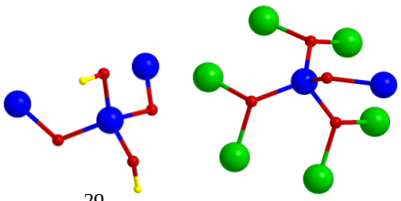 *^{29}Si/ca. -92.1 ppm* 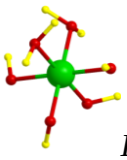 *Extraframework Al: attached to framework through hydrogen bonding (^{1}H/ca. 37 ppm)*

Figure 6-7. Three additional defects in the nanotube structure (numbered 6−8). Defects 6 and 7 account for about 2% of the overall ^{29}Si NMR signal. Defect 8 depicts other possible defective regions that might be represented by the −92.1 ppm peak. Also, it shows an extra-framework Al that is detected by ^{1}H NMR. Extra-framework Al can attached to outer or inner walls through hydrogen bonding with rather mobile −OH and $-OH_2$ groups.

1	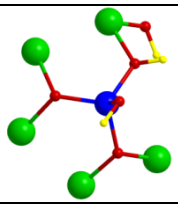	*^{29}Si/ca. -86.6 ppm* *^{1}H/ca. -0.5 ppm* *^{1}H/ca. 4.5 ppm*
2	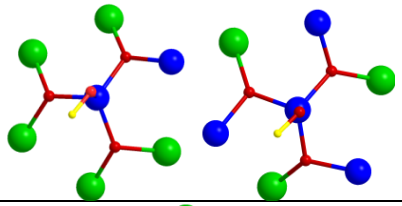	*^{29}Si/ca. -86.6 ppm* *^{1}H/ca. -0.5 ppm*
3	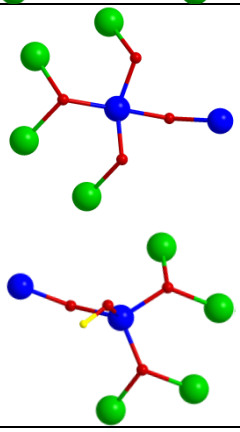	*^{29}Si/ca. -92.1 ppm* *^{1}H/ca. -0.5 ppm* *^{1}H/ca. 4.5 ppm (not depicted)*
4	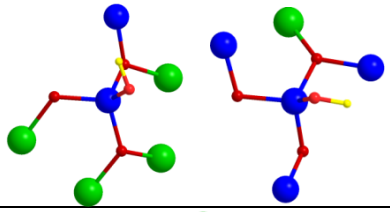	*^{29}Si/ca. -92.1 ppm* *^{1}H/ca. -0.5 ppm* *^{1}H/ca. 4.5 ppm (not depicted)*
5	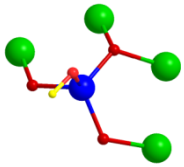	*^{29}Si/ca. -92.1 ppm* *^{1}H/ca. -0.5 ppm* *^{1}H/ca. 4.5 ppm (not depicted)*

Figure 6-8. Close-ups of the chemical environments of the Defects 1−5 in Figure 6-6, with corresponding NMR confirmations.

CHAPTER 7

CONCLUDING REMARKS AND FUTURE RESEARCH

7.1 Summary and Conclusions of this Work

In this thesis, significant advances in discovering novel design principles to control the structure and dimensions of single-walled metal oxide nanotubes at multiple length scales have been demonstrated. This knowledge constitutes a large leap over current empirical approaches for manipulating the synthesis of nanoscopic objects. To begin with, a detailed molecular-level account of the formation mechanism of single-walled aluminosilicate nanotubes – for the first time – is provided. It leads to a clear understanding of the main speciation and nanotube assembly processes. ESI−MS is shown to be an excellent tool for analysis of the precursor species in nanotube synthesis solutions. The structure of nanotube-like precursors are elucidated, including the proposed sheet-like precursor called “proto-imogolite”. In fact, it is shown that there are multiple precursors of this type, not just a single “proto-imogolite” precursor. Nanotube assembly is shown to be preceded by the formation of precursors that already possess a similar chemical coordination environment of the Al and Si atoms, as well as an inherent tendency to form curved nanostructures. The condensation of these proto-nanotube precursors into larger nanoparticles upon heating (as observed by the disappearance of these species in ESI−MS spectra) provides a clear connection to the subsequent formation of ordered nanotubes.

Such mechanistic understanding also provides a possible basis for engineering *curved nanoscale objects* (nanoshells and nanospheres) beyond simple inorganic nanomaterials and can create new classes of complex nanoscale objects of controlled shape, composition, size and structure from the minimum amount of matter necessary. The discovery of generalizable 'design rules' for constructing nanoscopic metal oxide objects of precise dimensions (e.g., 0-D and 1-D objects such as nanotubes, nanowires, and nanoshells) is of wide scientific and technological interest, but is currently in its infancy. In this thesis, two important steps towards this goal are demonstrated, utilizing the molecular-level insights obtained from this work. Firstly, it is shown that the diameter of metal oxide nanotubes can be 'shaped' with Ångstrom-level precision by directly controlling the shape and structure of molecular and nanometer-scale precursors responsible for nanotube formation. This was achieved by the use of different complexing ligands that allowed the precursor curvatures to be subtly varied. Secondly, the relationships between subtle alterations of the reactant composition, their effect on the structure and shape of the molecular and nanoscale precursors, and the curvature of the final nanotube were measured (at the molecular level). Thus, for the first time, the existence of a deliberate molecular-level approach to shaping nanoscale metal oxide objects with a precision that is difficult to attain by conventional approaches is shown. These novel concepts elucidated here will be of considerable scientific interest and moreover catalyze new 'molecular-level' thought in the design and processing of inorganic nanomaterials for a range of possible uses.

Following the study of AlSiOH nanotubes, AlGeOH nanotube formation is then studied in detail. Results confirmed the larger curvature of AlGeOH precursors in comparison to AlSiOH precursors in prenucleating nanotube solutions. Results also led to the finding of the importance of hydrolysis rate differences between Al and Si/Ge sources in controlling the nanotube lengths. The differences between AlSiOH and AlGeOH nanotube synthesis have been discussed in comparative detail. The higher hydrolysis rate of TEOG than TEOS can explain the observation of aluminates in only aluminosilicate synthesis solutions. Equally importantly, this knowledge is utilized to provide a route to shorten AlSiOH nanotube lengths. In particular, AlSiOH nanotube length is controlled by the use of an Al precursor with a different hydrolysis rate (modified Al-sec butoxide) or by controlling the hydrolysis rate of Si/Ge sources. Results also neatly explain the observed differences in reported nanotube lengths for AlSiOH and AlGeOH nanotubes in the literature.

Next, a quantitative model of metal oxide nanotube growth is developed. This four-step kinetic model describes the nucleation and growth stages of single-walled metal oxide nanotubes in the presence of three main kinds of species, namely precursors, amorphous nanoparticles, and growing nanotubes. The model is capable of capturing time-dependent length distribution trends of aluminosilicate and aluminogermanate nanotubes throughout the synthesis. It explains how nanotube populations evolve in synthesis time as a result of two different growth mechanisms: (1) *precursor addition* in which precursors are added to growing nanotube ends, and (2) self-assembly of already nucleated and grown nanotubes via so-called *oriented attachment* mechanisms. The model also shows the ability to predict time-dependent nanotube length distributions

quite accurately when experimental conditions are changed. This result is supported by the experimental data collected for hydrothermal synthesis at different reactant concentrations. Proposed nanotube growth model, after further development and tuning to investigate the effect of other key synthesis variables like the temperature, can be used: (1) to suggest new ways of controlling the synthesis of nanotubes and other nanoscopic objects, and (2) technologically in the scale-up of nanotube synthesis reactors.

To round off this thesis work, advanced NMR characterization tools are used to understand and elucidate local defect structures in a complex nanoscopic material, i.e., an aluminosilicate single-walled nanotube. Such information is of great value in predicting and controlling the functional properties of the nanotube, which depend critically on the structure and composition of the walls. In particular, comprehensive ^{1}H CRAMPS, ^{1}H MAS, ^{29}Si CP/MAS, ^{1}H$\rightarrow^{27}$Al and ^{1}H$\rightarrow^{29}$Si FSLG-HETCOR measurements on as-made and dehydrated nanotubes are performed. The ^{1}H CRAMPS and ^{1}H MAS experiments revealed the interaction between bound water molecules and surface hydroxyl groups (Al_2=OH and Si−OH sites), and specificially showed the existence of six types of protons in the aluminosilicate nanotubes. ^{29}Si CP/MAS experiments selectively enhanced the Si signals with variable contact times, exposing a variety of previously obscured Si environments and indicating differences in the proton pools surrounding these environments. ^{1}H $\rightarrow^{27}$Al and ^{1}H $\rightarrow^{29}$Si FSLG-HETCOR measurements gave direct information about protons coordinated either with Al or Si, and their evolution throughout the synthesis. 2D correlation studies also confirmed ^{1}H NMR chemical shift assignments.

7.2 Future Work

7.2.1 Kinetic Model Extensions

Rationally controlling the dimensions and structures of single-walled metal oxide nanotubes and other nanoscopic objects is of significant interest. Therefore, extensions to the proposed kinetic model in this thesis are a worthy topic for future investigations. Future studies might include studying temperature- and pH-dependent nanotube length distributions and determining the behavior of the reaction rate constants with temperature. Such a study is also of high importance in order to understand the formation of different nanoscopic shapes such as aluminosilicate and aluminogermanate nanoshells [167]. Also, incorporating the reaction steps leading to precursor evolution in prenucleating solutions would result in a more generalized description of nanotube formation. Modeling of reactions steps such as TEOS or TEOG hydrolysis [188, 189] and reactions between Al and Si species, would lead to determination of P_0 concentrations, an understanding of formation of aluminate side materials such as boehmite, and also even controlling of Al/Si or Ge ratios in final nanotube structures. With the aid of highly effective TEM sample preparation and characterization technique introduced in this thesis to measure nanotube length distributions, further refinements of the proposed kinetic model can easily be made and compared to experimental data.

In fact, it is believed that main differences in between AlSiOH and AlGeOH nanotube synthesis systems arise from the differences in hydrolysis rates of TEOS and TEOG. Therefore, modeling steps leading to precursor formation such as hydrolysis of

TEOS [188], TEOG [189], and ASB together with interactions between Al and Si/or Ge that form nanotube precursors and developing methods to experimentally confirm simulated precursor concentrations are crucial in understanding the morphological differences between two nanotubes, namely aluminosilicate and aluminogermanate nanotubes.

7.2.2 Understanding Nanoscopic Shape Control

A very interesting observation is the formation of allophane [187], which is a hollow single-walled aluminosilicate nanoshell (~4 nm diameter) with the same stoichiometry as imogolite, and synthesized from same reactants but at higher pH values. These single-walled shell-like nanomaterials may attract a great deal of attention due to their application in areas such as drug delivery [167]. An aluminogermanate analogue has also been recently synthesized [167]. Theory of single-walled nanotube formation introduced in this thesis, namely that "*curvature of cylindrical nanoscopic objects can be controlled by the shape of the precursors*", could therefore be generalized in order to explain the formation of shell-like nanoscopic structures. Studying their formation in aqueous solutions *via* similar approaches introduced in this thesis may provide such a generalization. These nanoshell materials have so far been synthesized from millimolar concentrations. This may hinder some of the techniques (e.g., NMR) for studying their formation mechanism. Therefore, higher yield synthesis of these hollow spherical objects should also be developed.

7.2.3 New Nanotube Compositions

In order to broaden the potential applications of single-walled metal oxide nanotubes in electronic, optical, and catalytic applications, it is desirable to develop both exploratory as well as rational approaches by which different metals such as Ga, Fe, Sn, Ti, or Au, Cu could be introduced into nanotube structure (either as a part of the nanotube wall or occluded inside the nanotube channel) to modify its properties. A few such examples could be found in the literature. Recently, carboxylato-modified gold nanoparticles are immobilized on the AlSiOH nanotube surface by electrostatic interactions, resulting in thermally stable free-standing films that can be used as color filters and can also find applications as catalytic membranes [190]. Fe-containing AlSiOH nanotubes have also been synthesized from solutions containing $AlCl_3/FeCl_3/Na_4SiO_4$ mixtures and found to be a unique oxidation catalyst to obtain phenol from benzene with H_2O_2 [191]. Fe substitutes octahedral Al in aluminosilicate minerals up to 30 mol.% and tetrahedral substitution does not occur [192]. Theoretical studies predict that the incorporation of Fe ($0.05 \leq x \leq 0.1$; $x = Fe/(Fe + Al)$) into the nanotube structure would result in a drastic 2-3 eV drop in the bandgap [193].

REFERENCES

1. Yucelen, G.I., et al., *Formation of single-walled aluminosilicate nanotubes from molecular precursors and curved nanoscale intermediates.* Journal of the American Chemical Society, 2011. **133**(14): p. 5397-5412.

2. Yucelen, G.I., et al., *Shaping Single-Walled Metal Oxide Nanotubes from Precursors of Controlled Curvature.* Nano Letters, 2012. **12**(2): p. 827-832.

3. Iijima, S., *Helical microtubules of graphitic carbon.* Nature, 1991. **354**(6348): p. 56-56.

4. Baughman, R.H., A.A. Zakhidov, and W.A. de Heer, *Carbon nanotubes-the route toward applications.* Science, 2002. **297**(5582): p. 787-792.

5. Fan, S., et al., *Self-oriented regular arrays of carbon nanotubes and their field emission properties.* Science, 1999. **283**(5401): p. 512-514.

6. Coleman, J.N., U. Khan, and Y.K. Gun'ko, *Mechanical reinforcement of polymers using carbon nanotubes.* Advanced Materials, 2006. **18**(6): p. 689-706.

7. Sandler, J., et al., *Development of a dispersion process for carbon nanotubes in an epoxy matrix and the resulting electrical properties.* Polymer, 1999. **40**(21): p. 5967-5971.

8. Niu, C., et al., *High power electrochemical capacitors based on carbon nanotube electrodes.* Applied Physics Letters, 1997. **70**(11): p. 1480-1482.

9. Avouris, P., Z. Chen, and V. Perebeinos, *Carbon-based electronics.* Nat Nano, 2007. **2**(10): p. 605-615.

10. Harris, P.J.F., E. Hernandez, and B.I. Yakobson, *Carbon nanotubes and related structures: new materials for the twenty-first century.* American Journal of Physics, 2004. **72**(3): p. 415-415.

11. Tenne, R., et al., *Polyhedral and cylindrical structures of tungsten disulphide.* Nature, 1992. **360**(6403): p. 444-446.

12. Remskar, M., *Inorganic nanotubes, nolecular- and nano-tubes*, O. Hayden and K. Nielsch, Editors. 2011, Springer US. p. 391-412.

13. Remskar, M., et al., *Inorganic nanotubes as nanoreactors: the first MoS_2 nanopods.* Advanced Materials, 2007. **19**(23): p. 4276-4278.

14. Li, Y.D., et al., *Artificial lamellar mesostructures to WS_2 Nanotubes.* Journal of the American Chemical Society, 2002. **124**(7): p. 1411-1416.

15. Jun, C., et al., *Low-temperature catalytic preparation of multi-wall MoS_2 nanotubes.* Science in China Series B: Chemistry, 2003. **46**(2): p. 191-195.

16. Tenne, R., *Inorganic nanotubes and fullerene-like nanoparticles.* Journal of Materials Research, 2006. **21**: p. 2726-2743

17. Golberg, D., et al., *Boron nitride nanotubes.* Advanced Materials, 2007. **19**(18): p. 2413-2432.

18. Chopra, N.G., et al., *Boron nitride nanotubes.* Science, 1995. **269**(5226): p. 966-967.

19. Ma, R., et al., *Hydrogen uptake in boron nitride nanotubes at room temperature.* Journal of the American Chemical Society, 2002. **124**(26): p. 7672-7673.

20. Chen, J., et al., *Electrochemical hydrogen storage in MoS_2 Nanotubes.* Journal of the American Chemical Society, 2001. **123**(47): p. 11813-11814.

21. Ivanovskaya, V.V., Enyashin, A. N., Medvedeva, N. I.m Ivanovskii, A. L., *Electronic properties of superconducting $NbSe_2$ nanotubes.* Phys. Stat. Sol., 2003. **238**(3): p. R1-R3.

22. Remscaronkar, M., *Inorganic Nanotubes.* Advanced Materials, 2004. **16**(17): p. 1497-1504.

23. Ou, H.-H. and S.-L. Lo, *Review of titania nanotubes synthesized via the hydrothermal treatment: Fabrication, modification, and application.* Separation and Purification Technology, 2007. **58**(1): p. 179-191.

24. Yao, B.D., et al., *Formation mechanism of TiO_2 nanotubes.* Applied Physics Letters, 2003. **82**(2): p. 281-283.

25. Tenne, R., *Advances in the synthesis of inorganic nanotubes and fullerene-like nanoparticles.* Angewandte Chemie International Edition, 2003. **42**(42): p. 5124-5132.

26. Chandrappa, G.T., et al., *Hydrothermal synthesis of vanadium oxide nanotubes from V_2O_5 gels.* Catalysis Today, 2003. **78**(1–4): p. 85-89.

27. Xu, J., et al., *Electrochemical properties of anatase TiO_2 nanotubes as an anode material for lithium-ion batteries.* Electrochimica Acta, 2007. **52**(28): p. 8044-8047.

28. Lim, S.H., et al., *Room-temperature hydrogen uptake by TiO_2 nanotubes.* Inorganic Chemistry, 2005. **44**(12): p. 4124-4126.

29. Rao, C.N.R., Nath, M. , *Inorganic Nanotubes.* Dalton Trans., 2003. **1**: p. 1-24.

30. Cradwick, C.P.G., Farmer, V. C., Russell, J.D, Masson, C. R., Wada, K., Yoshigana, N., *Imogolite, a hydrated aluminum silicate of tubular structure.* Nature Phys. Sci., 1972. **240**: p. 187-189.

31. Bursill, L.A., J.L. Peng, and L.N. Bourgeois, *Imogolite: An aluminosilicate nanotube material.* Philosophical Magazine A, 2000. **80**(1): p. 105-117.

32. Farmer, V.C., Adams, M. J., Fraser, A. R., Palmieri, F., *Synthetic imogolite: properties, synthesis, and possible applications.* Clay Minerals, 1983. **18**: p. 459-472.

33. Mukherjee, S., V.M. Bartlow, and S. Nair, *Phenomenology of the growth of single-walled aluminosilicate and aluminogermanate nanotubes of precise dimensions.* Chemistry of Materials, 2005. **17**(20): p. 4900-4909.

34. Mukherjee, S., *Synthesis, characterization, and growth mechanism of single-walled metal oxide nanotubes*, in *School of Chemical and Biomolecular Engineering*. 2007, Georgia Institute of Technology.

35. Konduri, S., S. Mukherjee, and S. Nair, *Controlling nanotube dimensions: correlation between composition, diameter, and internal energy of single-walled mixed oxide nanotubes.* ACS Nano, 2007. **1**(5): p. 393-402.

36. Wada, S.I., Wada, K., *Effects of substitution of germanium for silicon in imogolite.* Clays and Clay Minerals, 1982. **30**(2): p. 123-128.

37. Farmer, V.C., Fraser, A. R., Tait, J. M., *Synthesis of imogolite: a tubular aluminum silicate polymer.* J. Chem. Soc., Chem. Comm., 1977. **13**: p. 462-463.

38. Levard, C., et al., *Formation and growth mechanisms of imogolite-like aluminogermanate nanotubes.* Chemistry of Materials, 2010. **22**(8): p. 2466-2473.

39. Koenderink, G.H., S.G.J.M. Kluijtmans, and A.P. Philipse, *On the synthesis of colloidal imogolite fibers.* Journal of Colloid and Interface Science, 1999. **216**(2): p. 429-431.

40. Bonelli, B., et al., *IR spectroscopic and catalytic characterization of the acidity of imogolite-based systems.* Journal of Catalysis, 2009. **264**(1): p. 15-30.

41. Kang, D.-Y., et al., *Single-walled aluminosilicate nanotubes with organic-modified interiors.* The Journal of Physical Chemistry C, 2011. **115**(15): p. 7676-7685.

42. Bottero, I., et al., *Synthesis and characterization of hybrid organic/inorganic nanotubes of the imogolite type and their behaviour towards methane adsorption.* Physical Chemistry Chemical Physics, 2011. **13**(2): p. 744-750.

43. Kang, D.-Y., et al., *Single-walled aluminosilicate nanotube/poly(vinyl alcohol) nanocomposite membranes.* ACS Applied Materials & Interfaces, 2012. **4**(2): p. 965-976.

44. Guimarães, L., et al., *Imogolite nanotubes: stability, electronic, and mechanical properties.* ACS Nano, 2007. **1**(4): p. 362-368.

45. Kuc, A. and T. Heine, *Shielding nanowires and nanotubes with imogolite: a route to nanocables.* Advanced Materials, 2009. **21**(43): p. 4353-4356.

46. Park, J.-H.L., et al., *Current-voltage characteristics of water-adsorbed imogolite film.* Bulletin of the Korean Chemical Society, 2008. **29**(5): p. 1048-1050.

47. Lee, Y.-H.K., et al., *Conducting properties of polypyrrole coated imogolite.* Bulletin of the Korean Chemical Society, 2006. **27**(11): p. 1815-1818.

48. Oh, J., et al., *Imogolite as an electron emitter and a water sensor.* Journal of Materials Science: Materials in Electronics, 2007. **18**(8): p. 893-897.

49. Lijuan, L., et al., *The electronic structure of a single-walled aluminosilicate nanotube.* Nanotechnology, 2008. **19**(17): p. 175702.

50. Yah, W.O.Y., K.; Jiravanichanun, N.; Otsuka, H.; Takahara, A., *Imogolite reinforced nanocomposites: multifaceted green materials.* Materials, 2010. **3**(3): p. 1709-1745.

51. Yamamoto, K., et al., *Transparent polymer nanohybrid prepared by in situ synthesis of aluminosilicate nanofibers in poly(vinyl alcohol) solution.* Soft Matter, 2005. **1**(5): p. 372-377.

52. Bac, B.H., et al., *Surface-modified aluminogermanate nanotube by OPA: Synthesis and characterization.* Inorganic Chemistry Communications, 2009. **12**(10): p. 1045-1048.

53. Yamamoto, K., et al., *Preparation of a novel (polymer/inorganic nanofiber) composite through surface modification of natural aluminosilicate nanofiber.* The Journal of Adhesion, 2002. **78**(7): p. 591-602.

54. Konduri, S., et al., *Water in single-walled aluminosilicate nanotubes: diffusion and adsorption properties.* The Journal of Physical Chemistry C, 2008. **112**(39): p. 15367-15374.

55. Ohashi, F., et al., *Characterization of synthetic imogolite nanotubes as gas storage.* Journal of Materials Science, 2004. **39**(5): p. 1799-1801.

56. Zang, J., et al., *Flexibility of ordered surface hydroxyls influences the adsorption of molecules in single-walled aluminosilicate nanotubes.* The Journal of Physical Chemistry Letters, 2010. **1**(8): p. 1235-1240.

57. Imamura, S., Kokubu, T., Yamashita, T., Okamoto, Y., Kajiwara, K., Kanai, H., *Shape-selective copper-loaded imogolite catalyst.* Journal of Catalysis, 1996. **160**(1): p. 137-140.

58. Imamura, S., et al., *Imogolite: a possible new type of shape-selective catalyst.* Industrial & Engineering Chemistry Research, 1993. **32**(4): p. 600-603.

59. Qi., X., Yoon, H., Lee, S-H., Yoon, J., Kim, S-J., *Surface-modified imogolite by 3-APS-OsO_4 complex: Sythesis, characterization and its application in the dihydroxylation of olefins.* Journal of Industrial and Engineering Chemistry, 2008. **14**: p. 136-141.

60. Mukherjee, S., K. Kim, and S. Nair, *Short, highly ordered, single-walled mixed-oxide nanotubes assemble from amorphous nanoparticles.* Journal of the American Chemical Society, 2007. **129**(21): p. 6820-6826.

61. Farmer, V.C., et al., *Synthetic imogolite, a tubular hydroxyaluminium silicate,* in Developments in Sedimentology. 1979, Elsevier. p. 547-553.

62. Wilson, M.A., G.S.H. Lee, and R.C. Taylor, *Tetrahedral rehydration during imogolite formation.* Journal of Non-Crystalline Solids, 2001. **296**(3): p. 172-181.

63. Akitt, J.W., Farthing, A., *Aluminium-27 nuclear magnetic resonance studies of the hydrolysis of aluminium (III). Part 4. Hydrolysis using sodium carbonate.* Journal of the Chemical Society, 1981(7): p. 1617-1623.

64. Inoue, K. and P.M. Huang, *Influence of citric acid on the natural formation of imogolite.* Nature, 1984. **308**(5954): p. 58-60.

65. Hu, S., et al., *Cluster-based self-assembly route toward MoO_3 single-walled nanotubes.* Chemistry - A European Journal, 2010. **16**(6): p. 1889-1896.

66. Yang, H., C. Wang, and Z. Su, *Growth mechanism of synthetic imogolite nanotubes.* Chemistry of Materials, 2008. **20**(13): p. 4484-4488.

67. Zhao, Y., et al., *Growth and surface properties of boehmite nanofibers and nanotubes at low temperatures using a hydrothermal synthesis route.* Langmuir, 2007. **23**(19): p. 9850-9859.

68. Horvoth, E., et al., *Hydrothermal conversion of self-assembled titanate nanotubes into nanowires in a revolving autoclave.* Chemistry of Materials, 2007. **19**(4): p. 927-931.

69. Kragten, D.D., et al., *Structure of the silica phase extracted from silica/(TPA)OH solutions containing nanoparticles.* The Journal of Physical Chemistry B, 2003. **107**(37): p. 10006-10016.

70. Kirschhock, C.E.A., et al., *Aggregation mechanism of nanoslabs with zeolite MFI-type structure.* The Journal of Physical Chemistry B, 1999. **103**(50): p. 11021-11027.

71. Davis, T.M., et al., *Mechanistic principles of nanoparticle evolution to zeolite crystals.* Nat Mater, 2006. **5**(5): p. 400-408.

72. Sarpola, A., Hietapelto, V., Jalonen, J., Jokela, J., Laitinen, R. S., *Identification of hydrolysis products of $AlCl_3$.6H2O in the presence of sulfate by electrospray ionization time-of-flight mass spectrometry and computional methods.* Phys. Chem. Chem. Phys., 2007. **9**: p. 377-388.

73. Delak, K.M., T.C. Farrar, and N. Sahai, *^{29}Si NMR sensitivity enhancement methods for the quantitative study of organosilicate hydrolysis and condensation.* Journal of Non-Crystalline Solids, 2005. **351**(27-29): p. 2244-2250.

74. Kloprogge, J.T., et al., *A ^{27}Al nuclear magnetic resonance study on the optimalization of the development of the Al-13 polymer.* Journal of Non-Crystalline Solids, 1992. **142**: p. 94-102.

75. Allouche, L., et al., *Al-30: A giant aluminum polycation.* Angewandte Chemie, 2000. **112**(3): p. 521-524.

76. Öhman, L.O. and U. Edlund, *Aluminum-27 NMR of Solutions*. Encyclopedia of Magnetic Resonance. 2007: John Wiley & Sons, Ltd.

77. Casey, W.H., *Large aqueous aluminum hydroxide molecules.* Chemical Reviews, 2005. **106**(1): p. 1-16.

78. Vogels, R.J.M.J., Kloprogge, J. T., Buinin, P. A., Seykens, D., Jansen., J. B. H., Geus, J. W., *The tridecameric aluminum complex as an appropriate precursor for fibrous boehmite:A ^{27}Al NMR study on the partial hydrolysis of aluminum sec-butoxide.* Journal of Non-Crystalline Solids, 1995. **191**: p. 38-44.

79. Vogels, R.J.M.J., J.T. Kloprogge, and J.W. Geus, *Homogeneous forced hydrolysis of aluminum through the thermal decomposition of urea.* Journal of Colloid and Interface Science, 2005. **285**(1): p. 86-93.

80. Akitt, J.W., Farthing, A., *Aluminium-27 nuclear magnetic resonance studies of the hydrolysis of aluminium(III). Part 5. Slow hydrolysis using aluminium metal.* Journal of the Chemical Society, 1981(7): p. 1624-1628.

81. Barron, P.F., Wilson, M. A., Campbell, A. S., Frost, R. L., *Detection of imogolite in soils using solid state ^{29}Si NMR.* Nature, 1982. **299**: p. 616-618.

82. Mackenzie, K.J.D., Bowden, M. E., Meinhold, R. H, *The structure and thermal transformations of allophanes studied by ^{29}Si and ^{27}Al high resolution solid state NMR.* Clay and Clay Minerals, 1991. **39**(4): p. 337-346.

83. Corbin, D.R., et al., *Comparison of analytical techniques for the determination of silicon and aluminum content in zeolites.* Analytical Chemistry, 1987. **59**(22): p. 2722-2728.

84. Kim, Y., Lee, S. K., Kirkpatrick, R. J., *Effects of intermediate range structure on the ^{29}Si NMR chemical shifts of framework silicates: Results for analcime.* Americal Mineralogist, 2010. **95**: p. 1694-1700.

85. Neuhoff, P.S., J.F. Stebbins, and D.K. Bird, *Si-Al disorder and solid solutions in analcime, chabazite, and wairakite.* American Mineralogist, 2003. **88**(2-3): p. 410-423.

86. Arago, J., Vicent, C., Julian, B., Cordoncillo, E., Escribano, P., *New insights on organosilane oligomerization mechanisms using ESI-MS and 29-Si-NMR.* New J. Chem., 2009. **33**: p. 1100-1108.

87. Eberlin, M.N., *Electrospray ionization mass spectrometry: a major tool to investigate reaction mechanism in both solution and the gas phase.* J. Mass. Spectrom., 2007. **13**: p. 19-28.

88. Urabe, T., Tsugoshi, T., Tanaka, M., *Characterization of aluminum species with nitrate, perchlorate and sulfate ions in the positive and negative ion mode by electrospray ionization mass spectrometry.* J. Mass. Spectrom., 2009. **44**: p. 193-202.

89. Urabe, T., Tsugoshi, T., Tanaka, M., *Electrospray ionization mass spectrometry investigation of the blocking effect of sulfate on the formation of aluminum tridecamer.* Journal of Molecular Liquids, 2008. **143**: p. 70-74.

90. Urabe, T., Tsugoshi, T., Tanaka, M., Kumakura, S., *Study on chemical specieation in aluminum chloride solution by ESI-Q-MS.* Journal of Mass Spectrometry, 2007. **42**: p. 591-597.

91. Bussian, P., et al., *Speciation in solution: silicate oligomers in aqueous solutions detected by mass spectrometry.* Angewandte Chemie, 2000. **39**(21): p. 3901-3905.

92. Sarpola, A., Hietapelto, V., Jalonen, J., Jokela, J., Laitinen, R. S., *Identification of the hydrolysis products of $AlCl_3.6H_2O$ by electrospray ionization mass spectrometry.* Journal of Mass Spectrometry, 2004. **39**: p. 423-430.

93. Simonsen, M.E. and E.G. Søgaard, *ESI-MS investigation of the polymerization of inorganic polymers.* International Journal of Mass Spectrometry, 2009. **285**(1-2): p. 78-85.

94. Lin, Y., L, D., *Electrospray mass spectrometry studies of purified aluminum tridecamer in a 50:50 water/acetonitrile mixture.* J. Phys. Chem. A, 2009. **114**: p. 3503-3509.

95. Singhal, A., Keefer, K. D., *A study of aluminum speciation in aluminum chloride solutions by small angle x-ray scattering and ^{27}Al NMR.* Mater. Res. Soc. Symp. Proc., 1994. **9**(8): p. 1973-1981.

96. Sarpola, A., Hietapelto, V., Jalonen, J., Jokela, J., Laitinen, R. S., *Comparison of hydrolysis products of $AlCl_3.6H_2O$ in different concentrations by electrospray ionization time of flight mass spectrometer (ESI TOF MS).* 2006. **86**(13): p. 1007-1018.

97. Pereira, J.C.G., C.R.A. Catlow, and G.D. Price, *Ab Initio studies of silica-based clusters. Part I. Energies and conformations of simple clusters.* The Journal of Physical Chemistry A, 1999. **103**(17): p. 3252-3267.

98. Caratzoulas, S., D.G. Vlachos, and M. Tsapatsis, *Potential of mean force for tetramethylammonium binding to cagelike oligosilicates in aqueous solution.* Journal of the American Chemical Society, 2006. **128**(50): p. 16138-16147.

99. Hu, J., T.W. Odom, and C.M. Lieber, *Chemistry and physics in one dimension: synthesis and properties of nanowires and nanotubes.* Accounts of Chemical Research, 1999. **32**(5): p. 435-445.

100. Choi, W., et al., *Dynamics of simultaneous, single ion transport through two single-walled carbon nanotubes: observation of a three-state system.* Journal of the American Chemical Society, 2010. **133**(2): p. 203-205.

101. Zang, J., et al., *Self-diffusion of water and simple alcohols in single-walled aluminosilicate nanotubes.* ACS Nano, 2009. **3**(6): p. 1548-1556.

102. Venkatesan, B.M. and R. Bashir, *Nanopore sensors for nucleic acid analysis.* Nat Nano, 2011. **6**(10): p. 615-624.

103. Branton, D., et al., *The potential and challenges of nanopore sequencing.* Nat Biotech, 2008. **26**(10): p. 1146-1153.

104. Kang, D.-Y., C.W. Jones, and S. Nair, *Modeling molecular transport in composite membranes with tubular fillers.* Journal of Membrane Science, 2011. **381**(1–2): p. 50-63.

105. Levard, C.m., et al., *Synthesis of imogolite fibers from decimolar concentration at low temperature and ambient pressure: a promising route for inexpensive nanotubes.* Journal of the American Chemical Society, 2009. **131**(47): p. 17080-17081.

106. Barrett, S.M., P.M. Budd, and C. Price, *The synthesis and characterization of imogolite.* European Polymer Journal, 1991. **27**(7): p. 609-612.

107. Levard, C., et al., *Synthesis of Ge-imogolite: influence of the hydrolysis ratio on the structure of the nanotubes.* Physical Chemistry Chemical Physics, 2011. **13**(32): p. 14516-14522.

108. Na, K., et al., *Directing zeolite structures into hierarchically nanoporous architectures.* Science, 2011. **333**(6040): p. 328-332.

109. Kang, D.-Y., et al., *Dehydration, dehydroxylation, and rehydroxylation of single-walled aluminosilicate nanotubes.* ACS Nano, 2010. **4**(8): p. 4897-4907.

110. Horvath, G., Kawazoe, K., *Method for the calculation of effective pore size distribution in molecular sieve carbon.* Society of Chemical Engineers, 1983. **16**(6): p. 470-475.

111. Saito, A. and H.C. Foley, *Curvature and parametric sensitivity in models for adsorption in micropores.* AIChE Journal, 1991. **37**(3): p. 429-436.

112. Abramoff, M.D., Magelhaes, P.J., Ram, S.J., *Image processing with ImageJ.* Biophotonics International, 2004. **11**(7): p. 36-42.

113. Derouane, E.G., *The energetics of sorption by molecular sieves: surface curvature effects.* Chemical Physics Letters, 1987. **142**(3–4): p. 200-204.

114. Rege, S.U. and R.T. Yang, *Corrected Horváth-Kawazoe equations for pore-size distribution.* AIChE Journal, 2000. **46**(4): p. 734-750.

115. Rouquerol, J., P. Llewellyn, and F. Rouquerol, *Is the BET equation applicable to microporous adsorbents?*, in Studies in Surface Science and Catalysis, F.R.-R.J.R. P.L. Llewellyn and N. Seaton, Editors. 2007, Elsevier. p. 49-56.

116. Konduri, S., S. Mukherjee, and S. Nair, *Strain energy minimum and vibrational properties of single-walled aluminosilicate nanotubes.* Physical Review B, 2006. **74**(3): p. 033401.

117. Pelster, S.A., W. Schrader, and F. Schoth, *Monitoring temporal evolution of silicate species during hydrolysis and condensation of silicates using mass spectrometry.* Journal of the American Chemical Society, 2006. **128**(13): p. 4310-4317.

118. Thill, A., et al., *Physico-chemical control over the single- or double-wall structure of aluminogermanate imogolite-like nanotubes.* Journal of the American Chemical Society, 2012. **134**(8): p. 3780-3786.

119. Otsuka, H. and A. Takahara, *Structure and properties of imogolite nanotubes and their application to polymer nanocomposites inorganic and metallic nanotubular materials*, T. Kijima, Editor. 2010, Springer Berlin / Heidelberg. p. 169-190.

120. d'Espinose de la Caillerie, J.-B., et al., *^{27}Al MQ-MAS NMR as a tool for structure determination in nanocomposite materials: the nature of Al pillars in "Al13−heidi" pillared clays.* The Journal of Physical Chemistry B, 2002. **106**(16): p. 4133-4138.

121. Goodman, B.A., et al., *Structural studies of imogolite and allophanes by aluminum-27 and silicon-29 nuclear magnetic resonance spectroscopy.* Physics and Chemistry of Minerals, 1985. **12**(6): p. 342-346.

122. Nofz, M., et al., *^{27}Al NMR study of Al-speciation in aqueous alumina-sols.* Journal of Sol-Gel Science and Technology, 2006. **38**(1): p. 25-35.

123. Wei, J., J. Chen, and J.M. Miller, *Electrospray ionization mass spectrometry of organogermanium compounds.* Rapid Communications in Mass Spectrometry, 2001. **15**(3): p. 169-181.

124. Schaack, B.B., W. Schrader, and F. Schüth, *Detection of structural elements of different zeolites in nucleating solutions by electrospray ionization mass spectrometry.* Angewandte Chemie International Edition, 2008. **47**(47): p. 9092-9095.

125. Wood, S.A. and I.M. Samson, *The aqueous geochemistry of gallium, germanium, indium and scandium.* Ore Geology Reviews, 2006. **28**(1): p. 57-102.

126. Pokrovski, G.S. and J. Schott, *Experimental study of the complexation of silicon and germanium with aqueous organic species: implications for germanium and silicon transport and Ge/Si ratio in natural waters.* Geochimica et Cosmochimica Acta, 1998. **62**(21-22): p. 3413-3428.

127. Murnane, R.J. and R.F. Stallard, *Germanium and silicon in rivers of the Orinoco drainage basin.* Nature, 1990. **344**(6268): p. 749-752.

128. Pokrovski, G.S., et al., *An X-ray absorption fine structure spectroscopy study of germanium-organic ligand complexes in aqueous solution.* Chemical Geology, 2000. **163**(1-4): p. 151-165.

129. Hu, J., et al., *The fused silicate route to protoimogolite and imogolite.* Journal of Non-Crystalline Solids, 2004. **347**(1–3): p. 224-230.

130. Wu, J. and P.F. James, *Mullite formation from gels derived from tetraethoxysilane or tetramethoxysilane with aluminium sec-butoxide.* Journal of Non-Crystalline Solids, 1997. **221**(2–3): p. 297-301.

131. Romanelli, G., et al., *Phenol tetrahydropyranylation catalyzed by silica-alumina supported heteropolyacids with Keggin structure.* Applied Catalysis A: General, 2004. **261**(2): p. 163-170.

132. Sinkó, K., *Influence of chemical conditions on the nanoporous structure of silicate aerogels.* Materials, 2010. **3**(1): p. 704-740.

133. Henderson, E.J., et al., *Colloidally stable germanium nanocrystals for photonic applications.* ACS Nano, 2010. **4**(12): p. 7683-7691.

134. Bernards, T.N.M., et al., *The effect of TEOG on the hydrolysis-condensation mechanism of a two-step sol-gel process of TEOS.* Journal of Non-Crystalline Solids, 1992. **142**(0): p. 215-224.

135. de Souza Santos, H. and P. de Souza Santos, *Pseudomorphic formation of aluminas from fibrillar pseudoboehmite.* Materials Letters, 1992. **13**(4–5): p. 175-179.

136. McBride, M.B. and L.G. Wesselink, *Chemisorption of catechol on gibbsite, boehmite, and noncrystalline alumina surfaces.* Environmental Science & Technology, 1988. **22**(6): p. 703-708.

137. Panias, D. and A. Krestou, *Effect of synthesis parameters on precipitation of nanocrystalline boehmite from aluminate solutions.* Powder Technology, 2007. **175**(3): p. 163-173.

138. Vieira Coelho, A.C., et al., *Surface area, crystal morphology and characterization of transition alumina powders from a new gibbsite precursor.* Materials Research, 2007. **10**: p. 183-189.

139. Allouche, L., et al., *Al-30: A giant aluminum polycation.* Angewandte Chemie International Edition, 2000. **39**(3): p. 511-514.

140. Li, Y., et al., *Direct synthesis of Al−SBA-15 mesoporous materials via hydrolysis-controlled approach.* The Journal of Physical Chemistry B, 2004. **108**(28): p. 9739-9744.

141. Alipour, A., et al., *Preparation of submicron alumina from aluminum 2-methoxyethoxide.* Materials Letters, 2001. **48**(1): p. 15-20.

142. Buisson, P., et al., *Encapsulation of lipases in aerogels.* Journal of Non-Crystalline Solids, 2001. **285**(1–3): p. 295-302.

143. Hernandez, C. and A.C. Pierre, *Influence of the sol−gel acidic synthesis conditions on the porous texture and acidity of SiO_2−Al_2O_3 catalysts with a low Al proportion.* Langmuir, 1999. **16**(2): p. 530-536.

144. Yuan, Z.-Y. and B.-L. Su, *Titanium oxide nanotubes, nanofibers and nanowires.* Colloids and Surfaces A: Physicochemical and Engineering Aspects, 2004. **241**(1–3): p. 173-183.

145. Wang, D., et al., B_2S_3 *nanotubes: Facile synthesis and growth mechanism.* Nano Research, 2009. **2**(2): p. 130-134.

146. Zhou, Z. and Y. Deng, *Kinetics study of ZnO nanorod growth in solution.* The Journal of Physical Chemistry C, 2009. **113**(46): p. 19853-19858.

147. Ethayaraja, M. and R. Bandyopadhyaya, *Mechanism and modeling of nanorod formation from nanodots.* Langmuir, 2007. **23**(11): p. 6418-6423.

148. Peng, X., et al., *Shape control of CdSe nanocrystals.* Nature, 2000. **404**(6773): p. 59-61.

149. Xu, X., et al., *A kinetic model for nanocrystal morphology evolution.* ChemPhysChem, 2007. **8**(5): p. 703-711.

150. Joshi, U.A. and J.S. Lee, *Template-free hydrothermal synthesis of single-crystalline barium titanate and strontium titanate nanowires.* Small, 2005. **1**(12): p. 1172-1176.

151. Avansi Jr, W., et al., *Growth kinetics of vanadium pentoxide nanostructures under hydrothermal conditions.* Journal of Crystal Growth, 2010. **312**(23): p. 3555-3559.

152. Lee, E.J.H., et al., *Growth kinetics of tin oxide nanocrystals in colloidal suspensions under hydrothermal conditions.* Chemical Physics, 2006. **328**(1–3): p. 229-235.

153. Wong, E.M., J.E. Bonevich, and P.C. Searson, *Growth kinetics of nanocrystalline ZnO particles from colloidal suspensions.* The Journal of Physical Chemistry B, 1998. **102**(40): p. 7770-7775.

154. Chun Zeng, H., *Ostwald Ripening: a synthetic approach for hollow nanomaterials.* Current Nanoscience. **3**(2): p. 177-181.

155. Yella, A., et al., *Asymmetric tungsten oxide nanobrushes via oriented attachment and Ostwald ripening.* CrystEngComm, 2011. **13**(12): p. 4074-4081.

156. Zhang, Q., S.-J. Liu, and S.-H. Yu, *Recent advances in oriented attachment growth and synthesis of functional materials: concept, evidence, mechanism, and future.* Journal of Materials Chemistry, 2009. **19**(2): p. 191-207.

157. Lee, E.J.H., et al., *Oriented attachment: an effective mechanism in the formation of anisotropic nanocrystals.* The Journal of Physical Chemistry B, 2005. **109**(44): p. 20842-20846.

158. Zhu, W., S. Zhu, and L. Xiang, *Successive effect of rolling up, oriented attachment and Ostwald ripening on the hydrothermal formation of szaibelyite $MgBO_2(OH)$ nanowhiskers.* CrystEngComm, 2009. **11**(9): p.1910-1919.

159. Zhang, J., et al., *A multistep oriented attachment kinetics: coarsening of ZnS nanoparticle in concentrated NaOH.* Journal of the American Chemical Society, 2006. **128**(39): p. 12981-12987.

160. Jihoon, O., et al. *Field emission and electrical properties of imogolite*. in Vacuum Nanoelectronics Conference, 2004. IVNC 2004. Technical Digest of the 17th International.

161. Farmer, V.C., A.R. Fraser, and J.M. Tait, *Synthesis of imogolite: a tubular aluminium silicate polymer*. Journal of the Chemical Society, Chemical Communications, 1977(13).

162. Maillet, P., et al., *Growth kinetic of single and double-walled aluminogermanate imogolite-like nanotubes: an experimental and modeling approach.* Physical Chemistry Chemical Physics, 2011. **13**(7): p. 2682-2689.

163. Farmer, V.C., B.F.L. Smith, and J.M. Tait, *The stability, free energy and heat of formation of imogolite.* Clay Minerals, 1979. **14**(2): p. 103-107.

164. Maillet, P., et al., *Evidence of double-walled Al−Ge imogolite-like nanotubes. A Cryo-TEM and SAXS investigation.* Journal of the American Chemical Society, 2010. **132**(4): p. 1208-1209.

165. Ribeiro, C., et al., *A kinetic model to describe nanocrystal growth by the oriented attachment mechanism.* ChemPhysChem, 2005. **6**(4): p. 690-696.

166. Drews, T.O., M.A. Katsoulakis, and M. Tsapatsis, *A mathematical model for crystal growth by aggregation of precursor metastable nanoparticles.* The Journal of Physical Chemistry B, 2005. **109**(50): p. 23879-23887.

167. Bac, B.H., et al., *Single-walled hollow nanospheres assembled from the aluminogermanate precursors.* Chemical Communications, 2009. **38**: p. 5740-5742.

168. Ildefonse, P., et al., *^{27}Al MAS NMR and aluminum X-ray absorption near edge structure study of imogolite and allophanes.* Clays and Clay Minerals, 1994. **42**(3): p. 276-287.

169. Hiradate, S. and S.-I. Wada, *Weathering process of volcanic glass to allophane determined by ^{27}Al and ^{29}Si solid-state NMR.* Clays and Clay Minerals, 2005. **53**(4): p. 401-408.

170. Burkett, S.L. and M.E. Davis, *Mechanism of structure direction in the synthesis of Si-ZSM-5: an investigation by intermolecular ^{1}H-^{29}Si CP MAS NMR.* The Journal of Physical Chemistry, 1994. **98**(17): p. 4647-4653.

171. Burum, D.P. and A. Bielecki, *An improved experiment for heteronuclear-correlation 2D NMR in Solids.* Journal of Magnetic Resonance (1969), 1991. **94**(3): p. 645-652.

172. Bielecki, A., A.C. Kolbert, and M.H. Levitt, *Frequency-switched pulse sequences: homonuclear decoupling and dilute spin NMR in solids.* Chemical Physics Letters, 1989. **155**(4-5): p. 341-346.

173. van Rossum, B.J., H. Förster, and H.J.M. de Groot, *High-field and high-speed CP-MAS ^{13}C NMR heteronuclear dipolar-correlation spectroscopy of solids with frequency-switched Lee–Goldburg homonuclear decoupling.* Journal of Magnetic Resonance, 1997. **124**(2): p. 516-519.

174. Marion, D., et al., *Rapid recording of 2D NMR spectra without phase cycling. application to the study of hydrogen exchange in proteins.* Journal of Magnetic Resonance (1969), 1989. **85**(2): p. 393-399.

175. Bennett, A.E., et al., *Heteronuclear decoupling in rotating solids.* The Journal of Chemical Physics, 1995. **103**(16): p. 6951-6958.

176. Arancibia-Miranda, N., et al., *Use of isoelectric point and pH to evaluate the synthesis of a nanotubular aluminosilicate.* Journal of Non-Crystalline Solids, 2011. **357**(7): p. 1750-1756.

177. Zhang, W., et al., *A high-resolution solid-state NMR study on nano-structured HZSM-5 zeolite.* Catalysis Letters, 1999. **60**(1): p. 89-94.

178. Jaymes, I. and A. Douy, *New aqueous mullite precursor synthesis. Structural study by ^{27}Al and ^{29}Si NMR spectroscopy.* Journal of the European Ceramic Society, 1996. **16**(2): p. 155-160.

179. Xu, M., et al., *Low-temperature modification of mesoporous MCM-41 material with sublimated aluminum chloride in vacuum.* The Journal of Physical Chemistry B, 2002. **106**(47): p. 12140-12143.

180. Merzbacher, C.I., K.J. McGrath, and P.L. Higby, *^{29}Si NMR and infrared reflectance spectroscopy of low-silica calcium aluminosilicate glasses.* Journal of Non-Crystalline Solids, 1991. **136**(3): p. 249-259.

181. Maciel, G.E. and D.W. Sindorf, *Silicon-29 NMR study of the surface of silica gel by cross polarization and magic-angle spinning.* Journal of the American Chemical Society, 1980. **102**(25): p. 7606-7607.

182. Massiot, D., et al., *Modelling one and two-dimensional solid-state NMR spectra.* Magnetic Resonance in Chemistry, 2002. **40**: p. 70-76.

183. Huang, J., et al., *Characterization and acidic properties of aluminum-exchanged zeolites X and Y.* The Journal of Physical Chemistry C, 2008. **112**(10): p. 3811-3818.

184. Dieter, F., *Enhanced resolution in the ^{1}H NMR spectra of zeolite H-ZSM-5 by heteronuclear dipolar-dephasing spin-echo MAS.* Chemical Physics Letters, 1995. **235**(1–2): p. 69-75.

185. Jiang, Y., et al., *Solid-state nuclear magnetic resonance investigations of the nature, property, and activity of acid sites on solid catalysts.* Solid State Nuclear Magnetic Resonance, 2011. **39**(3–4): p. 116-141.

186. Botan, A., et al., *Hydrodynamics in clay nanopores.* The Journal of Physical Chemistry C, 2011. **115**(32): p. 16109-16115.

187. Creton, B., et al., *Structural model and computer modeling study of allophane.* The Journal of Physical Chemistry C, 2007. **112**(2): p. 358-364.

188. Provis, J.L. and D.G. Vlachos, *Silica nanoparticle formation in the TPAOH−TEOS−H_2O system: a population balance model.* The Journal of Physical Chemistry B, 2006. **110**(7): p. 3098-3108.

189. Rimer, J.D., et al., *Self-Assembly and phase behavior of germanium oxide nanoparticles in basic aqueous solutions.* Langmuir, 2007. **23**(5): p. 2784-2791.

190. Kuroda, Y., K. Fukumoto, and K. Kuroda, *Uniform and high dispersion of gold nanoparticles on imogolite nanotubes and assembly into morphologically controlled materials.* Applied Clay Science, 2012. **55**(0): p. 10-17.

191. Ookawa, M., et al., *Oxidation of aromatic hydrocarbons with H_2O_2 catalyzed by a nano-scale tubular aluminosilicate, Fe-containing imogolite.* Research on Chemical Intermediates, 2008. **34**(8): p. 679-685.

192. Iriarte, I., et al., *Synthesis of kaolinite with a high level of Fe^{3+} for Al substitution.* clays and clay minerals, 2005. **53**(1): p. 1-10.

193. Alvarez-Ramírez, F., *First principles studies of Fe-containing aluminosilicate and aluminogermanate nanotubes.* Journal of Chemical Theory and Computation, 2009. **5**(12): p. 3224-3231.